An Investigation into the Growth and Characterisation of Thin Film Radioluminescent Phosphors for Neutron Diffraction Analysis.

Thomas Miller

A thesis submitted in partial fulfilment of the requirements of The Nottingham Trent University for the degree of Doctor of Philosophy

Nottingham Trent University

May 2010

Abstract

This investigation studied the growth and characterisation of thin film phosphors to examine the feasibility of enhancing a solid-state neutron scintillation detector system for increased detection resolution and detection rate. Undertaken in collaboration with the neutron facility ISIS at the Rutherford Appleton Laboratory, it was to examine whether an improved radioluminescent detector could be designed, based on the application of thin film phosphors.

Optimisation for the detector was in the areas of increased luminescent emission from each neutron captured, increasing the rate of capture for each measurement and improved spatial resolution.

The current ZnS:Ag,Cl phosphor used at ISIS was characterised in terms of its luminescent emission properties and comparisons were made to thin films of potential phosphor materials and the source material used to create the thin films. The phosphors were characterised via photo and radio-luminescent excitation to examine the spectral emission and the luminescent decay properties.

Thin films were grown onto a silicon substrate from a ZnS:Ag,Cl phosphor source using RF magnetron sputtering and were characterised in terms of morphology, crystallinity and luminescent properties. Thin films grown using this technique were found to not produce visible emission when excited with UV excitation nor alpha excitation. Following further literature research and using the analysis technique of Rutherford Backscattering it was concluded that the chlorine charge compensation dopant was lost during the growth process resulting in incomplete incorporation of the luminescent silver dopant into the lattice.

A range of chlorine doping methods were examined in order to promote charge compensation within the thin films, with the most controlled method using ion implantation, carried out at the Ion Beam Facility at Surrey University. Three samples of ZnS were grown to 800nm, followed by implantation of 0.01at% of silver and either 0.01at%, 0.05at% or 0.20at% of chlorine. Following implantation the thin films were thermally annealed to activate the samples and characterised by their luminescent emission via photo- and radioluminescent excitation.

The result of the study was that although a luminescent emission was created using laser excitation, the emission using a ^{241}Am source was of such low intensity they were uncharacterisable using the detection setup. The emission spectrum created by ZnS:Ag,Cl using the PL setup was not the standard broadband emission peak centred around 450nm, but was distorted so that it preferentially enhanced the emission around 485nm, hence create a shoulder peak. This is not significant to the optimisation of the detector, but important to know for characterisation purposes.

The emission and decay characteristics of the wafer used for neutron detection by ISIS and the ZnS:Ag,Cl powder purchased from Phosphor Technology are the same. Combining this with extensive experience within the research group of growing ZnS and ZnS:Mn thin films made this powder a suitable as a potential target material for thin film growth.

Independent of the calibration problem, the PL emission spectrum from thin films grown using RF magnetron sputtering should have been the same as the PL emission spectrum of the target material used in this technique. However, once a thin film had been grown there was no resultant emission observed. Testing the thin films using Rutherford Back Scattering found that although there were relative proportions of zinc, sulphur and silver there was no chlorine detected.

Alternative method of forming a thin film of ZnS:Ag,Cl were investigated, with the most significant method using ion implantation. This technique can accurately implant the small concentrations of dopant required into a thin film with good distribution, hence requiring minimal thermal processing for the dopants to be incorporated into the lattice to activate it. The result was a thin film that when annealed in a furnace in air it rapidly oxidised, where as when annealed under vacuum this did not occur. After a period of eight hours annealing at 600°C a PL emission was observed from the implanted thin films. When the emission spectrum was analysed there was a series of emission peaks. There was potential that one of these peaks related to the ZnS:Ag,Cl emission, however there was a prominent peak at 575nm which when further analysed with RBS and PIXE confirmed there had been contamination of manganese in the thin films.

Abbreviations and Symbols

℃	Degree Centigrade
Å	Angstrom
α	Alpha
β	Beta
γ	Gamma
λ	Wavelength
μA	Microamps
μCi	Microcuries
μm	Micrometres
μs	Microseconds
τ_d	Decay time
at%	Atomic percent
a.c.	Alternating Current
a.u.	Arbitrary Units
b	Barns
C	Coulomb
CCLRC	Central Laboratory of the Research Councils
cps	Counts per second
CRT	Cathode Ray Tube
CVD	Chemical Vapour Deposition
EL	Electroluminescence
EPSRC	Engineering and Physical Science Research Council
eV	Electron volts
FWHM	Full Width Half Maximum
Hz	Hertz
IBA	Ion Beam Analysis
IBC	Ion Beam Centre
ISIS	ISIS (Neutron and Muon beam facility)
J	Joules
K	Kelvin
KeV	Kilo electron volts
Kg	Kilo gram
LASER	Light Amplification by Stimulated Emission of Radiation
m	Metre
mA	Milli amp
meV	Milli electron volts
MeV	Mega electron volts

mg	Milli gram
mm	Millimetre
MOCVD	Metalorganic Chemical Vapour Deposition
mol%	Mol percentage
ms	Millisecond
MV	Mega volts
mW	Milli watts
n	Refractive index
NTU	Nottingham Trent University
nm	Nanometre
ns	Nanosecond
OPO	Optical Parametric Oscillator
Q	Disintegration energy
PC	Personal Computer
PDF	Powder Diffraction File
PIXE	Proton/Particle Induced X-ray Emission
PL	Photoluminescence
PMT	Photomultiplier tube
ppm	Parts per million
PSD	Pulse Shape Discrimination
PSI	Phase-Shifting Interfermoetry
psi	Pounds per square inch
PZT	Piezoelectric Transducer
RAL	Rutherford Appleton Laboratory
RBS	Rutherford Back Scattering
RF	Radio Frequency
RL	Radioluminescence
s	Second
SSP	Surelite Separation Package
Torr	Torricelli
UV	Ultraviolet
VSI	Vertical Scanning Interferometry
W	Watt
wt%	Weight percentage
XRD	X-ray Diffraction

Chemical Abbreviations

Ag	Silver
Al	Aluminium
Ar	Argon
Au	Gold
B	Boron
Cl	Chlorine
H	Hydrogen
^{3}H	Tritium
HeCd	Helium dadmium - laser
He	Helium
KrF	Krypton Fluorine - laser
Li	Lithium
LiF	Lithium fluoride
^{6}LiF	Enriched lithium fluoride
Mn	Manganese
$^{1}_{0}n$	Neutron
N_2	Nitrogen - laser
Nd:YAG	Neodymium-doped yttrium aluminium garnet ($Nd{:}Y_3Al_5O_{12}$) - laser
Si	Silicon
YAG	Yttrium aluminium garnet ($Y_3Al_5O_{12}$)
YAP	Yttrium aluminium perovskite activated by Ce^{3+} ($YAlO_3$)
ZnS	Zinc sulphide
ZnS:Ag	Zinc sulphide doped with silver (possible additional dopants as well as silver)
ZnS:Ag,Cl	Zinc sulphide doped with silver and chlorine
ZnS:Cl	Zinc sulphide doped with chlorine
ZnS:Mn	Zinc sulphide doped with manganese
ZnS:Tm	Zinc sulphide doped with Thallium

.

Acknowledgements

The most significant individual in this work has been my director of studies, Prof. Wayne Cranton. Giving me this opportunity to undertake this PhD along with his guidance and support have been invaluable in making this thesis and PhD what it is - it has been a defining period in my life and has shaped me considerably. Only his unique qualities have meant that I have been able to create this thesis, a task that has dominated my life and proven to be very challenging. Special gratitude goes to my second supervisors, Dr. Demosthenes Koutsogeorgis and Dr. Robert Ranson for their support and input. Their knowledge and experience of research and the equipment have been invaluable. Thank you.

At the University of Surrey Ion Beam Centre, thanks goes to Dr. Chris Jeynes, Dr. Melanie Webb, and Dr. Andy Smith for their patience, assistance in these specialist fields and enthusiasm for this work.

At the Nottingham Trent University, thanks goes to Dr. Gary Hix, Amanda Richards and Prof. Clive Thomas for their assistance in all things XRD, Radioactive and unexpected questions. A thank you goes to Dr. Jer Wang Chan and Dr. Costas Tsakonas for their open door to all those every day questions that pop up every day. To Steve Burton and Tim Randall - technicians at the university, but were so much more, thank you for keeping the computer and pumps going.

Thanks goes to Nigel Rhodes and Robert Stevens at RAL, the industrial link with this project.

Finally, a gratefully acknowledge the financial support from Engineering and Physical Science Research Council (EPSRC).

Thank you to Mike Megaw, Natalie Zahra and Jonathon Townsend for their time and energy in assisting me with all things badly spelt, nonsensical and badly presented. There were lots, so thank you lots. With your nudges in the right direction, it came together.

To my fellow PhD student over my studies Dr. Sharron Wilson, Dr. Sook Voon Yap, Dr. Gabriel Boutaud, Carly Farrow and Neranga Abeywickrama for providing distraction when it was needed.

A special thanks goes to my parents John and Joy, their support has been incalculable.

Table of contents

ABSTRACT I

ABBREVIATIONS AND SYMBOLS III

CHEMICAL ABBREVIATIONS V

ACKNOWLEDGEMENTS VI

TABLE OF CONTENTS VII

1 INTRODUCTION 1

1.1 AIMS AND OBJECTIVES 1

1.2 CONTEXT STATEMENTS 1

1.3 SUMMARY OF THESIS 2

2 BACKGROUND REVIEW AND THEORY 4

2.1 NEUTRON DIFFRACTION ANALYSIS 5

2.1.1 Neutron Generation 8

2.2 NEUTRON SCINTILLATION 9

2.2.1 Neutron Capture 11

2.2.2 Phosphors for Neutron Detectors 12

2.2.3 Decay Time 14

2.2.4 Optimum Thickness 16

2.2.5 Noise Created by Gamma Radiation 19

2.2.6 Picture Element Size of Diffraction Pattern 22

2.3 PHOSPHORS 23

2.3.1 Dopants 24

2.3.2 Chlorine Co-activator 24

2.4 RADIOLUMINANCE (RL) 26

2.4.1 Radiation Types 27

2.5 LUMINESCENCE 28

2.5.1 Excitation Mechanism 29

2.5.2 *Emission Mechanism:* *32*

2.5.3 *Emission Spectrum* *33*

2.5.4 *Decay Time Constant* *35*

2.6 THIN FILM DEPOSITION BY SPUTTERING 36

2.6.1 *Growth* *37*

2.6.2 *Annealing* *39*

2.6.3 *Thermal Annealing* *40*

2.6.4 *Laser Annealing* *41*

2.6.5 *Alternative Methods of Depositing Thin Film* *41*

2.6.5.1. Evaporation 41

2.6.5.2. Low-viscosity Epoxy 42

2.6.5.3. Gas Phase Chemical Processes 42

2.6.5.4. Atomic Layer Deposition (ALD) 42

2.7 SUMMARY 44

3 EXPERIMENTAL TECHNIQUES 46

3.1 INTRODUCTION 46

3.2 THIN FILM DEPOSITION BY RF MAGNETRON SPUTTERING 47

3.2.1 *Electrode* *48*

3.2.2 *Target Material* *49*

3.2.3 *Substrate* *51*

3.2.4 *Heater* *53*

3.2.4.1. Heater Calibration 54

3.2.5 *Vacuum* *58*

3.2.6 *Processing Gas and Sputtering Pressure* *59*

3.3 ALTERNATIVE METHOD OF DOPING 60

3.3.1 *Thin Film Deposition by Sputter Coating* *61*

3.3.2 *Ion Implantation* *62*

3.4 THIN FILM CHARACTERISATION 65

3.4.1 *Reflectance Spectrometry* *65*

3.4.2 *Stylus Profiler* *66*

3.4.3 Optical Profiling System *68*
3.4.3.1. PSI Mode 68
3.4.3.2. VSI Mode 69
3.5 CRYSTAL STRUCTURE AND COMPOSITION CHARACTERISATION 69
3.5.1 X-ray Diffraction *70*
3.5.1.1. Powder Sample 72
3.5.1.2. Solid Target Sample 72
3.5.1.3. Thin Film Sample 72
3.5.1.4. Si Substrate Sample 72
3.5.2 Ion Beam Analysis *73*
3.6 LUMINESCENCE CHARACTERISATION 76
3.6.1 Samples *76*
3.6.2 Excitation by UV Laser Source *78*
3.6.2.1. Emission Spectrum from Photoluminescence 78
3.6.2.2. Decay Constant System 80
3.6.2.3. Uniformity 83
3.6.3 Excitation by Alpha Source *83*
3.7 SUMMARY 84
4 CHARACTERISATION OF PHOSPHORS 86
4.1 INTRODUCTION 86
4.2 METHOD 86
4.2.1 Phosphors *86*
4.2.1.1. ZnS:Ag,Cl (ISIS) 87
4.2.1.2. ZnS:Ag,Cl (Phosphor Technology) 87
4.2.1.3. ZnS:Cl 88
4.2.1.4. ZnS:Tm 89
4.2.1.5. ZnS:Mn 90
4.2.1.6. ZnS 91
4.2.2 Excitation *92*
4.2.3 Emission *92*
4.2.4 Uniformity and Repeatability *93*

4.3 RESULTS 94

4.3.1 Excitation Source 94

4.3.1.1. N_2 Laser 94

4.3.1.2. HeCd Laser 95

4.3.1.3. Nd:YAG Laser 96

4.3.2 Emission Spectra 98

4.3.2.1. ZnS:Ag,Cl (ISIS) 98

4.3.2.2. ZnS:Ag,Cl (Phosphor Technology) 103

4.3.2.3. Other Phosphors (ZnS:Cl, ZnS:Tm, ZnS:Mn, ZnS) 104

4.3.3 Decay Measurements 110

4.3.4 Alpha Excitation 115

4.3.4.1. Alpha Excitation 115

4.3.4.2. Alpha Emission 116

4.3.5 Uniformity and Repeatability of the ISIS Scintillator 116

4.3.5.1. Repeatability 120

4.4 CONCLUSION 120

4.4.1 Excitation Sources 120

4.4.2 Emission Spectra 121

4.4.2.1. Decay Time 122

4.4.2.2. Uniformity 123

5 DEPOSITION AND CHARACTERISATION OF THIN FILMS 124

5.1 INTRODUCTION 124

5.2 METHOD 124

5.2.1 Calibration 124

5.2.1.1. Pressure Sensors 125

5.2.1.2. Temperature 125

5.2.1.3. Thickness 126

5.2.1.4. Contaminants 127

5.2.2 Growth 127

5.2.3 Thin Film Characterisation 128

5.3 RESULTS 130

5.3.1 Calibration ... 130
5.3.1.1. Calibration of Trace Monitor ... 130
5.3.1.2. Heater Calibration ... 131
5.3.1.3. ZnS:Mn Calibration ... 134
5.3.2 Characterisation of ZnS:Ag,Cl Thin Film Phosphors ... 135
5.3.2.1. Thickness ... 136
5.3.2.2. Adhesion ... 137
5.3.2.3. XRD Analysis ... 137
5.3.2.4. Ion Beam Analysis ... 143
5.3.2.5. Luminescence Characteristics ... 145
5.4 CONCLUSIONS ... 145
5.4.1 Calibration ... 145
5.4.2 Thin Film Properties ... 146
5.4.2.1. Growth Parameters ... 146
5.4.2.2. Surface Characterisation ... 146
5.4.2.3. XRD Analysis ... 147
5.4.2.4. RBS Analysis ... 147
5.4.3 Chlorine Co-activator ... 148
6 ALTERNATIVE METHODS OF ZNS:AG,CL THIN FILM PHOSPHOR FABRICATION. 149
6.1 INTRODUCTION ... 149
6.2 METHOD ... 149
6.2.1 Diffusion ... 150
6.2.2 Sputter Coating ... 151
6.2.2.1. Incorporation of Cl (NaCl) ... 152
6.2.2.2. Incorporation of Cl (ZnS:Cl) ... 153
6.2.3 Ion Implantation ... 154
6.2.4 Ion Beam Analysis ... 157
6.2.5 X-ray Diffraction ... 157
6.2.6 Thermal Processing ... 158
6.3 RESULTS ... 159

6.3.1 Luminescence of Ag Sputter Coated Films 159

6.3.1.1. Luminescence of Samples Doped Using NaCl 161

6.3.1.2. Luminescence of ZnS:Cl 161

6.3.2 Ion Implantation 162

6.3.3 Ion Beam Analysis 166

6.3.3.1. PIXE 166

6.3.3.2. RBS Results 167

6.3.4 X-ray Diffraction 168

6.3.4.1. ZnS Thin Film on a Si Substrate 168

6.3.4.2. ZnS Thin Film on a Si Substrate with Ion Implanted Dopants 169

6.3.4.3. ZnS Thin Film on a Si Wafer Implanted With Ag and Cl Ions then Annealed in Air 171

6.3.4.4. ZnS Thin Film on a Si Wafer Implanted With Ag and Cl Ions and Annealed in Vacuum 173

6.3.5 Annealing 174

6.4 CONCLUSIONS 175

6.4.1 Sputter Coating 176

6.4.2 Ion Implantation 176

6.4.3 Ion Beam Analysis 178

6.4.4 XRD 179

6.4.4.1. Ion Implantation – Effects on Structure 179

6.4.4.2. Thermal Annealing – in Air 179

6.4.4.3. Annealing in Vacuum 180

7 CONCLUSIONS AND FUTURE WORK 181

7.1 CHARACTERISATION OF THE PHOSPHORS 182

7.2 DEPOSITION AND CHARACTERISATION OF THIN FILMS 183

7.3 ANNEALING OF THIN FILM 184

7.4 FUTURE WORK 184

7.4.1 Deposition 184

7.4.2 Annealing 185

7.4.3 Radioluminescence 186

7.4.4 Micro-engineering 188

7.4.5 Co-dopant 191

7.5 SUMMARY 191

8 REFERENCES 192

9 APPENDIX 201

9.1 ION BEAM ANALYSIS 201

9.2 FIGURES 208

9.3 TABLES 216

9.4 EQUATIONS 218

1 Introduction

1.1 Aims and Objectives

The aim of this work has been to study the growth and characterisation of thin film phosphors to investigate the feasibility that in thin film form it could have improve properties over an existing self-supporting wafer based neutron scintillation detector system. Areas of improvement are focused on increased detection resolution and detection rate. This was undertaken in collaboration with the ISIS neutron facility at the Rutherford Appleton Laboratory, to examine whether an improved radioluminescent detector could be designed, based on the application of thin film phosphor scintillation.

The three main areas that were considered for potential optimisation of the radioluminescent detector are:

i) Increasing the luminescent emission after each neutron captured,

ii) Increasing the rate-of-capture for each measurement,

iii) Improving the spatial resolution of the detector.

The objectives of this project were consequently to undertake a detailed background literature review, characterise a selection of phosphors, test the feasibility of thin film growth using these materials for use as scintillators, and to undertake detailed characterisation of the resultant thin films in order to consider the feasibility of use in an enhanced neutron detection systems.

1.2 Context Statements

The Engineering and Physical Sciences Research Council (EPSRC) and the Council for the Central Laboratory of the Research Councils (CCLRC) funded this Case Studentship. The industrial funding component, CCLRC, is from ISIS, a neutron experimental facility at the Rutherford Appleton Laboratory (RAL) in Oxford.

ISIS is the world's most successful pulsed spallation neutron source, utilising nuclear bombardment of protons into a heavy metal target to create beams of neutrons. The facility provides beams of neutrons and muons that enable scientists to probe the microscopic structure and dynamics of matter in scientific areas encompassing Physics, Chemistry, Earth Science, Materials Science, Engineering and Biology. The work using neutron diffraction analysis plays a major role in shaping the understanding of subjects ranging from magnetism and superconductivity to chemical surfaces and interfaces. Dr. Nigel Rhodes (n.j.rhodes@rl.ac.uk), who works at ISIS, was linked to this project, as an external advisor.

The work was carried out in the Displays & Imaging research laboratory at Nottingham Trent University (NTU), which is lead by Prof. Wayne Cranton. Research by this group is based on growing thin films using RF magnetron sputtering for the application of thin film conductors and electroluminescent displays.

1.3 Summary of Thesis

Chapter 1

This chapter provides the general overview of the thesis and its context.

Chapter 2

This chapter is a background review of the subjects involved in the project. The literature review presented includes:

- The production of neutrons used in neutron diffraction analysis.
- The interaction of neutrons with matter.
- The capture of neutrons and conversion to an electrical signal using a phosphor scintillator.
- The process of luminescent emission by phosphors.
- Methods for improving detection efficiency and rate of detection.
- Alternative approaches to neutron detection including thin films and micro engineering.
- Sputter deposition and other techniques to grow thin films of phosphor material.
- The characterisation techniques employed during this body of work.

Chapter 3

This chapter describes the experimental equipment and techniques used throughout the project with details of the specific systems developed and modified for this research.

Chapter 4

This chapter presents results from the characterisation of the scintillator wafer (consisting of ZnS:Ag,Cl phosphor, ^{6}LiF neutron converter and a binder) used at ISIS for neutron detection and phosphors powders used within this project. Luminescent characterisation to determine emission spectrum and decay time was undertaken after excitation of the phosphors to produce photoluminescent and radioluminescent.

Chapter 5

The chapter details the investigation into depositing thin films of the ZnS:Ag,Cl phosphor onto a substrate using RF Magnetron Sputtering. These thin films were then characterised for photoluminescence, film thickness, surface roughness, crystallinity (by X-ray diffraction) and chemical composition (by ion beam analysis).

Chapter 6

Methods other than RF magnetron sputtering were investigated to study the incorporation of the dopants into thin films. A significant area of the work presented in this chapter was the application of ion implantation of thin films and how it could be used to ensure a thin film containing the suitable dopants in the correct ratios for effective luminescence. These implanted samples were characterised using the same techniques as these of sputtered thin films in Chapter 4.

Chapter 7

A summary of the conclusions derived from the work and the possible direction for further experimentation and research.

2 Background Review and Theory

The focus of this work has been to investigate the feasibility of utilising thin film phosphors in the application of neutron diffraction analysis. This has the potential for improving the measurement technique by improving the detection efficiency and detection response rate of neutrons after their interaction with a target material. Detection response rate is important for gaining understanding of interstitial stages of a reaction or process. Diffraction patterns of a material before a reaction, at the end of a reaction and intermediate points during the reaction provides key information of the process occurring.

The aim of this chapter is to provide an understanding of the subjects involved in this research and the appropriate technology background to determine the feasibility of fabricating a thin film phosphor that may be suitable for the application of neutron detection. The thin film phosphor should have the potential for improved neutron detector efficiency, detection rate and enhanced spatial resolution.

The review commences with information on neutron diffraction analysis, neutron generation and the qualities of the neutron detector that are important for neutron diffraction analysis - focusing on the two stages of neutron detection (i.e. neutron capture and radioluminescent emission). The chapter concludes with a discussion of the methods that can be used to form thin films and ways in which characteristics of the phosphor can be improved after its growth as a thin film.

This body of work has been carried out with cooperation of ISIS, the worlds leading source of pulsed neutrons [1, 2]. ISIS provides scientists and engineers with beams of neutrons and muons to probe the structure and dynamics of matter at the atomic scale. More than half the ISIS instruments use scintillator detectors and provide a versatile tool for the requirements of the individual instruments [2].

The name ISIS is not an acronym, but is derived from Isis, the Egyptian goddess of rebirth and a segment of the River Thames that flows near by and through Oxford, also named Isis. This is a fitting name as ISIS used equipment previously constructed for the Nimrod and Nina accelerators, which had been decommissioned.

2.1 Neutron Diffraction Analysis

The 1994 Nobel Prize in Physics was awarded to Bertram Brockhouse and Clifford Shull for their contributions to the development of the neutron diffraction and neutron spectroscopy techniques [3, 4]. They helped answer the questions of where atoms "are" and of what atoms "do".

Neutrons have been known as building blocks in the atomic nucleus from the early part of the 20th century (In 1935 Chadwick won a Nobel prize for his discovery of the neutron). Neutrons can be characterised by their energy and separated into four groups, as shown in Table 2.1.

Table 2.1: Neutron types grouped by their energies [5, 6]**.**

Neutron Type	Energy
Thermal neutrons	~0.53eV
Slow or Epithermal neutrons	0.53-100eV
Medium-Velocity neutrons	Up to 20 KeV
Fast neutrons	Above 20 KeV

Enrico Fermi made the important discovery that “slow" neutrons with energy of approximately 0.53eV, later named thermal neutrons, showed a much greater inclination to interact with matter than “fast” neutrons. Thermal neutrons are said [7] to be in thermal equilibrium with matter they are diffusing through because they have an energy that is similar to that of the binding energy between atoms. It is this property of thermal neutrons that make them suitable for determining the positions and movements of atoms in a material [8].

A pulsed neutron beam ‘fired’ at a crystal or poly crystalline material has the effect of being deflected off the initial path at specific angles due to the ordered nature of a target material. The deflections are unique to the composition, arrangement and the crystallinity of the material. Neutron scatter is quantified by a concave bank of detectors encircling the target material (Figure 2.1).

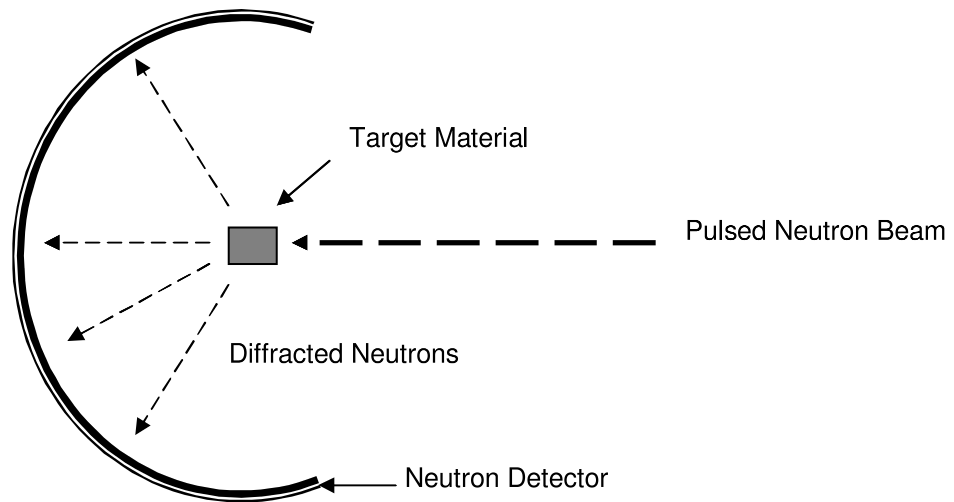

Figure 2.1: Basic design of a neutron diffraction analysis technique.

Once measured, an image is formed of the neutron intensities creating a diffraction pattern, which will show areas with and without neutron detection (Figure 2.2). 'Hot spots', where there are high amounts of incident neutrons, indicate an ordered crystal where neutrons have acted as waves and created constructive interference. Dark spots, where it is devoid of neutrons, indicate disorder or destructive interference. The patterns are unique to specific atomic structures, so when interpreted these patterns can determine properties of the target material.

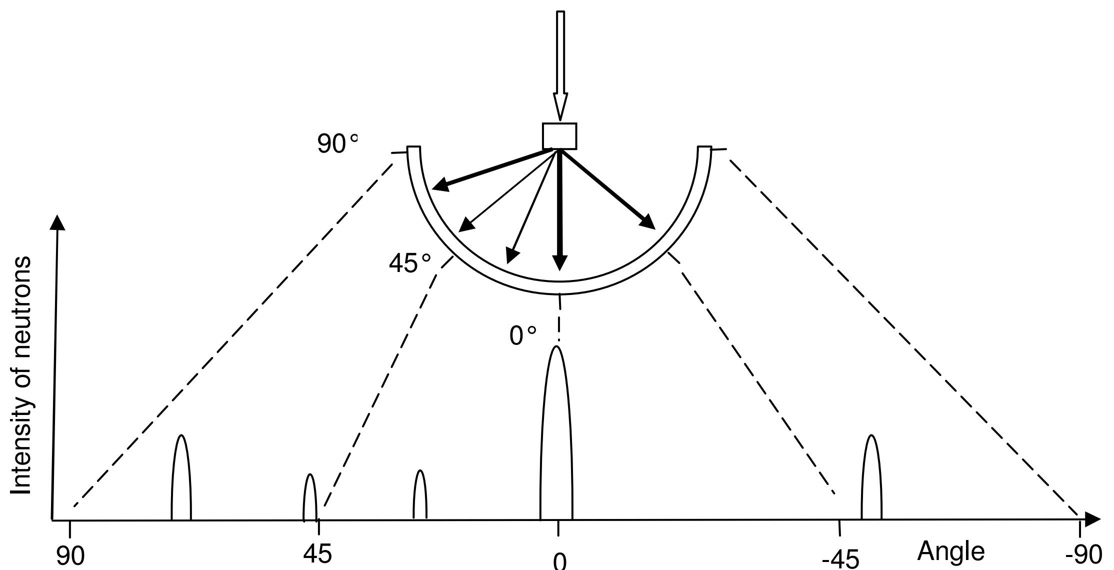

Figure 2.2: A representation of a 2D captured pattern for neutron diffraction analysis.

Neutrons are used in this analytical technique to probe a target material instead of elements such as hydrogen or helium, electromagnetic radiation or other subatomic particles, due to their

very small size and neutral charge. The neutral charge means that they are influenced primarily by mass and not electrical charge, thus allowing them to probe deeper into bulk materials. It is the nucleus which is the dominant factor in neutron diffraction rather than the electron shell because this is where nearly all the mass of an atom is located. The diameter of the nucleus is of the order 10^{-4} smaller than the diameter of the atom (nucleus + electron cloud ~10^{-10} m) [9] and gives neutrons a much longer mean free path. This makes neutron diffraction considerably more accurate than X-rays or electrons (common constituents for structure analysis).

However, X-ray or gamma radiography is more commonly used rather than neutron radiography due to the requirement of a nuclear reactor or a large accelerator in order to generate the intensity of neutrons required for high-resolution imaging with a short exposure time [10, 11].

The neutral charge of the neutron makes it preferable in determining atomic structure, but also makes the detection of neutrons difficult. There are several methods for detecting neutrons - the one linked with this work is neutron scintillation.

A highly sensitive scintillator sheet detects the neutrons by capturing these uncharged elemental particles in a chemical reaction. Neutron capture creates energetic products that create a visible emission, by the process of radioluminescence, which in turn is then guided along thousands of optical fibres to a coded multi-anode photomultiplier. This then converts the light into a proportionally enhanced electrical signal, which is amplified and the signal is interpreted by software on a computer to create the diffraction pattern.

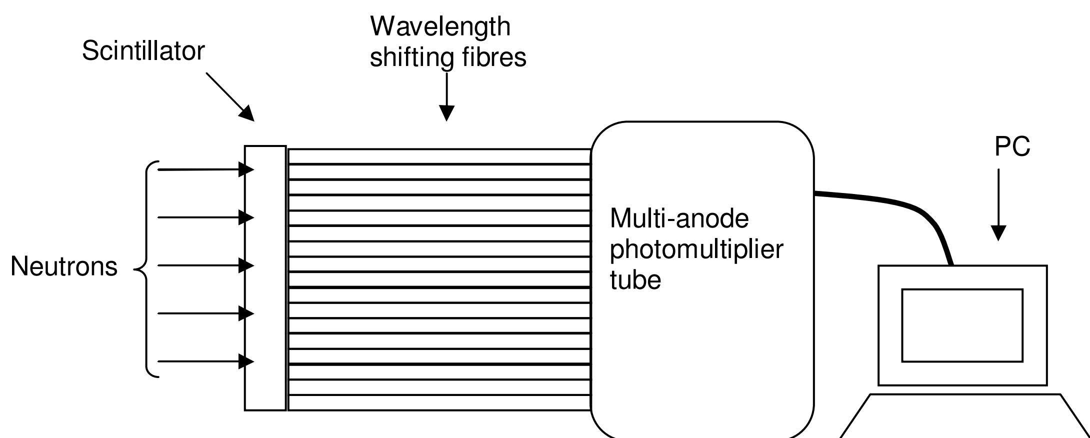

Figure 2.3: A representation of a neutron detector, after [12, 13]**.**

Figure 2.3 shows the general setup of a neutron detector and how the scintillator is incorporated into the detector. Figure 2.4 shows how this is incorporated into creating the bank

of detectors. The fibre-coded elements method is used for large-area systems successfully at ISIS.

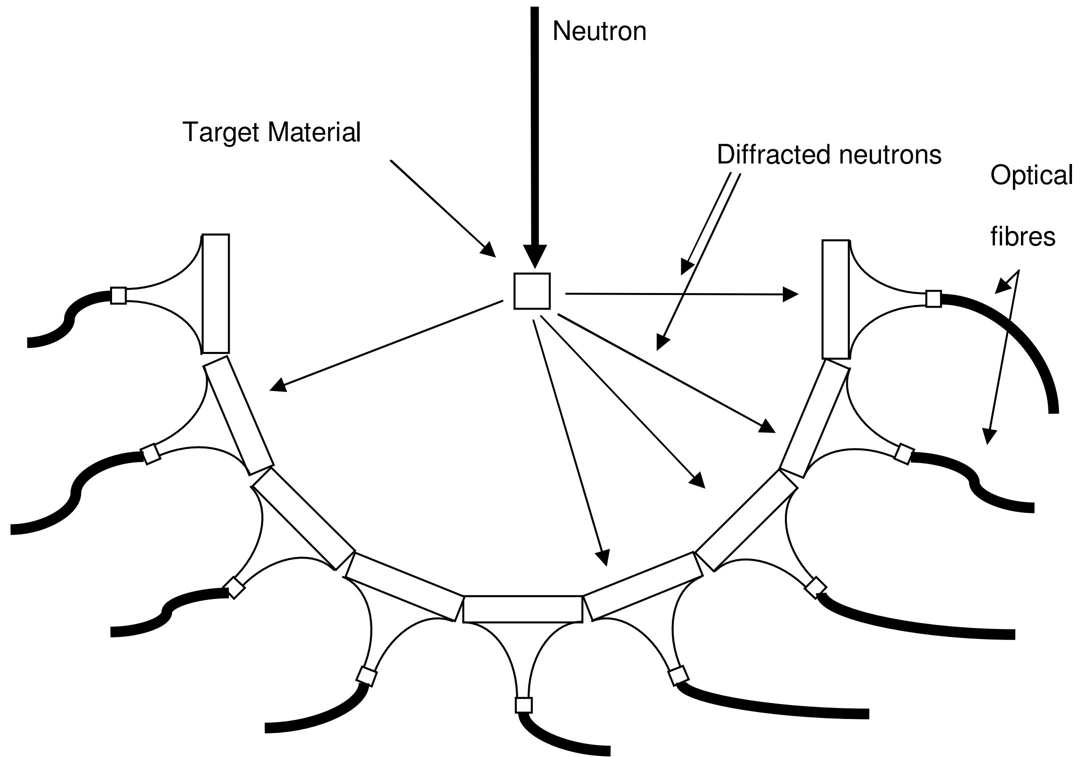

Figure 2.4: 2D representation of a neutron diffraction technique.

2.1.1 Neutron Generation

ISIS creates thermal neutrons by a process of spallation [14]. This is a vigorous nuclear reaction by bombardment of protons into a heavy metal target [7], effectively using nuclear "evaporation" [15]. Protons are accelerated to energies of 800MeV with a current of 200 µA and fired at a tantalum (Z=73) target to produce a high power neutron source [14]. This process of bombardment repeats 50 times per second with pulses of 100ns [16] and creates a pulsed neutron emission. The neutrons are emitted radially from the heavy metal target and are directed along beam lines towards target samples [15].

Neutrons, as a free-particle, have a mean lifetime of approximately 1000 seconds [8]. This period is sufficient for the neutron to progress from the source, through a target material and to the detectors.

Prominent neutron spallation sources other than RAL in Oxford include SNS in Tennessee USA [17, 18] and J-PARC in Japan [12]. Along with these, there are 14 more neutron scattering facilities in Europe, 11 in the Americas and 6 across the rest of the world.

2.2 Neutron Scintillation

The scintillator is made up of two parts, the first captures the neutron and the second creates luminescent emission.

The ideal neutron scintillator should have [19, 20]:

- High detection efficiency - the ability for the scintillator to capture the neutron by using a high-density material or one with a high neutron capture cross-section.
- A cost effective manufacturing process - low cost materials or a practical growth technique permits low cost manufacturing.
- Chemical, thermal and mechanical stability – a scintillator needs to be inert/non-hygroscopic, temperature insensitive for emission yield, and low or uniform thermal expansion.
- High count-rate and coincidence timing [21] - a fast count rate is achieved from a short decay time and low intensity afterglow.
- Good spatial resolution and signal-to-noise ratio - can be improved by having a higher light yield.
- Suitable emission wavelength for detection – an emission wavelength that is tuned to the peak detection efficiency of the photodetector for reduced noise (or vice-versa).
- Radiation resistant - a neutron scintillator would require insensitivity to other forms of radiation so that noise is not introduced to the system. It also required that the detector does not deteriorate over time in the presence of radiation.
- Efficient transmission of light to a photodetector – the movement of emitted light would use a material with a similar reflection index to the other components to reduce reflection. When the refractive Index (n) is 1.5, it is considered optimal in order to match the window of the photomultiplier tube [19].

For each application that uses a scintillator, the above factors would be weighted differently for importance. For example, neutron diffraction analysis for rapid measurements have the most important properties being a fast count rate with a low noise-to-signal ratio to deliver the most images within a period with a limited noise component.

A neutron converter initially captures the incident neutron and breaks down into products with large (MeV) amount of kinetic energy [22]. These charged products cause excitation of neighbouring particles while reducing in momentum as energy transfers. The excited particles then emit light radially from the phosphor; hence, the emission profile is not related to the direction of travel of the excitation source. Collection of the emitted light is dependent on the integration area of detection for the point source and the loss mechanisms before the light reaches the detector.

An alternative for position sensitive phosphor detectors is ^{3}He gas [23]. This method has high neutron-detection efficiency and high signal to noise ratio but has a spatial resolution of ~5mm, which is not suitable for focused measurements, required for this area of study.

Scintillators are synthesised by solid-state reactions between raw materials at high temperatures [22]. Once formed, the scintillators are typically based on a self-supporting thick film, where light scattering and absorption compromise the spatial resolution. If a thin film phosphor was to be fabricated with sufficient neutron detection capabilities, it opens up the possibility to employ micro fabrication techniques to produce detector arrays with integrated scintillator layers – hence potentially enhancing the spatial resolution capability of the detector. Associated with this would be a reduction of the scintillator thickness, which would subsequently reduce the detection efficiency. This could be resolved by appropriate engineering of the structures, in order to make use of inherent light guiding properties of thin film phosphors (typically with refractive indices greater than two).

2.2.1 Neutron Capture

There are two requirements for an effective neutron converter, a large capture cross-section to ensure an efficient neutron capture [24] and reaction products with the potential to stimulate a large number of excitations [25]. Each material has a different capture cross-section (stopping power) for neutrons, which is dependent on the energy of the neutron.

ISIS use a scintillator made with an enriched lithium fluoride (^6LiF) neutron. When a neutron reacts with enriched lithium in the converter it creates an exothermic reaction, forming an alpha particle ($^4He_2$) and a tritium particle ($^3H_1$) with a large amount of energy (4.78 MeV) in the form of particle momentum. This can be expressed as $^6Li(n,^3H)\alpha$ [19, 26] or

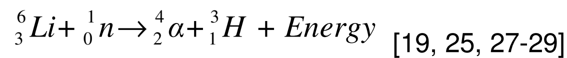

$$^{6}_{3}Li + ^{1}_{0}n \rightarrow ^{4}_{2}\alpha + ^{3}_{1}H + Energy$$ [19, 25, 27-29]

Where *Li* is lithium, *n* is neutron, *α* is an alpha particle and *H* is tritium. Typically, neutron reaction is denoted by B(n,c)C [14, 26] for the reaction: $B + n \rightarrow C + c$. Where *n* is the neutron, *B* is the capture nucleus and *C* and *c* are the products of the reaction.

ISIS used ^6LiF because of its large capture cross-section for thermal neutrons (^6LiF - 520b) and the efficiency of the process. Another advantage of ^6Li is that there is less gamma radiation produced in the neutron reaction than other neutron converters. ^6LiF is less efficient than ^6Li (945 barns at 26meV [21, 24]), but without fluorine, lithium is not stable in air and will oxidise, therefore requiring a shield (and hence reduced efficiency). Naturally occurring Li has two isotopes, ^6Li (7.5%) and ^7Li (92.5%) [30, 31]. ^6Li is preferred rather than the ^7Li because of its larger cross-section for thermal neutrons (^6Li - 941b, ^7Li - 45.5b) [30]. To obtain the more effective ^6Li isotope, a quantity of the naturally occurring Li is collected and the heavier ^7Li isotope is progressively filtered leaving increased concentrations of ^6Li isotope.

The reported energy released in the ^6Li–n reaction range from 4.71 to 4.8 MeV [21, 25, 27-29, 32]. Where the energy released is divided between the alpha and tritium particle and is reported to be in the region of 2.05 and 2.74 MeV respectively [24, 27, 28]. However, the energy released can be calculated from Einstein's equation that links mass and energy

(Equation 1) due to conservation of energy. The energy of the two particles can also be calculated assuming conservation of momentum.

$$E = mc^2 \qquad \textbf{Equation 1}$$

Where E is energy, m is mass and c is the speed of light in a vacuum. Hence, the energy released was calculated to be 4.784 MeV, which is split into 2.056MeV and 2.728MeV for the alpha and tritium respectively.

Typical examples of neutron converters are presented in Table 2.2 and Table 2.3.

Table 2.2: Common neutron reactions and the energy distribution to the products [9, 10].

Neutron Reaction	Energy distribution of reaction products
$^{10}B+^{1}n\rightarrow^{4}He+^{7}Li$	He/Li = 1.49/0.86 (MeV)
$^{6}Li+^{1}n\rightarrow^{4}He+^{3}He$	$^{4}He/^{3}He$ = 2.05/2.73 (MeV)
$^{235}U+^{1}n\rightarrow f_1+f_2$	f_1/f_2 = 97/65 (MeV)
$^{1}H+n\rightarrow^{2}H+\gamma$	$^{2}H/\gamma$ = 2.25 MeV

Table 2.3: Capture cross-section of a group of elements along with their distribution energy [21].

Element	Capture cross-section, b (barns)	Disintegration energy, Q (MeV)
^{3}He	5400	4.79
^{6}Li	945	4.79
^{10}B	3841	2.79

An alternative form of neutron scintillator to the two part scintillator, like ^{6}LiF-ZnS:Ag,Cl, is one where the phosphor will also act as the neutron converter, such as Gd_2O_2S:Td [25]. The Gd acts as the neutron capture element [26, 29, 33], has a very large capture cross-section (70,000b for ^{157}Gd and 17,000b for ^{155}Gd with thermal neutrons [29]) but also emits internal conversion electrons.

2.2.2 Phosphors for Neutron Detectors

The main properties that are desirable for a phosphor in neutron diffraction analysis is to produce high intensity emission, fast decay time and have low gamma sensitivity [2].

- A greater intensity of emission permits a greater detection range. Hence, with a strong emission there are a greater number of divisions for neutron flux. A greater emission from neutron interactions also improves the signal-to-noise ratio.

- A fast decay time improves the speed in which a diffraction pattern can be captured hence improving the rate at which multiple diffraction patterns are captured. This is important for dynamic systems where a process or reaction is occurring.
- Low gamma sensitivity permits greater resolution by reducing noise that a gamma interaction creates. This is achieved by reduced gamma detection or improved discrimination of the gamma component.

The ZnS:Ag,Cl phosphor is used by ISIS for neutron diffraction analysis as it is reported to be the best commercially available phosphor for brightness characteristics for radioluminescence [34]. It is a mature phosphor within the field of cathodoluminescence [35] and has been used in emissive displays, such as CRT screens and some radar screens, dating back over 100 years. However, ZnS:Ag,Cl is not suited for decay time measurements, because the phosphor decay time is too long [36].

It is worth noting at this point of the thesis, that when referencing the ZnS:Ag phosphor, the co-dopant has been included if known. Where the co-dopant is unknown or is a description of all ZnS doped with Ag phosphors, it was been left as ZnS:Ag. As discussed in Section 2.3.2, the charge compensator was not specifically referred to within some of the research papers and previous investigations, due to its assumed non-influence of the resulting emission spectra.

The ZnS:Ag,Cl phosphor has a blue emission spectrum as shown in Figure 2.5 with a peak intensity at 450nm and FWHM of 55nm [34, 37].

Husk [38] tested if the photoluminescence efficiency of ZnS:Ag was directly proportional to irradiation intensity. Below 10^8 photons/sec/cm^2 the link between PL emission and excitation became non-linear. They believed saturation quenching to be responsible for the non-linearity. Calibrated into the system this would not affect the result, as the detection equipment would compensate for this. This characteristic of ZnS:Ag can be ignored in the experimental setups performed during this work as the excitation energy has been kept constant throughout experiments.

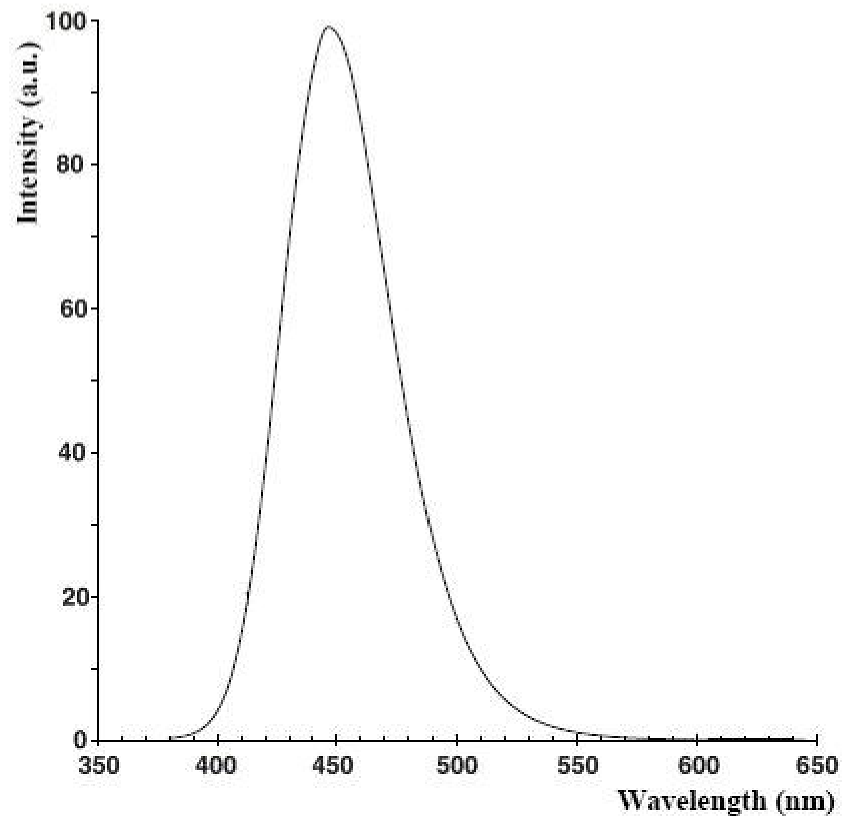

Figure 2.5 A typical luminescent spectrum of ZnS:Ag,Cl, with permission from Phosphor Technology [34].

On the topic of sensitivity, McElhaney [37] says that the ZnS:Ag phosphor was temperature independent between -20 ºC and 54ºC, covering the entire temperature range to which it would likely be subject to.

2.2.3 Decay Time

ZnS:Ag produces a visible emission from α rays, which has a short lifetime of 200ns [36, 39, 40]. The weak point in terms of rapid measurements is that the ZnS:Ag phosphor also has a long 'afterglow' (slow component) of approximately 100μs which leads to a poor count rate of 100kcps [39]. The value for the slow component has also been quoted to be 5.0μs [41]. The fast and slow decay components can be separated by choosing an appropriate integration time, e.g. 0.4μs for the short component and 4.0μs for the long component. However, once the slow component has been removed the signal becomes too weak for the diffraction analysis technique to function correctly [42].

Dopants effect the decay rate, Husk [38] reported that their ZnS:Ag phosphor contained trace elements of Nickel (Ni) at a quantity 1×10^{-5} at% of nickel and was as a co-dopant in the ZnS:Ag. Matsubayashi [42] used a range of Ni concentrations (0-200ppm) for the purpose of reducing the decay time. This was achieved with an optimum of 50ppm for the dominant slow decay component and the fast component, which was improving at the 200ppm limit.

Yasuda [36] compared the decay time of YAP ($YAlO_3$:Ce) and YAG ($Y_3Al_5O_{12}$:Ce) as potential replacements to ZnS:Ag. From Table 2.4 it shows that YAP and YAG have 30% and 11% of the light output of ZnS:Ag respectively, but the decay times are much faster, with YAP having the quickest decay time of 25ns.

Table 2.4: Properties of YAP, YAG and ZnS:Ag alpha detectors.

	YAP	**YAG**	**ZnS:Ag**
Relative light output (%)	30	11	100
Peak wavelength (nm)	370	550	450
Scintillation decay time (ns)	25	70	200

Table 2.5 is an amalgamation of some potential scintillators, showing that ^{6}LiF-ZnS:Ag emits nearly twice as many photons per neutron than its closest rival, but the others have the potential to increased count rates.

Table 2.5: Potential scintillators with corresponding photon emission and decay constant [11, 33, 43-45]**.**

Phosphor	**Photons emitted per neutron**	**Decay constant**
$Li_6Gd(BO_3)_3$:Ce	36,000	200ns
Cs_2LiYCl_6:Ce	70,000	1μs
Cs_2LiYBr_6:Ce	88,000	89ns
Y_2SiO_5:Ce/^{6}LiF	40,000	37ns
ZnS:Ag/^{6}LiF	160,000	200ns

The $Li_6Gd(BO_3)_3$ scintillator has been considered as a replacement to the ^{6}LiF-ZnS:Ag,Cl at ISIS due to its fast decay constant. However, this scintillator is expensive to create due to the number of specific isotopes that are required [46]. One of the key reasons for its continued interest in spite of the cost aspect is that it can be optimised for specific neutron energy regions by changing the isotopic composition of three primary absorbers - Li, Gd, B [11].

An alternative to decay time, which is the standard measurement for determining maximum measurement rate, is the rise time. This can also be used to distinguish between events and the cause of the events - e.g. neutron or gamma interaction. The YAP ($YAlO_3$:Ce) phosphor

[36] has a smaller rise time, smaller FWHM and gives a much greater relative resolution than ZnS:Ag (Table 2.6).

Table 2.6: Rise-time properties of α and β(γ) rays observed from the YAP and ZnS:Ag powders.

	Rise time (ns)	FWHM (ns)	Resolution (%)
YAP	211	3.1	1.5
ZnS:Ag	476	22	4.6

2.2.4 Optimum Thickness

Total light output is dependent on the number of luminescent events and the average light output. ZnS:Ag is opaque [2, 25, 47, 48] to its own emitted light, meaning an emission which is not close to the surface and radiating away from the phosphor has the potential to be re-absorbed. The thinner the ZnS:Ag scintillator is, the greater proportion of luminescence has the potential to escape the boundaries of the phosphor. However, this is at the expense of a reduced volume for the charged particles to transfer its energy to the phosphor, so less luminescence would occur. Hence, having more of the energy deposited at the surface of the phosphor means that a greater proportion of the emission will not be reabsorbed. For this scintillator the detected emission from the phosphor is predominately due to α-particles and not ^{3}H particles, as α-particles have a shorter mean free path than ^{3}H particles. The trace length of ^{3}H-particles and α-particles in ZnS is 32μm and 6μm for respectively [27].

The optimum thickness for the purpose of achieving maximum count rate from the ZnS:Ag excited using a ^{210}Po alpha particle source was reported by Mantler-Niederatter to be 15μm [48]. When the phosphor was thinner than this, the reduced absorption of the incident energy become prominent causing the count rate tails off. More specifically for the ^{6}LiF-ZnS:Ag,Cl , the optimum thickness of ^{6}LiF and ZnS was tested [48] for improved emission from the detection of α-particles and ^{3}H particles. Differing mean ranges of α-particles and ^{3}H particles meant that the optimal thickness reported was 4μm for α-particles and 20μm for ^{3}H particles in ^{6}LiF. This was further illustrated by the optimal thickness of ZnS being 6μm for α-particles and 32μm for ^{3}H particles. With a combined α-particle and ^{3}H-particle source, the result was an optimum thickness of 20μm for ^{6}LiF and 15μm for ZnS. Yasuda reported [36] that the optimum density for YAP and ZnS:Ag for α counting is 5-7mg cm^{-2} and 10mg cm^{-2} respectively. A 250μm thick ^{6}LiF-ZnS:Ag was shown [23] to create maximised peak. Although it has been reported that the

maximum thickness is 500μm for ZnS:Ag [25]. Tyrrell [23] developed 10,000 photons per thermal neutron within the 250μm of ^{6}LiF-ZnS:Ag, while others [11, 49] reported an emission of greater than 150,000 photons per neutron. With the largest being created using a Li-based scintillator with the ZnS:Ag phosphor creating in the region of 160,000 light photons per neutron [50]. Counting the photon emission from the scintillator with a know number of incident neutrons is the gauge to the efficiency of the scintillator.

The neutron converter and the phosphor can be formed as separate layers (Figure 2.6), so when energetic ions are produced in the neutron converter layer, they are required to progress through the remainder of the converter to reach the phosphor where a radioluminescent emission can be created. The alternative is a scintillator in a homogeneous mixture of converter and phosphor, which can create emission within any volume of the material (Figure 2.7).

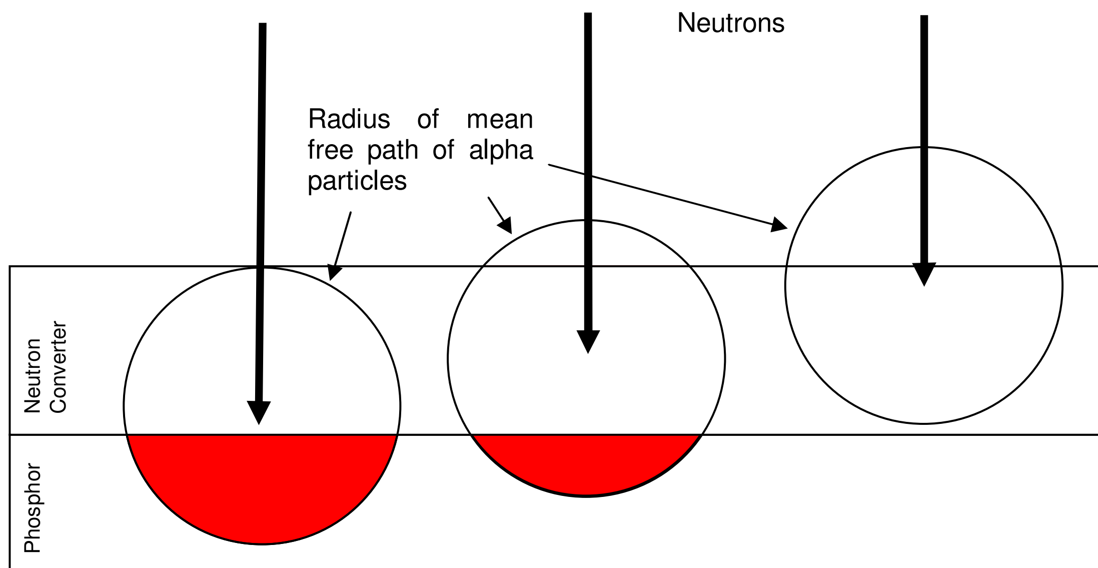

Figure 2.6: Neutrons incident on layered neutron converter and phosphor.

The relative merits of the layered approach are that precise quantities of the components can be built up and will be of the greatest density. However, a homogeneous mixture of the components is of a lower density and would require a greater volume for the neutron to be captured and for the energy from reaction products to be transferred. The defining advantage of the homogeneous mixture is that the reaction products are not required to travel in a specific direction to reach the second active component.

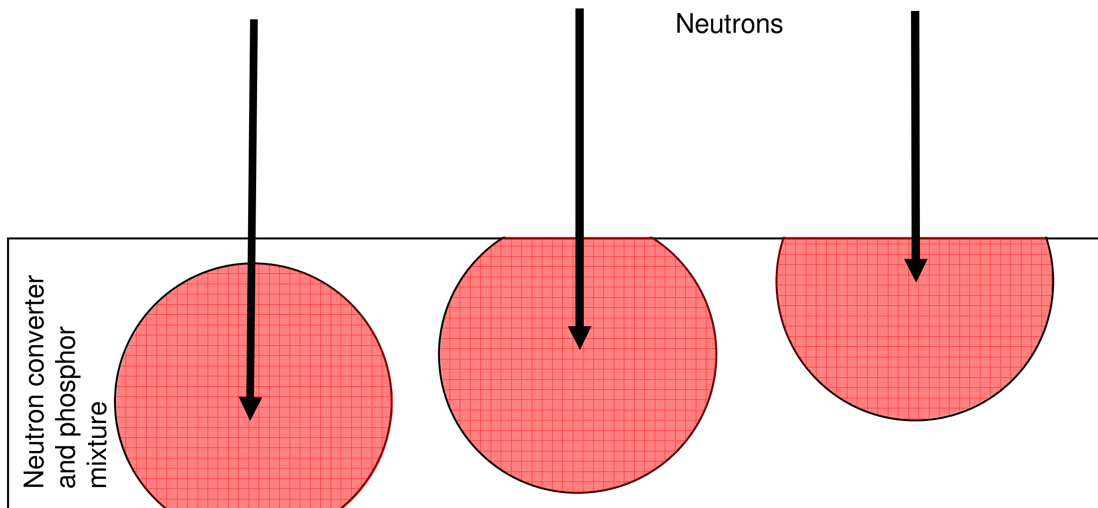

Figure 2.7: Neutrons incident on a mixture of neutron converter and phosphor.

A balance is required for this method so a suitable ratio of ^{6}LiF as the neutron converter and ZnS:Ag as the phosphor is attained to achieve optimum detection efficiency. Without enough ^{6}Li neutrons will not be captured and with insufficient ZnS:Ag the products of the Li-n reaction will not create enough radioluminescence (RL).

Spowart [32] reported that 18800 photons were emitted per captured thermal neutron from a scintillator made of LiF:ZnS:binder in the ratio of 1:3:1 of a thickness of 0.022cm (220µm). Without a binding agent the scintillator components would be in a non cohesive powder. Although ratios of 4:1, 2:1 [25] and 6:4 [34] for ZnS:Ag/^{6}LiF are also used in neutron detection screens. ISIS concluded following their own investigation that the ratio of four ZnS to one LiF (by weight) was the most productive, this is the equivalent of 1:1 of ZnS:LiF (by number) [51].

Beyond a point, a reduction in scintillator thickness has the effect of reducing the efficiency of neutron capture. However, ISIS has been able to improve the detection efficiency whilst maintaining the optimum optical path length. Changing the angle in which the incident neutrons intercept the scintillator [2, 25, 46, 48, 52] (Figure 2.8).

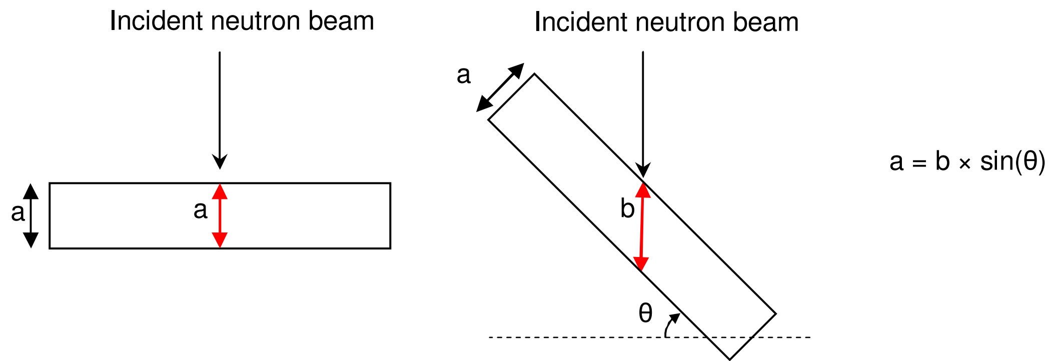

Figure 2.8: Representation of scintillator in respect to the incident neutrons to achieve greater detection efficiency.

Rotating the scintillator away from a perpendicular angle to which the surface of the scintillator makes with the incident neutron beam increases the detection volume perceived by the intercepting neutron. Therefore, whilst the capture capabilities have increased, the capability of the radioluminescent emission to escape the scintillator remains the same.

2.2.5 Noise Created by Gamma Radiation

The neutron beams used at ISIS are accompanied by gamma radiation due to the events occurring in the heavy metal target [47, 53]. Gamma radiation causes photon emissions within the phosphor. However, because they do not interact with the target in the same way as neutrons, these emissions will generate noise within the diffraction pattern. The ability to discriminate an emission caused by a gamma interaction and an emission caused by an alpha/neutron interaction determines the accuracy of the readings. ^{6}LiF-ZnS:Ag is used on a large scale at ISIS due to high light yield along with low gamma response. ISIS tested the ZnS:Ag phosphor for gamma sensitivity with a ^{60}Co gamma source and has shown it to have a lower than 10^{-8} counts per incident gamma [2] and between 10^{-6}-10^{-8} for 1MeV gamma [25]. This provides a strong signal to noise ratio, so delivering a high quality neutron scattering data.

There are two main ways to discriminate against gamma radiation, (1) making the ratio of light emitted from an alpha/neutron interactions much greater than that from a gamma interactions or (2) Pulse Shape Discrimination (PSD). There are several types of PSD; the zero crossing method and charge compensation are discussed.

The Zero-Crossing method of PSD can be an effective tool while using standard commercially produced electronics. It requires two signals from the photomultiplier, one a linear signal the other a timing signal. The linear signal conveys decay rate information within its shape, and energy information within its amplitude. The timing signal measures the pulse shape from one of the linear signals. Two light decays from two different sources (e.g. neutron and gamma) can be discriminated if their decay times are different. The decay time affects the shape of the bipolar pulse from the amplifier, and the time from start to when the voltage crosses zero is longer for the slower decay. Typically a 100ns difference between the fast and slow decay zero-crossing time over a period of 2500ns (2.5µs) is sufficient for discrimination [9, 48] (Figure 2.9).

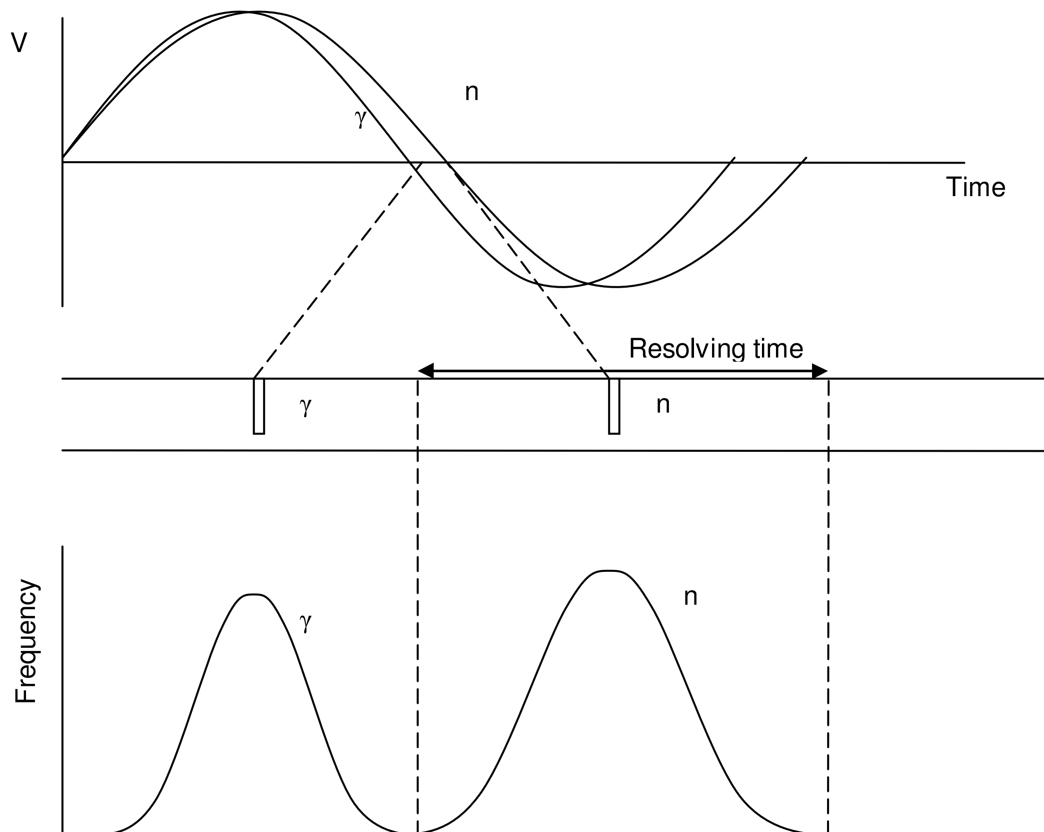

Figure 2.9: Zero crossing method of pulse shape discrimination: bipolar pulse shapes, signal timings, timing spread of zero crossing signal, after [54].

The zero crossing method requires careful setting up and is not effective over a wide dynamic pulse range unless great care is taken to eliminate any DC levels on the linear pulse. The charge compensation method uses only the anode pulses with the photomultiplier running at a low enough voltage that the output pulse is linearly proportional to light output from the

scintillator. The anode is directly coupled to two integrating circuits operating in parallel. Each will integrate over different periods and the comparison of the two-integrator outputs means that a decision can be made as to whether the pulse was induced by an alpha/neutron or gamma ray. This is dependent on the pulses being distinct enough to be resolved as two different events [9] (Figure 2.10).

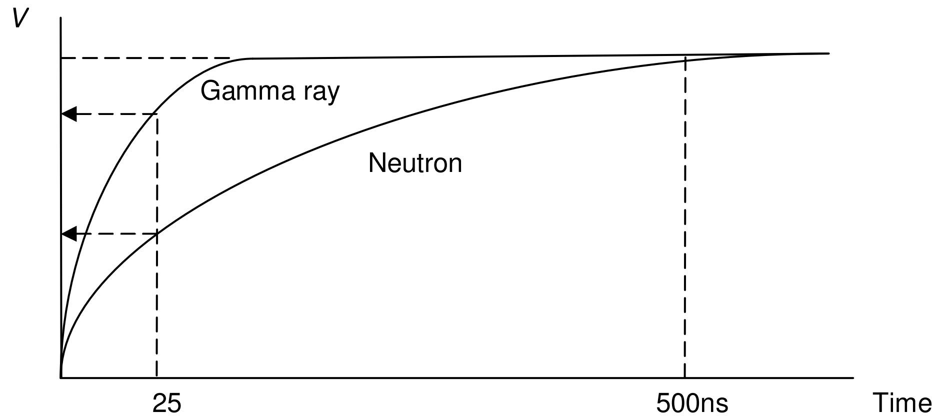

Figure 2.10: Charge comparison method of pulse shape discrimination. Integrator outputs as a factor of time for gamma-ray and neutron signals, after [9].

An example of charge comparison is shown by the phosphor $Bi_4Ge_3O_{12}$ (BGO) [55], which has poor PSD. $Bi_4Ge_3O_{12}$ (BGO) has a spillover (the fraction of one interaction recorded in the second region of interest) of 35% from a ^{233}U source (alpha) and a $^{90}Sr/^{90}Y$ source (beta). Whereas, a mixture of CaF_2:Eu and ZnS:Ag has only 9% spillover, producing distinctly different pulse shapes from alpha and beta interactions. This indicates that each type of radiation can be resolved, giving a much greater degree of PSD.

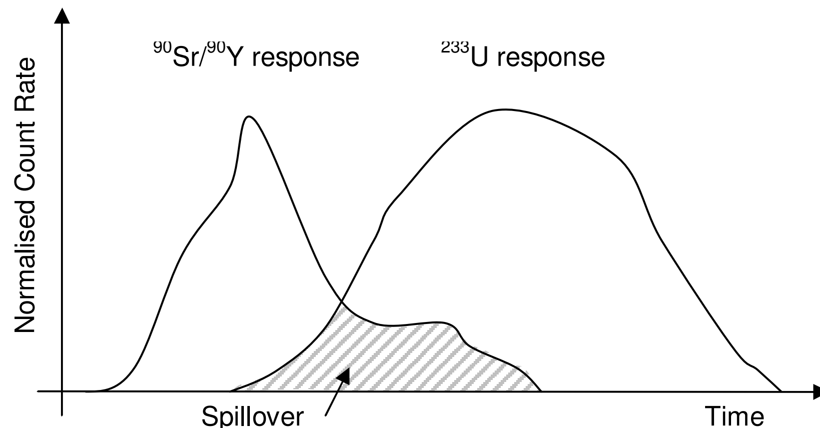

Figure 2.11: An example of a pulse shape spectrum from an alpha and beta source.

CsI:Ti, CsI:Na and BaF_2 scintillators have been characterised for their alpha-gamma discrimination [56] (Table 2.7) and concluded that the best scintillator of the selection was CsI:Ti due to its good scintillation characteristics and had a γ/α discrimination of up to 6 MeV of γ-ray energy.

Table 2.7 .α- and γ-light yield (Λ_α, Λ_γ; photoelectrons/MeV) of CsI:Tl, CsI:Na and BaF_2 crystals

Excitation source	Type of radiation	Energy of radiation	CsI:Ti	CsI:Na	BaF_2
^{22}Na	γ	1.27 MeV	9800	-	2700
^{241}Am	γ	0.06 MeV	-	16700	-
^{244}Cm	α	5.4 MeV	5350	378	720

The semi conducting crystalline scintillator ZnSe:Te is reported [57] to be a promising α-detector due to a high α/γ ratio (up to 1.0). Comparing this to CsI:Tl which has 0.67 α/γ ratio, would suggest that ZnSe:Te was better, however, scintillators of an adequate size cannot be grown using this phosphor at present.

An improved α/γ ratio for CsI:Tl can be achieved at reduced temperature suggesting a draw back to using CsI:Tl is temperature dependency [58]. Hence, if incorporated into a neutron detector, the detector would need to be temperature controlled to allow repeatable and accurate results.

A group of alpha scintillators, including NaI:Tl, CsI:Tl, CsI:Na, BGO (bismuth germinate) GSO:Ce (gadolinium silicate, activated by cerium), CWO (cadmium tungstate), BaF_2, LiI:Eu and ZnSe:Te have been examined and concluded that from this selection the most appropriate α-radiation detector was single crystal CsI:Tl. This was due to it having the best scintillation characteristics, was the cheapest and was the most feasible.

2.2.6 Picture Element Size of Diffraction Pattern

For large areas, where the pixel number is greater than 10^6, a time response of 1-10μs is sufficient. For rapid measurements, a response ≤100ns is occasionally required to cope with high frame rates [39]. Therefore, if a PSD with more than 10^6 pixels is required, ZnS:Ag needs to be altered or replaced to fit this requirement.

The Japanese Spallation Neutron Source has position sensitive neutron detectors (PSND) with pixel sizes from 0.25 to 1000mm^2 and sensitive areas from 0.04 to 40m^2 [19].

Cross fibre and ^{3}He detectors, alternative techniques for neutron for neutron detection, have a spatial resolution of 0.5mm and 5mm respectively [23]. However, they are let down in either signal-to-noise ratio or detection efficiency.

2.3 Phosphors

The name phosphor originated in the early 17th century, originally meaning "light bearer" in Greek. It is quite a general term, and is described as a "solid luminescent material" [22]. The first reported use of a phosphor material was a phosphorescent paint from a seashell in 10th century China.

Luminescence is a term given to cover both fluorescence and phosphorescence. Fluorescence denotes the imperceptible, short after-glow from a phosphor. This is a period of time less than 10ms, which is not perceptible by the human eye. Phosphorescence is denoted as a long afterglow that can be of several hours in length.

The term 'light' is sometimes associated with phosphors, in terms of emission wavelength this is the visible region of the electromagnetic spectrum (390 to 770nm) and those in the neighbouring regions, near ultraviolet (10nm to 390nm) and near infrared (770nm to 1000µm).

Characteristics of phosphor emission are defined primarily by the chemical composition and arrangement of the host lattice and dopant ion. Most are composed of a transparent crystalline or polycrystalline lattice and dopant. The host lattice defines the framework of the phosphor and is the bulk of the material. The activator, a small concentration of intentionally added impurity atoms, distributed throughout the host lattice gives the phosphor its specific luminescent properties. Therefore, the luminescent processes can be divided into two parts - the processes in the host lattice and those that occur in and around the activator.

The addition of dopants to a lattice can enhance various properties such as increased emission intensity. Other types of dopant called luminescence killers, such as Fe, Ni and Co [34, 43] can be added to a phosphor to reduce the intensity of luminescence, which is undesirable, but also has the potential to reduce scintillation decay time. This can be useful for enhancing signal to noise ratio and increasing the number of neutron diffraction patterns created within a period.

Rapid measurements are used as part of a dynamic system; hence, a reduced decay time means a more detailed picture of a process can be captured [22]. This is one of the main objectives of this research project. Therefore, careful doping of phosphors with materials said to be luminescent killers can be beneficial to the optimisation of the phosphor.

2.3.1 Dopants

In the luminescence process, a very small number of dopant atoms, typically less than 1000 parts per million, are excited and take part in the emission of light [22]. The concentration of the dopant can be stated in the form of parts per million (ppm), atomic percentage (at%), weight percentage (wt%) or molar percentage (mol%). Each notation derives for specific applications and can be carried through from its manufacture.

The optimum Ag concentration in the ZnS:Ag phosphor was investigated to create maximum emission efficiency and was quoted [59] to have 1×10^{-4} to 1×10^{-2} g/gram of Ag in ZnS. This concentration created an emission spectrum with two emission peaks, one at 460nm and the other at 520nm. This difference to the standard model of ZnS:Ag phosphor emission with a peak intensity at 450nm [34, 37] can be explained by possible overlapping of the second peak at 520nm into the 450nm peak. However, this does not explain the 520nm emission peak, but is likely to be a separate relaxation route for the excited electron caused by excess doping.

The Phosphor Handbook [22] has a number of Ag concentration values with the predominant value being around 0.1at%. Other values have been quoted as being 170ppm [18], for ion implantation this was 10^{14} – 10^{15}cm^{-2} [60], although up to 1at% [61] has been used. The quoted values for the co-dopant charge compensator, chlorine are less in number and have been quoted to be Cl 40ppm [62]. The limited information was likely due to a lack of understanding of the phosphor.

2.3.2 Chlorine Co-activator

Researching the ZnS:Ag it have been found that there have not been complete clarity in the understanding of this phosphor. There is a ZnS host lattice and Ag dopant however, the ZnS:Ag phosphor requires a co-activator, also called a charge compensator for Ag to be

incorporated into the lattice. However, the co-activator is typically not referred to in the literature. Only when the dopant is integrated into the lattice structure does it give the emission characteristic associated with that dopant, hence activating the phosphor. The co-activator used with ZnS:Ag, and is typically either aluminium, chlorine and nickel. Thus, what was originally labelled and understood to be ZnS:Ag from Phosphor Technology or ^{6}LiF-ZnS:Ag scintillator wafer from ISIS was actually ZnS:Ag,Cl and ^{6}LiF-ZnS:Ag,Cl respectively.

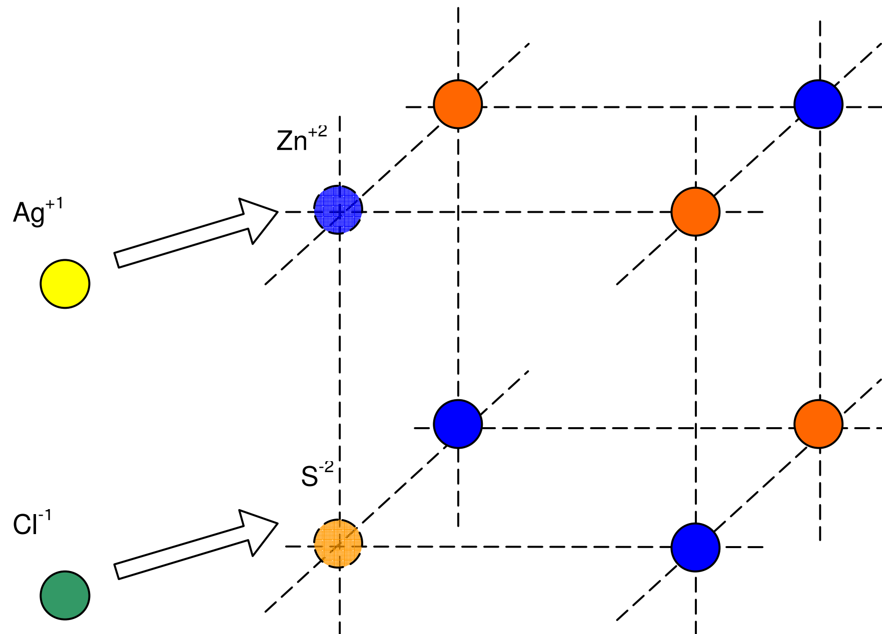

Figure 2.12: A representation of how silver and chlorine ions are incorporated a ZnS cubic lattice.

The chemistry of how silver is incorporated into the ZnS lattice it made evident that without chlorine, charge neutrality will not be maintained (Figure 2.12). The Ag ion is incorporated into the ZnS lattice by replacing a Zn ion, where Ag ions have a +1 charge and zinc ions have a +2 charge, so creating a charge difference of +1. The chlorine ion with a -1 charge neutralises the charge difference by replacing a sulphur ion with a charge of -2. Without a charge compensator, as Ag ions are incorporated into the lattice an electrical charge would develop, hindering further activation of the phosphor by electrically repelling the Ag ions.

Contacting the supplier[1] of the phosphor provided an understanding of the background in the formation of the ZnS:Ag,Cl phosphor. They use a NaCl (salt) flux agent to incorporate the Cl

---

[1] David Pendrill, Phosphor Technology, Norton Park, Norton Road, Stevenage, Herts, SG1 2BB

into the material at a concentration of between 1-5%. The actual incorporated concentration being the matching number to the Ag dopant with the remainder being washed away.

2.4 Radioluminance (RL)

RL is the emission of photons by a phosphor material after excitation by ionising radiation, such as alpha (α), beta (β) and gamma (γ) radiation [7, 22]. For α, β and tritium particles, the process in which the phosphor atoms are excited are by momentum transfer from coulombs forces [54], i.e. the interaction of electrical fields.

In the early years (1932) of RL phosphor development, Walton and Cockcroft observed visible emissions from a thin layer of zinc sulphide powder spread on a glass disc. The excitation source emitted alpha particles, which had been created by the disintegration of lithium atoms via proton bombardment. After a period of time when the individual's eyes had adapted to the darkened environment, referred to as "dark-adapted eyes" [26], the emissions could be viewed through the glass disk using a microscope.

A charged particle penetrating the media distorts the electron orbits of atoms in its vicinity. For a positively charged particle, this results in an atomic bound electron being attracted towards it. As the charged particle progresses its influence on the atom deteriorates and the electron reverts to its original orbit (Figure 2.13).

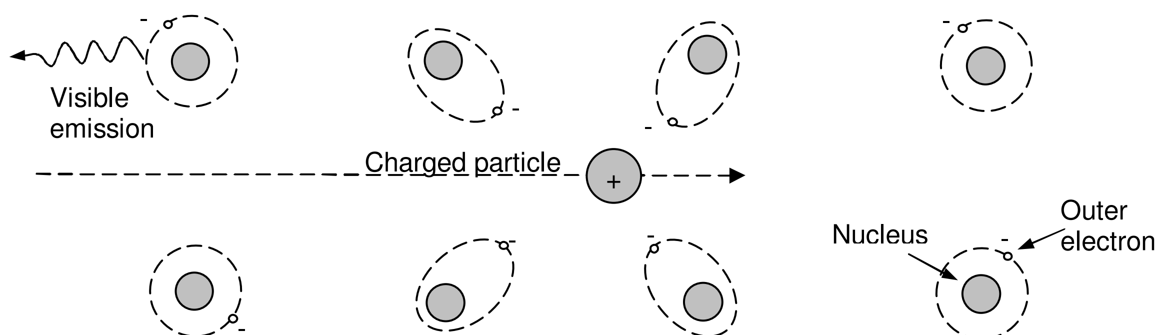

Figure 2.13: Effect of a charged particle on electron orbits of atoms in its vicinity.

In this process, the high-energy charged particle transfers momentum as it distorts the orbit of the electron. This puts the atom into the excited state by promoting the electron across the bandgap to a higher energy level. The excited atom then releases this energy as an electron

falls to its ground state and emits light with characteristic associated to the energy level transitions.

ISIS use zinc sulphide doped with silver (ZnS:Ag,Cl) as the RL phosphor in their neutron detection equipment[29, 43, 63]. Combined with the phosphor is a neutron converter made of enriched lithium fluoride (^{6}LiF). A reaction of a neutron particle with the lithium causes it to break down into alpha (α) and tritium ($^{3}H_{1}$) particles. Both of these products create RL within the ZnS:Ag,Cl phosphor.

2.4.1 Radiation Types

First discovered during research on radioactivity, the alpha particle (α) is made up of two neutrons and two protons [7] and is therefore sometimes referred to as the nucleus of a helium atom (^{4}He). Alpha particles are emitted during radioactive decay of unstable elements such as uranium [64]. An alpha particle is atomically stable due to the balanced number of neutrons and protons, but its electronic charge of 2e makes the alpha particle very reactive. This means the mean free path of an alpha particle is the shortest of the main three radiation types (α,β,γ), which is typically less than 6cm in air [9], and can be stopped by a thin piece of paper. The charge of a proton is $+1.6\times10^{-19}$C, therefore an overall charge of an alpha particle ($^{4}He^{2+}$) is twice this ($+3.2\times10^{-19}$C).

Tritium (^{3}H) is an unstable form of hydrogen consisting of two neutrons and one proton [64]. Tritium is produced along with alpha particles in a ^{6}Li-neutron reaction. Like an alpha particle, it has an electronic charge associated with it, which is 1e ($+1.6\times10^{-19}$C). It is more commonly know as a β source with a half-life of 12.33 years and decay energy of 0.018590 MeV. However, for the neutron-lithium reaction it has similar characteristics to an α particle - and should be thought of as a charged element with kinetic energy and not a β emitter.

Gamma radiation is emitted by the nucleus of an atom as a side product of another decay processes or reactions. The emitted electromagnetic radiation is typically in the wavelength

range of 10^{-10}m to 2×10^{-13}m (equivalent to 10^4eV to 5×10^6eV) [7], which is associated with gamma radiation. Due to their short wavelengths, they have a long mean free path, where high-energy gammas require several centimetres of lead to be stopped.

ISIS creates neutrons by the high-energy impact of protons on a tantalum target, which also produces gamma radiation. Phosphors are prone to producing an emission from their interaction with gamma, hence phosphors are characterised for this sensitivity. A method to reduce gamma sensitivity is to optimise the detector thickness for α and $^3H_1$ particle detection. The mean free path is greater for gamma than α or $^3H_1$, so a detector with reduced thickness detects fewer gammas. Gamma is still detected by the phosphors and the emission produces noise within a neutron diffraction pattern. Processing the emission or diffraction pattern is able to further discriminate against gamma to produce a more accurate result.

2.5 Luminescence

Luminescence was first described in 1888 by E. Wiedman [65] as "… all those phenomena of light not solely conditioned by the rise in temperature". Wiedman's description was a way of differentiating between the visible emissions observed from a heated object producing blackbody radiation and those visible emissions produced by other means. This description has been refined and is more technically described as the emission of electromagnetic radiation from a substance as a result of any non-thermal process [7].

Luminescence is a key area of this research and is one of the later stages of neutron detection using a scintillator. The presence of and distribution of scattered neutrons are detected via their capture by a scintillator. The capture of neutrons starts a process that creates visible luminescence; this is a repeatable and predictable process, which delivers reliable results.

The emission of light by ionising radiation such as the products of neutron capture is a variant of luminescence, called radioluminescence (RL). This is the emission of light after excitation by ionising radiation, such as α, β and γ radiation [22]. RL is one instance of luminescence, other examples [66] are photoluminescence (PL) [65], electroluminescence (EL) [67], cathodoluminescence (CL) [65] and chemiluminescence (or chemoluminescence) [68].

Significant differences between each of the types of luminescence are the excitation sources and the process by which the excitation is applied. The two relevant to this work are photoluminescence (PL) and radioluminescence (RL). For RL the excitation source is charged particles and for PL this is traditionally UV light from a laser source or lamp. When the phosphor material absorbs energy from the excitation source it is placed into an excited state. The luminescent centres remain in an excited state momentarily before returning to a non-excited state and in doing so, release the absorbed energy as a visible emission (and some heat) without any permanent alteration to the phosphor material.

2.5.1 Excitation Mechanism

When the phosphor absorbs energy it promotes an atomic electron from one quantum state to another of higher energy quantum state [7]. This can also be thought of as an electron being promoted from one electron shell to another higher shell. An atom has a set of discrete electronic energy levels defined by the bound electrons orbiting the nucleus. In a crystalline structure, the proximity of one atom to others means that the path of the electron orbiting the neutron is distorted, causing the electronic energy levels to become less defined and broaden into bands.

The atomic structure of RL and PL phosphors that were examined are polycrystalline, this is where there are many crystallites of varying sizes and orientations along with some area of amorphous material (Figure 2.14).

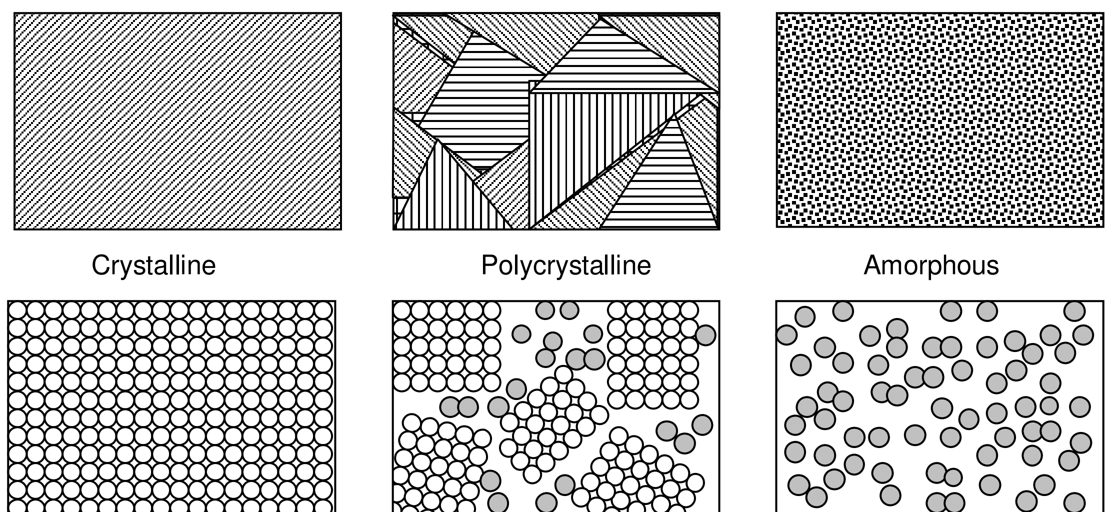

Figure 2.14: Types of atomic structure.

Basic periodic atomic structures for which materials can be categorised are as rock salt, zinc-blende, hexagonal (Figure 2.15), trigonal and tetrahedral [69]. The phosphor under investigation has a ZnS lattice in the zinc-blende arrangement, however with increased temperatures/pressures it transitions into the wurtzeite structure, which has different characteristics. When talking about a phosphor material, the bulk of the material is described as the host crystal lattice.

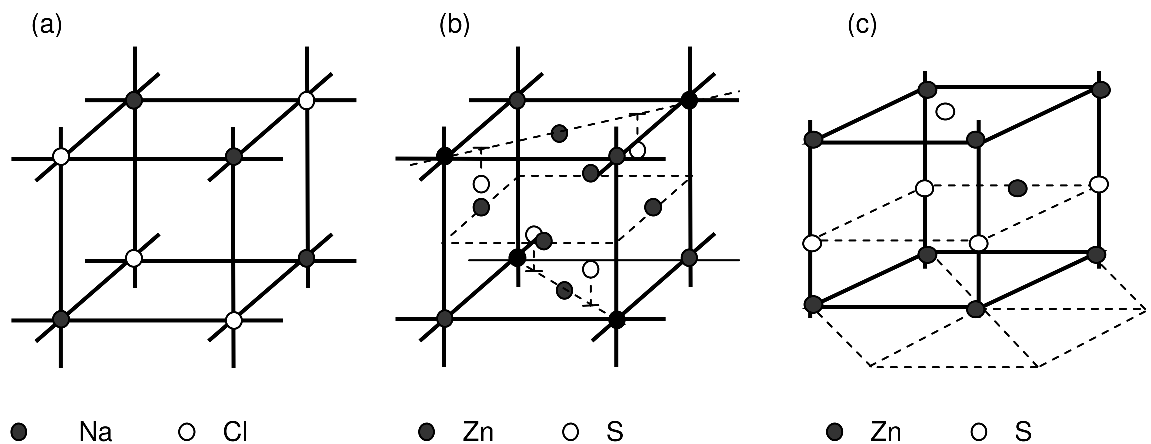

Figure 2.15: Configuration of the atoms in three kinds of crystal structure. (a) rock-salt type, (b) zinc-blende type, and (c) wurtzeite type respectively, after [22].

In an inorganic phosphor material, whose lattice is generally made of a semiconductor material, the electrons occupy an energy band called the valence band when in their ground state. With sufficient energy, the electrons are given the potential to be excited across an energy range called the bandgap and into an energy band called the conduction band (Figure 2.16). The bandgap is formed by the host crystal lattice and are typically within the range of 0.18-3.6eV (at 300K for InSb and ZnS respectively [70]) for semiconductors. Following this excitation and without continued excitation energy, the electron falls from the conduction band into a non-occupied energy state within the valence band.

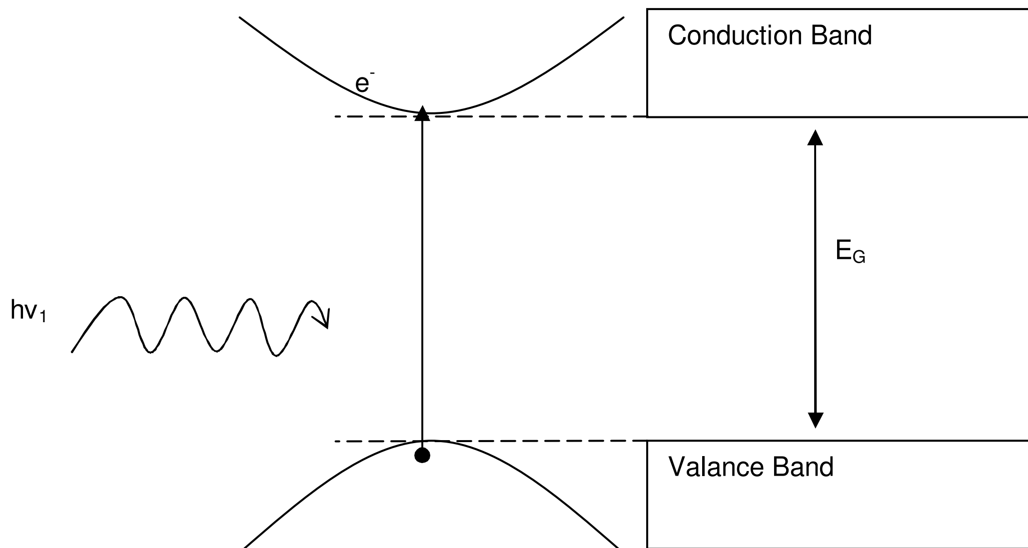

Figure 2.16: Example of excitation of an electron across the bandgap (for this case a direct bandgap) from the valence band to the conduction band.

For the phosphor to become excited it requires the excitation energy to conform to an allowed energy change, for luminescent emission this tends to be an excitation energy greater than the bandgap. For a PL phosphor with an UV excited source, this means that the energy required to cross the bandgap is smaller than the energy associated with the UV photons. With semiconductor materials with a bandgap in the range of 0.2 - 5eV, the required wavelengths would need to be medium infrared to near ultra violet (248nm - 6.9µm). For the ZnS semiconductor with a bandgap in the region of 3.6eV at room temperature [60, 71-73], this is an excitation source with a wavelength of 344nm.

The bandgap is not fixed and is dependant on factors such as crystallinity and ambient temperature. Different manufacturing methods and the environmental condition in which the measurements are taken can produce slightly different emission spectra.

The process of energy transfer from the excitation source to the phosphor material differs between RL and PL. This creates differences in efficiency of the phosphor when excited by different excitation sources. For PL, a beam of high-energy photons penetrates the absorbing medium with the intensity reducing exponentially as a function of thickness (Equation 2) [22, 47].

$$I = I_0 \exp(-\alpha x) \qquad \textbf{Equation 2}$$

Where I is the intensity of light at distance x into the media, I_0 is the intensity of light incident minus reflected light and α is the attenuation coefficient of the media (cm^{-1}).

Equation 2 defines the intensity of the incident radiation as it transmits into a medium. It can be used for other forms of excitation, such as neutrons, gamma radiation and ionised particles other than UV light. The absorption coefficient makes the equation specific to the different phenomena. For PL this is linked to the wavelength energy of the incident light and the density of the material. For gamma radiation, this is defined by the combination of photoelectric effect, Compton scattering and pair production [54]. For neutron beams, this is defined by the combination of scattering and capture [26]. For charged particles, this is the momentum (mass and speed) of the particle, the effect of Bremsstrahlung and the density of target material.

For PL, each incident photon of light has the potential to create an excitation. Once the photon of light is absorbed, it will not be able to excite a second emission.

The nucleus of an atom with its protons and neutron contains nearly the entire mass of the atom, with each neutron and proton having a rest mass of approximately 1.67×10^{-27} Kg (939.57 MeV/c^2) [7]. The mass of a proton is almost 2000 times the mass of an electron, with a neutron having a similar mass to a proton. For RL, this means that the energy associated with a charged particle has the potential to create thousands of phosphor emissions [23].

2.5.2 Emission Mechanism:

Once the material has been excited and an electron has been promoted across the bandgap into the conduction band. Without continued excitation, the electron loses its energy in a series of transitions - when in a doped system (Figure 2.17). Where hv_2 and hv_3 are the energy of the emissions relating to the wavelength (v).

The energy released is defined by the difference in energy between energy levels. Small transitions create emissions with small energy, so long wavelengths. Whereas, larger transitions like those across the bandgap create shorter wavelengths.

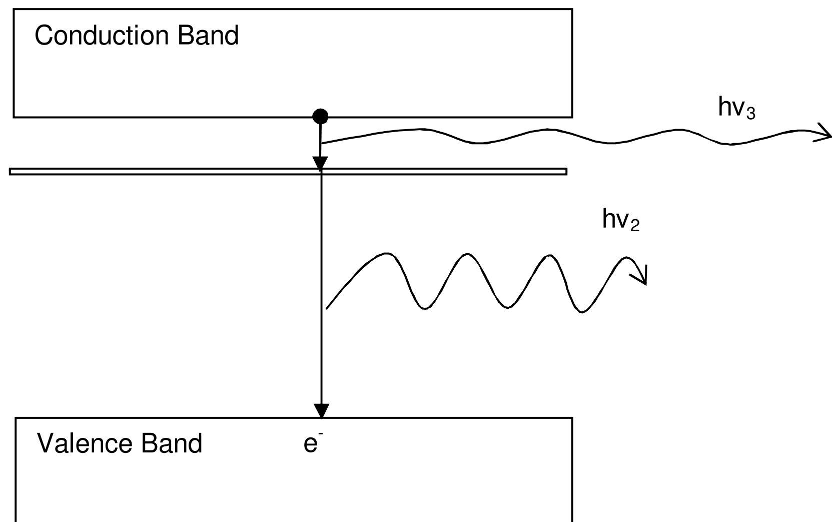

Figure 2.17: Band diagram of emission from a doped phosphor

An example of an energy band diagram for a ZnS:Ag wide bandgap semiconductor phosphor is shown in Figure 2.18. This has two defined energy levels within the bandgap which can participate in the electron energy transition and hence the emission process. The lower energy level is associated with the Ag dopant and the higher one is anion vacancies - crystal defects.

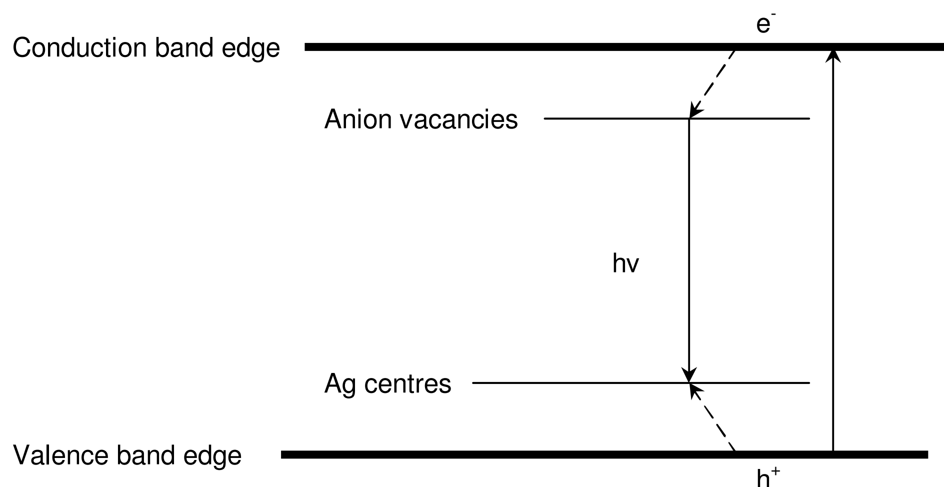

Figure 2.18 The Schematic diagram of energy levels of the ZnS:Ag nanocrystals, after [61]**.**

This is an example where a charge compensator has not been referenced and anion vacancies have been incorporated into the system to maintain charge neutrality.

2.5.3 Emission Spectrum

For the identification of phosphor emission spectra (intensity versus wavelength), ideally the emission would create a sharp full energy peak, although the effects of photon and electron

fluctuations leads to a broadening of emission peaks. Therefore, there is a limit to the detail that can be extracted in a complex spectrum with overlapping peaks. An isolated full energy peak closely resembles the Gaussian function in shape. The emission spectrum can be characterised by the wavelength at the peak intensity, the counts associated with the peak intensity and the Full Width Half Maximum (FWHM). The FWHM gives a comparable measurement of peak width for emission spectra that may have fluctuating intensities [9]. Two peaks are resolvable if they are separated by greater than the FWHM [22] (Figure 2.19).

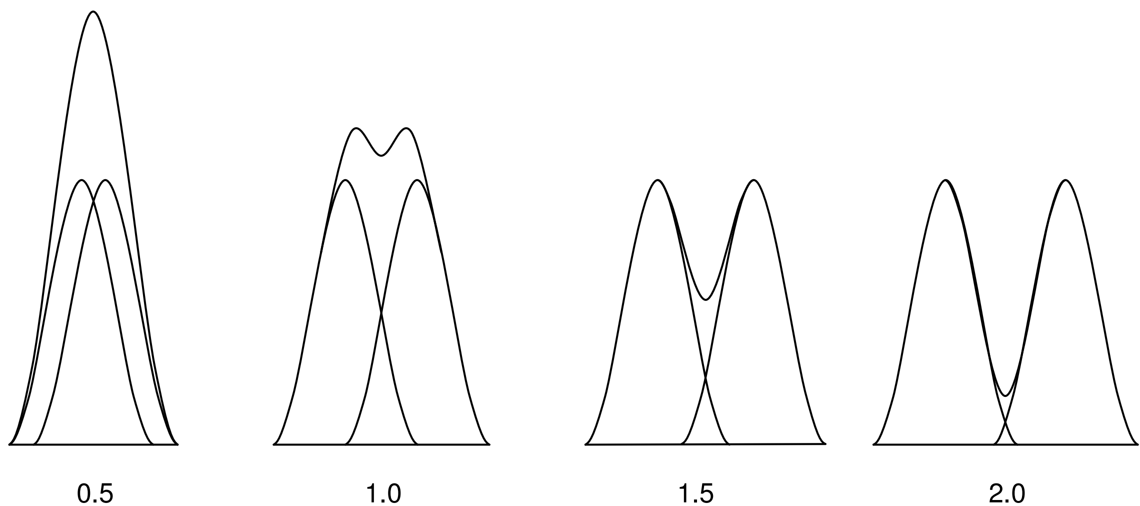

Figure 2.19: Summation of two Gaussian peaks with separations of 0.5, 1.0, 1.5, 2.0 FWHM (after [22]**)**

With this information, an unknown emission spectrum can be compared to other known emission spectra and a selection of candidates can be drawn upon.

The controlled addition of specific elements in specific quantities to a semiconductor has the potential to add defined energy levels within the bandgap, as shown in Figure 2.19. The addition of an energy level within the bandgap means that as electrons loose energy, they can make additional transitions. So, while the bandgap for ZnS is 3.6eV the emission peak from a ZnS:Ag phosphor is centred around 450nm [34, 37], the equivalent to 2.8eV. Similarly, the emission peak from a ZnS:Mn phosphor is centred around 584nm [22], equivalent to 2.1eV.

Each phosphor has a unique combination of bandgap and dopant energy levels within the bandgap.

The concentration of dopant can be optimised for maximum emission intensity. An increased dopant concentration increases the number of luminescent centres where emission can occur. However, counteracting this is a broadening of the dopant energy level due to the increased

concentration of dopant. The maximum emission efficiency is reached when improvement from additional active areas balances the reduction of emission due to broadening of the dopant level. The addition of excess activators or luminescent killers, which reduces the emission intensity, is called quenching or concentration quenching.

Doping therefore affects the emission spectrum of phosphor, as well as the rate at which the intensity of the emission reduces after the initial excitation. When quantified this is a method of describing decay time.

2.5.4 Decay Time Constant

A key variable of luminescence is the time taken for the excited electron to return to its ground state and is linked to the quasi-stable state in a luminescent centre, the type of phosphor bandgap (direct or indirect) and radiative versus non-radiative decay route via dopant energy levels.

When the phosphor is excited with a pulsed excitation source, it triggers periods of excitations followed by emissions, an emission with a characteristic luminescent decay - or afterglow (Figure 2.20). Over time intensity of the emission from a phosphor with one primary emission route follows a repeatable trend, which can be mapped using an exponential function (Equation 3).

$$I(t) = I_0 \exp\left(\frac{-t}{\tau_d}\right) \quad [74] \qquad \textbf{Equation 3}$$

Where $I(t)$ is the emission intensity after t seconds, I_0 is the initial of emission intensity and τ_d is the decay time constant.

Emission spectra that have multiple emission peaks tend to be indirect and have several emission routes, this leads to additional decay curves. Equation 3 can be expanded for a phosphor with two primary decay routes that create two overlapping decay curves (Equation 4). This facilitates definition of the initial peak intensity and decay times for both decay curves.

$$I(t) = I_0 \exp\left(\frac{-t}{\tau_0}\right) + I_1 \exp\left(\frac{-t}{\tau_1}\right) \quad [75] \qquad \textbf{Equation 4}$$

τ_0 and τ_1 are the decay time constants for the two decay curves, I_0 and I_1 are the initial intensity of emission at $t = 0$.

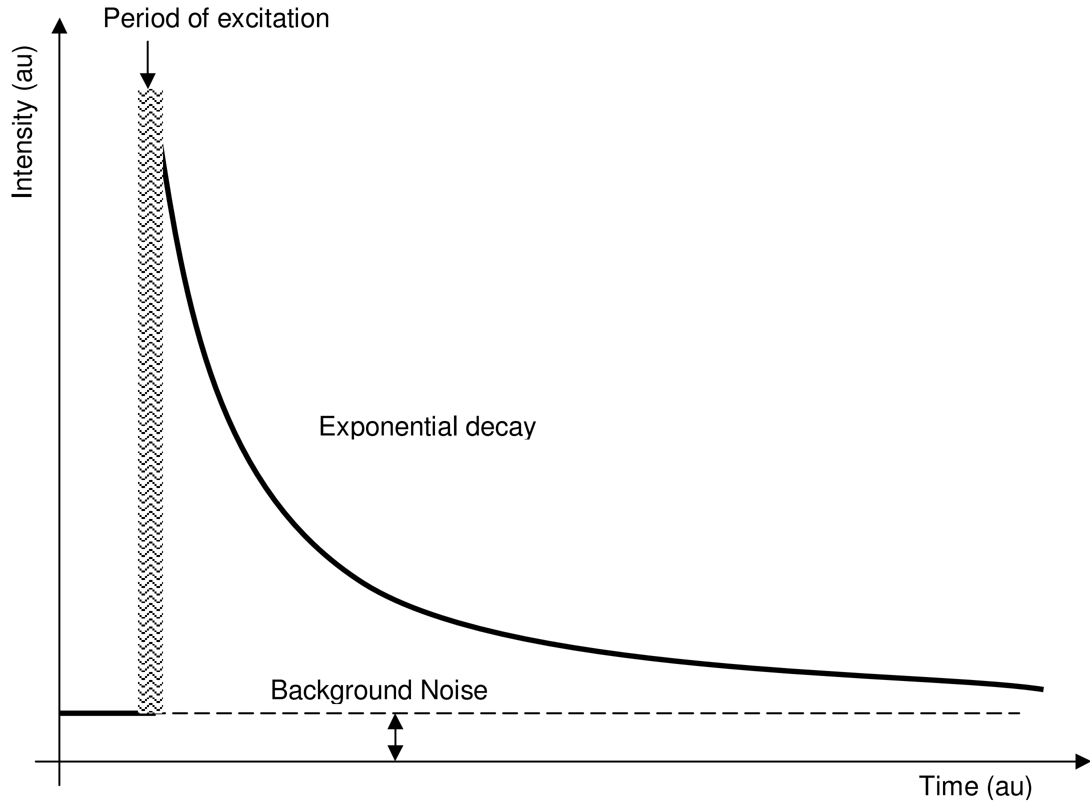

Figure 2.20: A drawing of the intensity of emission from a phosphor over time, as an example of the decay curve.

Decay times from phosphors vary greatly, for example hexagonal ZnO:[Zn] has a short decay time in the region of 10^{-6} seconds where as tetragonal ZnF_2:Mn is magnitudes longer, at 0.1 seconds [74].

2.6 Thin film deposition by sputtering

Thin films of scintillator are used in the field of radiation detection, primarily for weakly penetrating particles, such as protons and alpha particles [54]. Using the technique of thin film deposition the thickness can be of one or two orders of magnitude smaller than the minimum in other detector configurations. This work focuses on inorganic scintillators - not plastic scintillators, organic scintillators, gaseous scintillators or glass scintillators. This is due to inorganic (which includes semiconducting ZnS) scintillators have the best combination of characteristics suited for neutron diffraction analysis.

Sputtering is the most frequently used thin film deposition technique, not only in the displays industry but also for fabrication of microcircuits [76].

There are many deposition technologies for material formation [77] of thin films for forming layers in the thickness range of a few nanometres to approximately ten microns. The deposition technologies can be classified as purely physical, such as evaporative methods, purely chemical, such as gas- and liquid-phase chemical processes, or those that overlap the two processes, the physical-chemical processes.

Thin films phosphors have been grown using RF Magnetron Sputtering, a branch of the sputtering technique, for many years by the Displays and Imaging Group currently at NTU, originally under the supervision of Professor Clive Thomas and now Professor Wayne Cranton [76, 78, 79].

2.6.1 Growth

Sputtering is a form of glow-discharge technology [77], where surface atoms are ejected from a target fitted to an electrode by the process of momentum transfer by bombarding ions. Sputter deposition has become a generic term for a variety of processes such as diode sputtering, reactive sputtering, bias sputtering, ion beam sputtering (used in surface analysis), plasma processes and magnetron sputtering.

Generally, the minimum ion energy for sputtering is the binding energy of the most weakly bound surface atoms (Table 2.8).

The incident ions are created in two sputter deposition classes, plasma and ion beam. The target surface is immersed in the plasma class, while the ion beam class is separated from the target surface with ions extracted from the source and 'fired' at it. Both of these techniques are used within this work in differing ways.

Table 2.8: The binding energies of combinations of elements within the target material [30].

Bond	Bond strength	
	($D_0$298/kcal mol^{-1})	($D_0$298/kJ mol^{-1})
Ag – Ag	39±3	205±13
Ag – Cl	81.6	341.4
Ag – S	51.9	217.2
S – Zn	49±3	205±13

Zn – Zn	7	29

The main advantage of the Magnetron Sputtering technique over others is its combined use of magnetic and electric field at the target surface. Target-generated secondary electrons do not bombard the substrate because they are trapped near the target and so do not contribute to increased substrate temperatures and radiation damage. This allows temperature sensitive substrates (e.g. plastics) and surface sensitive substrates (e.g. semiconductor devices) to be used in thin film growth with minimal adverse effects.

To produce high-energy ions necessary for sputtering, an adequate voltage across an electrode and an appropriate gas pressure are required, the gas will then break down into a plasma discharge.

The target material fixed on the electrode acts as a cathode due to a net negative charge during a.c. potential. The operating frequency applied to the electrode to maintain the sputtering is in the region of 10MHz [78], hence the term radio frequency (RF) sputtering. The positive ions are accelerated towards the cathode with sufficient energy to cause sputtering of the target material. The sputtered material radiates outwards from the target, which results in the growth of a thin film of target material on all surfaces it is incident upon. A substrate is positioned opposite the target material so that a large quantity of the sputter material has the potential to condense on it.

A primary factor in this technique is power - an increase to the power delivered to the electrode will increase the kinetic energy of the collisions increasing the sputter yield. A lower gas pressure will allow this sputtered material to have a longer average mean free path, meaning a greater quantity of sputtered material will reach the substrate.

The diode plasmas have difficulty depositing or sputtering insulator targets and using a gas such as O_2, can cause the cathode to oxidise and insulate the surface of the target. For RF magnetron sputtering, a small part of the electrical cycle, the cathode and anode are electrically reversed. This eliminates charge build-up on an insulating surface by providing an equal numbers of ions and then electrons per electrical cycle, and hence, permits insulators, conductive materials and metals to be sputtered in a reactive environment [72].

The incorporation of a strong static magnet parallel to the cathode surface enhances the rate of growth on the substrate and the sputter rate. The magnetic field increases the concentration of ions near to the target material, increasing the sputter rate. Alternatively, it can also facilitate an overall lower gas pressure within the chamber whilst maintaining a sputter rate. A reduced gas pressure increases the mean free path of the sputtered material. Lower gas pressure also improves film quality by reducing bombardment by the gas particles.

These factors combined together in this method of sputtering to produce higher deposition rates than conventional methods and lend themselves to economic, large-area industrial applications. Ghosh [72] gives a detailed description of parameters typically used to deposit ZnS using RF Magnetron sputtering, summarised in Table 2.9.

Table 2.9: Deposition Parameters used for RF magnetron sputter deposition of ZnS [72].

Parameter	Values
Deposition Time	10 to 30 minutes
RF Power	180W
Electrode Distance	3cm
Sputter Gas	Argon
Gas Pressure	0.1mbar
Substrate used	Glass, Si
Substrate Temperature	300K

2.6.2 Annealing

Once the desired thickness has been grown and sputtering has stopped, thin films often require annealing. The purpose of annealing is to improve the crystallinity of the thin film [76]. Typically, at the point where the thin film adheres to the substrate, the thin film will have adapted the crystal structure and interatomic spacing of the substrate. At greater film thicknesses, the deposited material starts to form its own natural crystal structure. This is one where internal forces from atomic repulsion and atomic bond are at their lowest level.

ZnS:Ag,Cl is the primary phosphor under investigation, the movement of Ag within thin films of ZnS can occur via two methods [80]. Firstly, the random vibrations within the material that leads to a 'slow' movement of atoms diffusing into grains. Secondly, there is a 'fast' migration as atoms travel along grain boundaries. Fast migration occurs at lower temperatures (80-400ºC) than the slow migration for Ag in ZnS. Therefore, slow migration permits the integration of the

silver ions into the ZnS lattice, where as the fast migration would distribute the silver ions within the thin film.

The Arrhenius-type relation (Equation 5 [22, 80]) expresses the diffusion coefficient (*D*) in semiconductors like ZnS:

$$D = D_0 \exp\left(-Q / kt\right) \qquad \text{Equation 5}$$

Where D_0 is a frequency factor, *Q* is the activation energy for diffusion, *k* is Boltzmann constant, and *T* is the absolute temperature.

This equation describes the movement of atoms within a bulk material, but has been shown by Bacaksiz [80] to closely represent diffusion Ag in ZnS thin films of 3μm. Caution should be paid to films thinner than this, as the reduced dimensions can effect the movement of dopants within the bulk material.

2.6.3 Thermal Annealing

The application of thermal annealing provides the atomic vibrations required for atoms in a thin film (or bulk material) to reorder so that the thin film has an increased quantity in the crystalline form. There will remain some disorder due to the difference in the crystal size of the substrate and the thin film material, creating an interface layer.

When sputtering, or depositing in general, it is often necessary to consider a pre-bake process for the substrate preparation. The level of prebake required is determined by the level of annealing required post growth. When a greater temperature is used post-deposition rather than prior to deposition, there is a tendency for the wafer to outgas further. The expelling gas forces the deposited thin film away from the substrate leaving detectable pinholes in the film or even crazing of the film.

2.6.4 Laser Annealing

The Displays and Imaging research group at Nottingham Trent University has been using Laser annealing successfully for ZnS:Mn thin films [81]. This annealing method is designed for thin films due to the limited penetration of the UV laser energy utilised. It is a form of rapid thermal

annealing where a precise amount of energy is deposited in an exact area of a thin film. With sufficient energy, the atomic bonds are spontaneously broken down and the atoms in the thin film reforms into a new more ordered crystalline structure.

2.6.5 Alternative Methods of Depositing Thin Film

Phosphor screens can be produced by different methods including sedimentation, spraying, screen-printing and doctor blade [25]. This work is centred on thin film growth with RF Magnetron Sputtering being the primary technique. It has the advantage of being able to sputter conductive and non-conductive materials, grow very thin films with strong uniformity and negligible contamination, but it is not the only method of depositing a thin film, each method has advantages and disadvantages, some of which are described below.

2.6.5.1. Evaporation

Thermal and vacuum evaporation are two of the oldest techniques used for depositing thin films and still widely used for depositing metal and metal alloys. This process can be described in three steps:

- a vapour is generated by boiling or subliming a source material;
- the vapour is transported from the source to a substrate, and;
- the vapour is condensed to a solid film on the substrate surface.

Mantler-Niederatter [48] states that ZnS:Ag was created using the Balzers method of vaporising ZnS, Ag and Al-nitrites from directly heated Mo boats with ratios of 10:1:3 of ZnS, Ag and Al respectively. Suda [82] used ZnS:Ag (0.1 mol%) with $AlCl_3$ and $ZnCl_2$ to create a 5-6µm thin film onto SnO_2 glass substrate using evaporation.
The best carrier temperature quoted by Mantler-Niederatter for depositing the material using heated Mo boats is at 250℃. This value was optimal for this type of experiment and it will give an indication of the region of temperatures that are most suited for depositing ZnS:Ag phosphors. Mantler-Niederatter [48] goes on to say that greater luminescence was achieved by thermally annealing the sample in an oxygen-free nitrogen atmosphere at 650℃ for 1 hour.

2.6.5.2. Low-viscosity Epoxy

McElhaney [37, 83] uses a low-viscosity epoxy to mix with 800mg of ZnS:Ag powder to create a suspension. When the suspension is put into a mould and left for a period the ZnS:Ag phosphor particles settles to the bottom of the epoxy and cure with the phosphor density of 8mg/cm^3. The epoxy is transparent to visible emission from the phosphor and is thin enough (1.3mm) to cause limited interference to incident alpha particles.

2.6.5.3. Gas Phase Chemical Processes

Methods of film formation by chemical processes in the gas or vapour phases include chemical vapour deposition (CVD) and thermal oxidation. CVD is a materials synthesis process whereby constituents of the vapour phase react chemically near or on a substrate surface to form a solid product. The main advantage of CVD is its versatility for synthesizing both simple and complex compounds with relative ease at generally low temperatures.

Shiiki [35] uses the Metalorganic chemical vapour deposition (MOCVD) technique to grow a thin film of ZnS:Ag,Cl to a thickness of 600nm for the purpose of creating an EL display.

2.6.5.4. Atomic Layer Deposition (ALD)

Also referred to as atomic layer epitaxy (ALE), along with high precision thickness control it has excellent uniformity and low pinhole density [84]. This deposition technique grows a thin film to thicknesses with an accuracy of an atomic layer, something the other techniques cannot achieve. Alternating exposures of a substrate to reactants causing a monolayer to grow, repeated alternating reactants cause the growth of the thin film further, one atomic layer at a time.

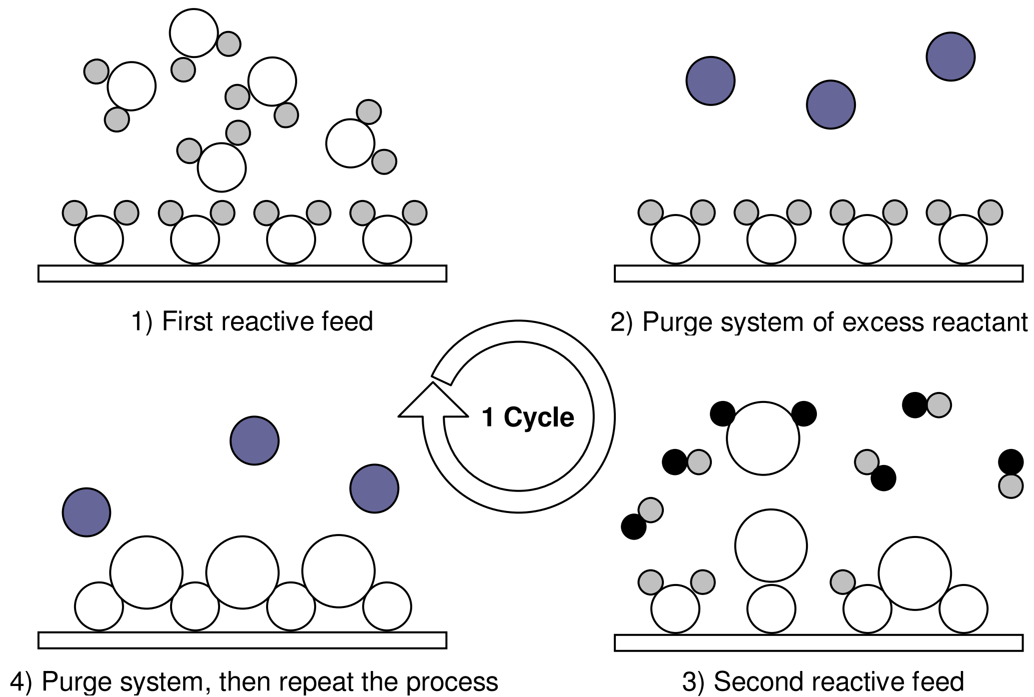

Figure 2.21: An illustration of the ALD process, after [85].

Polycrystalline ZnS thin films were grown by ALD [73, 86] using the reactants:

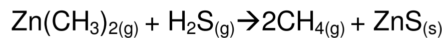

$$Zn(CH_3)_{2(g)} + H_2S_{(g)} \rightarrow 2CH_{4(g)} + ZnS_{(s)}$$

Hsu [73] use H_2 gas to purge the system (Figure 2.21 [Stage 2+4]) between reactant stages. The draw back to ALD is the time required to deposit a film due to the requirement that the reactants be applied separately. The ALD growth that produced the most uniform ZnS growth was observed at 300°C [86] with a growth rate of 0.07nm per cycle, no impurities of any detectable amount was observed. Although, Hsu [73] found that a temperature between 100°C and 160°C was the most effective for growth, which was at 0.27nm per cycle.

An interesting aspect of ALD that Kim [86] reported on was that above 400°C the hexagonal (wurtzite) phases began to appear. This is considerably lower than in other processes, which are traditionally at the transition point quoted in literature [30, 30, 87], that being 1295K (1022 ºC).

To incorporate a Mn dopant into ZnS to form a ZnS:Mn thin film (a commonly used phosphor in EL) they use a method of simultaneously pulsing $Mn(thd)_3$ with Diethlyzine (DEZn - $(C_2H_5)_2Zn$) during 1% of the DEZn pulses [84]. Hence, effectively creating a layer of Mn once in every 100 layers.

2.7 Summary

The results of the literature study show that for neutron diffraction measurements any new scintillator to be considered requires a fast decay time and large emission intensity. The preferred decay time would be in the order of hundreds of nanoseconds with an intensity that was no less than half of that provided by the standard ZnS:Ag powder phosphor scintillators. Formed into a thin film and incorporated into a microstructure the phosphor would potentially fulfil the third requirement, - an increased spatial resolution. This technique could improve light detection via the use of inherent light guiding properties of these films, hence reducing the necessity for an intense emission.

^{6}LiF-ZnS:Ag has been used by ISIS for its benefits in a number of areas. ^{6}LiF is used for its chemical stability whilst maintaining a high capture cross-section. It reacts with neutrons to liberate two products, both of which create a RL emission with limited gamma radiation. ZnS:Ag is used for its very bright luminescent emission, insensitivity to gamma radiation and hence good gamma discrimination. The disadvantage of ZnS:Ag is its long afterglow. This afterglow can be removed from the signal to leave just the fast decay component (200ns). However, the emission related to the fast decay component is considerably weaker in comparison to the afterglow and so becomes unsuitable for this technique.

The optimum thickness for the ZnS:Ag phosphor is related to the excitation form and the energy of the excitation. This would be less significant if the phosphor was transparent to its own emitted light. However, ZnS:Ag is opaque to its emission, meaning that once luminescence is created it requires a limited density of material for it to transit out of the phosphor to be detected.

When quoted in the literature, the Ag concentration used has been typically around the 0.01at% level [22], but there have been reports of up to 1at% [61]. For thin film phosphors, consistently doping to a level of 0.01at% is problematic, introducing possible complications if there was a loss mechanism in the growth procedure. With phosphors of higher concentrations, a loss of 0.01at% of dopant would be hard to observe, however when 0.01at% is the dopant concentration this would mean the entire dopant was lost from the phosphor.

From the literature, it is evident that there are alternative phosphors available for replacing ZnS:Ag with faster decay times. However, the weakness for these phosphors is typically the

intensity of light compared to ZnS:Ag. The phosphor that has the most potential is Cs_2LiYBr_6:Ce (Section 2.2.3 - Table 2.5), but at nearly half the intensity of ZnS:Ag this might be too much of a loss to compensate for the improved decay time. However, this is still a significant emission and with the possibility of optimising, it could be brought closer to ZnS:Ag's 160,000 photons per neutron.

The two phosphors that have potential are Cs_2LiYBr_6:Ce and $YAlO_3$:Ce, as seen in Table 2.10.

Table 2.10: Emission intensity of three phosphors and their decay time.

	$YAlO_3$:Ce	Cs_2LiYBr_6:Ce	ZnS:Ag
Relative light output (%)	30*	55*	100
Scintillation decay time (ns)	25	89	200

*Values achieved by two separate comparisons to ZnS:Ag.

The decay times are likely to be the fast component and not the dominant afterglow that is pronounced in the ZnS:Ag, as shown by the ZnS:Ag reading. Without knowledge of the methodology of the measurement, an accurate judgement of the decay times cannot be made. This leads to the assumption that the decay times quoted are either accurate and do not contain a strong afterglow or that the afterglow and fast component are inherently linked and an improvement in one improves the other.

An aspect that has been highlighted was the testing with PL and RL for the luminescent materials. While the phosphor will be used for a radioluminescent application, several reports use PL as a characterisation tool, probably due to the difficulty in making repeatable RL measurements with significant luminescent intensity being produced. Hence, for this work, the intensity of the PL and RL emissions were examined along with other luminescent characterisation measurements - including emission spectrum and decay time.

3 Experimental Techniques

3.1 Introduction

The previous chapter presented the background information on how phosphors are used in neutron scintillation and how they have the potential to be grown as a thin film using RF Magnetron sputtering. This chapter discusses the precise method used to grow thin films and the methods by which the films are characterised.

Thin films were grown onto silicon substrates to a thickness of between 50nm and 3µm using an RF Magnetron sputtering system. Following deposition, the thin films were thermally annealed to promote crystallinity. The thin films were then studied in terms of surface characterisation, crystallinity, composition, and luminescent (PL and RL) characterisation.

Surface characterisation was undertaken using a set of metrology tests to examine the thickness and surface roughness of the deposited films, based on use of three independent techniques - reflectance spectroscopy, stylus profilometry, and optical profilometry. The crystal structure and composition were examined using X-ray Diffraction (XRD) and Ion Beam Analysis (IBA). The characterisation for the luminescence examines the emission spectrum and decay constant versus excitation by either UV laser irradiation or ionising radiation. There are several different phosphors tested in forms such as powder, pressed pellet, thin film and a self-supporting wafer. The excitation sources for these phosphors were a UV laser source to create photoluminescence (PL) and an alpha radiation source to create radioluminescence (RL).

The experimental work was carried out primarily within the thin film facility of NTU [78, 79, 81, 88-92], which is part of the Displays Research Group. During this research project, the entire facility, originally located in the Newton Building of the City campus, was relocated to a new site on the Clifton Campus. This required a complete de-commissioning of all deposition and characterisation systems for relocation, re-construction and commissioning as part of the new facility at Clifton. The author was responsible for the equipment used in this project, which allowed a complete re-calibration of the deposition parameters as part of the re-build/re-commission, as discussed below.

3.2 Thin film deposition by RF Magnetron sputtering

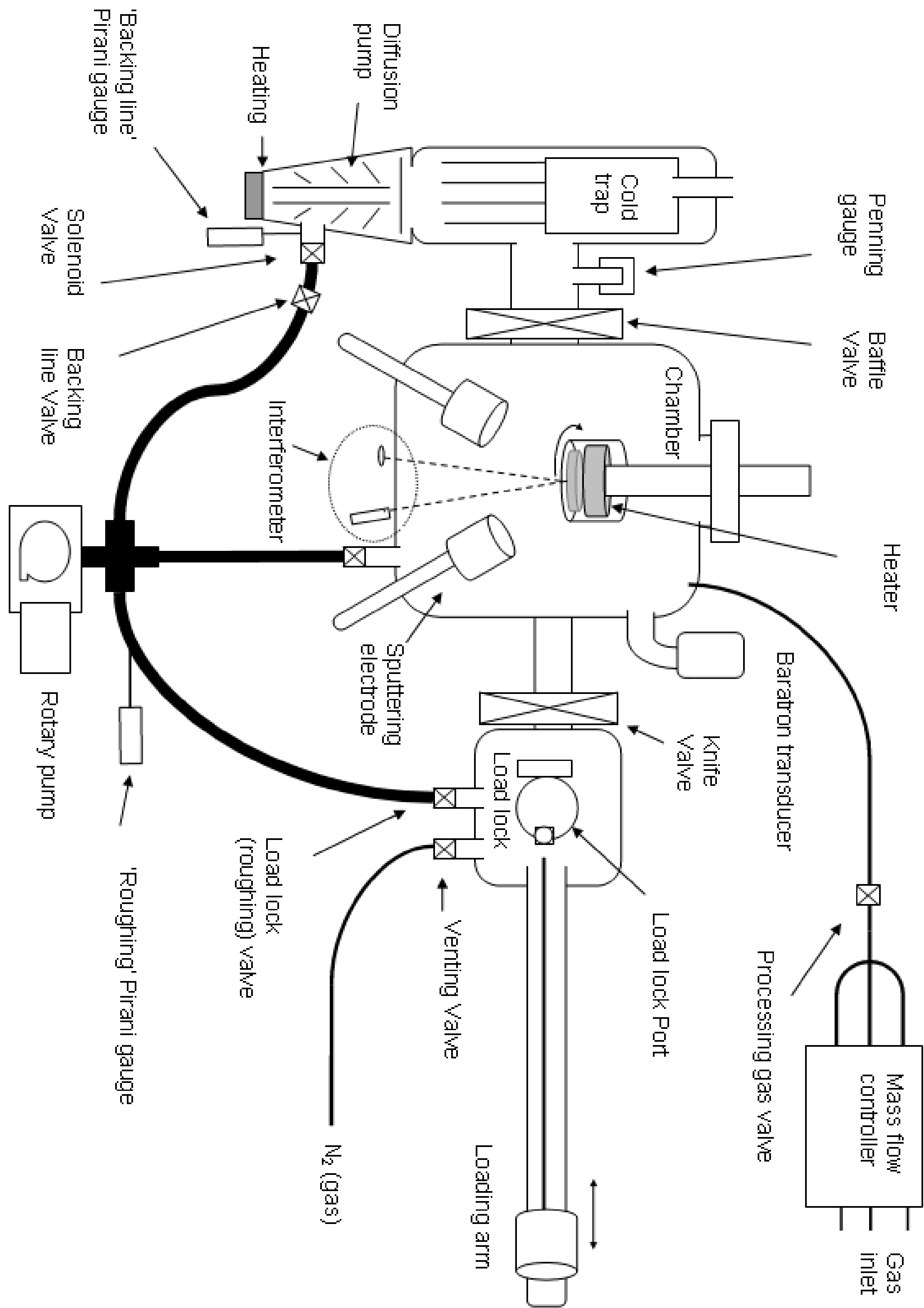

Figure 3.1: Diagram of the sputtering system used for thin film deposition of phosphor material.

The technique chosen to grow a film was dependent upon achieving a high level of film uniformity and a well controlled thickness. The technique used was RF Magnetron sputtering for its ability to deposit insulators and wide bandgap semiconductors with a very high level of purity and uniformity [81]. Sputtering of a target material is a controlled process for depositing a high purity, polycrystalline film onto a substrate. For this project, the deposition was undertaken in a custom designed, multi-electrode sputtering system (Figure 3.1) manufactured by Scanwel Ltd.

There are numerous controllable variables in RF magnetron sputtering with optimum parameters differing with phosphor and the type of luminescent excitation. This investigation looked at changing three of these variables, film thickness, deposition temperature and annealing temperature.

3.2.1 Electrode

An RF Plasma Products power unit (RF5S), tuner and matching unit supply the power to a Kurt J. Lesker Torus 5 M electrode. With a target secured to the electrode an electrical potential is applied to the base of the target to create the driving force for sputtering. The electrical current is delivered to the electrode at a frequency of 13.56MHz - hence the term Radio Frequency (RF). The sputtering process generates sufficient heat to deform the copper electrode head. To prevent this, the electrode as well as the matching unit and the diffusion pump are water-cooled.

The chamber has four electrodes loaded with up to four target materials. This allows multiple targets to be used either simultaneously or in sequence – creating a mixture or layering of materials. Multiple targets require a reorientation from a position directly opposite the substrate to one where all are equidistant and at the same angle in respect to the substrate. The electrodes are arranged at an angle of 45° from the horizontal and positioned at a distance of 15cm (± 5cm) from the substrate (Figure 3.2). Films grow with a uniform thickness on the substrate using this multiple electrode system by rotating the substrate during the deposition period.

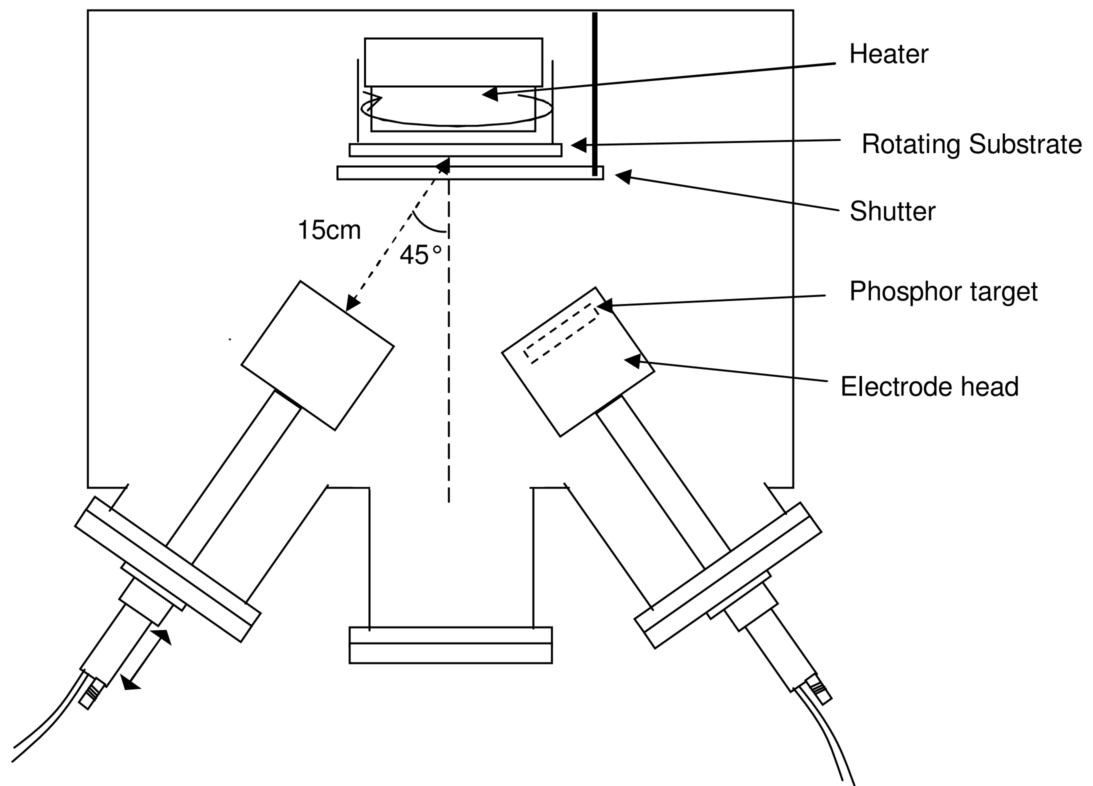

Figure 3.2: Orientation of electrodes in respect to the substrate for simultaneous / multiple sputtering.

3.2.2 Target Material

A ZnS:Ag,Cl phosphor powder (0.01at% Ag) from Phosphor Technology Ltd. was used as the target material for thin film growth. Prior to its use as a target for sputtering, the phosphor powder was compacted into a three-inch stainless steel dish (Figure 3.3 & Figure 3.4). This uses a pressure of 205 bars (3000 Psi), which is maintained for a period of approximately 10 minutes while the powder compresses as trapped gas is released and hence the pressure reduces marginally.

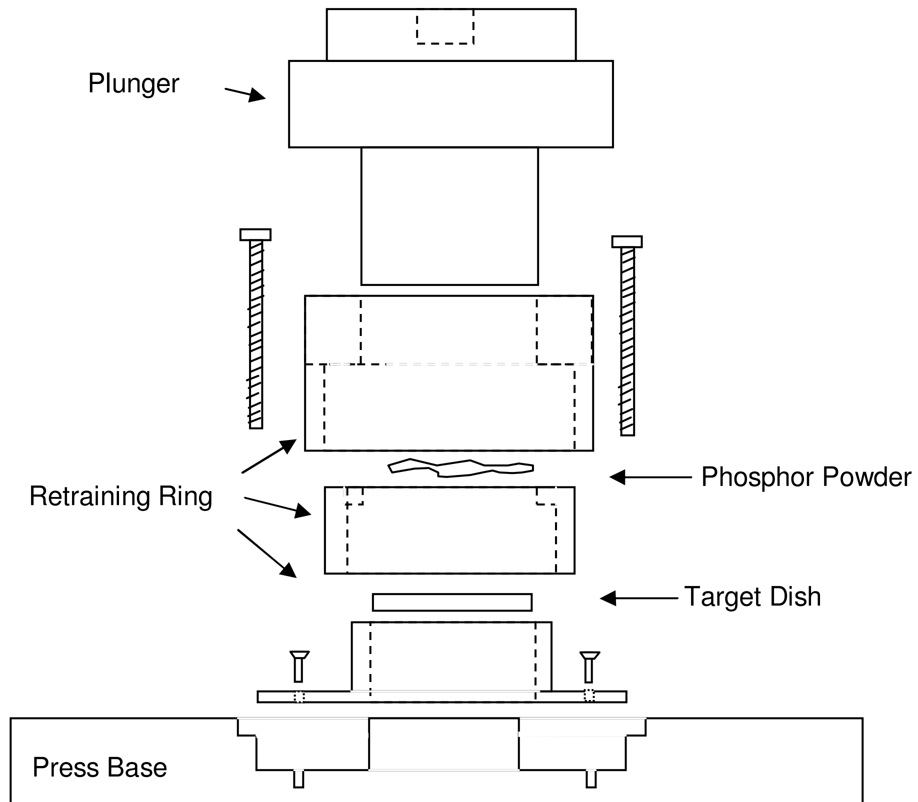

Figure 3.3: Setup for creating a pressed phosphor target in a hydraulic press.

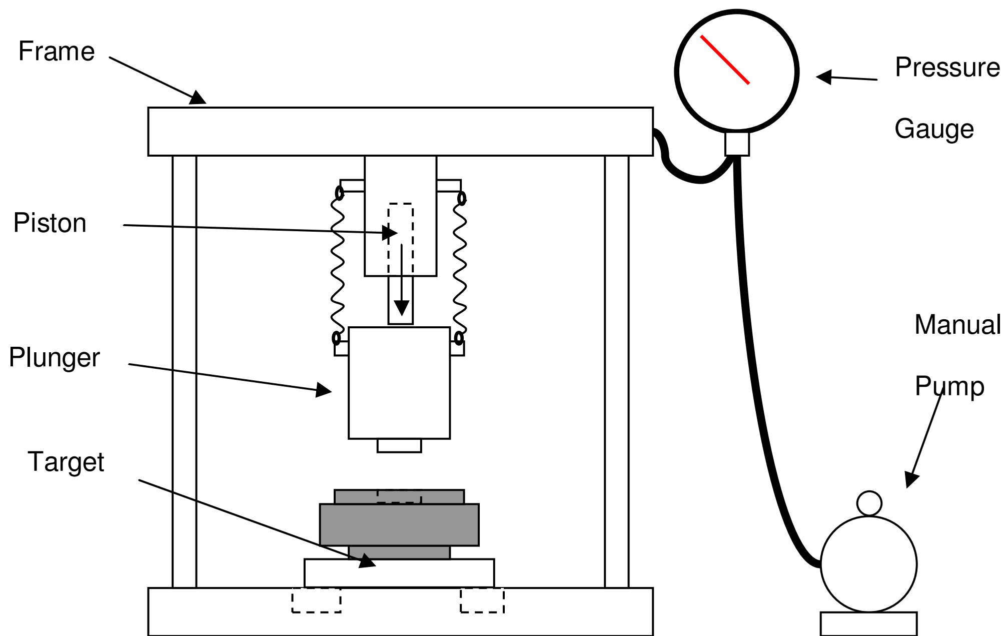

Figure 3.4: Pressed powder phosphor target used in a hydraulic press.

It is important that the surface of the phosphor target is smooth to maximise the sputtering lifespan within the RF magnetron sputtering chamber. Surface imperfections in the target create hot-spots in localised areas because of increased sputter rate. Left unchecked this

allows the sputter process to penetrate through the material within minutes. If this occurs, it continues to worsen until a localised region of that target has been sputtered away. With deposition time typically being between two and eight hours this can happen unobserved. If sputtering is left running, it begins to sputter the stainless steal dish then the electrode head, introducing contaminants into the system.

An alternative to a pressed powder target is a solid target. This, as the name suggests, is a more compacted version of a pressed powder and is self-supporting, so does not require the metal tray. The increased density of the target also means that there is more material to sputter, which therefore lasts longer than the pressed powder target and is less prone to sputter-through. However, specific “off-the-shelf” solid phosphor targets are not commercially available. Previous experience in the group and with industrial collaborators has shown that vacuum or hot pressing of phosphor powder produced inconsistent results.

3.2.3 Substrate

The sputtered phosphor material requires a substrate to condense upon in order to form the thin film - a 100mm silicon wafer is used for this purpose in this work. The Si wafers are single crystals with very low contamination and are cut from a column along the (100) plain. Si is commonly used for ZnS thin film growth [72, 78]. One surface of the wafer is highly polished while the other is etched to create a rough surface. A polished surface allows a uniform thin film thickness to be grown and, in the system it also provides an optical surface to reflect laser light as part of the in-situ thickness monitor. Growth rate of a thin film in this system is not entirely predictable, as there are some factors that can change even though all controllable variables have been maintained. These factors can produce differences in sputter rate and growth rate between samples leading to variations in the deposition time. The most prominent variable would be target aging, which creates an increased sputter rate as the target is used over its lifetime. The laser monitoring technique was essential for when a specific thickness of film was required. For in-situ thickness monitoring, a visible (670nm) laser diode is directed at the wafer (and growing film) and reflected back onto a photodiode. Over time as the film grows in thickness, the reflected laser light goes through a series of intensity oscillations, from light to

dark. This is due to optical interference effects – varying between constructive and destructive as the thickness (and subsequently the optical path length) of the deposited transparent film increases.

The laser diode creates a continuous wave of monochromatic radiation (670nm, 1mW). The photodiode creates an analogue electrical signal that was passed to a Pico Log ADC-16 High Resolution Data Logger and Pico Log Recorder software to convert it to a digital format for display, manipulation and measurement by a computer (Figure 3.5).

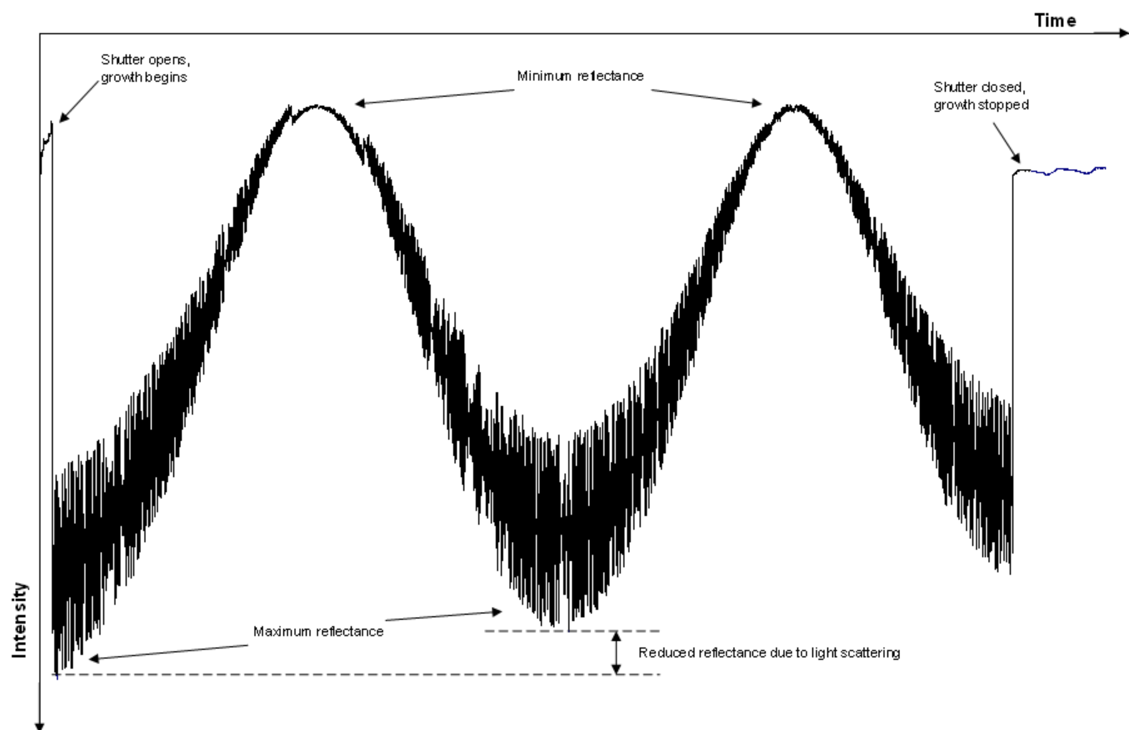

Figure 3.5: Typical interferometer pattern from the growth of a thin film on a Si substrate.

From the interference pattern, an approximation of the film thickness can be based on a predetermined result that 5.5 cycles was equivalent to a thickness of 800nm. Therefore, 1 cycle is 145nm or 0.69 cycles is 100nm. This is related to the relationship between constructive interference and optical path length. Where the incident light on a thin film will be reflected at a series of thin film thicknesses depending on the wavelength of the incident light, i.e. $2nd = m\lambda$, where n is the refractive index, d is the film thickness, m is an integer value and λ is the wavelength of the incident light

A shutter within the chamber can be rotated into position between the substrate and the sputtering source material, providing a method by which the period of thin film growth can be accurately controlled. A controlled start of growth is important, so that the plasma has become

stabilised and a presputter of the target has removed the 'rubbish' layer on the surface of the target.

3.2.4 Heater

One of the main parts of the chamber is the substrate heater, since substrate temperature and post deposition annealing have a significant effect on the fabrication and film characteristics.

The heater controller (VSW Technology heater power supply) delivers a power to a ceramic resistance heater element using percentages of maximum power, rather than Wattage. The heater is mounted above a rotating heater-substrate holder, which permits rotation of the substrate for enhanced uniformity. Heat radiates across the short distance of the vacuum from the element to the reverse side of the substrate. The temperature-controlled heater has a c-type thermocouple built into the system, suited for a temperature range of 0°C to 2320°C (oxygen free atmosphere), is positioned above the heater relaying an electrical current to a display that provides a live temperature calculated from the current. This temperature readout can be correlated to a temperature of the substrate.

The substrate is suspended in a substrate rotator within the chamber, which is approximately 20mm below the heater. Rotating the substrate promotes a uniformity of heat distribution across the wafer and in a multiple-target system with electrodes positioned at an angle to the substrate normal; this means a more uniform film deposition.

There are three stages of temperature control during thin film growth: outbaking, deposition temperature and annealing. Before deposition of a thin film the substrate is prepared by outbaking, heat is applied to the substrate to outgas particles absorbed onto the surface of the silicon wafer. During deposition, the substrate was temperature controlled, which influences thin film growth rate, which in turn influences the crystallinity. Following the deposition and whilst still under vacuum within the chamber the films are thermally annealed to promote crystallinity using the same heater as used in the previous two processes. Thermal annealing within the chamber provides a controlled atmosphere where the level of contaminants is considerably reduced.

To achieve the higher annealing temperatures, typically temperatures over 600℃, the shutter shown in Figure 3.2 was used to reflect heat transmitted through the wafer back towards it. Therefore, a higher wafer temperature was achieved whilst not exceeding the maximum tolerable temperatures of the chamber. This was determined by a rubber 'o'-ring with a temperature tolerance of 250℃, which joins the lid of the chamber to the base. The drawback to this method is that it can cause impurities to be introduced to the system from the shutter by outgassing of contaminants absorbed during a period when the chamber is opened, or from previous depositions.

3.2.4.1. Heater Calibration

For ZnS:Mn, the optimum temperature for thin film deposition using RF Magnetron sputtering is reported as 190℃ [78, 79] which should be an indication for the optimal temperature for depositing ZnS:Ag,Cl in RF magnetron sputtering.

The temperature of the substrate can be determined by relating this temperature measurement to a calibration curve.

Prior to the relocation of the system, the power required to bring the substrate to a temperature of 190℃ was 7.8% of the total output of the VSW Technology heater power supply. To achieve a required substrate temperature, power was delivered to the heater as a percentage with an accuracy of one decimal place. This reading was true for the time and date of the previous calibration. Since then, the author has completed a de- and re-commissioning of the system. This required a re-calibration of the system to determine the accuracy of previous values.

There were two methods used to measure the temperature, the use of adhesive thermal dots and thermocouples.

Omega Engineering Thermal dots are non-reversible temperature labels, representing a range of temperatures of approximately 25℃ using five temperature markers. Once a temperature has been reached that corresponds to one of the dots, that dot blackens permanently. Used as a tool to corroborate a previous temperature measurement, it is seen more often as a safety feature on mechanical objects to reduce overheating or the chances of burning. These dots are on a 15mm diameter sticker that was fixed to the polished surface of a silicon substrate and

represent the temperature of thin film growth. After heat treatment, the silicon wafer is removed and the thermal dots observed to evaluate the maximum temperature.

The ranges of thermal dots that the supplier provides does not extend to the temperature range of a typical thermal anneal (~500℃). Therefore, an incomplete measurement range and poor accuracy (approximately ±5℃) make this technique only useful as a corroborative tool. They offer a temperature guide but lack the necessary accuracy and reliability, whereas a thermocouple provides real time readings with an accuracy of 0.1℃.

K-type thermocouples were attached to a virgin substrate and linked to a Eurotherm 8156 display via a vacuum feed-through (Figure 3.6). Along with a calibration of the applied heater power to temperature at the growth surface, there were two calibrations carried out, both using two thermocouples in parallel. The tests were of the temperature calibration for the heater with the difference between the upper and lower surface of the substrate and the difference in temperature across the lower surface of the substrate where the thin film is grown.

The calibration was to determine how the heater transmits heat to the substrate and was used to determine temperature differences between the top and bottom surface of the substrate (results presented in Figure 3.8 and Figure 3.9). This provided an accurate measure of annealing temperature for ion-implanted samples (see section 6.2.3) as well as a general guide for deposition and annealing temperatures of the thin film.

A difference in temperature across the surface of the substrate can affect the deposition rate and uniformity of the thin film. To monitor the temperature the thermocouples were attached at the edge of the substrate and another at the centre. This allowed simultaneous measurement of heat distribution over the sputter surface area of the silicon wafer for the deposition and annealing temperature ranges, results of this are in section 5.3.1.2.

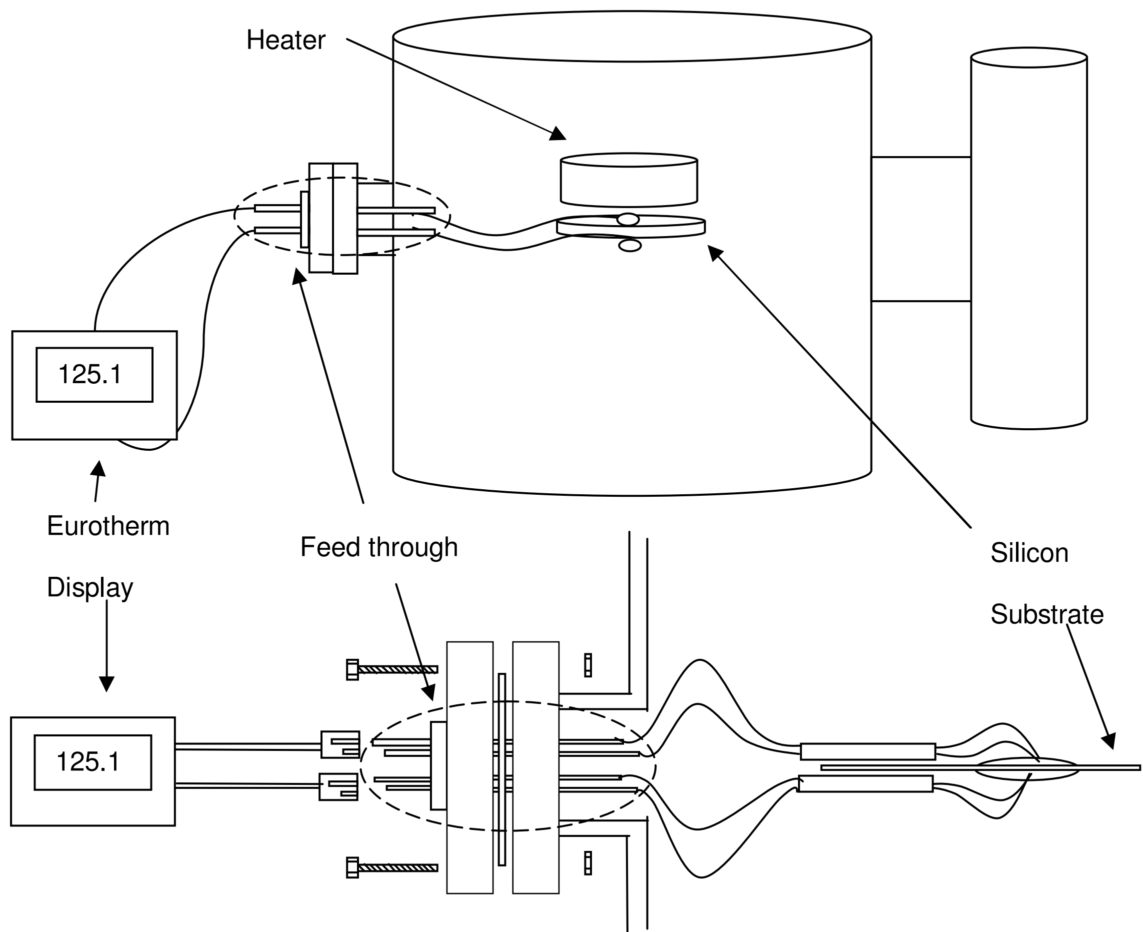

Figure 3.6: A representation of the setup required for the temperature calibration of a silicon wafer using thermocouples.

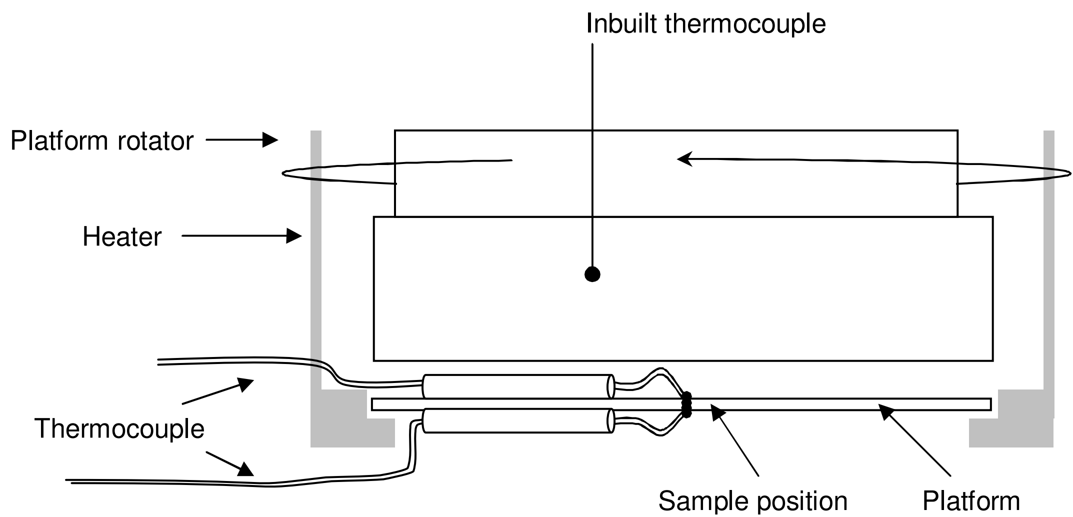

Figure 3.7: System setup for the annealing of implanted samples using the RF magnetron sputtering system.

The ion-implanted samples were annealed using the heater in the chamber, using a Si wafer to cradle the samples in a positioned under the heater element. It was the temperature of the top

surface of the Si wafer where the ion-implanted samples would be positioned which was under investigation instead of the surface where the sputtered material is condensing to form a thin film (Figure 3.7).

The two thermocouples attached to the dummy sample were removed once the calibration was complete leaving the inbuilt thermocouple as a calibrated temperature reference, which provided live measurements. Combined with the applied heater power, the reading from this thermocouple can be used to determine the expected annealing temperatures of the samples.

The temperature difference between the reference temperature and the bottom surface remained level over the power range of 10% and 50% with a range of temperature differences of between 54°C to 75°C (Figure 3.8). The temperature difference between the reference temperature and the top surface was linear with an increase in temperature difference starting at 134°C for 10% power and raising to 263°C at 50%.

At 5% power the ambient chamber temperature was the dominant effect on the temperature sensors and this measurement gives uncharacteristic results so was not included as a data point in these conclusions.

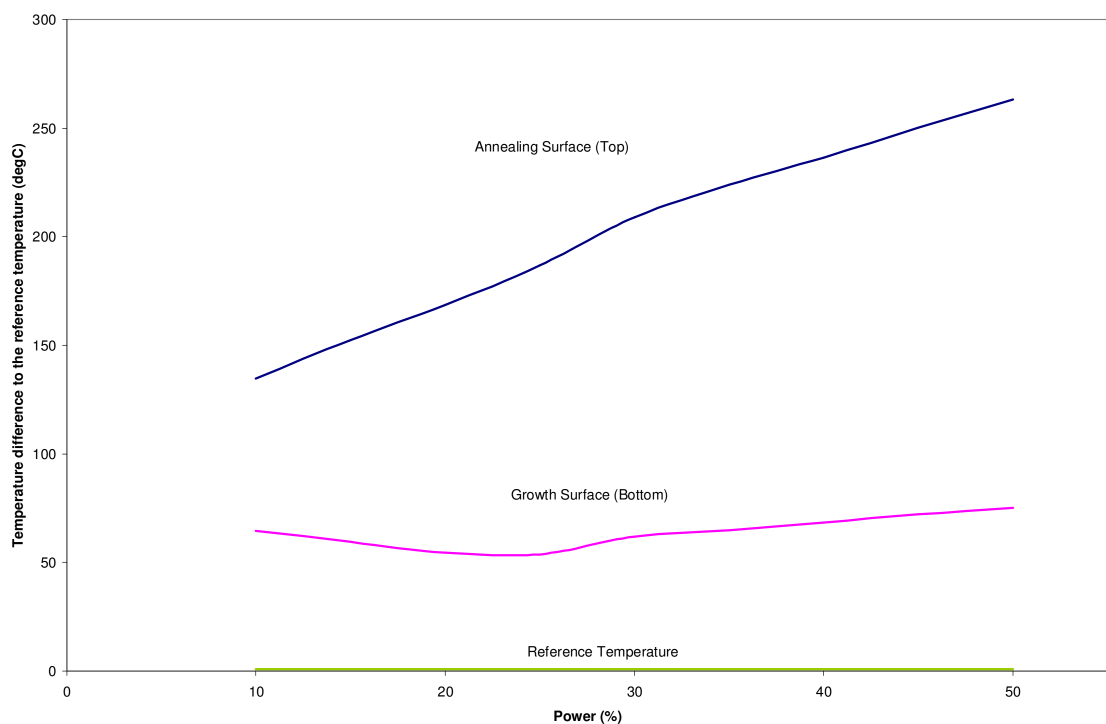

Figure 3.8: Temperature Difference between the reference temperature and the top and bottom surface of the Si wafer when using the shutter.

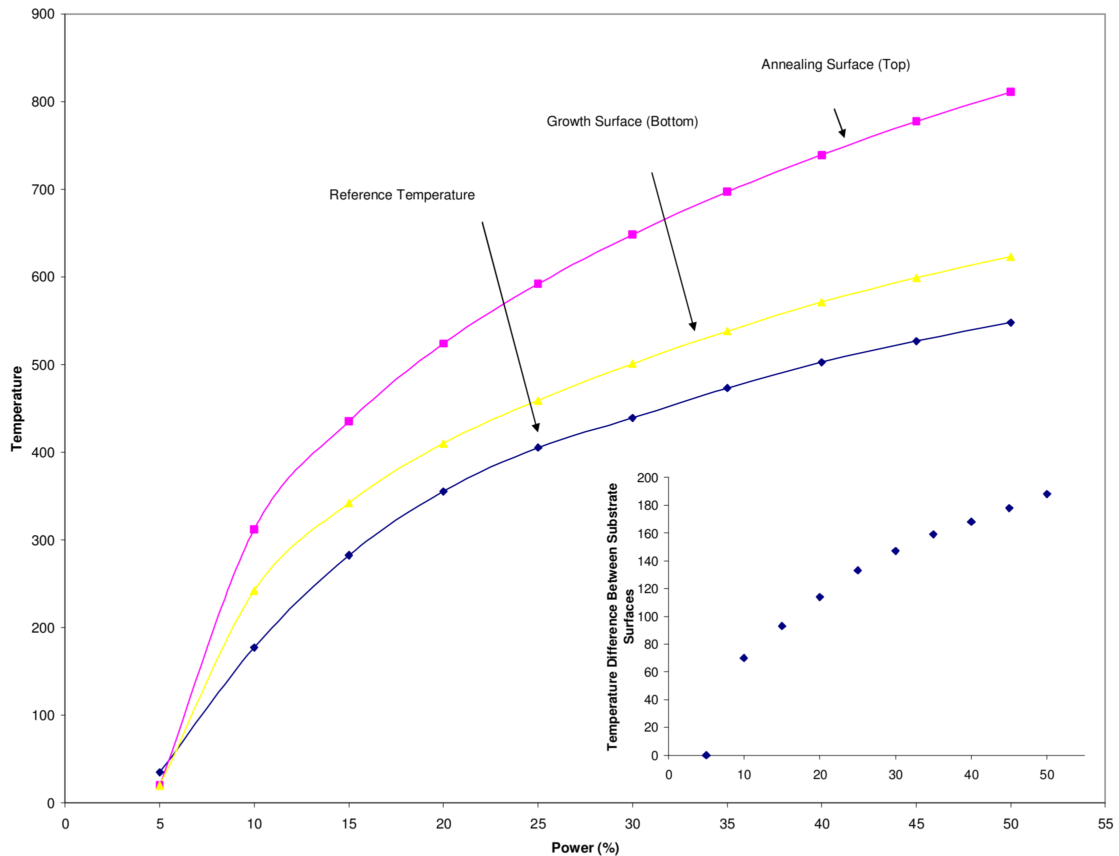

Figure 3.9: Calibration curve of the temperatures for the top and bottom surface of a Si wafer using a shutter. Insert - Temperature difference between the top and bottom surface.

There was a reducing rate of temperature difference between the top and bottom surface of the Si wafer over the range of applied powers (Figure 3.9 - Insert). The upper surface was always hotter than the lower surface (Figure 3.9), which was expected, as it is closer to the heater.

3.2.5 Vacuum

The vacuum within the sputtering system is maintained using a diffusion pump backed by an Elnor Motors V370C rotary pump. The vacuum is monitored in real time using four pressure sensors: two Pirani, a Penning and a Baratron. Two Balzers Pirani gauges, linked to a Balzers TPG 300 Total Pressure Controller, monitor the vacuum in the mbar scale. One monitors the vacuum created by the rotary pump (roughing line), while the other monitors the exhaust pressure from the diffusion pump (backing line). The Pirani gauge uses a heated metal filament suspended into the chamber. Gas particles within the chamber conduct heat, therefore a lower

number of gas particles would cause higher filament temperatures. For a given filament temperature there will be a corresponding vacuum pressure.

A Penning Gauge measures the vacuum created by the diffusion pump in mbar. It generates ions at a cathode, if the mean free path of these ions is shorter than the distance between the cathode and an anode, an electrical current cannot be created. Therefore, with increased vacuum there are less particles, hence a longer mean free path of the ions and a greater current is created.

The final gauge is a MKS Instruments Inc. Baratron, this gauge uses a capacitive diaphragm that changes shape in response to the relative pressure on the diaphragm. It uses the mTorr scale (1mTorr = 1.3332×10^{-3}mbar) and is primarily for measuring the vacuum relative to the base pressure of the chamber. It monitors the partial pressure level of the processing gas within the chamber to maintain a constant flow and pressure during the sputtering process.

3.2.6 Processing Gas and Sputtering Pressure

To initiate sputtering of the target material, a partial pressure of a processing gas is supplied to the vacuum of the chamber. High electrical alternating potential at the electrode causes an electrical discharge and the generation of plasma including charged ions. The positive ions are accelerated towards the phosphor target and the momentum transfer from these ions to the target material cause the material to expel outwards. Inside the electrode head there is a strong magnet, that creates a localised area of increased plasma containment near the target. This increases the sputter rate, allows a lower overall partial pressure or a combination of the two.

There are three control mechanisms for the processing gas: type of gas, flow rate and partial pressure. The type of processing gas is an important property, typically, it is an inert gas to reduce contamination of the film, but alternative methods can use other gases or mixtures of gases such as sulphur, oxygen and nitrogen to alter or improve thin film properties via reactive sputtering.

The chamber was supplied with processing gas at a constant flow rate, which was then removed by the pumping system – controlled via use of a baffle valve. 4nmL/min (normalised millilitres per minute - ml/min at 1 atmosphere and at 0℃) of argon gas is supplied to the

chamber using an Aalborg GFC/7 Mass Flow Controller (MFC) tuned to argon gas. To initiate sputtering 25mTorr of partial pressure is maintained within the chamber, and then reduced to the deposition partial pressure of 3mTorr.

The processing gas can be viewed as a known contaminant in the chamber, but is chosen to minimise the contamination of the thin film. Other sources of particles can be present in the chamber, which can be detrimental to the film by causing pinholes, degrade the crystallinity or become luminescent killers.

A method of classification for the potential quality of a film is the base pressure of the system. A chamber that can achieve an ultra high vacuum (UHV), 10^{-9} mbar, is required to minimise contamination. The chamber used here utilises a load lock and loading arm to insert virgin substrates and remove processed films. This reduces contaminants entering the sputtering chamber while maintaining base pressure and a quick turn of samples. Samples are loaded from within a class 100 clean room into the entry port of the system. A controlled source of clean, dry, nitrogen gas was used to vent the load lock (and sputtering chamber when required) to further maintain a low level of contaminates. In addition, multiple targets mean that the chamber does not need to be opened as often to replace used targets with new ones.

Targets are loaded onto individual electrodes whilst the chamber is at atmospheric pressure, meaning that gas particles come into direct contact with all surfaces within the chamber and some will non-chemically bond. Once the vacuum has been reapplied, the process of out-gassing begins. This can be improved by applying heat to the outside (heat strips) and inside of the chamber (conduction heater). A combination of both provides the heat required to move the gas particles from the walls whilst continued pumping expels the gases from the chamber. Without these measures, gas particles would seep from the chamber over time and during processing, reducing the vacuum and increasing contaminants.

3.3 Alternative Method of Doping

As an alternative to sputter deposition of ZnS:Ag,Cl, attempts were made to use different techniques to dope thin films of ZnS with the luminescent dopant (and charge compensator).

Films of ZnS were deposited by sputtering using the system discussed above, and dopants were then added by the techniques, which are discussed here.

3.3.1 Thin Film Deposition by Sputter Coating

This technique uses sputter coating (Emitech K-575 Coater) to deposit Ag on to ZnS. Sputter coating is a similar technique to RF magnetron sputtering, but utilises DC sputtering, hence only works for conductive material that can be negatively charged. This method of sputter coating was considerably quicker but less accurate in terms of thickness deposited and did not use a load locked system – as a result there was a greater risk of contamination than with the RF Magnetron sputtering system.

A vacuum of 10^{-5} mTorr was created within the sputtering chamber before the injection of argon (Ar) processing gas. Sputtering of the silver source material occurs by bombardment of the fast heavy particles (Ar) that erodes the target material. The ejected source material is propelled outward and condenses on the surface of the specimen, to grow to a preset thickness through a contact mask to define doped regions (Figure 3.10). The masks primary function was to attenuate Ag when depositing on the thin film. A minimum duration of Ag sputtering was preformed, this meant that without the mask the ratios of Ag to ZnS would make the Ag dopant level vastly greater than the required quantities to create a ZnS:Ag,Cl with the optimum dopant concentration. The aspect ratio of the Ag on ZnS ranged from 1:4 to 1:40. However, this was enhanced using a suitable ratio of ZnS thin film thickness to Ag thickness to give a volume ratio of 1:120 and 1:1200 of Ag to ZnS, which equates to 0.83% and 0.0833% (by volume) respectively.

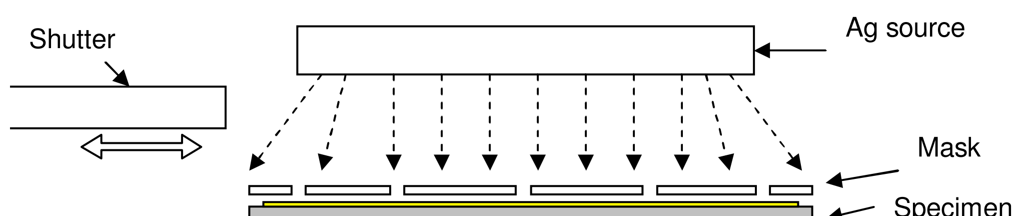

Figure 3.10: Arrangement of sputter coater for the deposition of Ag onto ZnS thin film through a mask.

Before the deposition, a pre-sputter is carried out (a period where the top surface of the source was allowed to erode) to remove the oxidised or contaminated layer and was sputtered onto a shutter positioned between the sample and target. The sputter coater automatically determines the growth period by use of a crystal thickness monitor - measuring the changing natural frequency of the sample as a mass of silver was sputtered onto it. For each sputtered element, the system was calibrated to relate frequency to a desired thickness measurement defined by the user.

Thermal annealing of the sample promotes the Ag to diffuse from their spot locations into the ZnS thin film, with sufficient annealing dopants become distributed uniformly.

3.3.2 Ion Implantation

Ion implantation uses a technique where energetic ions from a specific source gas are accelerated towards a sample in order to dope via direct implantation. This is a 2 MV High Energy Implanter backed up by a Implantation Sample Holders for up to 400mm diameter samples, for hot or cold implantation and with up to 40µA beam current The ions then penetrate into the target sample and come to rest at a predictable distance into it. On entering a target material, the energetic ions transfer energy through a series of collisions with atoms within the target. In doing so, this can displace the target nuclei from its original lattice sites, causing disorder to the lattice material. There is also the risk of sputtering of the target when there is sufficient implantation energies.

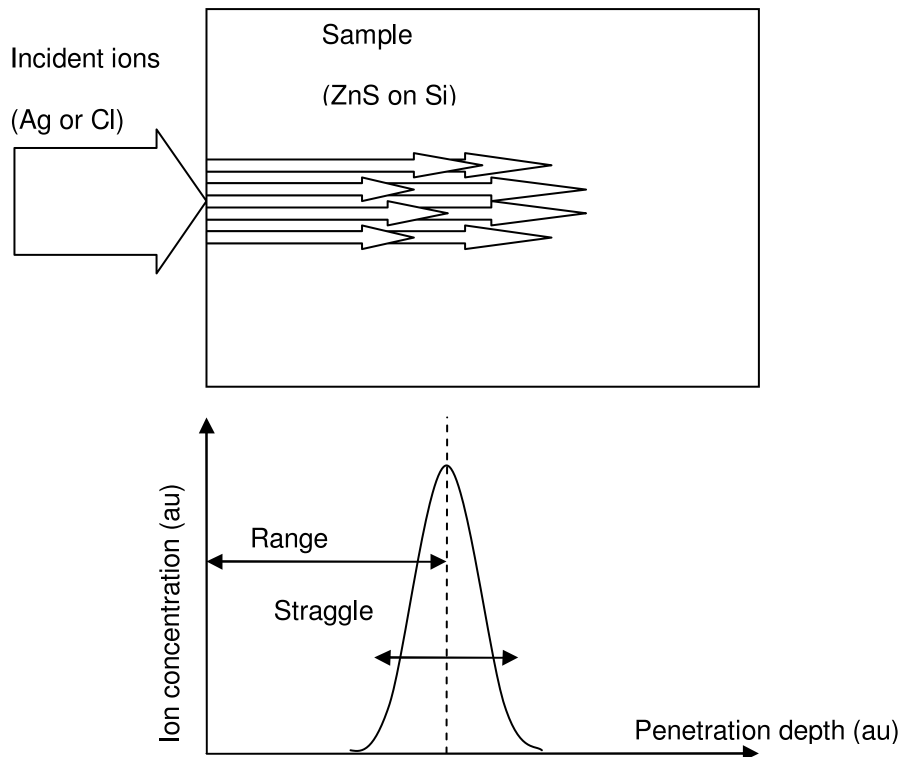

Figure 3.11: Representation of ion implantation with a single implantation energy into a target and its resultant depth profile.

The depth to which the ions penetrate is determined by the momentum (i.e. its mass and speed) given to the ion and the stopping power of the target material (i.e. its density). Ions with a single energy penetrate differing depths; with the average distance, described as the *range*, R_p. The non-uniform distribution of ion concentration within the target material generally resembles a Gaussian distribution. The spread of penetration distances around the average depth, described as the straggle, σ_p (Figure 3.11). The exception to this is highly ordered materials, where it is possible for the ions to penetrate greater distances by travelling along crystal planes. This problem can be compensated by positioning the target at an obtuse angle to the incident ions so that crystal planes are not 'viewed'.

The target sample cannot directly obtain a uniform distribution of ions by a single ion implantation. However, each implantation energy and implantation element has a corresponding range and straggle giving a reproducible depth profile. Hence, a more distributed deposition of the ions within the sample was obtained by using multiple implantation stages with differing implantation energies. This creates a series of overlapping profiles that spans the volume of the sample.

The straggle of ions and the penetration distance are linked by Equation 6, which shows that at increased penetration, a greater amount of spread would be observed.

$$C(x) = \frac{\Phi}{\sqrt{2\pi}\sigma_p} \exp\left[-\frac{(x - R_p)^2}{2\sigma_p^2} \right]$$ **Equation 6**

Where *C(x)* is the impurity concentration at a depth *x*, σ_p is the straggle, R_p is the range and Φ is the total dose implanted, which can be calculated by measuring the ion beam current and integrating it over the time of implantation.

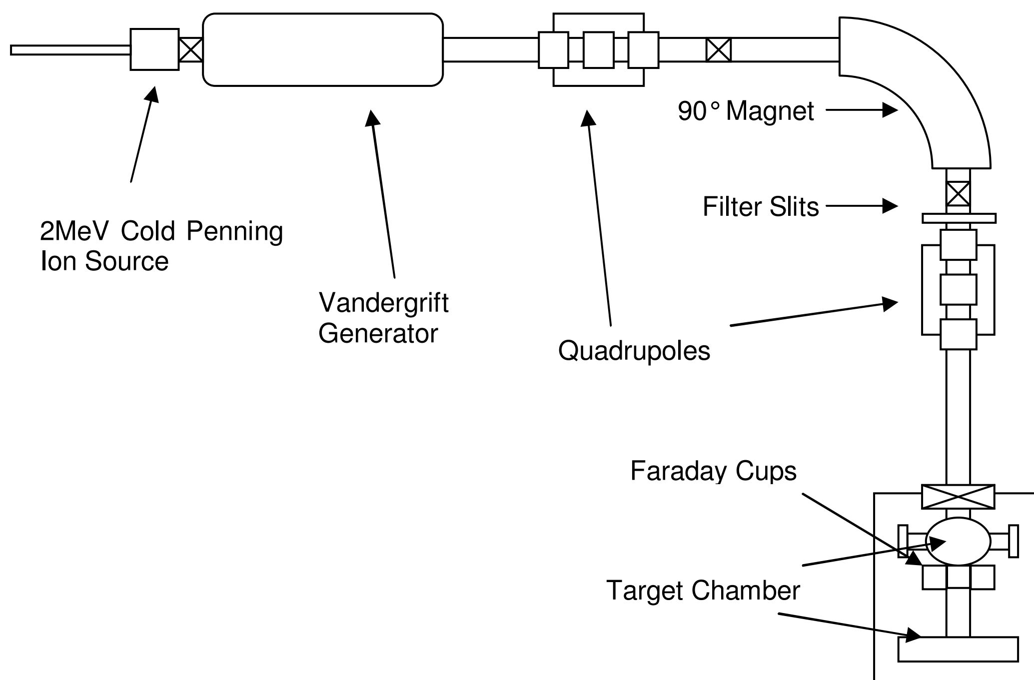

Figure 3.12: Schematic of the ion implantation method.

To create the ions for implantation a plasma is created at the ion source, which causes a target material to be sputtered. The sputtered material is extracted and accelerated along a beam line under vacuum (10^{-7}mbar), focused by a quadrupole before being filtered by the 90° magnet and slits to produce a single element with a single energy (Figure 3.12). Before reaching the target, it is again focused by a second quadrupole and is raster scanned across the sample and four faraday cups. The charge detected on the Faraday cups is translated into a measurement for the number of deposited ions in to the target material.

3.4 Thin Film Characterisation

Following a deposition of a thin film on to a substrate, the samples were characterised. The initial tests, directly following the deposition, were thickness measurements to cross-calibrate the interferometer and surface topography to determine film uniformity.

The thicknesses of the deposited films are measured using three techniques: reflectance spectroscopy, stylus profiling and optical profiling. These techniques vary in their accuracy and all have limitations. The techniques can also measure reflective index and surface roughness.

3.4.1 Reflectance Spectrometry

The Filmetrics Thin film Analyser F20 uses an optical transmission/reflectance spectroscope. It measures the thickness and the optical properties of reflective index (*n*) and roughness (*k*) of the films [93].

A broadband emission from a tungsten-halogen bulb is transmitted to the film sample by a fibre optic cable containing seven fibres, six illumination fibres surrounding a single detection fibre (Figure 3.13).

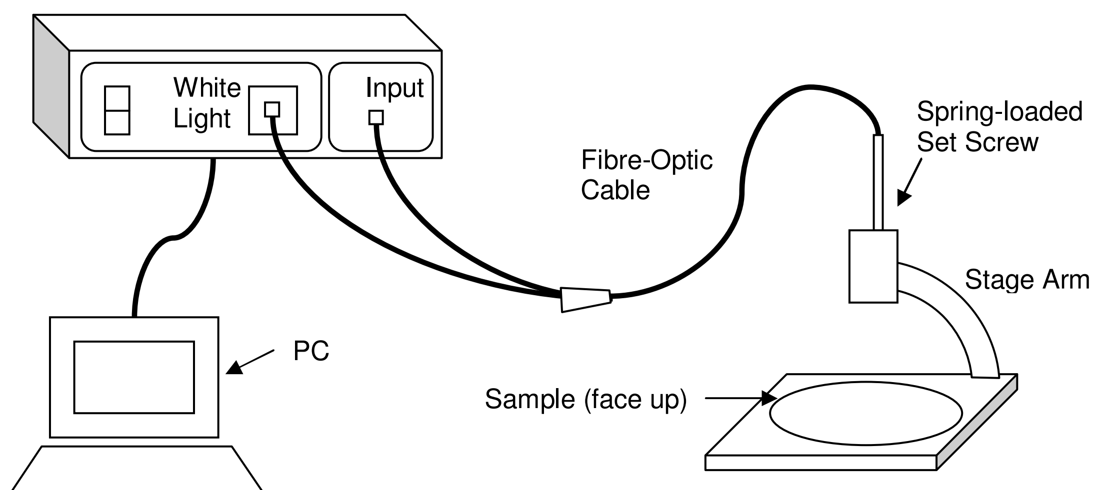

Figure 3.13: General setup of the Filmetrics thin film analyser for reflectance spectroscopy, after [93].

An interference pattern is created when the light reflects off interfaces created by changes in reflective index associated with different thin films (Figure 3.14). An interpretation of the intensity of reflected light versus wavelength is able to determine the thin film characteristics, such as its thickness, optical constants and roughness. An in-phase peak fits the equation:

$$\lambda = \frac{2nd}{i}$$ **Equation 7**

Where λ is wavelength, n is the reflective index, d is the film thickness and i is an integer. The greater the thickness of film the more oscillations are present over a given wavelength range. This measurement technique works on a similar principle as the technique used to measure the film thickness during growth using the technique described in section 3.2.3.

The amplitude of the oscillations is determined by the refractive index and extinction coefficient of the films and substrate. By analysing the period and amplitude of these oscillations, the thickness and optical properties (n, k) of multiple films can be determined.

Limitations of this technique are that films must be optically smooth and uniform over the 20×20 mm detection area. This technique has a thickness range of 15.0nm to 50µm, with an accuracy of 0.4% or 1.0nm (which ever is the greater).

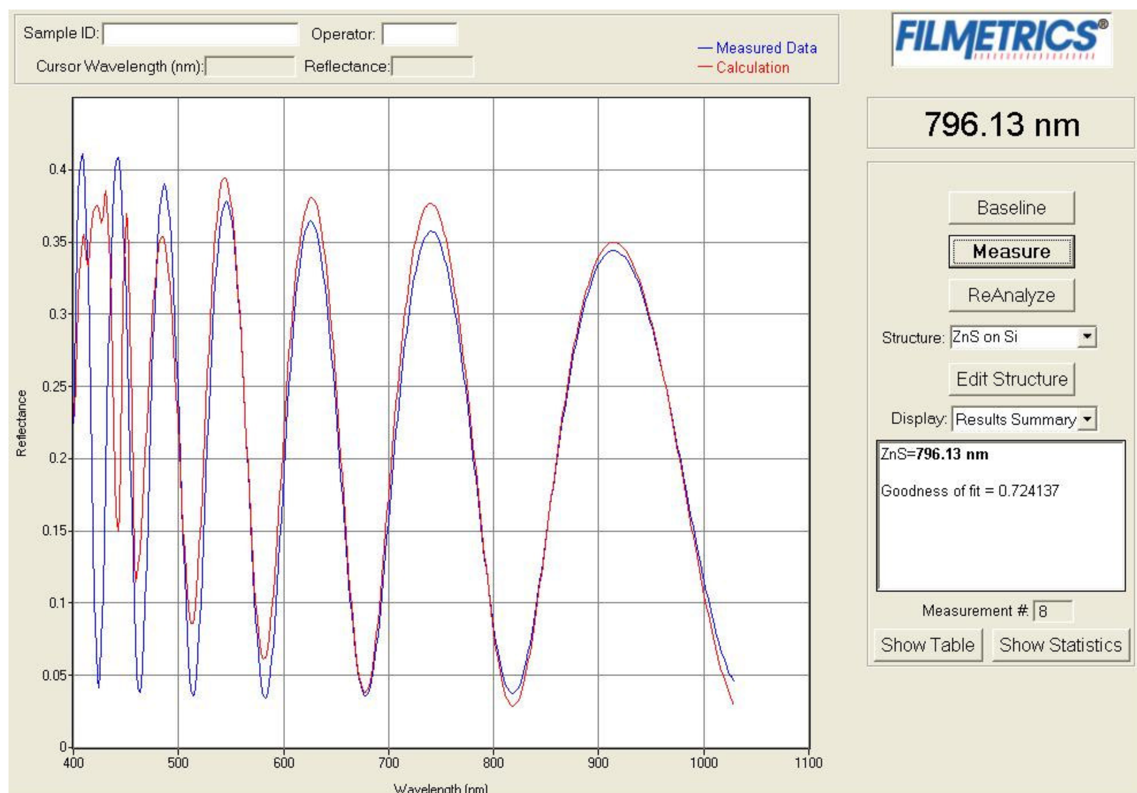

Figure 3.14: Typical measured and calculated reference spectra for ZnS on Si.

3.4.2 Stylus Profiler

The Dektak 6M takes electromagnetic measurements by moving a sample beneath a diamond-tipped stylus (radius of 12.5µm) [94]. As the high-precision stage moves the sample, the stylus

rides over the sample surface and surface variations cause the stylus to be translated vertically. Electrical signals corresponding to stylus movement are produced and converted to a digital format and stored in the computer memory, for manipulation and measurement.

The stage moves a sample beneath the stylus according to a user defined programme of scan length, speed and stylus force (between 1 mg and 15mg).

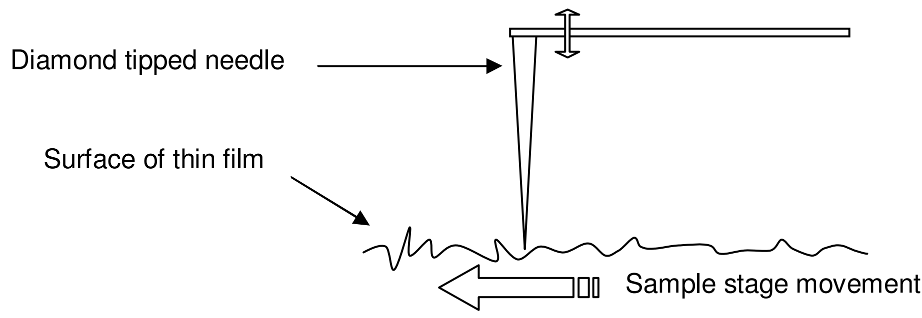

Figure 3.15: General description of Dektak 6M for stylus profiling.

Horizontal Resolution is 300 data points per second with scan duration anywhere from 3 to 100 seconds. There is a maximum of 30,000 data points available per scan and the scan length from 50µm to 30mm. The number of data points can be calculated by:

$$\text{Number of data points / Scan} = \frac{\text{Scan Length (in µm)}}{\text{Horizontal Resolution (in µm)}}$$

Or

$$\text{Number of data points / Scan} = 300 \times \text{Scan Duration (in seconds)}$$

By rearrangement, the theoretical maximum horizontal resolution becomes $1.\dot{6}nm$. The vertical range is 50Å to 26,620kÅ, with a vertical resolution of 1Å at 65Å, 10Å at 655kÅ and 40Å at 2620kÅ.

The drawback to the stylus profiler is that it gives a 2D interpretation of the sample and it needs a very well defined film edge to determine thickness measurement for thin film samples. The region that the stylus transits has the potential to miss features or give an unbalanced interpretation of the film.

3.4.3 Optical Profiling System

The Wyko NT1100 is a versatile, non-contact, optical profiling tool that measures a wide variety of surfaces and samples [95]. It uses two technologies to measure a range of surface heights:

phase-shifting interferometry (PSI) and vertical scanning interferometry (VSI). PSI mode allows the user to measure smooth surfaces and small steps, while VSI mode allows the measurement of rough surfaces and steps up to several millimetres. For surface roughness measurements of film samples PSI mode was used while thickness measurements of the film were achieved using the VSI mode [95]].

3.4.3.1. PSI Mode

PSI mode uses filtered white light (centred at 632nm) split into two beams. One beam is sent to the sample, reflected back and then recombined with the other beam, which has been reflected off a reference sample. When the sample beam and the reference beam are recombined, they create an interference pattern (Figure 3.16).

A phase shift between the test and reference beams is created using a piezoelectric transducer linearly to move the reference surface a known distance. The system records the intensity of the interference patterns for many different phase shifts and converts this information to phase data by integrating the intensity data.

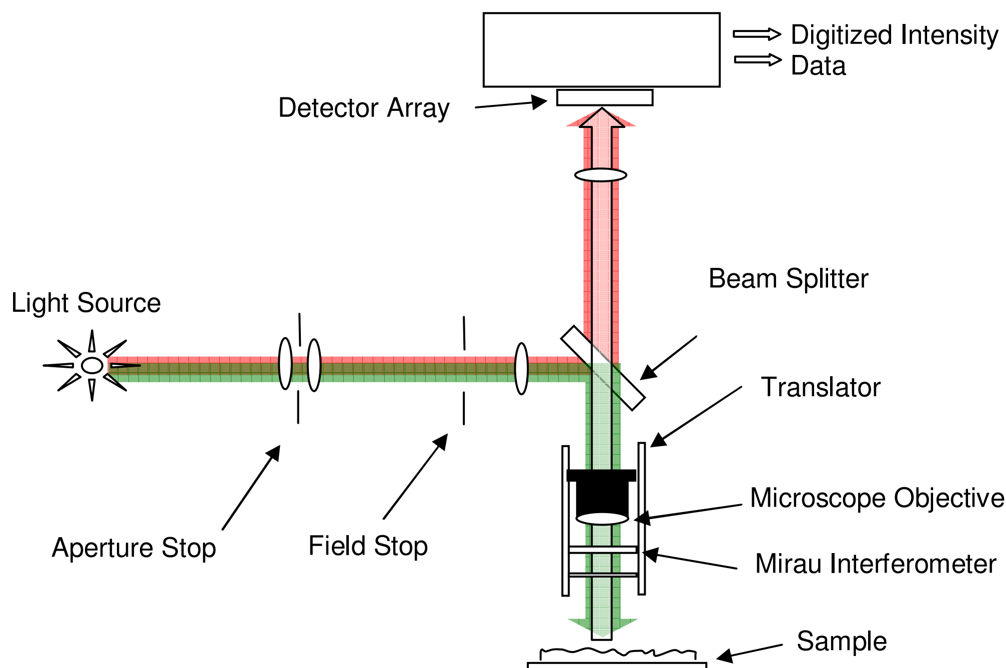

Figure 3.16: General setup of the Wyko NT1100 system for optical profiling.

For adjacent measurement points greater than λ/4 the height error is in multiples of λ/2 and the phase data cannot be reliably reconstructed. A maximum vertical range of 160nm can be

measured with a resolution of 0.3nm. Therefore, to resolve rougher surfaces or step height for surface thickness, VSI mode was used.

3.4.3.2. VSI Mode

VSI mode is a similar technique to PSI where a white light beam is split and then recombined to produce interference pattern. However, in VSI mode the white light is filtered with a neutral density filter and preserves short coherence wavelengths of the white light. The system measures the degree of fringe modulation, or coherence, instead of the interference fringes.
The intensity of the interference fringe is at its greatest intensity at the focal point. When the interferometer objective lens moves vertically to scan the surface at varying heights, each data point has a corresponding focal length that will correlate to a vertical component. This will create a three dimensional map with a vertical range of up to 2mm with a resolution of 3nm.

By cross calibration of thickness measurements using both the physical and optical systems, there is a robust facility for thickness characterisation. The most suited method for thickness measurement is the reflectance spectrometry primarily for its ease of use. Step changes are suitable for the stylus profiler whilst surface topography is suited to the optical profiling system.

3.5 Crystal Structure and Composition Characterisation

Surface analysis provides basic information about the film morphology, whereas an understanding of crystallinity and composition of the film requires additional set of tests. X-ray Diffraction (XRD) and Ion Beam Analysis (IBA) were used to determine crystal form, atomic spacing and chemical composition.

3.5.1 X-ray Diffraction

X-ray diffraction (XRD) is a non-destructive technique to identify crystalline phases and orientation of a crystal or polycrystalline material [96]. This technique was employed to examine

how growing and annealing of a thin film grown from a ZnS:Ag,Cl phosphor target affects the composition, crystal size and crystal structure.

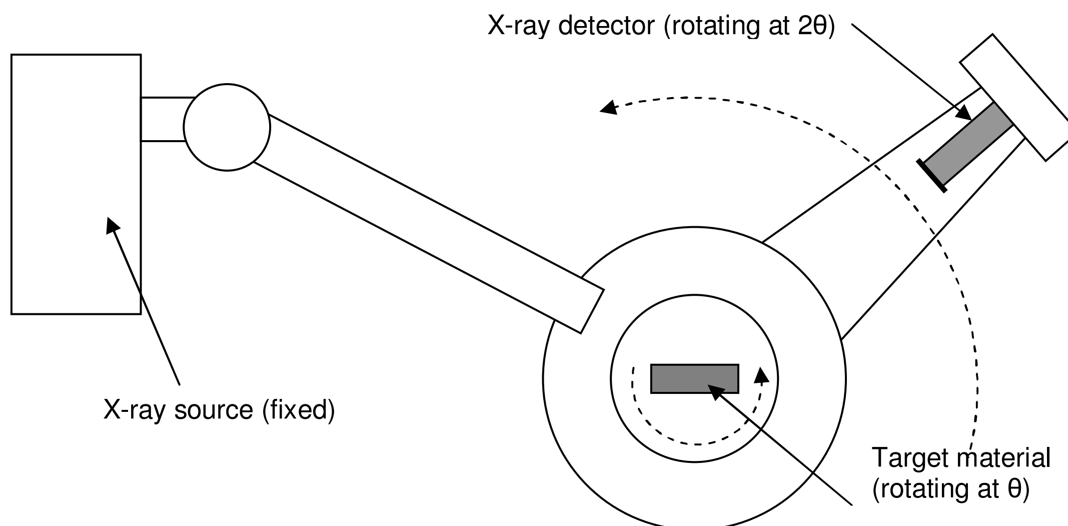

Figure 3.17: General setup of the XRD machine.

The XRD system that used for these experiments was the Philips PANalytical X'Pert Pro system (Figure 3.17). It operates at 45KeV and 40mA; the operational technician sets these values. A broad range of X-ray wavelengths are created from a copper target (Figure 3.18) with characteristic intensity peaks at 1.5443Å ($K\alpha_2$), 1.54056 Å ($K\alpha_1$) and 1.3922 Å ($K\beta_1$). The emission is filtered to produce monochromatic radiation (λ = 1.54056 Å) using a germanium crystal. The crystal absorbs all but the most intense X-ray peak (Cu-$K\alpha_1$) from the copper target source.

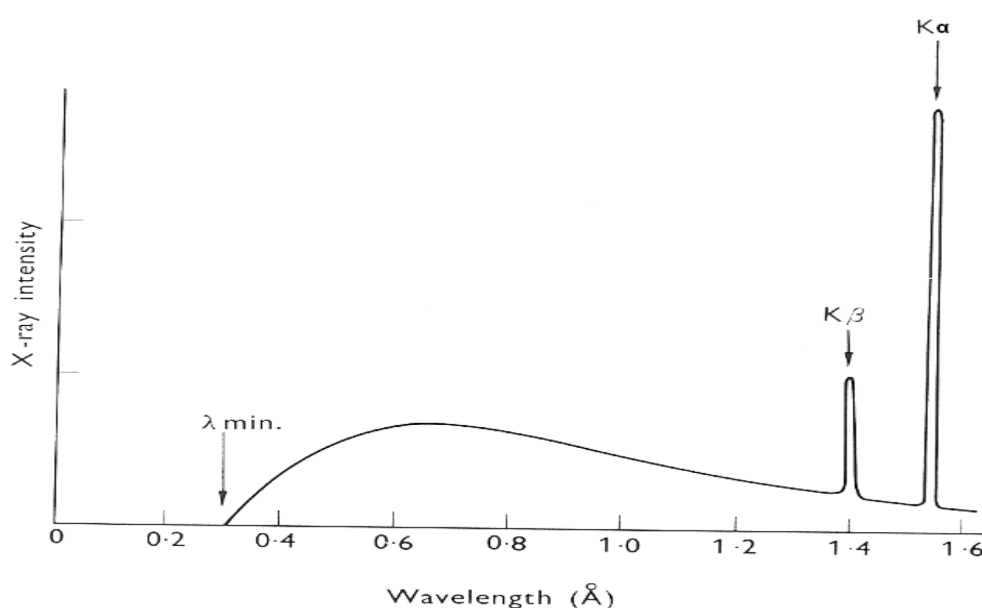

Figure 3.18: Emission spectrum of X-rays emitted by a Cu target at 35 KeV excitation

The germanium crystal absorbs wavelengths using Bragg diffraction from the (111) face, which is tuned to permit only the $K\alpha_1$ X-rays to transit the filter. The area of the X-ray beam that intercepts the sample creates the target area, at the axis point. The X-ray source is held in a fixed position while the X-ray detector and the sample are rotated with high precision to angles of 2θ and θ respectively (where θ is the angles of incidence the X-rays have perpendicular to the sample surface).

The X-ray source is fixed, the sample holder rotates at θ while the X-ray detector moves at 2θ so that the rules associated with Bragg diffraction are met. To ensure that the X-rays intercept the samples at the θ angle the samples are fixed within the detector with differing fittings, called stages, depending on the sample form (e.g. solid, powder, thin film). There are two stages used, the spinner and the flat stage.

Powder samples are formed into a single, loosely compacted disk held in a stainless steel container and then fitted into the spinner. Samples that are self-supporting like the thin film samples on the Si substrate and the solid targets are held in the flat stage using a simple sprung clip. A user defined program consisting of start-angle, end-angle, step-size and time-per-step was created to collect an XRD pattern by entering a set of parameters or a previous program was opened containing a set of parameters. From this, various other parameters are deduced such as total time of integration.

3.5.1.1. Powder Sample

The spinner stage is used for the ZnS:Ag,Cl powder where the quantity of power used is of sufficient thickness that the incident X-rays do not penetrate through the sample. An XRD pattern of this sample determines the structural properties of the source material that was used as the target material for growing thin films using RF magnetron sputtering.

3.5.1.2. Solid Target Sample

Before the addition of silver and chlorine by ion implantation, a film of ZnS was deposited onto a silicon substrate to a thickness of 600nm using RF Magnetron sputtering. The source material used to create the film is a solid target of ZnS. An XRD pattern of the solid target would show changes to the material as it was grown into a film.

3.5.1.3. Thin Film Sample

The films were grown to a thickness of 800nm on a 100mm Si wafer using RF Magnetron sputtering and are held in the flat-stage. The films are grown from a pressed ZnS:Ag,Cl powder or a solid target of ZnS. Due to the limited thickness of the sample, the resulting XRD pattern will form two over-lapping patterns, comprising of the thin film sample and the substrate. This was due to X-rays penetrating through the polycrystalline thin film and interacting with the single crystal Si substrate. While the film was the first material the X-rays are incident upon, the substrate would still produce a more intense signal than the film due to it being a highly ordered material.

3.5.1.4. Si Substrate Sample

XRD patterns of the reference material were not always reliable or specific to the samples used. Therefore, a sample of the Si substrate was analysed so that the peaks can be accurately identified when analysing a film sample. For a reliable measurement of the substrate that can then be referenced to the film measurements, the same collection parameters (start angle, end angle, collection duration per step and angle of separation per step) as the film samples were used. These XRD patterns allow the Si XRD pattern to be identified and removed as an artefact from the film samples.

3.5.2 Ion Beam Analysis

The Ion Beam Facility at Surrey University [97, 98] was used to characterise the composition of films deposited from a ZnS:Ag,Cl phosphor target using the RF Magnetron sputtering system. This characterisation was primarily to determine elemental composition and concentration.

Two detectors are used within the system positioned at 10° and 30° to the ion beam line, with the beam perpendicular to the sample.

Two analytical techniques were used in this work, Rutherford Backscattering (RBS) and Proton/Particles Induced X-ray Emission (PIXE). A beam of $^{4}He^{+}$ or $^{1}H^{+}$ was used to probe the target materials and had energies of 1.5MeV and 2.5MeV respectively (Figure 3.19).

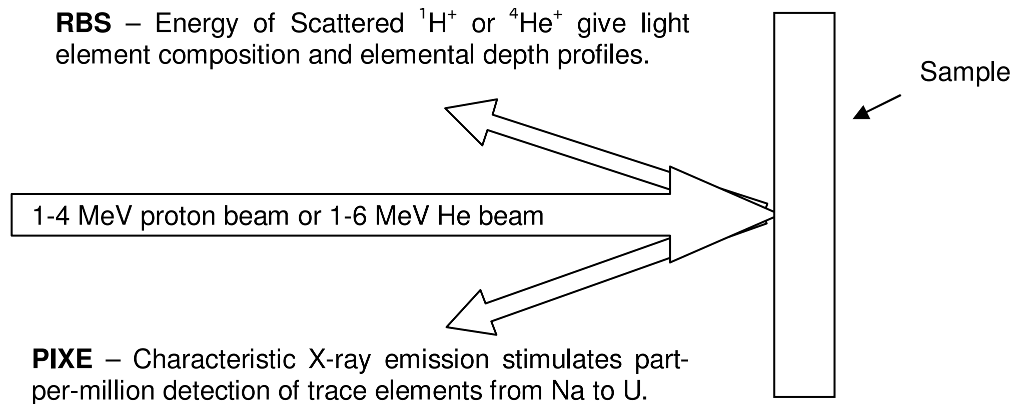

Figure 3.19: Depiction of RBS and PIXE interaction with a target material, after [99].

RBS uses coulombic interactions with the target material to produce scattered ions from nuclear collisions with energies depending on the mass and depth of the target atom [99, 100]. The detection limit of a heavy element in a light matrix is approximately 0.1%, but can be used to quantify PIXE, so increasing that resolution. This technique was used for depth profiling, which has a resolution of less than 20nm.

Mass and depth are a function of energy due to kinematics and electronic energy loss respectively, making mass-depth ambiguous. There exists no general analytical inversion of energy spectra to extract depth profiles. However, general inversion numerical algorithms based on simulated annealing was used by the Ion Beam Centre (IBC) using DataFurnace© code.

From a source of hydrogen or helium gas, ion of ^{1}H or ^{4}He are created and then accelerated through an analysing magnet. The purpose of the magnet is to filter the ions with respect to their momentum energy, giving them a single energy. The tandem accelerator draws the negatively charged ion towards it using a strong positive charge. The ions are then stripped from the atoms and due to the same positive charge are accelerated away towards the quadrupoles. The quadrupoles focuses the ions, which are diverging due to their like charge before an injection magnet delivered the ions along a beam line to a test area (Figure 3.20).

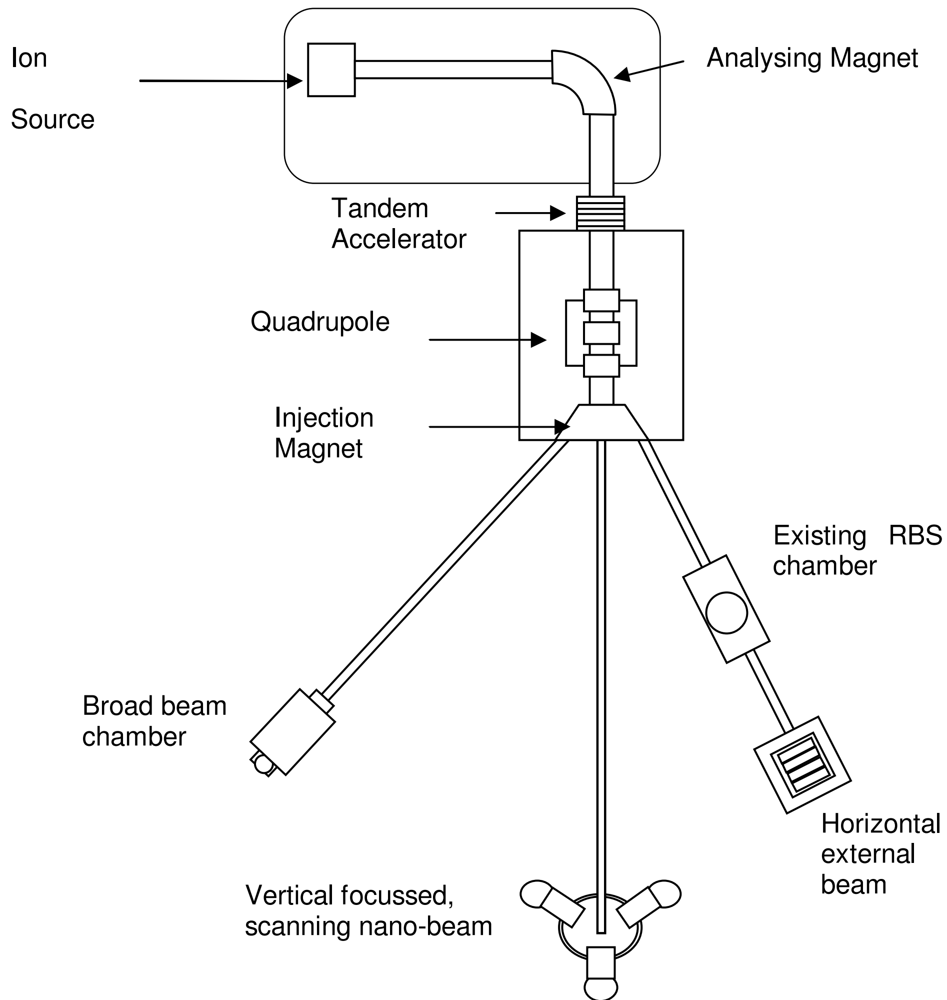

Figure 3.20: Schematic of the ion beam analysis technique, after [100] **.**

The strengths of RBS are that it can simultaneously detect multi elements, provide high-resolution depth information and analytical cross-sections, making it an accurate and traceable technique. The weaknesses are an insensitivity to light elements in heavy matrix and a low cross-section making microbeam use difficult.

For stoichiometric ZnS, the expected components would be equal parts of zinc and sulphur, and for the dopant levels used, the expectation is for equal parts of silver and chlorine, with silver having a concentration of 0.01at%. The intensity of the signal is directly related to the concentration as well as the atomic number of the element. Relative intensity between equal concentrations of Zn and Ag resulted in a measurement of 900cpc (counts per channel) and 2209cpc from the atomic number squared (Z^2).

Table 3.1: Relative intensities of elements detected using RBS.

Element	Atomic Number	Count (cpc)	Relative Intensity
Zn	30	900	1

S	16	256	0.28
Ag	47	2209	2.45
Cl	17	289	0.32

Choosing Zn and Ag as the two elements best able to determine relative intensities, Zn has a high concentration and the largest atomic number of this group of elements, so would create the largest count and Ag would produce the largest count of the two dopant elements.

For a concentration of 0.01at% of Ag this would give a ratio of 5000 parts of Zn to 1 part of Ag. Using this concentration ratio and relative response to these two elements, there would be 2037 counts of Zn to 1 count of Ag (or ~10,000 counts of Zn to 5 counts of Ag).

As for S and Cl, they should have the same concentrations as Zn and Ag respectively but require the Z^2 factor, i.e. sulphur has a relative emission intensity of 28% of the intensity of zinc and chlorine has a relative emission intensity of 13% (0.32 / 2.45 = 0.13) of the intensity of silver.

The incident ion creates an inner shell vacancy by exciting the electron of the atom, which will subsequently cascade from the outer shell and emit characteristic X-rays. A measure of the X-ray energy determines the atomic number. The count determines the concentration. This is a high yield trace element analysis technique that detects all elements simultaneously (Na - U), so can detect ‘unexpected’ elements. The yield can be calculated from fundamental physics, so can accurately measure sample with a minimal dependence on standard reference materials. It also has a very low background due no primary bremsstrahlung, allowing the detection limit to be 1-10ppm. The strengths of PIXE are multi element detection from a single data analysis and a high lateral resolution. The weakness is that on its own it cannot provide depth information.

3.6 Luminescence Characterisation

Luminescent emission was characterised in two main ways for the purposes of this project, spectral intensity and decay time.

A plot of light intensity over time determines the decay constant. The decay constant is formed as a description of a decaying system reducing exponentially from a maximum (Equation 8).

$$I(t) = I_0 \exp\left(\frac{-t}{\tau_d}\right)$$ **Equation 8**

Where *I(t)* is the intensity after time (*t*), I_0 is the initial intensity of emission and τ_d is the decay constant.

This constant can be found by measuring the time taken for the emission of light to reduce from its peak intensity to 1/e (37%) of it [101] or from 90% to 10% of the peak intensity. The method chosen and the one that would provide the most accurate value for decay time was a curve-fitting feature within the software package Microsoft Excel. An exponential decaying curve is mapped to part of the decaying curve and from the equation of the line a value for $-1/\tau_d$, is derived.

3.6.1 Samples

A sample of the phosphor currently in use at ISIS in their neutron detection equipment was provided; the results from a characterisation of this sample would become the benchmark that improvements were measured against. The sample from ISIS is composed of ^6LiF-ZnS:Ag,Cl in a homogeneous particle mixture of the neutron converter (^6LiF) and the RL phosphor (ZnS:Ag,Cl).

A comparison to the ISIS sample was made using a ZnS:Ag,Cl phosphor powder from Phosphor Technology Ltd., used to form the targets for thin film deposition. Characterisation of the phosphor in powder form required a horizontal surface, with the excitation source coming from a position above the sample. Various methods were tried to optimise this measurement, with the most suitable technique using a quantity of the phosphor powder pressed into a 5mm radius cylindrical pellet (Figure 3.21). Varying thicknesses of pellet were created depending on the quantity of powder used in each press. The pellets can then be installed in an upright measuring system or fixed in one position, hence improving repeatability and permit a greater degree of freedom.

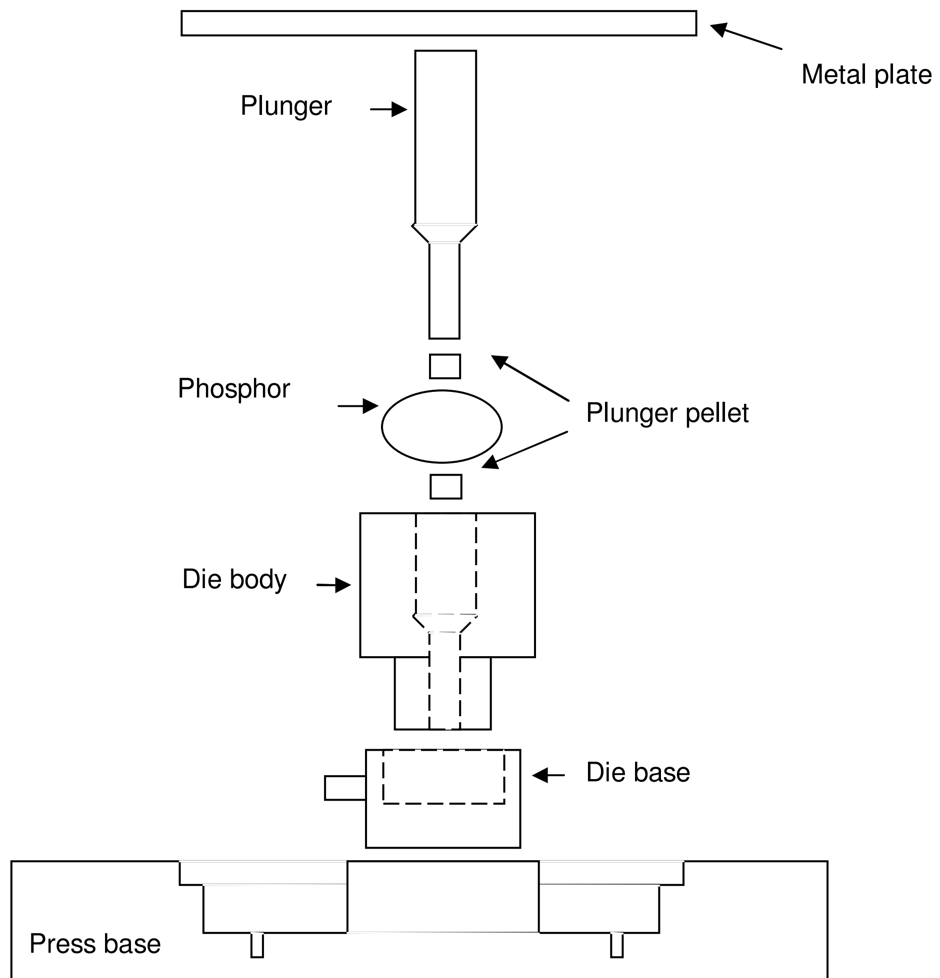

Figure 3.21: Pellet Press setup to create 5mm phosphor pellets.

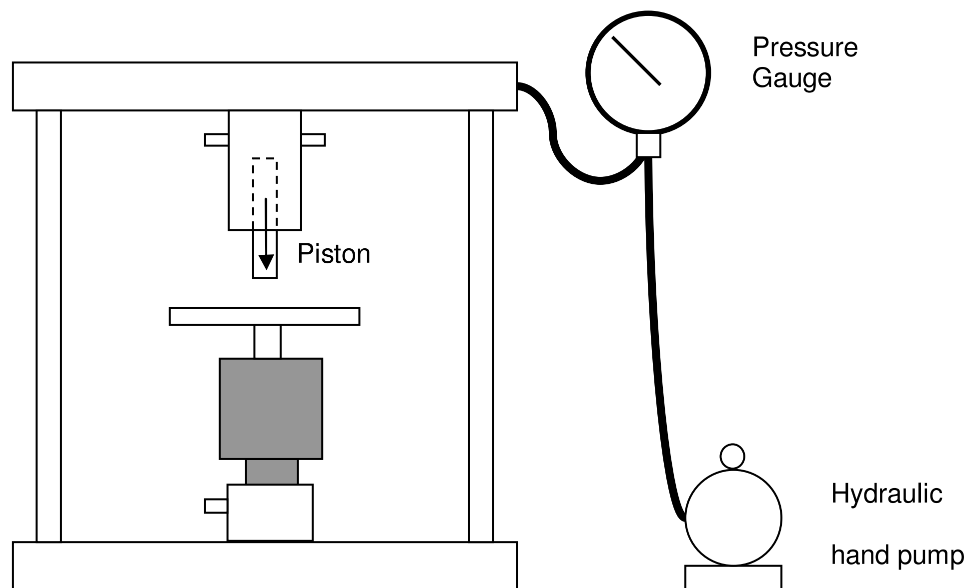

Figure 3.22: The hydraulic press in which the body of the pellet press (Figure 3.21) is used.

Pellets where pressed to the same pressure (205 bars / 30,000 psi) as when forming the phosphor targets used in film deposition (Figure 3.22). The targets are delicate and a faint touch or jolt can distort them, whereas the pellets with their much-reduced quantity of powder were self-supporting and can be held in a bulldog clip.

3.6.2 Excitation by UV Laser Source

3.6.2.1. Emission Spectrum from Photoluminescence

The sources used to excite the phosphor were a nitrogen (N_2) laser, a neodinium - doped yttrium aluminium garnet (Nd:YAG) laser and a helium cadmium (HeCd) laser, each producing a different wavelength (see Table 3.2). Once the phosphorous material produces PL, the emission was filtered to remove stray laser emission, guided by a fibre optic to a spectrometer, the collected light is processed and an emission spectrum is displayed on a computer monitor, or can be manipulated or saved (Figure 3.23).

Table 3.2: Properties of lasers used to excite the phosphor.

Laser	Type	Wavelength	Equivalent energy	Frequency
N_2	Laser Science Inc VSL-337ND	337nm	3.678 eV	Pulsed,20Hz
Nd:YAG	Continuum	266nm	4.660 eV	Pulsed,20Hz
		355nm	3.492 eV	
		532nm	2.330 eV	
HeCd	Omnichome – Series 74	326nm	3.802 eV	Continuous

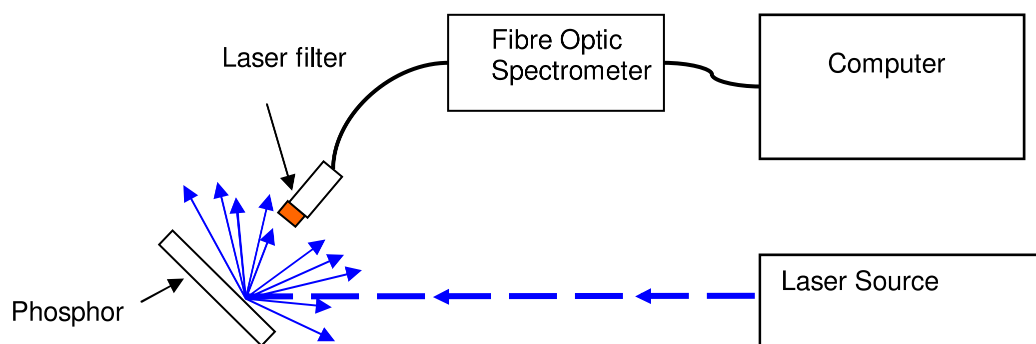

Figure 3.23: Experimental setup of equipment for the capture of the emission spectrum from the phosphor when excited by a UV laser.

The N_2 and HeCd lasers create monochromatic light, the Nd:YAG laser produces four wavelengths of light and require the Surelite Separation Package (SSP) to filter the emission to a single wavelength. The Nd:YAG laser can also be used with an Optical Parametric Oscillator

(OPO) Panther unit to produce a user defined emission wavelength of between 215 and 2550nm (Figure 3.24).

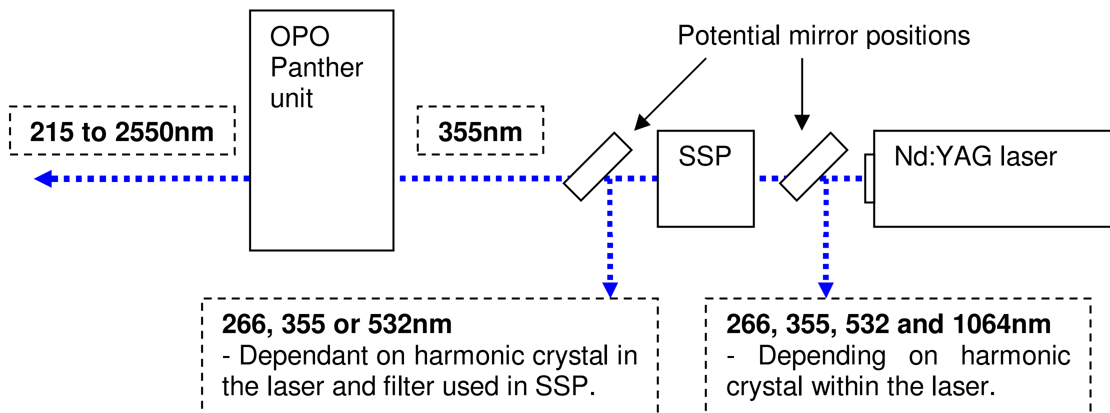

Figure 3.24: The emission wavelengths achieved by the Nd:YAG laser.

A 340nm cut-on filter is positioned before the emitted light enters the fibre-optic to reduce UV laser light reflected from the phosphor sample from entering the collection apparatus.

A quartz 1mm diameter fibre optic transmits the PL emission from the phosphor to the spectrometer. The properties of quartz mean that UV, IR as well as visible light emissions are guided to the spectrometer. If the fibre were not quartz but glass, false reading would be created by incident UV light absorption generating luminescence within the glass.

An Ocean Optics S2000 and Ocean Optics S4000 spectrometers were used to capture the emission spectrum using a high-sensitivity linear CCD array. The S2000 spectrometer measures the emission intensity over the wavelength range of 332.3nm – 1009.58nm, while the S4000 has a range of 179.1nm to 887.9nm. The most significant user controlled variable associated with the spectrometer was the integration time (detection period). A weak emission requires a long integration time, whereas a strong emission would require a shorter period. A long integration is influenced less by noise from the detection system or noise from stray light. A short integration time can create a fluctuating emission spectrum if the excitation source is pulsed and has a frequency comparable to the integration time. A method to reduce fluctuating emission and noise (other than to link the collection period to the integration time or increase the emission collected) is to average the number of emissions. This collects the data from multiple emission spectra and averages the intensity at each wavelength, which reduces the noise component in weak emissions and the fluctuations in strong emissions.

The spectrometer was calibrated using a tungsten light source, which produces a broad repeatable emission spectrum. The spectrometer compares the tungsten emission spectrum to a reference emission spectrum, and the software then configures the spectrometer to match its measured spectrum with that of the reference spectrum by altering its intensity response. The accuracy of the wavelengths from the measured spectrum were further tested by using La_2O_2S:Eu and La_2O_2S:Tb phosphor which have multiple peaks with thin bandwidths, as shown by Yap [102].

3.6.2.2. Decay Constant System

The source used to excite the phosphor for these experiments was a Laser Science Inc VSL-337ND nitrogen (N_2) laser, which creates a 20Hz pulsed ultraviolet radiation at 337nm (3.678 eV). A pulsed source was required to allow observation and measurement of the luminescent decay between excitation pulses. Once the phosphor material produces the PL emission, a quartz rod guides it to a filter, it then passed through a monochromator to isolate the wavelength of interest, and the emission was then amplified and converted to an electrical signal by a photomultiplier tube (PMT). This electrical signal was then monitored using an oscilloscope with the transient luminescent properties captured via a PC for analysis.

The emission from the phosphor is guided to a 9558QB photomultiplier tube (PMT) by a 12mm diameter quartz rod. Just as the quartz optical fibre does not introduce artefacts into the emission spectrum, the quartz rod and the quartz window on the PMT will not introducing additional emissions either. To ensure the reflected laser emission does not dominate the decay spectrum a 340nm cut-on filter was incorporated between the quartz rod and monochromator in the experimental setup. The same filter was used in the emission spectrum measurements.

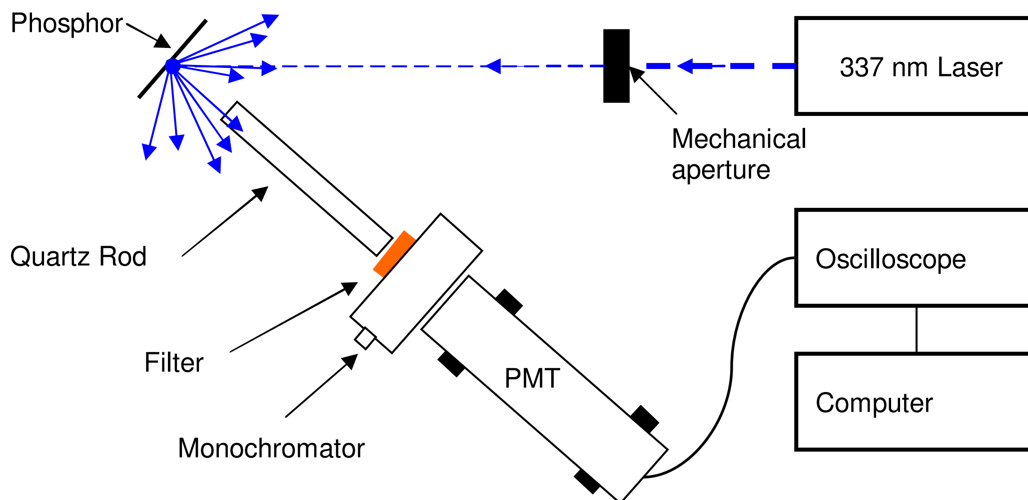

Figure 3.25: Experimental setup of equipment for the capture of the decay spectrum from the phosphor when excited by a N_2 laser.

Unlike a standard filter, which has a fixed value for which wavelengths are filtered, the monochromator was installed to be changeable and filter all but a small band of user defined wavelengths. The monochromator uses a diffraction grating to split the wavelength from incident light into a spectral spread. High precision dial with an accuracy of 0.2nm directs the emission to an exit port. The monochromator uses a 3nm-slit window to ensure a narrow wavelength band whilst maintaining sufficient intensity.

The filter along with the monochromator removes the optical laser component from the emission. However, it is not sufficient to remove the laser component from the detected signal. The laser component is reintroduced to the measurement due to electromagnetic interference created by the pulsing of the laser. If the PL signal was weak in comparison to the signal created by the laser interference, there is likely to be some overlapping of signals. If sufficiently weak, the laser component dominates the PL component and can be misinterpreted as the PL signal.

Light in the UV, visible and IR range enters through the PMT quartz window and is converted into an electrical signal, which is amplified many thousands of times. The PMT produces high gain for low noise whilst having a high frequency response and large area of collection (25mm aperture), earning it an essential place in nuclear and particle physics.

The electrical signal is passed from the PMT to a Gould (DSO) 4072 oscilloscope, where time-per-division, voltage-per-division, trigger level and a pre-post trigger is manipulated to display a decay curve. The image on the oscilloscope can be averaged for many decay curves to

increase accuracy by reducing noise. The oscilloscope is linked to a computer and when a suitable decay curve is presented, a LabView program on the computer captures the signal and exports it to a text file that can then be imported into the Excel program for curve fitting.

For each excitation event (each laser pulse), the profile of the curve follows a set pattern. When the phosphor is excited and an emission is created, the intensity increases rapidly until a maximum is reached. The reduction in emission intensity follows a curve that can be defined mathematically by Equation 8. This reduction in intensity is a much slower process than the initial increase. The decay constant was found by fitting the decay curve captured using the setup shown in Figure 3.25 to Equation 8 (Section 3.6). This equation is suitable for only single exponential decay curves, where all emitted light goes through one main energy change as it crosses the bandgap. This generally gives one peak in the emission spectrum which was true for the ZnS:Ag,Cl phosphor.

Within a single phosphor material, there can be multiple emission routes for the electron can emit energy as they fall to a ground level state. This can create multiple overlapping decay curves, and require a double exponential equation (Equation 9) to accurately describe the decay curve of the two decay rates. The equation describes two decay processes that have their own initial intensity and accompanying decay rate. A phosphor with multiple decay rates typically has more than one emission peak, as each process of energy loss is likely to create a different wavelength.

$$I(t) = I_1 \exp\left(\frac{-t}{\tau_1}\right) + I_2 \exp\left(\frac{-t}{\tau_2}\right)$$ **Equation 9**

Where *I(t)* is the intensity of emission at time *t* (in seconds). I_1 and I_2 are the initial intensity of light of first decay mode and second decay mode respectively. τ_1 and τ_2 are the decay constant of first decay mode and second decay mode respectively. To confirm that the ZnS:Ag,Cl phosphor is a single decay and not just that one decay curve dominated a weaker decay curve, three decay measurements were taken at specific wavelengths within the range that the ZnS:Ag,Cl emitted.

3.6.2.3. Uniformity

An important quality of the sample provided by ISIS was uniformity. A non-uniform sample can give spurious results and inaccurate intensity measurements. Nine positions across the surface of the sample were selected and at each of these positions, a spectrum was taken and compared. The laser beam was directed through a 10mm diameter circular iris before reaching the sample to ensure a consistent size and shape of beam incident at each of the nice positions.

Laser fluence is a significant factor relative to the resultant emission intensity, so changes in emission intensity require a stable laser source. The lasers available were tested for their stability and the most stable source chosen for the task.

3.6.3 Excitation by Alpha Source

The excitation of a phosphor by an ^{241}Am alpha source uses a very similar luminescence characterisation setup as the photoluminance system presented in Figure 3.23). The difference is the proximity of the source to the phosphor being much reduced. The laser can be directed, whereas the alpha particles are only able to travel a short distance in air, hence the source is brought as close to the phosphor as possible while a fibre optic is placed in a position to collect the emission (Figure 3.26).

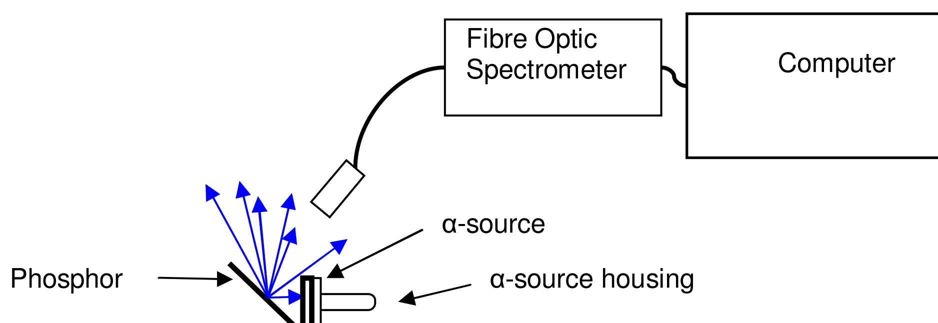

Figure 3.26: Experimental setup of equipment for the capture of the emission spectrum from the phosphor when excited by an alpha source.

Although the alpha source does not create a pulsed emission the decay time setup can be used to provide relative emission intensities of the phosphors by turning the PMT upright and laying the ISIS wafer on top with the alpha source on top of that (i.e. similar to the operation of a radiation detector). The alpha particles penetrate the phosphor and create RL, the emission

escapes from the surface where incident alpha particles struck as well as the reverse, due to the its thickness. The same can be done for the powders by forming the sample as a thin layer of powder on a silica wafer and placing this onto the PMT window. The powder makes it necessary for this orientation of the PMT (Figure 3.27).

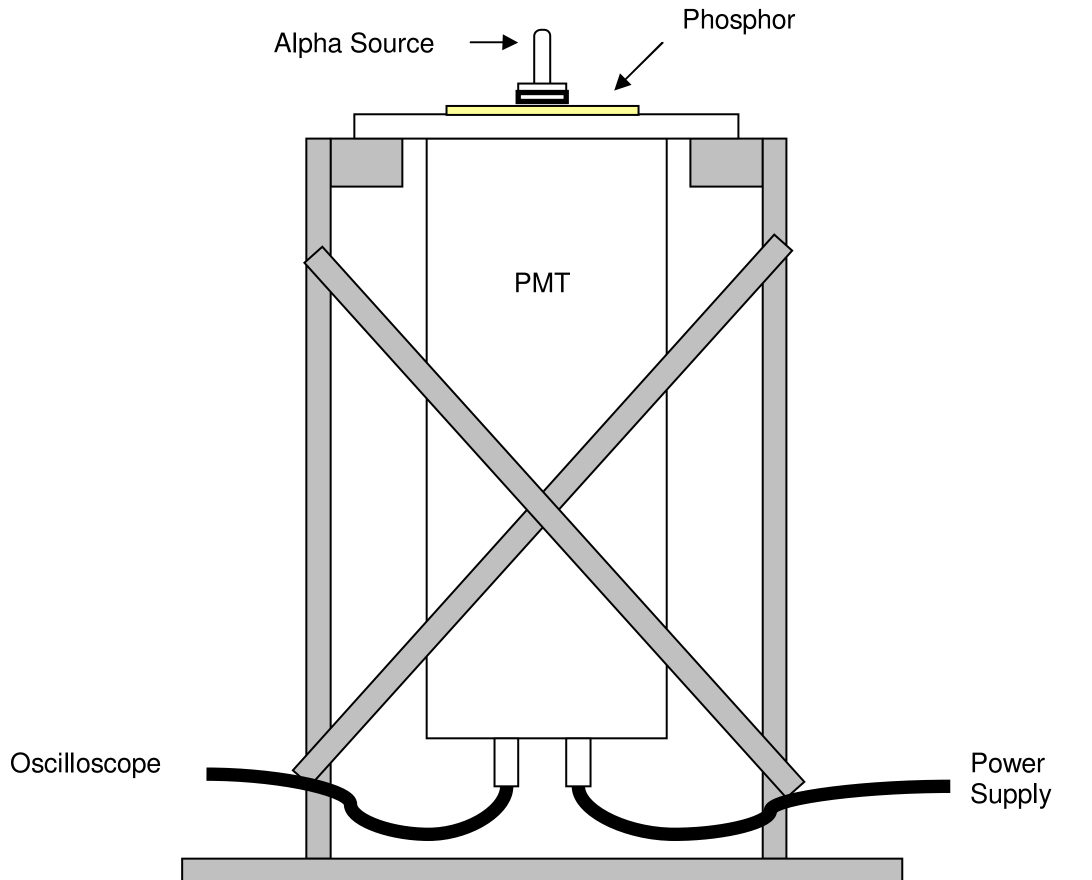

Figure 3.27 Experimental setup for the detection of relative emission intensities from phosphors under alpha excitation using a PMT.

3.7 Summary

This chapter has presented the process that was used to grow thin films using RF magnetron sputtering. It also presents the variables associated with this technique and how they affect the characteristics of the phosphor thin film. There is a presentation of two alternative methods of doping ZnS thin films and their merits.

Once grown, the thin films are characterised in terms of their thickness, uniformity of thickness and surface roughness to determine the quality of thin film grown using RF magnetron sputtering.

To characterise the effects that the deposition process has on the phosphor material the materials are characterised by their crystal composition and crystal structure using XRD and IBA.

These characterisation techniques give indications about the luminescent properties of the phosphors. This is directly tested by excitation by UV sources and an alpha radiation source to create PL and RL. The emission spectrum of the phosphors and their decay times are examined.

4 Characterisation of Phosphors

4.1 Introduction

The hardware used by ISIS for neutron detection analysis is a two-stage neutron scintillator. A phosphorescent material and a neutron converter in a homogeneous mixture form the scintillator. The converter captures the highly stable uncharged particle in a chemical reaction, the products of which are energetic electrically charged particles. For a specific group of phosphors these charged particles excite luminescent centres that create a visible emission – known as radioluminescence

The research presented in this chapter details the luminescent characterisation of the phosphor currently used by ISIS along with phosphors that are used during this investigation. Characterisation of these luminescent materials is undertaken to examine potential phosphors for use as thin films – thin film experimentation is discussed in Chapter 5. It was necessary to establish whether the same emission characteristics were observed when excited by charged particles as well as by UV light.

4.2 Method

The measurement techniques are presented in Chapter 3. The methods by which the phosphors are characterised are described below.

4.2.1 Phosphors

The phosphors characterised in this chapter each have a significant purpose as part of the overall investigation:

- The ISIS wafer (^{6}LiF -ZnS:Ag,Cl) determines the current operating characteristics of the scintillator used within the neutron diffraction analysis technique.

- The ZnS:Ag,Cl phosphor powder forms the source material used for growing thin films by RF magnetron sputtering (Chapter 5).
- The ZnS:Cl phosphor powder forms the flux for testing a potential method of incorporating Cl into a thin film (Chapter 6).
- ZnS:Tm phosphor powder was tested along with ZnS:Ag,Cl for its possible use as a RL phosphor. As another ZnS based phosphor, it had the potential as being a RL phosphor and was available.
- A pressed powder target of ZnS:Mn was used as the source material to grow thin films by RF magnetron sputtering for calibration work (Chapter 5).
- A ZnS solid target was used as the source material to grow thin films by RF magnetron sputtering for use in ion implantation (Chapter 6).

4.2.1.1. ZnS:Ag,Cl (ISIS)

This scintillator is a white self-supporting wafer (89.32 × 66.00 × 0.40mm) with one surface visually smooth, the reverse is rougher in appearance. The wafer comprises of a ^{6}LiF neutron converter and a ZnS:Ag,Cl luminescent phosphor in a homogeneous particle mixture.

This material was tested for its emission properties by using alpha (^{241}Am) and UV (N_2, HeCd, Nd:YAG) irradiation as the excitation. The characterisation of the sample is presented in terms of its emission spectrum, transient decay properties and intensity distribution across the sample.

4.2.1.2. ZnS:Ag,Cl (Phosphor Technology)

GL47/N-C2[2] - zinc sulphide (ZnS) doped with silver (Ag) is a white powder with the silver at a concentration of 80mgAg/Kg, which is the equivalent of 0.01at% [103]. The excitation and emission spectrum (provided by the supplier) of the GL47/N-C2 phosphor is shown below (Figure 4.1).

[2] Phosphor Technology Ltd, Norton Park, Norton Road, Stevenage, Herts, SG1 2BB

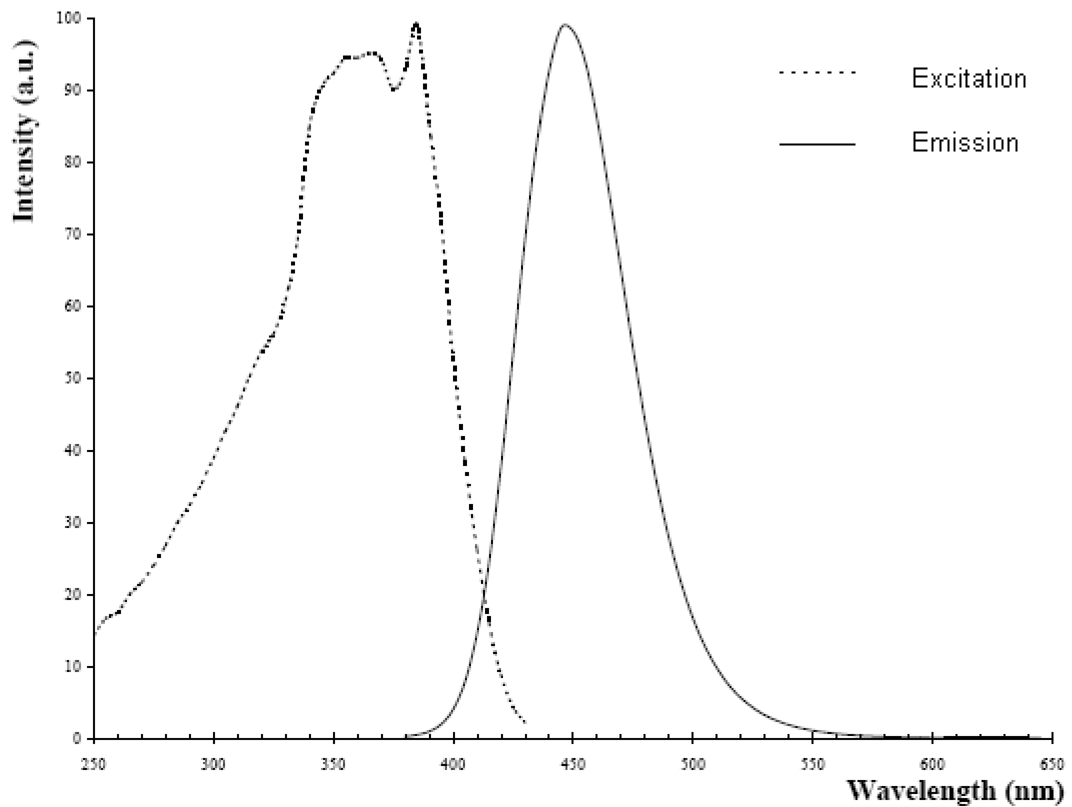

Figure 4.1: Excitation and Emission spectrum of ZnS:Ag,Cl purchased from Phosphor Technology Ltd, with permission [103].

This spectrum presents a peak wavelength emission at 450nm and a FWHM of 57nm.

This phosphor was used as the source material in the growth of thin films by RF magnetron sputtering and the material supplied was characterised for its emission spectrum and decay time, using alpha and laser excitation.

4.2.1.3. ZnS:Cl

GL17/N-X[1] – zinc sulphide (ZnS) doped with chlorine (Cl) is a white powder with the chlorine at a concentration of 4at% [104]. The excitation and emission spectrum of the GL17/N-X phosphor is shown below (Figure 4.2).

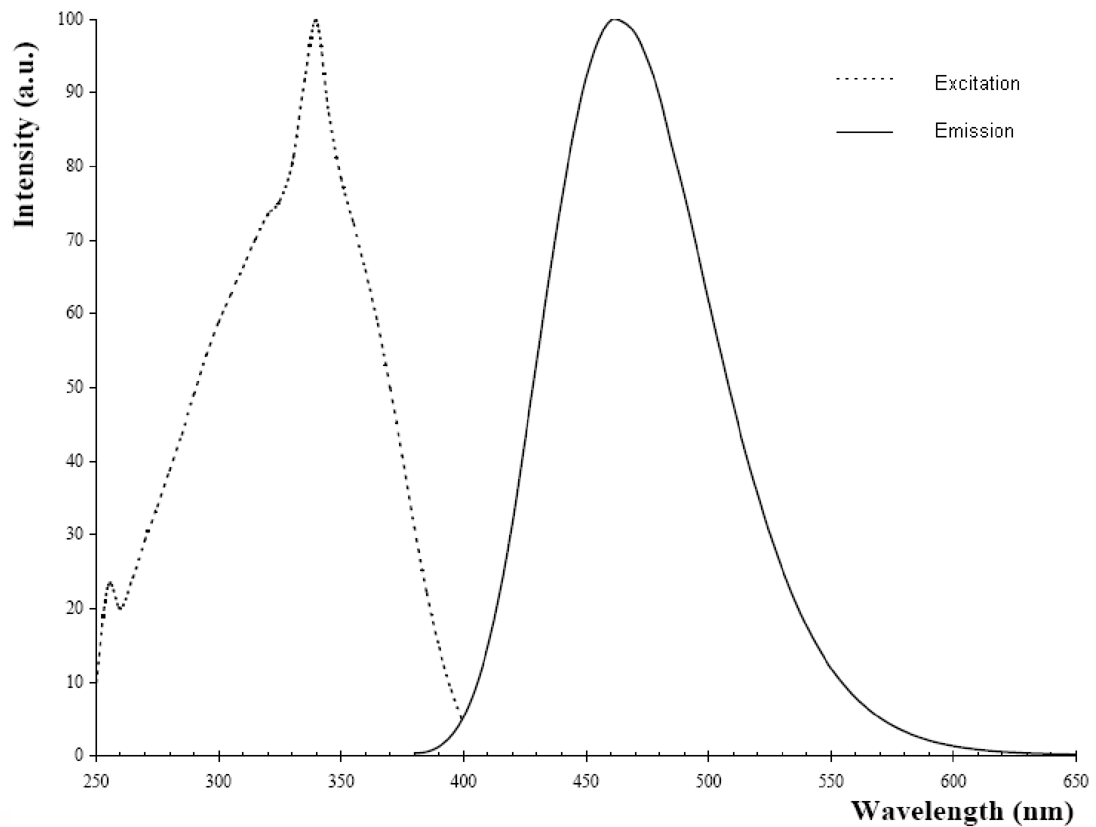

Figure 4.2: Excitation and Emission spectrum of ZnS:Cl (GL17/N-X) , with permission from Phosphor Technology Ltd. [104].

This spectrum presents a peak wavelength emission at 461nm and a FWHM of 51nm.

ZnS:Cl was used in this study as part of a technique to incorporate chlorine into a ZnS thin film. It could potentially effect the emission of other samples, hence it was characterised by its emission spectrum when excited by alpha particles and UV laser light.

4.2.1.4. ZnS:Tm

GL:29/Tm[1] – zinc sulphide (ZnS) doped with thulium (Tm) is a pale green powder and has a concentration of 3.00% w/w of TmF_3 and 0.05% w/w of Cu [105].

This was one of many phosphors that were used for evaluation by alpha excitation and later tested for photoluminescence and decay time. The evaluation phosphors were to provide additional data that would potentially verify uncertainties observed during the testing of radioluminescence.

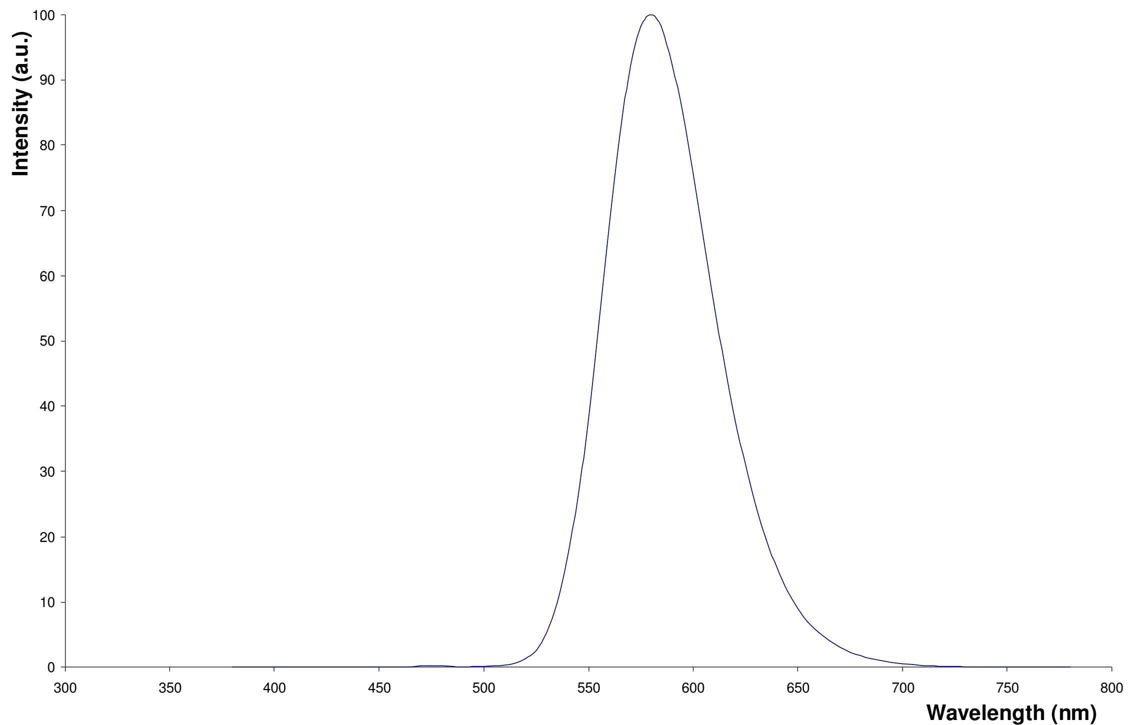

Figure 4.3: Emission spectrum of ZnS:Tm (GL:29/Tm) excited by 360nm light, with permission from Phosphor Technology Ltd. [105]**.**

4.2.1.5. ZnS:Mn

GL:29 M/B-A[1] - zinc sulphide (ZnS) doped with manganese (Mn) and copper (Cu) is a white powder [106]. The GL:29 M/B-A1 has a concentration of 0.43 at%.

A characteristic reported [22] for ZnS:Mn is that the PL properties change depending on whether in bulk or thin film form. The peak emission is 584nm in bulk form, while it was 590nm in thin film form and its FWHM had broadened. A similar change occurred to the excitation spectrum, the peak excitation wavelength is 332nm for bulk and 265nm for thin film form.

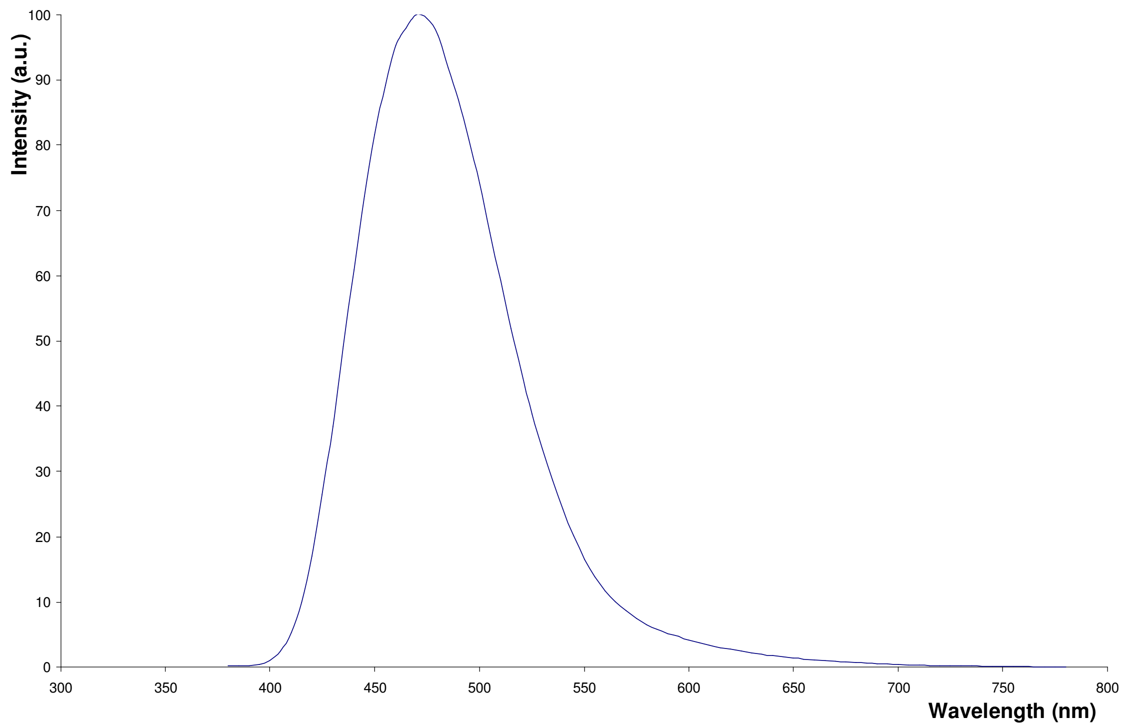

Figure 4.4: Emission spectrum of ZnS:Mn (GL:29 M/B-A) excited by 360nm light, with permission from Phosphor Technology Ltd. [106].

4.2.1.6. ZnS

Z1-9006-D1[3] - zinc sulphide (ZnS) is a 76.2mm white solid disk 4mm thick [107]. The Z1-9006-D1 has a purity of 99.99% and was used as a target to grow undoped thin films. This material should produce an emission that is the band gap energy of the ZnS semiconductor. However, there are references [73, 108] that report ZnS having an emission spectrum. One [108] provides an excitation and emission spectra of ZnS nanocrystals that are then annealed. The result of this was that there was an emission reported under each of the conditions, peak emission as synthesised was at 450nm, 700℃ anneal (1hour) was at 490nm and 900℃ (1hour) was at 510nm.

.

[3] Testbourne Ltd. Unit 12, Hassocks Wood, Stroudley Road, Basingstoke, Hampshire, RG24 8UQ

4.2.2 Excitation

Three laser excitation sources (N_2, HeCd and Nd:YAG) were used to stimulate photoluminescence (PL) using 337, 325, 266 and 355nm UV excitations. One alpha source (Americium^{241}) was used to stimulate radioluminescence (RL).

A variation in emission intensity was expected for these phosphors due to an efficiency related to the excitation wavelengths. Using the excitation spectrum, efficiencies of each of the laser sources for the ZnS:Ag,Cl phosphor were calculated and are displayed Table 4.1.

Table 4.1: Efficiency of ZnS:Ag,Cl (Phosphor Technology) to different laser excitations.

Laser	Excitation Wavelength (nm)	Relative Intensity (%)
N_2	337	75
HeCd	325	57
Nd:YAG	266	20
	355	95

The output powers of the laser and the phosphor efficiency relative to the excitation laser wavelength are the main criteria to observe uniformity of emission and repeatability of the system. A study of each of the lasers was carried out to test the fluence of emission against time to determine the laser stability.

The alpha source was an ^{241}Am and was chosen due to its use by others for alpha luminescent testing of ZnS:Ag [39, 42] and other radioluminescent phosphors [109]. It produces alpha particles with an energy of 5.485MeV [54]. Compared to the energy of the alpha and tritium in the neutron-lithium reaction, it has twice the energy and hence will penetrate a greater distance.

4.2.3 Emission

Following excitation, the phosphor emits light, which is characterised by its emission spectrum and decay time (as described in chapter 3). The emission spectrum provides information on the intensity of the emission over a range of wavelengths and the relative intensity between phosphors. The decay time provides a measurement for the rate to which the intensity of the

emission reduces. To a lesser degree, the relative intensities between phosphors can also be gained using the decay time technique.

4.2.4 Uniformity and Repeatability

Uniformity of emission intensity was important for making a detector that would produce an accurate response to neutron interactions. Testing the uniformity of the ISIS wafer for emission intensity at set positions across its area was undertaken to provide a comparative assessment of the required uniformity desired for the thin films.

The main factor affecting the emission intensity is the fluence of the excitation source. A greater flux density of UV light or alpha particles leads to greater emission intensity. To test the stability of power output from the lasers, a Melles Griot Broadband Power Meter was positioned at the exit port of the laser to collect data for fluence over time.

For the uniformity test the Nd:YAG laser emitting 266nm was used to excite the phosphor in the experimental setup described in Chapter 3. A total of 50 consecutive emission spectra were collected and averaged by the system at an integration time of 150ms, making an effective detection period of 7.5 seconds. This setting was used so as to prevent saturation of the spectrometer and reduce fluctuations and noise produced by the use of pulse excitation. Nine tests were carried out at eight locations and covered one part of the ISIS phosphor (Figure 4.5). To verify possible changes between the start and end of the experiment the first location was retested to determine potential error or alterations. These locations were defined in a grid system to highlight potential trends that could run across the sample.

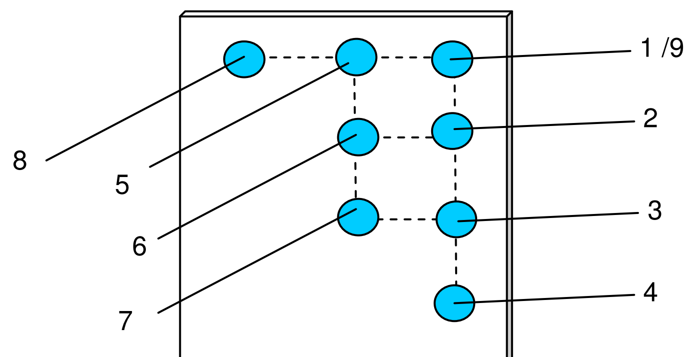

Figure 4.5: The arrangement of test location over an area of the ISIS wafer.

This test for uniformity was also used to examine repeatability to determine the robustness of the experimental setup by repeated testing.

4.3 Results

The lasers are characterised for their power and the stability of this power for the purpose of finding the most suitable laser for uniformity and repeatability measurements.

The phosphors were characterised by their emission spectrum and decay time using laser and alpha sources.

4.3.1 Excitation Source

Each of the lasers produced a different power, with more than an order of magnitude difference between each of them (Table 4.2). The values within this table were collected from the results presented in section 4.3.1.1 to 4.3.1.3. The range of output for each laser was derived by maximum output minus minimum output over a period of 2 hours.

Table 4.2: Stability of laser power

Laser	Frequency	Excitation Wavelength	Start Power	Power after 2 hours	Maximum Range in Power Fluctuation	
N_2	Pulsed (20Hz)	337 nm	0.81 mW	0.71 mW	0.11 mW	13.4%
HeCd	Continuous	325 nm	22.0 mW	22.0 mW	3.0 mW	14.6%
Nd:YAG	Pulsed (20Hz)	355 nm	1.05 W	1.05 W	0.05 W	4.8%

4.3.1.1. N_2 Laser

The power of the N_2 laser changes continually, starting at 0.8mW the power initially increased by 0.03mW over a period of 30 minutes, before progressive reduction in intensity as shown in Figure 4.6.

A ‘cool down’ period of the N_2 laser was introduced to investigate whether or not it was possible to regenerate the initial lasers output power. After an excitation period of eight hours, the laser was switch off for a period of 20 minutes (On-Off 1 - Figure 4.6), then reapplied to determine the

restored power output. This was repeated for a switched off period of 10 minutes (On-Off 2 - Figure 4.6).

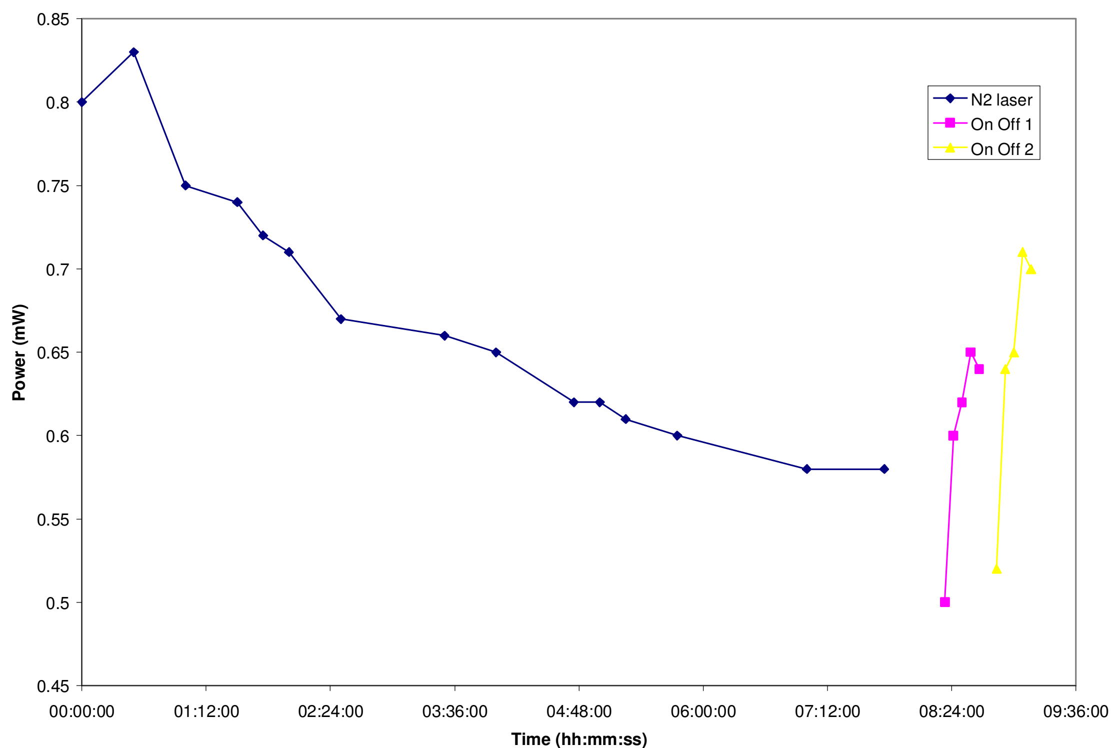

Figure 4.6: Power of laser emitted by the N_2 laser against time with two periods of 'cool down'.

There was not enough regeneration to return the power to the initial value observed at the start of the test.

For further uniformity measurements, the phosphor was exposed to the N_2 laser for periods of up to 2 minutes during which an emission spectrum was captured, followed by a period of 'cool down' (~2mins). The process was repeated as required. The cool down duration of ~2 minutes was chosen as a suitable duration, that the user would be expected to wait for the test to not become too extended and beyond usefulness.

4.3.1.2. HeCd Laser

The power from the HeCd laser was higher than the N_2 laser (N_2 [max.] = 0.84mW, HeCd ≈21mW), and although the most significant grouping of output powers were between 20-21mW it also produced four readings over 22mW (Figure 4.7). However, the HeCd laser produced a sufficient laser intensity to cause the phosphor (ZnS:Ag,Cl) to blacken and was therefore used when a more intense laser source was required, but was not the best option.

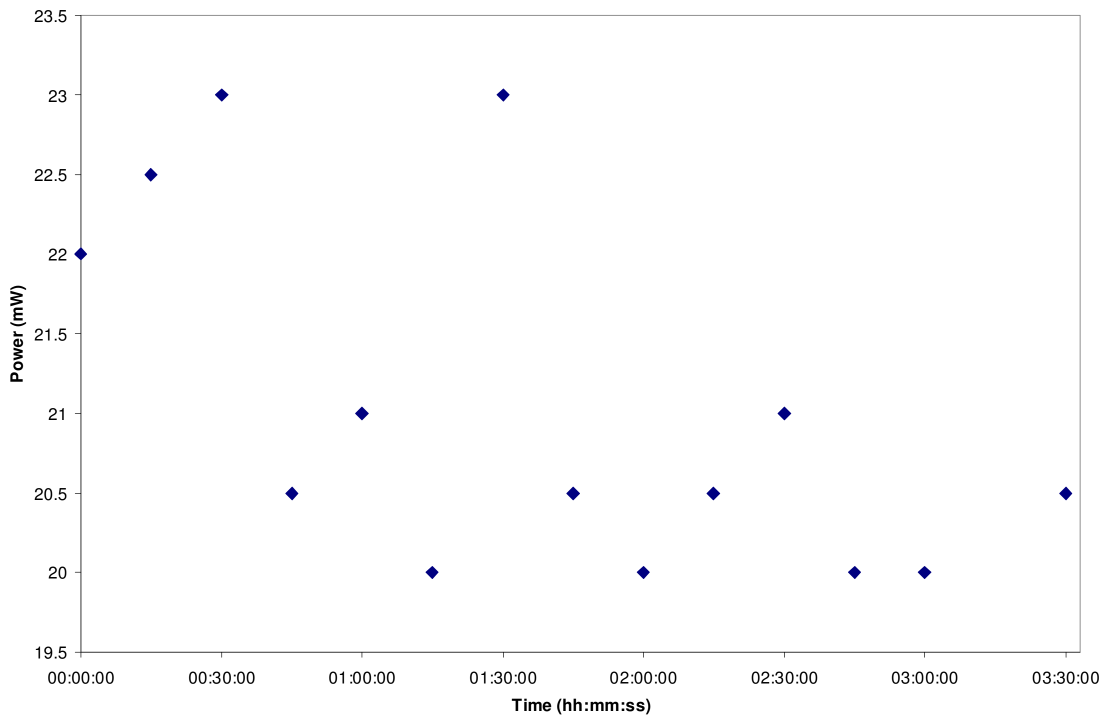

Figure 4.7: Power of laser emitted by the HeCd laser over time.

4.3.1.3. Nd:YAG Laser

The Nd:YAG laser can be tuned using harmonics to produces four principle emission wavelengths (266, 355, 532, 1064nm). There is then a Surelite Separation Package (SSP), which filters the undesired wavelengths, resulting in only the chosen wavelength to be emitted after the unit. After the SSP, a series of mirrors were used to direct the selected laser. In order to maximum the power output at the selected wavelength, the harmonic crystals were tuned accordingly.

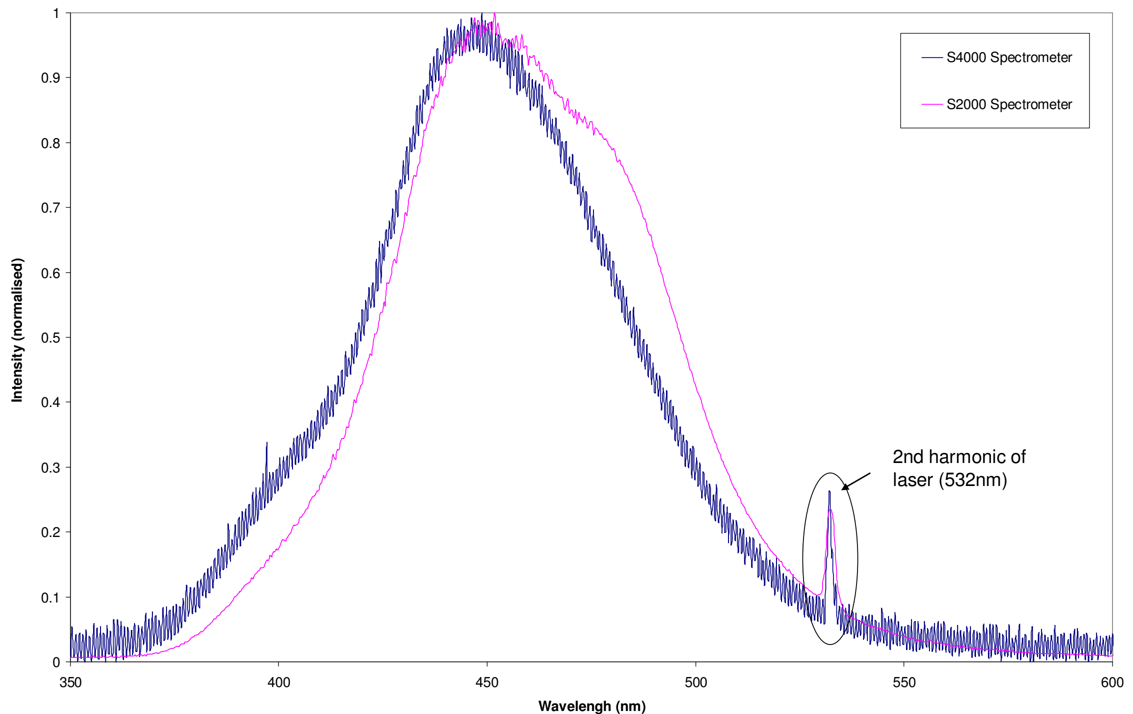

Figure 4.8: The ISIS wafer excited primarily by 266nm but also exhibiting its second harmonic (532nm). Spectra are captured using two spectrometers (S2000, S4000),

During calibration the laser was tuned to its maximum output, but once tuned the output power was reduced sufficiently to prevent damage (observed as blackening) to the phosphor. Though the SSP and mirrors were designed to reduce unwanted laser wavelengths there was still some present in the emission spectrum (Figure 4.8).

The power from the Nd:YAG laser at 266nm and 355nm has a fluctuation that can only be measured by the power meter with a sensitivity of with 0.05W per division and so produced one of two readings, 1.00W or 1.05W (Figure 4.9). Two tests where carried out on this laser as indicated by *Nd:YAG* and *Nd:YAG (Repeat)* in Figure 4.9. The result of 0.05W fluctuation was derived, however this with a more suitable power meter a truer measurement could be gained. This does not deter from the result that the Nd:YAG laser produced the most stable result, in terms of percentage fluctuation, of the lasers tested even if the fluctuation was twice as large.

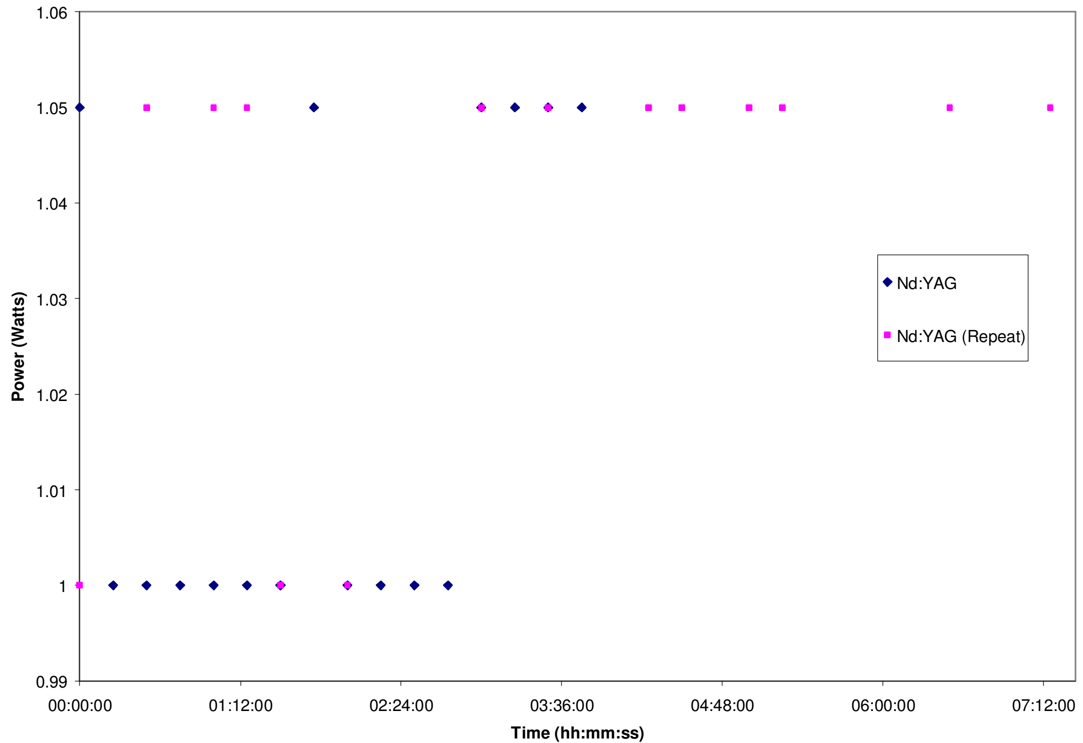

Figure 4.9: Power of laser emitted by the Nd:YAG laser against time, with a repeat test.

4.3.2 Emission Spectra

4.3.2.1. ZnS:Ag,Cl (ISIS)

Following excitation of the ISIS scintillator sample by the lasers, the emission spectrum was of a broad peak around the wavelength of 450nm with a FWHM of 77nm. A comparison of the emission when excited by the Nd:YAG laser in conjunction with the OPO panther unit at three wavelength (307, 320, 337nm) resulted in emission spectra with minimal variation when normalised (Figure 4.10). The three peaks observed between 600nm and 700nm are due to the second harmonics of the excitation source, i.e. (614, 640, 674nm). The peak intensities between the emission spectra did not follow the trend predicted by the excitation spectra provided by Phosphor Technology, as can be seen in Table 4.3.

Table 4.3: Peak intensity measurement from the emission spectra of three excitation wavelengths and their comparison to the expected relative intensities

Excitation Wavelength (nm)	Peak Intensity (counts)	Peak Intensity (normalised)	Expected Peak Intensity (%)	Expected Peak Intensity (normalised)
307nm	1088	0.88	45	0.59
320nm	1048	0.85	55	0.73
337nm	1230	1.00	75	1.00

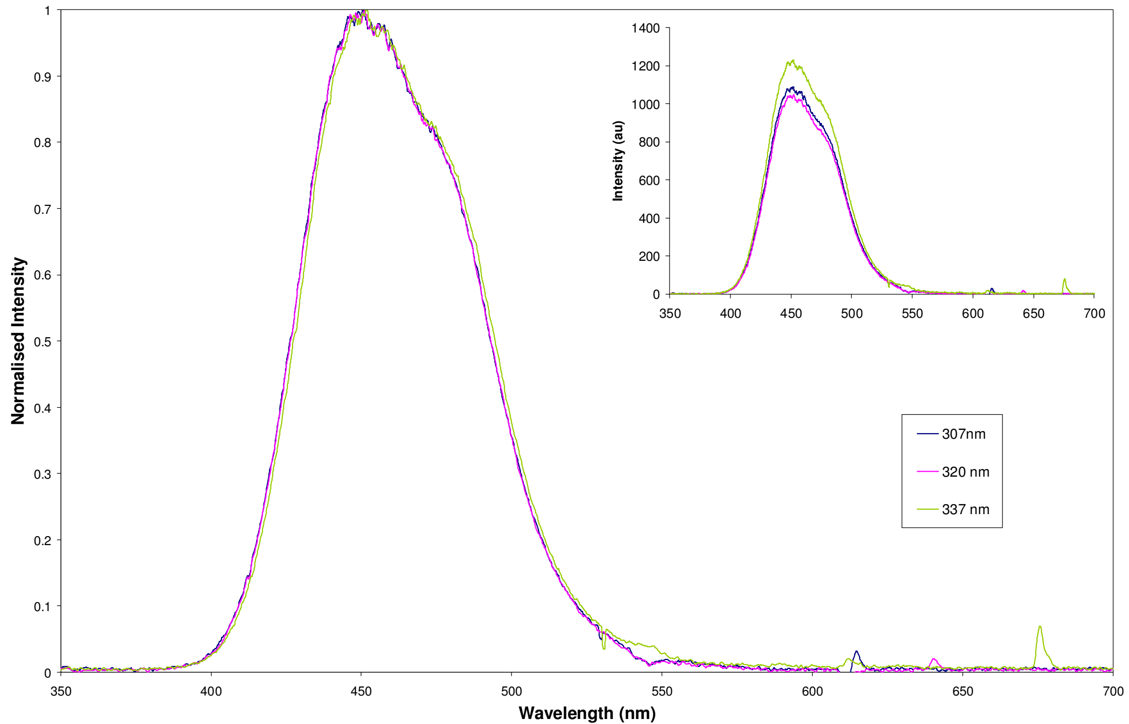

Figure 4.10: Normalised PL emission spectrum from the ISIS scintillator excited by 307, 320 and 337nm laser wavelengths. Insert - arbitrary units of the same three emission spectra.

These emission spectra produced a different distribution of energy intensity versus wavelengths to ones seen in the literature. In addition to the expected peak at 450nm [34, 58, 83], a shoulder peak was observed in the emission spectrum.

Comparing the FWHM of the measured emission peak to a selection of those that have been presented in the literature (Table 4.4) [34], it can be seen that there was a distinct increase to the upper wavelength that defines the FWHM. This difference creates an increase in the FWHM of approximately 14nm.

Table 4.4: Peak intensity and FWHM of the ZnS:Ag,Cl phosphor from literature and measurement.

	Peak	Lower	Upper	FWHM (nm)
Measured peak	450nm	425	496	71
Phosphor Technology measurement [103]	450nm	423	480	57
Average literature measurement [34, 58, 83]	450nm	425	480	55

To understand this result in more detail, the shoulder peak must be characterised. From the literature a set of discrete intensity versus wavelength values were defined to represent the 450nm peak. Using these values and subtracting them from the measured emission spectrum, resulted in a set of values that define the shoulder component (Figure 4.11).

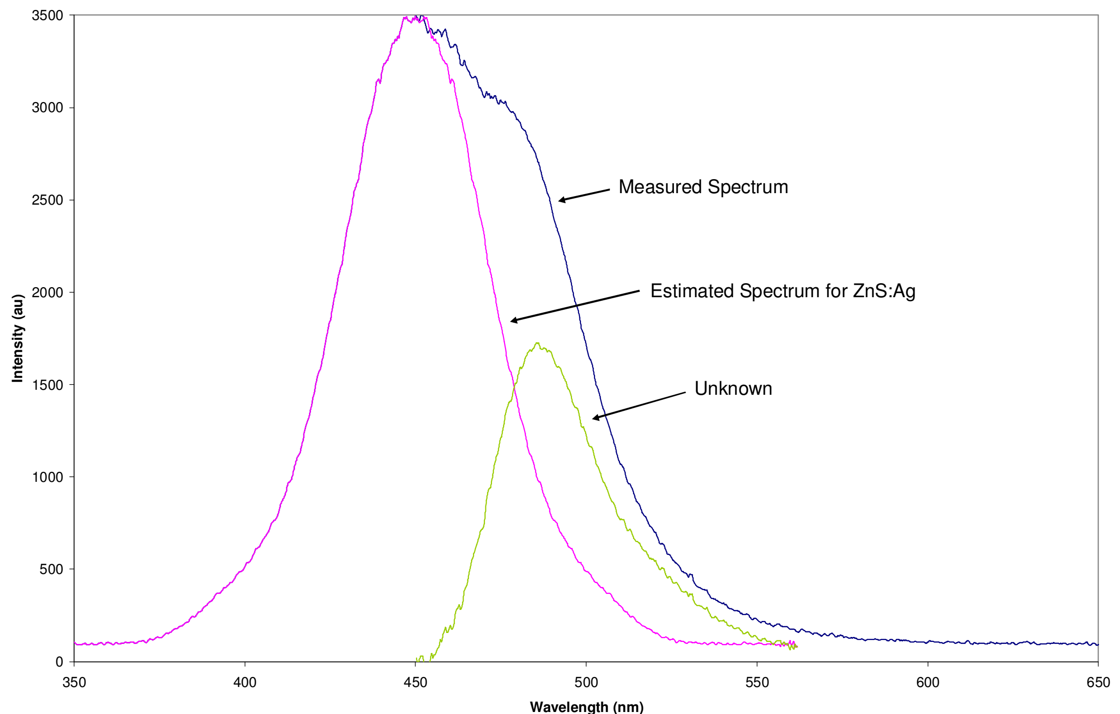

Figure 4.11: Measured PL emission spectrum from the ISIS phosphor excited by N_2 laser (337nm) resolved into two peaks.

When resolved into two peaks, the shoulder peak was defined as a 486nm peak, with a FWHM of 38nm at approximately half the peak intensity of the 450nm peak.

There could be a number of causes for this shoulder peak. Noise, a contaminated phosphor, a variant of ZnS:Ag,Cl, an incorrectly calibrated spectrometer or a time dependant component to the emission spectrum that has been preferentially enhanced.

Noise can be generated by the introduction of stray light from alternative light sources such as florescent lighting, table lamp lighting and fluorescent materials within the light collection and detection equipment. However, the emission spectra were collected in a dark room with considerable effort made to reduce all light sources interfering in the detection method. The use of quartz instead of glass to guide the emission also means that additional luminescence was not created in the experimental setup. Regular control measurements using a virgin Si wafer as the target or closing the shutter to the laser to stop excitation were taken as background

measurements to enhance the accuracy of the resultant emission spectra. The dominant source of noise was found to be generated by the spectrometer; it was repeatable with some variation to its intensity.

Additional routes for electrons to release energy can produce an altered emission spectrum. However, no variant of the ZnS:Ag,Cl phosphor has been found to produce an emission spectrum with the observed shoulder peak due to contamination (deliberate or accidental). Nor has an altered state of the ZnS:Ag,Cl been reported that would preferentially emit more strongly around the 485nm wavelength.

It has been reported [35, 110] that there is a time dependent component to the emission spectrum. While it appears that there is a single emission, it is suggested that there were actually a series of distinct emissions that combine to form the emission spectrum. This suggests that the spectrometer is exhibiting a preferentially enhanced response to a peak centred on 485nm at some duration into the emission process. Shiiki [35] uses delay times of 3, 10, 50, 100 and 200μs, which creates a peak emission starting at 460nm (3μs) and ends at ~490nm (200μs). Romero [110] uses a period up to 15μs, which has a peak intensity starting at ~400nm (<3.3μs).

A suitable experimental setup, where the laser triggers the spectrometer to capture an emission spectrum for each laser pulse, would mean that a time related emission spectrum could be examined. However, the smallest capture duration the spectrometer was capable of attaining was 3.0ms. A period of 10μs or smaller would be suggested for the emission stages to be observed, when taking into account the decay time of the ZnS:Ag,Cl phosphor (~30μs). As well as this, only part of the emission would be captured each time, hence, the intensity would also be reduced along with an increase in the observed noise component.

Both ZnS:Ag,Cl samples (from ISIS and Phosphor Technology) produced the shoulder peak. A sample of the powder was returned to Phosphor Technology for testing by their own equipment for PL. The result from this was that when excited by 337nm UV light both samples produced

an emission spectrum that was the same as provided in the specifications. This was for peak shape as well as peak intensity wavelength.

In response to this, the spectrometer was recalibrated using the technique devised by the spectrometer manufacturer, by using LS-1-CAL tungsten halogen lamp and calibration software. The lamp produces a repeatable, broad emission that the spectrometer then detects. The calibration software matches the measured emission to an expected emission, altering intensities where required. However, this calibration did not affect the measured emission spectrum for the ZnS:Ag,Cl samples - the shoulder peak remained. The fibre optic and filter were also examined and shown to cause no significant difference in the emission peak.
Once an alternative spectrometer was made available and the emission spectrum from both spectrometers were compared a distinct difference was observed (Figure 4.12).

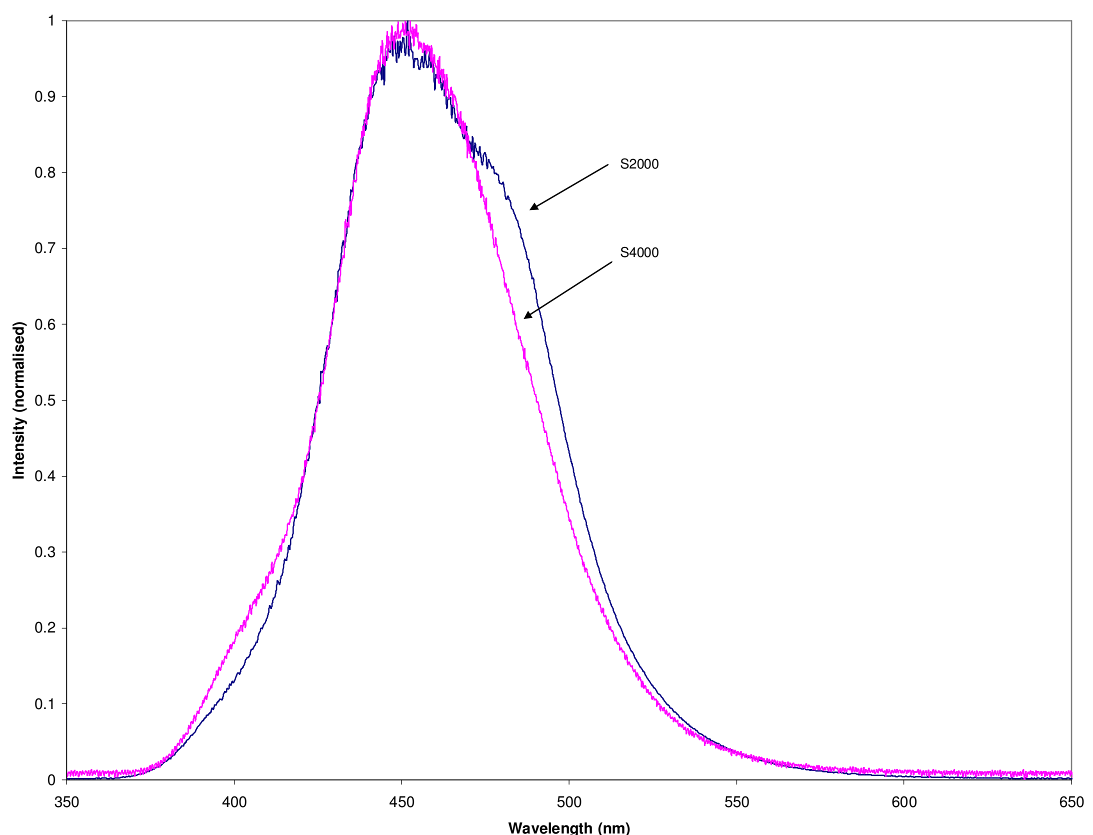

Figure 4.12: Normalised emission spectrum created by two spectrometers by the excitation of a ZnS:Ag,Cl phosphor powder using the N_2 laser.

A characteristic of the S4000 spectrometer was emission spectra with a greater noise component than the S2000. To compensate for this, the area of excitation was expanded from

approximately 1mm^2 to 25mm^2, increasing the intensity of the emission detected and reducing the relative noise component. This meant that the other variables, i.e. integration time (400ms), averaging (20) and the position of the optical fibre in relation to the emission source, were maintained.

There are two changes in the shape of the emission spectra produced by the two spectrometers. The emission spectra measured via the S2000 spectrometer have a shoulder peak that was evaluated to be at 486nm, which is absent from the spectra measured via the S4000. The other is a shoulder peak observed at approximately 395nm in the emission spectrum produced by the S4000, which is not present in the S2000 emission spectrum.

4.3.2.2. ZnS:Ag,Cl (Phosphor Technology)

A comparison of the emission spectrum of ZnS:Ag,Cl phosphor from ISIS and Phosphor Technology (Figure 4.12) can be seen in Figure 4.14 for each spectrometer. The emission spectra peak at 450nm for both detectors, but due to the shoulder peak in the S2000 the FWHM is 6.5nm wider at 71.9nm compared to 65.7nm for the peak from the S4000.

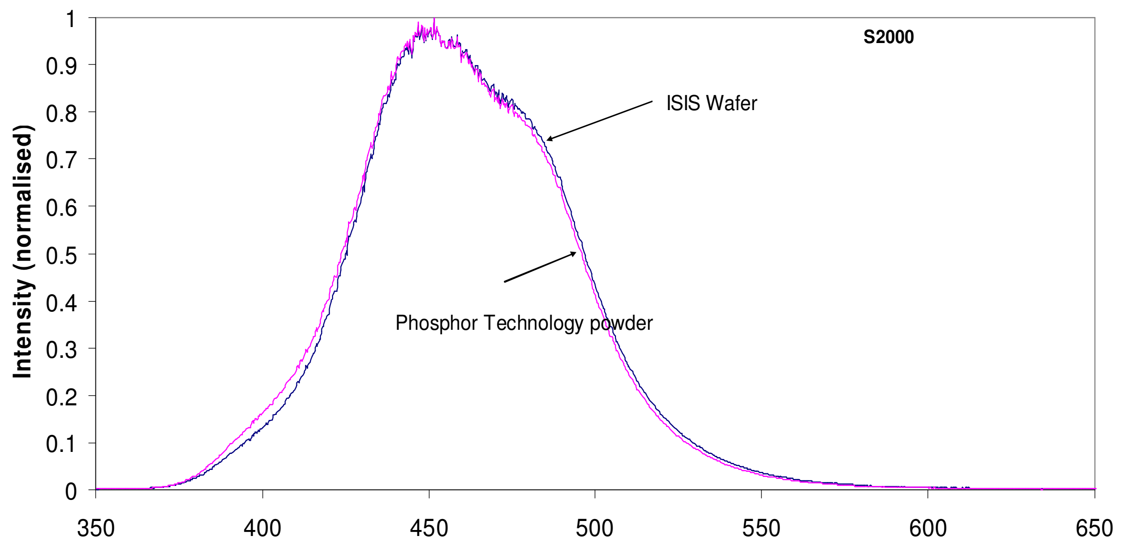

Figure 4.13: A normalised emission spectrum of ZnS:Ag,Cl phosphor using an S2000 spectrometers excited using the N_2 laser.

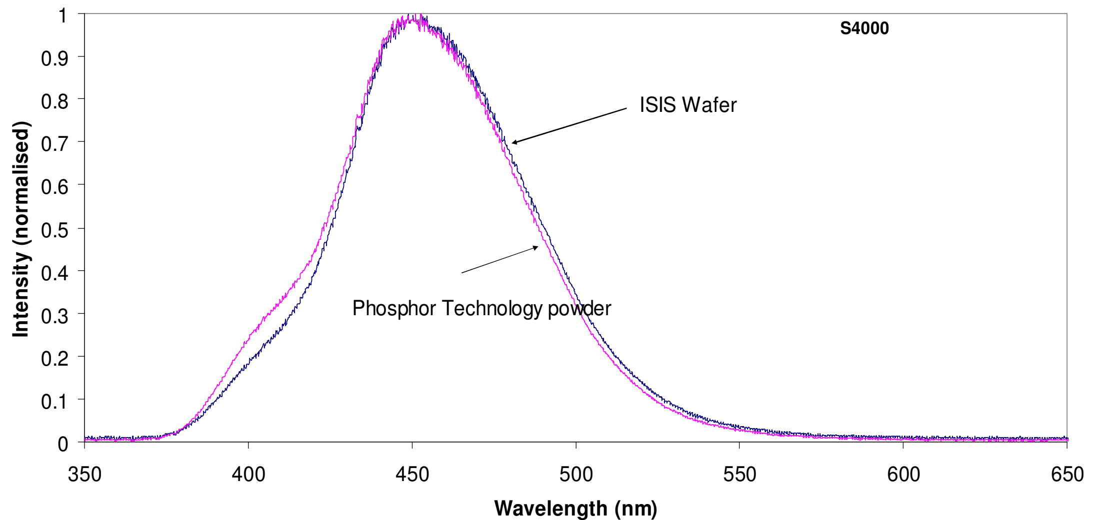

Figure 4.14: A normalised emission spectrum of ZnS:Ag,Cl phosphor using an S4000 spectrometers excited using the N_2 laser.

The are minor differences between the normalised spectra of the two ZnS:Ag,Cl samples measured using the two spectrometers. There is a shift in the emission wavelength at half maximum intensity of approximately 2nm and an accompanying change to the FWHM of less than 1nm (Table 4.5). This is sufficiently small that it can be assumed a spectrometer feature and not a feature of the phosphor.

Table 4.5: Extrapolated data comparing the FWHM of the ZnS:Ag,Cl phosphor by two spectrometers.

		FWHM (nm)	Difference (nm)	Wavelength shift at half max	
				Lower limit (nm)	Upper limit (nm)
S2000	Phosphor Tech	72.5	0.9	1.9	1.1
	ISIS	71.7			
S4000	Phosphor Tech	65.9	0.2	2.0	1.8
	ISIS	65.7			

4.3.2.3. Other Phosphors (ZnS:Cl, ZnS:Tm, ZnS:Mn, ZnS)

Using the combined emission spectra from the S2000 and S4000 spectrometers the following normalised spectra formed for these phosphors purchased from Phosphor Technology (ZnS:Cl, ZnS:Tm, ZnS:Mn) and Testbourne (ZnS) were measured.

The emission spectra for the ZnS:Cl (Figure 4.15) peaks at 487.9nm and 480.7nm for the S2000 and S4000 spectrometers respectively. Due to the difference in shape, there is also a

difference in the FWHM, 78.8nm and 87.8nm for the S2000 and S4000 spectrometers respectively.

The emission spectra for ZnS:Tm (Figure 4.16) both peak at 455nm, but due to the shoulder peak in the S2000 the FWHM is 12nm wider, 77nm compared to 65nm for the peak from the S4000.

The emission spectrum for ZnS:Mn (Figure 4.17) peaks at 577nm and 583nm for the S2000 and S4000 respectively. However, FWHM for both emission spectra are 56nm.

The emission spectra for ZnS (Figure 4.18) peak at 488nm and 480nm for the S2000 and S4000 spectrometers respectively. Due to the difference in shape, there is also a difference in the FWHM, 74nm and 88nm for the S2000 and S4000 spectrometers respectively.

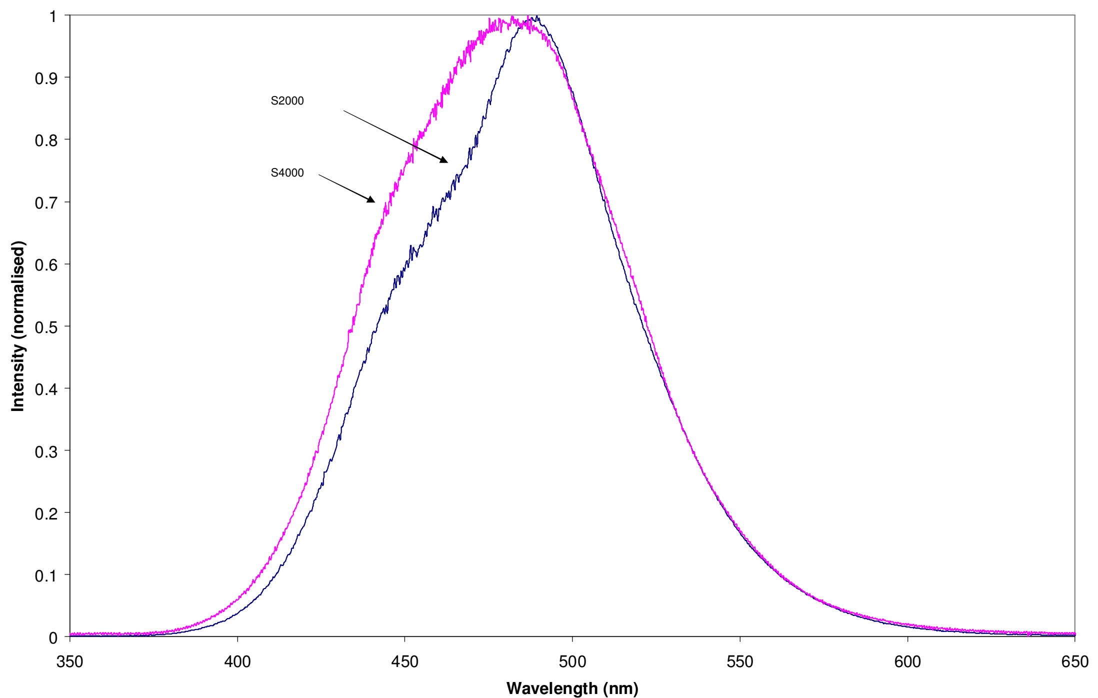

Figure 4.15: A normalised emission spectrum of ZnS:Cl phosphor using an S2000 and S4000 spectrometers excited using the N_2 laser.

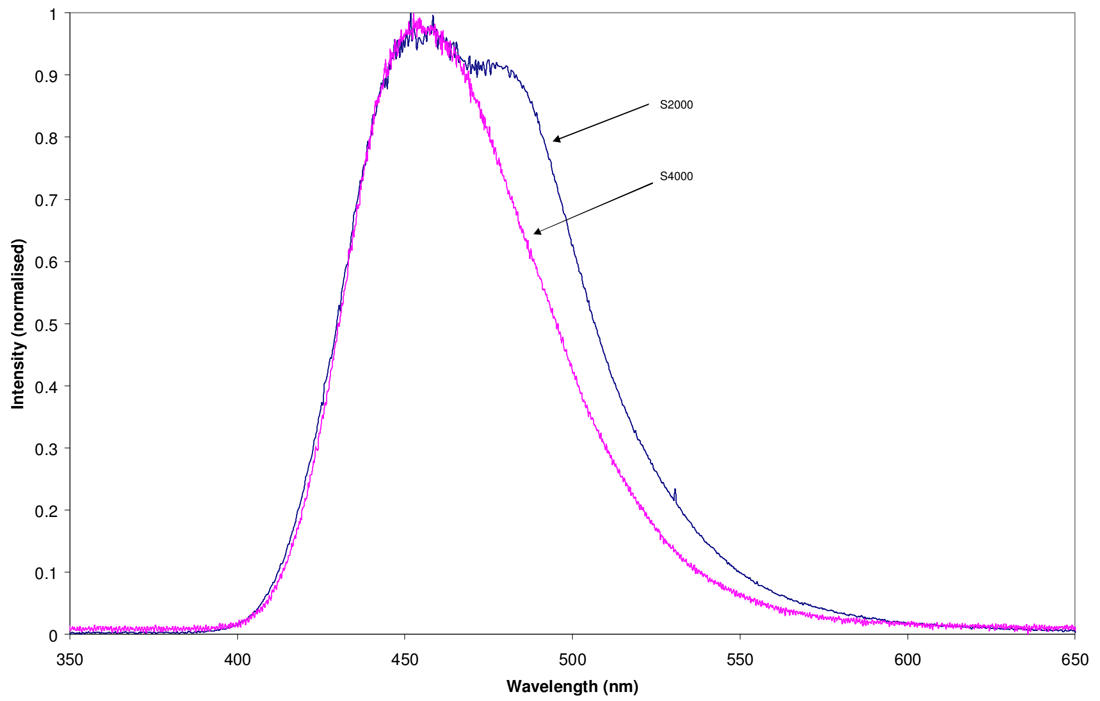

Figure 4.16: A normalised emission spectrum of ZnS:Tm phosphor using an S2000 and S4000 spectrometers excited using the N_2 laser.

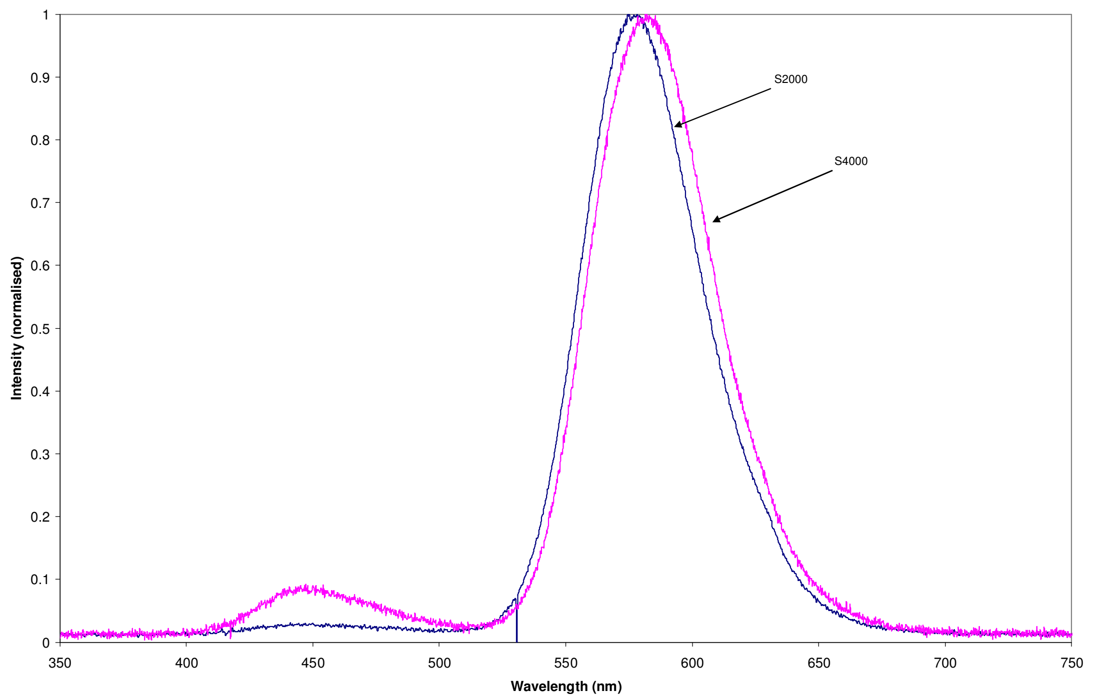

Figure 4.17: A normalised emission spectrum of ZnS:Mn phosphor using an S2000 and S4000 spectrometers excited using the N_2 laser.

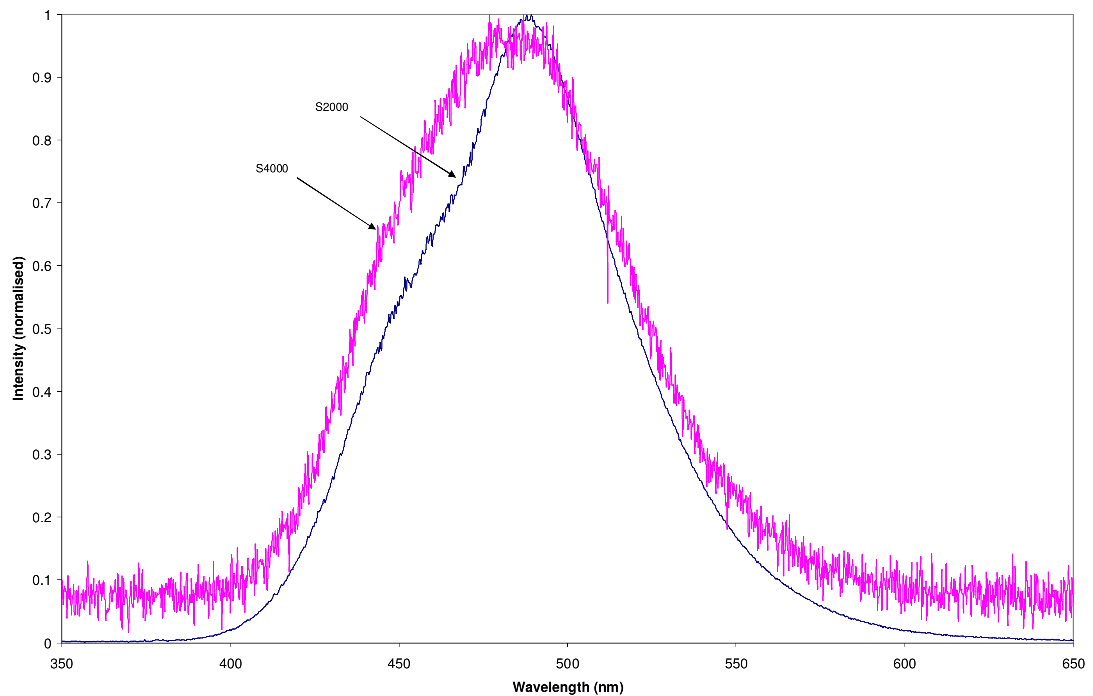

Figure 4.18: A normalised emission spectrum of ZnS solid target using an S2000 and S4000 spectrometers excited using the N_2 laser.

The wavelength of the peak intensity and the FWHM of the peak of each emission from each spectrometer are presented in Table 4.6.

Table 4.6: Wavelength of peak intensity and FWHM data for the phosphor samples excited by a N_2 laser.

	Spectrometer	Peak Intensity (λ)	FWHM
ZnS:Ag,Cl (ISIS)	S2000	450.1	71.3
	S4000	449.8	64.8
ZnS:Ag,Cl (Phos Tech)	S2000	450.1	71.9
	S4000	450.1	65.7
ZnS:Cl	S2000	487.9	78.8
	S4000	480.7	87.8
ZnS:Tm	S2000	454.0	77.1
	S4000	454.2	65.5
ZnS:Mn	S2000	577.9	55.1
	S4000	582.4	56.7
ZnS	S2000	488.6	74
	S4000	476.9	90.3

The emission spectrum of the six samples using the S2000 (Figure 4.19) and S4000 (Figure 4.20) spectrometers has been plotted as a comparison between the samples.

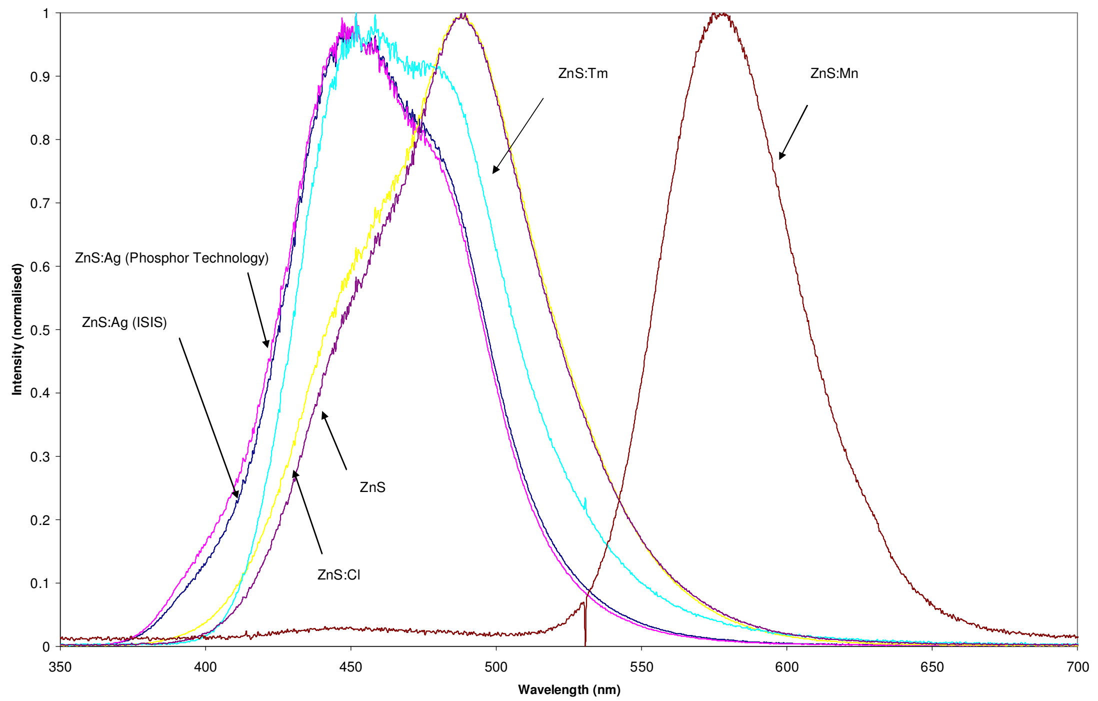

Figure 4.19: A combination of the emission spectra created by the six samples using the S2000 spectrometer.

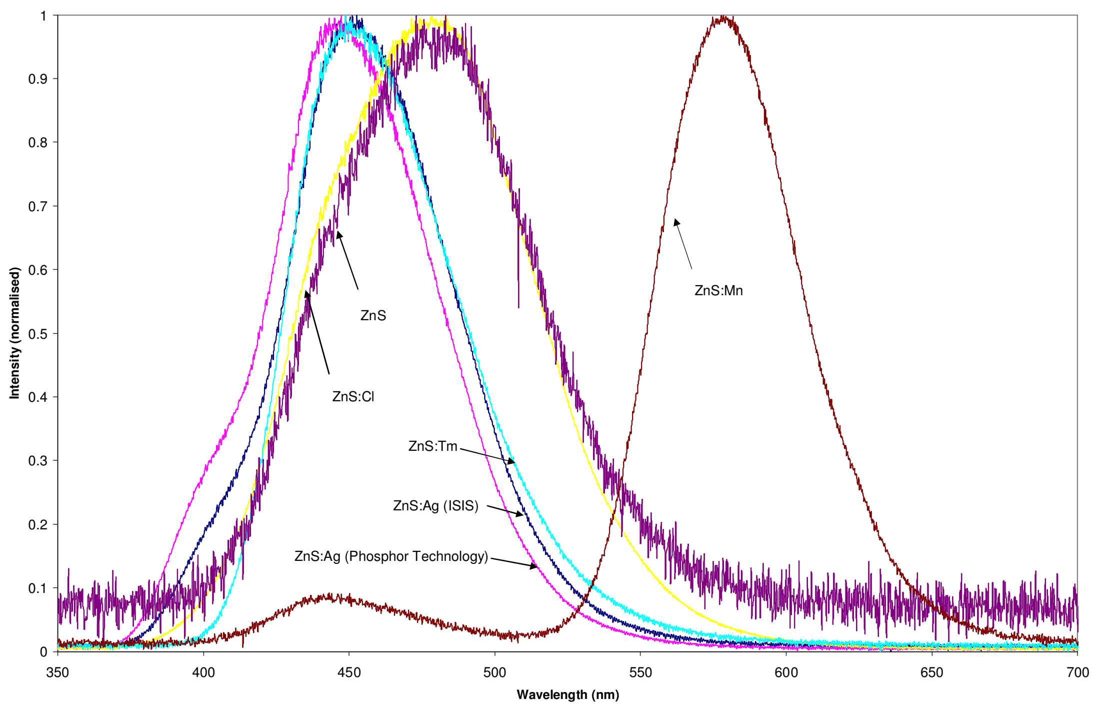

Figure 4.20: A combination of the emission spectra created by the six samples using the S4000 spectrometer.

The relative emission intensity between these phosphors are characterised using the N_2 laser in the excite/cool-down method to ensure laser power consistency - as described in the Section 4.3.1.1. The results should be taken as an indication of the relative emission intensities, but are

not absolute. The values for the emission intensities are given in Table 4.7 and presented graphically in a normalised intensity chart (normalised to the maximum intensity measured for each spectrometer) in Figure 4.21.

Table 4.7: Intensity measurements for the phosphors using two spectrometers.

Phosphor	Intensity (au)		Normalised Intensity	
	S2000	S4000	S2000	S4000
ZnS:Ag,Cl (ISIS)	3065	21757	0.32	0.76
ZnS:Ag,Cl (Phosphor Tech)	3573	28593	0.37	1.00
ZnS:Cl (Phosphor Tech)	9634	27509	1.00	0.96
ZnS:Tm (Phosphor Tech)	1143	9596	0.12	0.34
ZnS:Mn (Phosphor Tech)	2429	14818	0.25	0.52
ZnS (Testbourne)	2866	18783	0.30	0.66

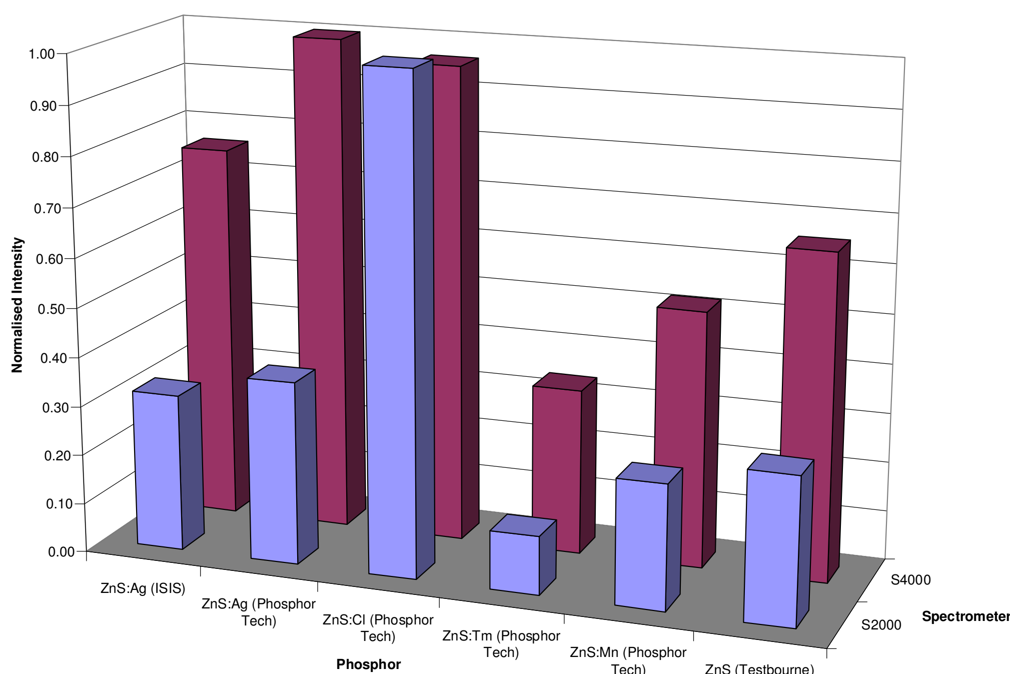

Figure 4.21: Normalised peak emission intensity of six phosphors using a N_2 laser excitation source.

The samples are from different sources and are in powder, solid target or from the ISIS self-supporting wafer, these differences effect emission intensity due to surface roughness. The phosphors are manufactured by different groups, which remove another aspect of control that would allow the different samples to be compared with certainty. However, all variables that can be controlled have been made to be consistent between experiments in Figure 4.21. The controlled variables are the light collection equipment, the laser, surface roughness of sample and light capture capabilities (relative position of fibre optic, laser beam and sample).

4.3.3 Decay Measurements

An example of decay measurement is shown below (Figure 4.22), where two distinctly separate decay processes are resolvable. The peak at ~10μs is the laser component and the peak at ~30μs is the phosphor component. Difficulty in interpreting a decay curve is encountered when the phosphor decay component is weaker than the laser decay curve.

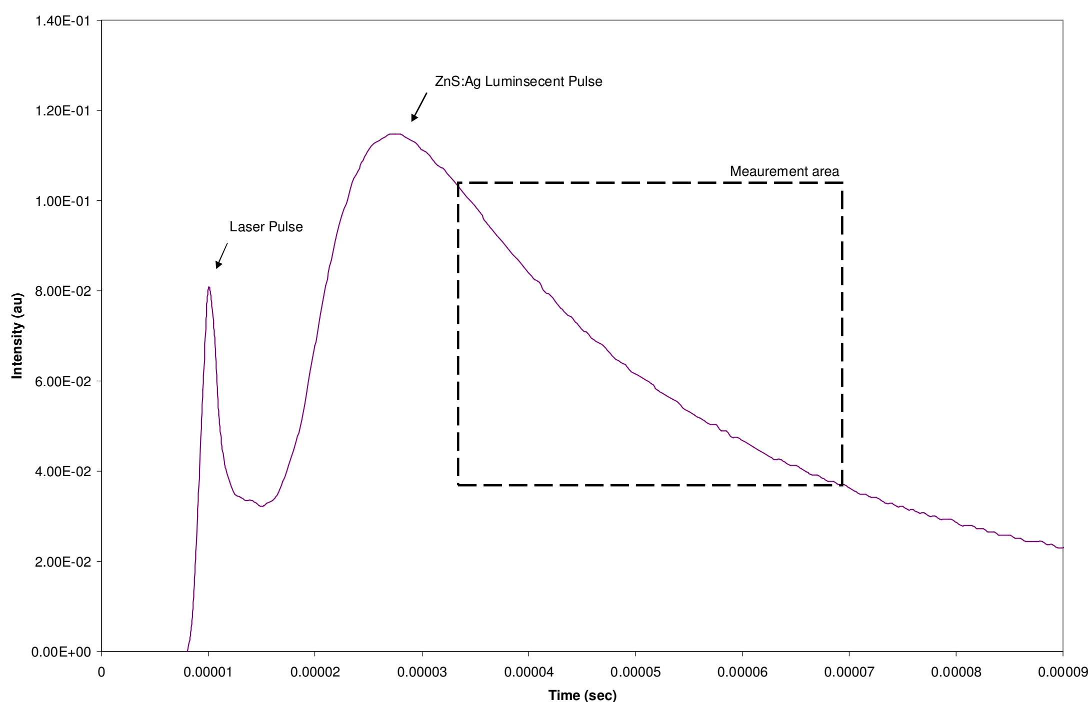

Figure 4.22: A typical image generated by the PMT and oscilloscope, with the highlighted area being the general region where decay time measurements were taken.

The presence of the laser component was not due to inadequate filtering. There was a 340nm cut-on filter and a monochromator incorporated into the experimental setup, removing all but a user defined bandwidth of 3.2nm from the PL emission. The laser component was due to interference created by the electromagnetic field produced during lasing. This was tested by closing the laser shutter and observing that the laser noise signal remains.

The bandwidth of the monochromator was tested with use of the spectrometer and the ZnS:Ag,Cl phosphor. The phosphor was excited with the N_2 laser to create an emission that was directed to a monochromator fitted with the 3nm slit aperture. A fibre optic was positioned at the exit port of the monochromator and guided the emission to the spectrometer. Tuning the monochromator to 450nm and then 500nm produced emission spectrum with peaks that had FWHM of 3.2nm (Figure 4.23).

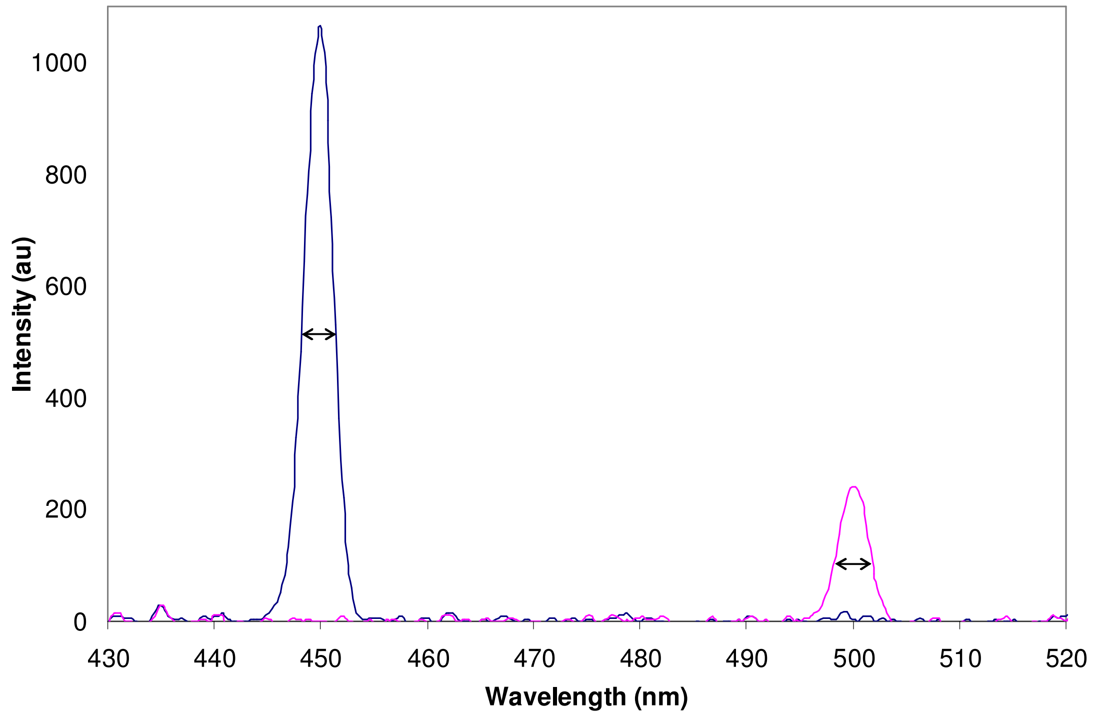

Figure 4.23: Emission spectrum filtered using the monochromator when tuned to 450nm and 500nm.

At the extremities of the curve, the area near the peak and the long tail section, the curve does not conform to the standard exponential fit and distorts an exponential representation of the curve, due to multiple exponential components. It is the approximate region between 10% and 90% of the peak intensity that is examined, which is dominated by a decay that can be described by a single exponential fit. The measured test region was given an exponential trend line and a log scale applied to the intensity axis. This scaling made the trend line appear linear, as well as the region of the decay curve that conforms to an exponential decay. The trend line was then extended or reduced along the data set to most accurately fit the line.

Shown in Figure 4.24 and Figure 4.25 are the decay curves for the ZnS:Ag,Cl wafer from ISIS, ZnS:Ag,Cl powder from Phosphor Technology respectively. Using the monochromator, the decay was characterised at three wavelengths, 440, 485 and 510nm. These wavelengths were originally chosen as part of the characterisation of the emission spectrum due to the 485 nm shoulder peak observed by the S2000 spectrometer. Different luminescent emission processes generally exhibit a different emission wavelength and decay time, which is characteristic of the electron transitions involved. If there was a correlation observed between the decay time at the

wavelengths 440, 485 and 510nm, it might suggest that the shoulder peak was due to contamination or a variation of the ZnS:Ag,Cl as it would be using a different transition route that would have a different decay time.

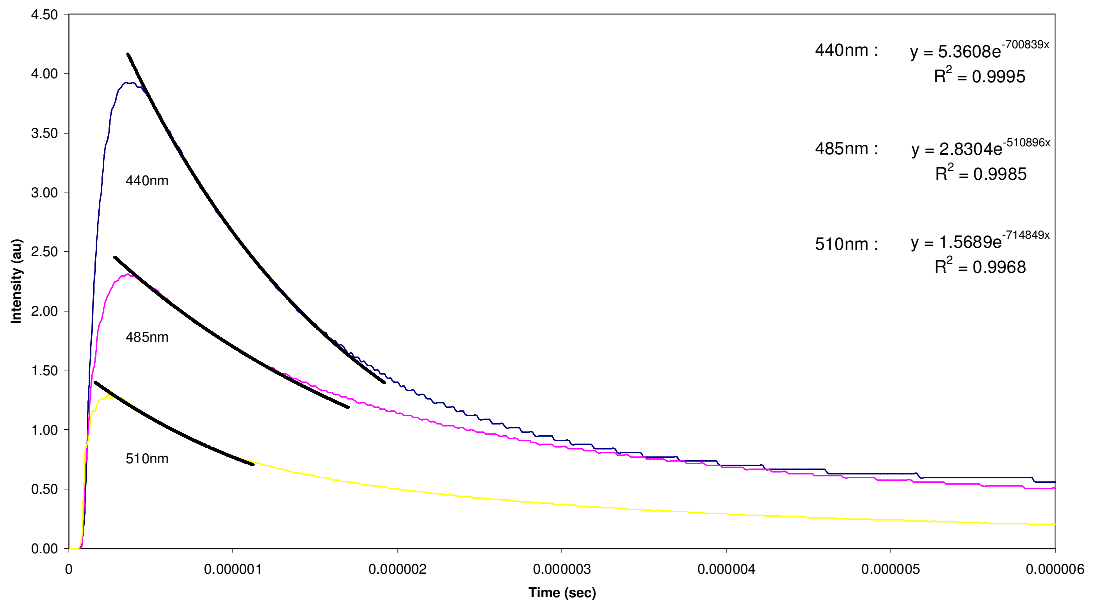

Figure 4.24: Decay measurements of the ISIS scintillator at the wavelengths 440, 485 and 510nm and the exponential equations expressing the experimental fit to the decay curves

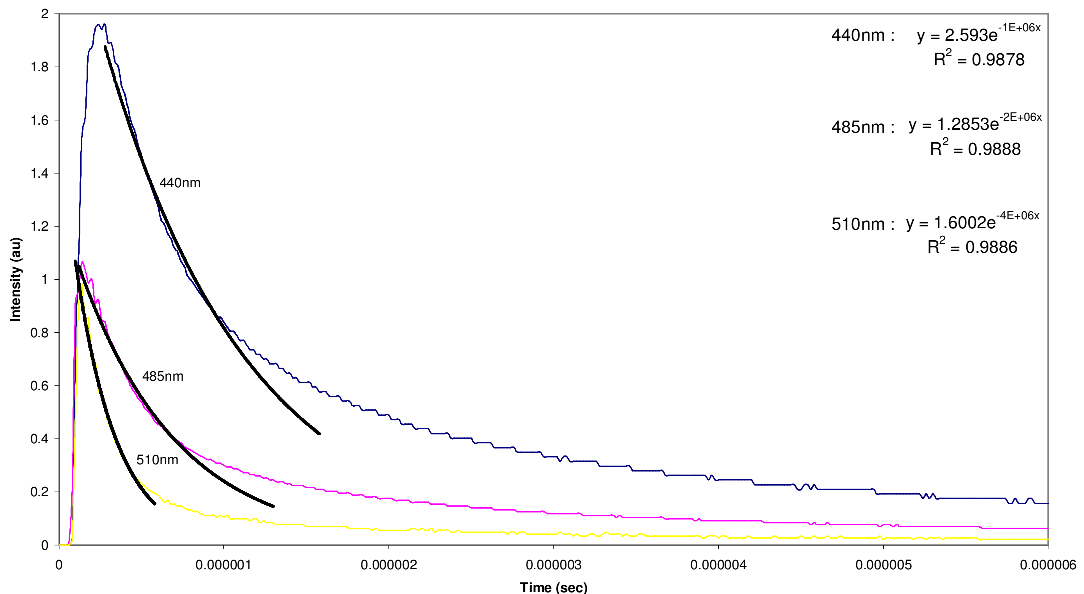

Figure 4.25: Decay measurements of the ZnS:Ag,Cl phosphor measured at the wavelengths (440, 485 and 510nm) and the exponential equations expressing the decay curves.

The ZnS:Ag,Cl powder was measured again for its decay characteristics at 430nm and 450nm (Figure 4.26). The difference between this experiment and the previous one performed on the ZnS:Ag,Cl powder was the enhanced emission collection to increase detected emission

intensity. With an increased detected intensity the relative noise component, observed in the decay curve as a fluctuation, would be reduced and hence enhance the decay curve exhibited by the phosphor.

A control decay curve was collected by closing the shutter of the N_2 laser while still lasing and capturing a measurement (Figure 4.27). This decay curve represents the inherent laser electromagnetic noise component.

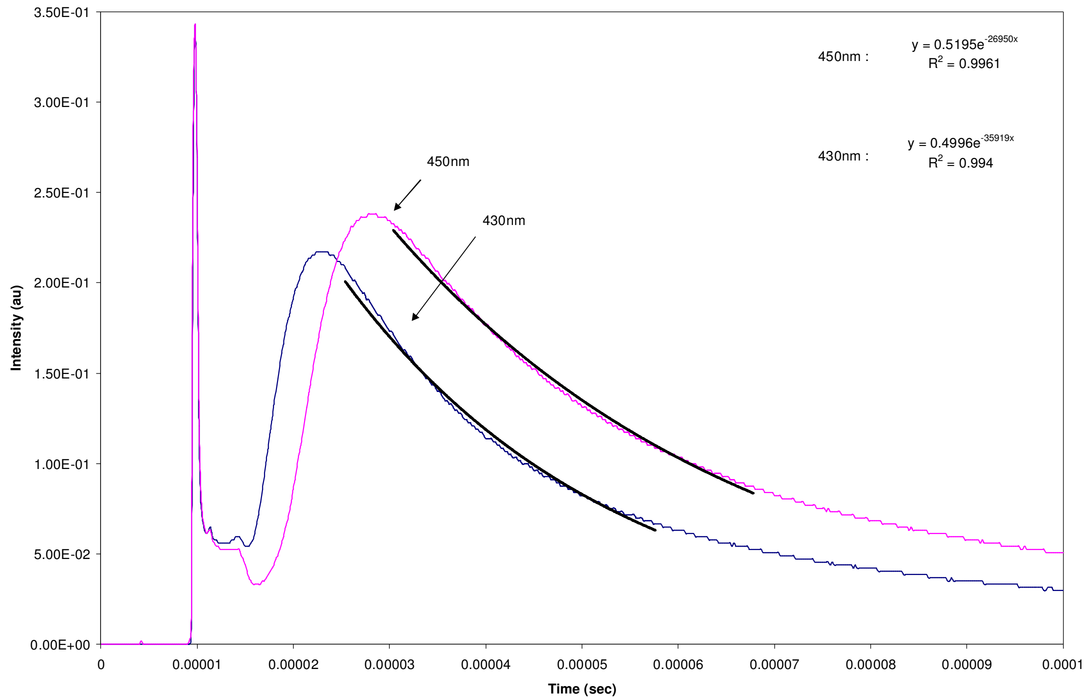

Figure 4.26: Decay measurements of the ZnS:Ag,Cl phosphor measured at the wavelengths (430 and 450nm) and the exponential equations expressing the decay curves.

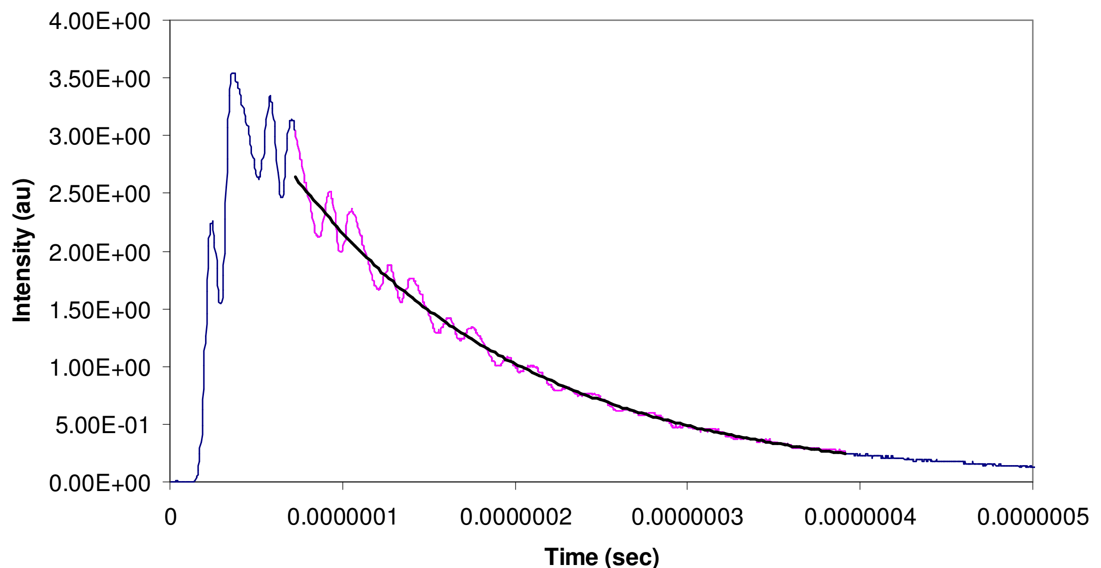

Figure 4.27: A decay curve detected without the excitation of a phosphor.

For the data that forms the decay curves, they were fitted with an exponential function and the decay times are presented in Table 4.8.

Table 4.8: The data extracted from decay curves of three phosphors at three wavelengths.

Phosphor	Detection Wavelength	Exponent	Decay Time
ZnS:Ag,Cl (ISIS)	440nm	-700839	1.43μs
	485nm	-497275	2.01μs
	510nm	-714849	1.40μs
ZnS:Ag,Cl (Phosphor Technology)	440nm	-1154200	866ns
	485nm	-1675790	597ns
	510nm	-4024357	248ns
ZnS:Ag,Cl (Phosphor Technology)	430nm	-35919	27.8μs
	450nm	-26950	37.1μs
No phosphor		-7430436	135ns

The ISIS sample exhibits an average primary decay time of 1.61μs, within the region of the total after glow component (30μs) as quoted in the literature review.

The Phosphor Technology sample exhibits a different range of decay values to the ISIS sample. The average decay time of this phosphor is 570.3ns, and goes as low as 248ns, depending on excitation wavelength, which is close to the fast decay component typically quoted in the literature (200ns).

The ISIS sample did not exhibit a marked difference in decay time at the three detection wavelengths, whereas the Phosphor Technology sample decay time reduced from 866ns to 248ns, a 71% reduction, when excited by 440nm and 510 nm, respectively.

4.3.4 Alpha Excitation

4.3.4.1. Alpha Excitation

The ^{241}Am alpha source has a 432 years half-life, with the products being an alpha particle and ^{237}Np. Hence, the activity of the sample whilst initially being quoted on delivery as 5μCi would now be 4.87μCi after 25 years. ^{237}Np has a half-life of 2.144×10^{6} years and also produces alpha particles in its decay, hence the source and products produce alpha particles.

Testing the source with a Series 900 mini-monitor Geiger Muller tube at positions 0, 5, 10, 15 and 20mm from the source, it produced a count rate of alpha sources in air (Figure 4.28).

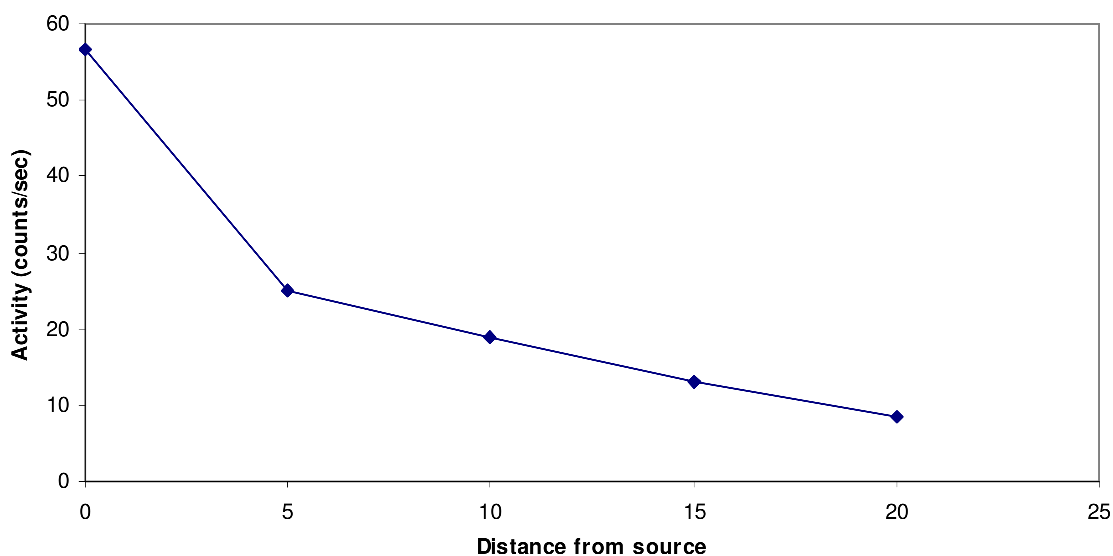

Figure 4.28: Activity detected at distances from the ^{241}Am source in air.

When the ISIS sample was sandwiched between the alpha source and the detector, an activity of 13cps was measured. Meaning, the ISIS wafer stops approximately 80% of the alpha particles from a ^{241}Am source. However, the energy of the alpha particles from the ^{241}Am source is greater than the alpha particles from the neutron-lithium reaction. Hence, the ISIS wafer would have captured a greater proportion if the energy were the same as the neutron-lithium reaction.

4.3.4.2. Alpha Emission

The aspect of the luminescent characterisation presented some difficulties, as the observed radioluminescent emission was very weak in intensity. This was due to either weak activity from the alpha source or poor RL efficiency of the phosphor. To put this into context; neither the spectrometer nor a commercially available digital single lens reflex camera was able to detect an emission other than background noise. The emission was observed only in a darkroom, with the alpha source positioned as close to the phosphor as possible and for the emission from the phosphor to be moving within the peripheral vision of dark-adapted human eyes. The reason for this elaborate description was the extent needed for the emission to be observed, the human vision system has a higher sensitivity to brightness contrast in the peripheral vision than the

centre of the field-of-view (fovea), while also being more sensitive to movement than stationary items, only then being possible to view the emission.

Of the phosphors discussed within this chapter, the ISIS scintillator and the ZnS:Ag,Cl powder tested positive to creating a visible emission via alpha excitation.

Continuous emission of radiation by the alpha source does not permit the decay time to be observed using a photomultiplier tube. However, the PMT was used in an attempt to determine if there was sufficient RL emission to create a signal. With a suitable range of voltages, relative intensity measurements could be taken between samples using alpha excitation.

The result of this was that there was no alteration to the voltage displayed on the oscilloscope, meaning, the detection system was not sensitive enough to register the emission for it to create a voltage change.

4.3.5 Uniformity and Repeatability of the ISIS Scintillator

The Nd:YAG laser excitation source with its stable (± 0.05W) irradiance intensity was chosen as the most reliable for quantative measurements. The varying output intensity of the N_2 laser made it unsuitable and the HeCd laser caused blackening of the phosphor.

In conjunction with the Nd:YAG laser, the spectrometer used 150msec integration period and 50 averaged spectra to create one emission spectrum (one data point on Figure 4.29), this did not eradicate emission intensity fluctuations, but did considerably reduce them. The source of remaining fluctuations was thought to be variations in the period between pulses. Consecutive peak emission intensities were collected for six periods over 100 minutes. Though there was a spread of peak emission intensities in Figure 4.29, there was a distinct trend for the average value to reduce over time.

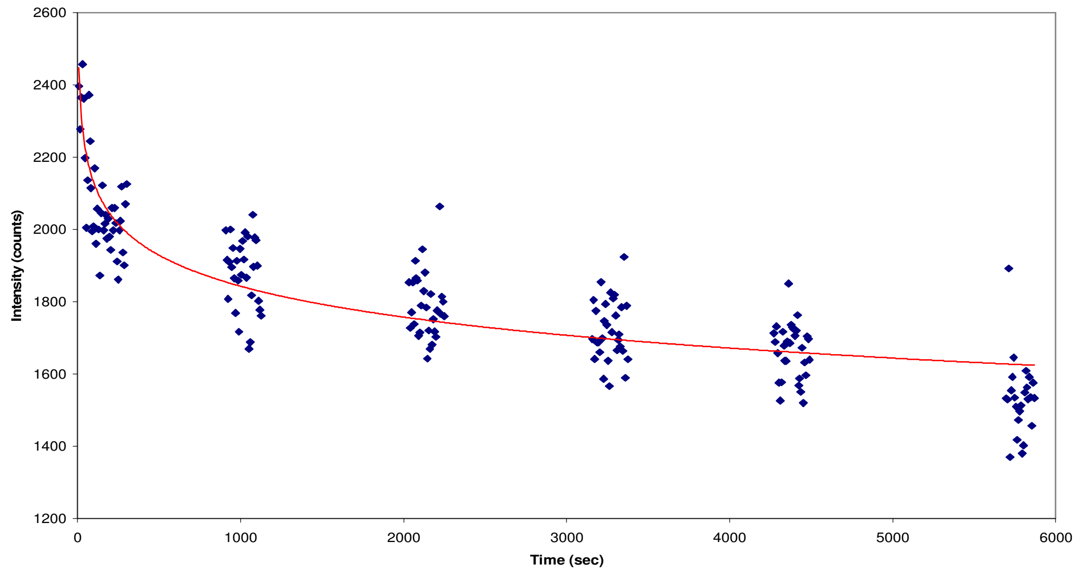

Figure 4.29: Peak intensity measurements against time for the ISIS phosphor using a Nd:YAG laser at 266nm excitation.

Over the 100 minute period of excitation that was examined, the peak intensity (measured at 450.13nm) initially reduced rapidly and did not stabilise within the remaining test period. Within the first minute the intensity reduced by approximately 20% and continued to reduce for the remainder of the period. This trend was reproducible and could be approximated mathematically using a power function (red line - Figure 4.29).

Directly following this period of excitation, the laser was intercepted prior to reaching the sample, initiating a period of 15 minutes where the laser was blocked. It was then reapplied for a period of ~8 minutes and measured for peak intensity values. A further ~8 minutes of measurements were taken after a 20 minutes 'cool down' period to complete this portion of the test. The results of these cool down periods can be seen in Figure 4.30, which consists of the last two measurement periods from Figure 4.29 (blue marks with red line) and the 15 and 20 minute cool down periods (pink and yellow marks) with the accompanying emission intensities post cool down. The purpose of this was to test the affect of prolonged irradiance and the potential for the sample to regain the emission intensity following a break in exposure.

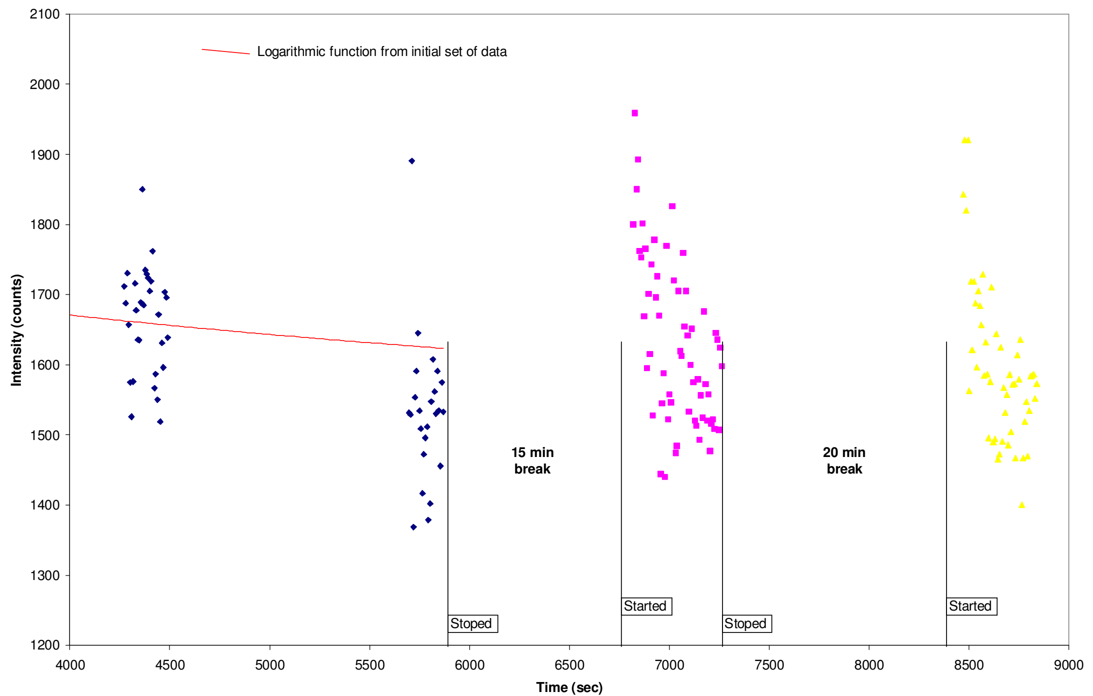

Figure 4.30: Peak intensity measurements against time with 15 and 20 minute break in excitation for the ISIS phosphor using a Nd:YAG laser at 266nm excitation, a continuation of Figure 4.29.

It was observed that the intensity of the emission after the cool down periods (Figure 4.30) did not return to the maximum seen at the beginning of the experiment (Figure 4.29). The emission intensity reduced more rapidly in the retest than in the original exposure. In addition to a 15 and then a 20 minute break in excitation, a 16 hour break was also tested which still showed that the initial intensity observed at the start had not returned.

For the uniformity measurements, a similar test was repeated at the 8 locations across the ISIS wafer in the arrangement shown in Figure 4.5. Instead of absolute intensity values, a comparison of the initial intensity and the rate of intensity decay were examined. Spectrometer variables used for this test were an integration period of 150ms and 50 averaged spectra. Fifty peak intensity values were recorded immediately following the introduction of laser excitation, equivalent to period of 375 seconds. With continued exposure, a period of 1200 seconds was allowed to pass before a further 30 peak intensity values were taken, equivalent to 225 seconds. Using the collected data, a power function ($y = Ax^B$) was fitted to mathematically describe the emission intensity over time, so making it possible to compare samples.

Retesting of the start position showed a reduction in intensity of 111 counts (3.7%) when comparing the *A* values of the power function (Figure 4.31). The intensity reduced more quickly for the retest position compared to the other sample positions. A full list of the intensity and exponent values is presented in Table 4.9.

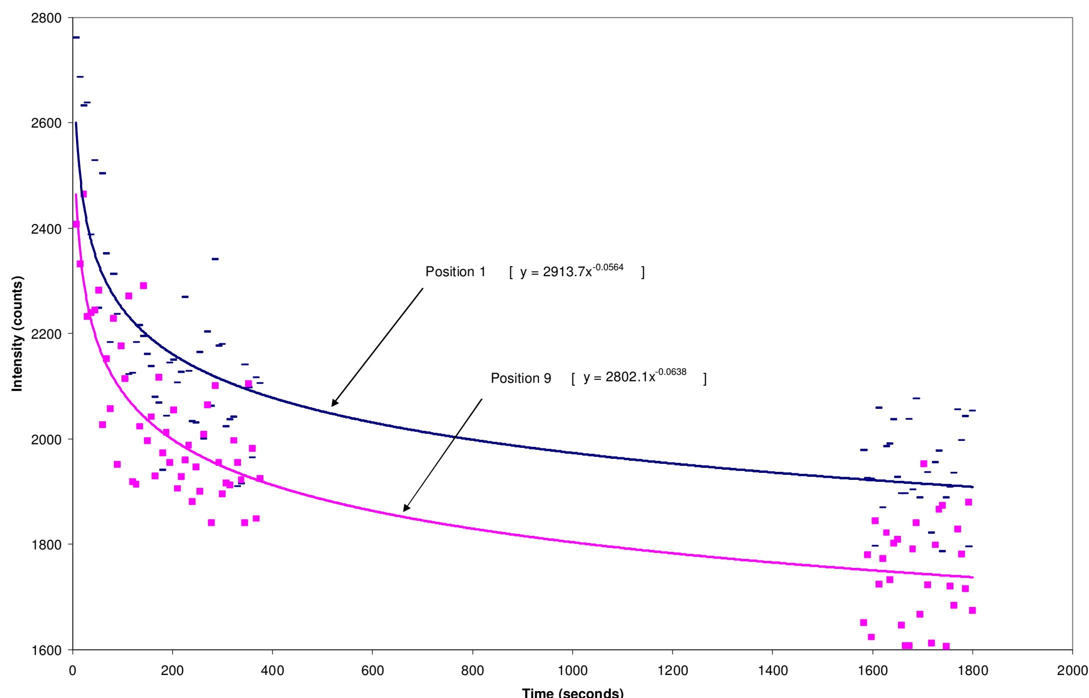

Figure 4.31: Repeat peak intensity measurements of ZnS:Ag,Cl (ISIS) excited by Nd:YAG (255nm).

Table 4.9: Extrapolated data of peak intensity measurements for the ZnS:Ag,Cl (ISIS) phosphor.

Position	A (Initial intensity)	B (Exponent)
1	2913.7	-0.0564
2	2770.4	-0.053
3	2887.5	-0.0603
4	3001.8	-0.0622
5	2474.8	-0.0472
6	2538	-0.0521
7	2710.3	-0.0606
8	2885.2	-0.0625
9	2802.1	-0.0638
Range*:	527 (±9.5%)	0.0166 (±14.3%)

* Position 9 is not included in the range values

Of the eight test locations (not including position 9), the maximum and minimum values from the derived results were at the positions 4 and 5.

A comparison of the extracted data from the eight locations presented no clear trend to the values that make up the derived power function along either axis of the wafer. This means that using this method a difference in the uniformity of emission of ±9.5% was observed.

4.3.5.1. Repeatability

The repeatability tests demonstrated that repeated testing of a phosphor degraded the efficiency both temporarily and permanently (Figure 4.31).

4.4 Conclusion

The work presented in this chapter details the observations of a group of phosphors used in this work and the characteristics of each. The most significant finding is the difference in emission intensity between PL and RL. RL as measured with available sources was so weak that it made emission spectrum measurements impossible using the detection method chosen. The possibility of alternative sources was investigated, including via equipment at ISIS, but was not successful.

4.4.1 Excitation Sources

It was found that the best excitation source for the uniformity tests was the Nd:YAG laser, due to its stability over long periods of time and its small fluctuations. Comparing this to the operating manual that accompanies the laser and the stability closely matched the measured stability. For the 355nm emission the stability is ±4%, with 532nm and 266nm having a stability of ±3.5% and ±7% respectively. This makes the measure ±4.5% error a close match. It would appear 532nm would be the best excitation wavelength due to its small error. However, the emission efficiency related to this wavelength means that it would not create an emission.

Although used predominantly within this work, the N_2 laser was the least effective for creating a stable excitation source and measuring relative emission intensities between samples. However, it was used extensively due to its monochromatic emission, ease of use, reliability and quick start up time. The HeCd laser, though generally stable, also produced fluctuations that would distort the peak emission intensity between measurements. Any of the lasers could

be used when comparing intensity measurements if there is additional processing on the emission spectrum to produce a normalised intensity by factoring excitation power along with emission intensity.

4.4.2 Emission Spectra

The emission spectra from the phosphors investigated were observed to be different to the expected emission spectra. For the S2000 spectrometer, this was evident as a preferential enhancement around the 485nm wavelength (Figure 4.12, Figure 4.16). Whereas, the S4000 spectrometer appeared to preferentially enhance the detected emission around 400nm (Figure 4.12) and 450nm (Figure 4.15, Figure 4.17, Figure 4.18).

The comparison of the emission spectra of the two spectrometers, as well the result from the Phosphor Technology characterisation of the returned sample, indicated a spectrometer calibration issue. Although this is important to the characterisation of a phosphor and comparison between phosphor, the importance of it to the project is much less, as the exact emission spectrum is not a factor that is significant in this work. There was not an additional dopant or form of the phosphor identified that would be expected to generate the observed anomalous emissions, and an additional light source causing noise was ruled out using experimental rigour. However, although there were differences between the measured emission spectra and the reported emission spectra in the literature, they were repeatable and changes to the peak position and shape between samples were determinable.

There is a minor change observed in the emission peak of the two ZnS:Ag,Cl samples other than their difference to the literature and difference between the spectrometers utilised here. These changes are less than 2nm and should therefore be not thought of as significant within these experiments with the possible errors and variation.

The reported emission spectrum of the ZnS:Cl, peak intensity at 461nm and FWHM of 51nm (Figure 4.2 [104]), was distinctly different to the detected emission spectrum, peak intensity at 480-488nm and FWHM of 79-88nm (dependent on which spectrometer was used). Potentially this was due to considerable enhancement of 485nm by both spectrometers, which is not understood.

A quality of the ZnS:Cl emission was that it very closely represented the ZnS emission spectrum (Figure 4.19, Figure 4.20). This would suggest that while there is Cl within the sample, it is either not incorporated into the ZnS lattice or the energy level associated with Cl does not occupy a position within the bandgap to create a luminescent decay route. The Cl would also suffer from the same problem to which the silver does, i.e. it would require a charge compensator for it to be incorporated into the lattice. Hence, the chlorine is likely to occupy interstitial locations within the ZnS lattice of the material examined.

4.4.2.1. Decay Time

Reports on the literature state that the decay time of ZnS:Ag,Cl is ~ 200ns for the fast component and ~30μs for the dominant afterglow. The fast component can be measured when there is a high cut-off level and in doing so the emission will reduce by such an extent that the alpha excitation will not be detectable over the gamma radiation (noise). At ISIS, the dominant afterglow is used when detecting the alpha excitations.

With the results presented here, for increasing excitation wavelength the ZnS:Ag,Cl powder appeared to demonstrate a transition from the afterglow component to the fast component, as it went from 866ns to 248ns. This was not present in the ISIS ZnS:Ag,Cl wafer sample which exhibited a steady decay rate of between 1.4μs and 2.0μs. The intensity of the emission reduced as the wavelength increased and along with this, there was an increase in the fluctuation of the curve.

Comparing the decay curve for the weakest emission (Powder - 510nm) that exhibited the most fluctuation against the control decay curve presented some similarities. Fluctuations are present in both decay curves and have similar decay time 248ns and 135ns respectively. With a further reduction in intensity of emission these decay curves are likely to become more similar. Indeed, retesting of the ZnS:Ag,Cl powder with improved emission collection confirmed this, the decay curves were now representing a decay time relating to the afterglow.

4.4.2.2. Uniformity

The observed reduction of emission intensity was significant; however, with a laser with a smaller intensity emission it was likely to be less dramatic. The difference in emission intensity observed between RL and PL would potentially make this characteristic insignificant, but would need to be tested to confirm this. Initially, a test using a laser with reduced fluence would give an indication if this was accurate, if RL emission detection remained elusive.

Using the results obtained for the ISIS wafer, it would mean that there was a range of emission intensities that the thin films would be required to accommodate.

5 Deposition and Characterisation of Thin Films

5.1 Introduction

Using the information gathered from the characterisation of the bulk phosphors, the potential use of thin film phosphors was investigated by examining the feasibility of growing thin films of ZnS:Ag,Cl phosphor by the technique of RF Magnetron Sputtering for use as a scintillator.
The ultimate objective is to fabricate the scintillator phosphor as a thin film onto a substrate that can then be used to form an array of detecting elements. These would have the potential to increase the spatial resolution of scattered neutrons following their interaction with a target material, so improving detection capabilities of the neutron diffraction analysis system.

5.2 Method

The research was concerned with studying the parameters required to produce films with the potential for future integration with a detector substrate. The characteristics of interest are the adhesion, uniformity of thickness, surface characteristics and growth rate, in combination with the luminescent properties, which are linked to the internal lattice structure and dopant incorporation. The ZnS:Ag,Cl powder from Phosphor Technology was used as the primary source material for this study - using RF Magnetron Sputtering to grow thin films onto Si substrates for characterisation.

5.2.1 Calibration

During this programme of research, a period was set aside for the laboratory to be moved between campuses located several miles apart, due to the relocation of the department. This required the decommissioning and recommissioning of all experimental systems used in this work. During this process the opportunity to recondition the sputtering system was taken by the author. Moving the sputtering chamber involved decommissioning, removal of sensitive parts and transportation before reconditioning. All electrical components were disconnected from the

chamber, the water for cooling was isolated for removal and fragile elements, such as the loading arm and substrate heater were removed and packaged separately for transportation.

Reconditioning involved the removal of previously sputtered material from all surfaces within the sputter chamber, maintenance of the electrodes, replacement of water conduits used for cooling, and calibration of the sensors and monitoring systems.

Following the maintenance, the sources of possible contaminants within the chamber were water leakage from an electrode, particulates left from the cleaning process and absorbed particles from the air, that later outgas. All these factors can cause non-uniformity of the thin film structure or become luminescent killers within a phosphor film. To determine the effectiveness of the system following the move and maintenance, films of the phosphor ZnS:Mn, which is used by the group for display research was deposited in the system to act as a benchmark to ensure that luminescent films could be produced, i.e. to indicate whether there are any serious contamination issues.

5.2.1.1. Pressure Sensors

The pressure sensor for absolute pressure within the sputtering chamber was calibrated along with other pressure sensors of the same type. Four Baratron sensors were used to monitor a vacuum created by the pumping system of the sputtering chamber. This generated four simultaneous measurements of a single vacuum pressure. The most recently calibrated sensor was used as the control and the other sensors where calibrated to this measurement. The most significant pressure sensor for deposition was the Baratron, which measures partial pressure of the processing gas during deposition. This sensor was recalibrated to zero reading when the pressure of the chamber was at the best base pressure ($\times 10^{-7}$ mbar). The range of the Baratron was 1Torr, making it unsuitable to measure the complete pressure range – hence this technique of zeroing.

5.2.1.2. Temperature

An accurate temperature measurement was important for deposition and annealing. The deposition temperature affects the growth rate and uniformity of the thin film. Annealing temperature affects the crystallinity of the thin film, which in turn affects the emission intensity. The experimental method used for the temperature calibration is presented in Chapter 3 and

describes the calibration of the heater for deposition and annealing temperatures. The calibration was of ambient deposition temperatures produced at 80W and 100W sputtering electrode power, along with annealing temperatures from 350℃ to 600℃, with and without a shutter. In addition to the exposed surface of the substrate, the temperature difference across the wafer during these processes was also evaluated.

5.2.1.3. Thickness

Control of final growth thickness uses a trace monitor and provides data to determine thickness in real-time. The monitoring of thickness allows the deposition period to be adjusted to compensate for changes of sputter and growth rates. The trace monitor uses reflected monochromatic laser light from the depositing film surface, providing an optical indication of thickness via the change in reflected intensity due to interference. As a film grows in thickness an intensity profile oscillating between maximum and minimum values is produced and from this an evaluation of film thickness was determined from calibration data.

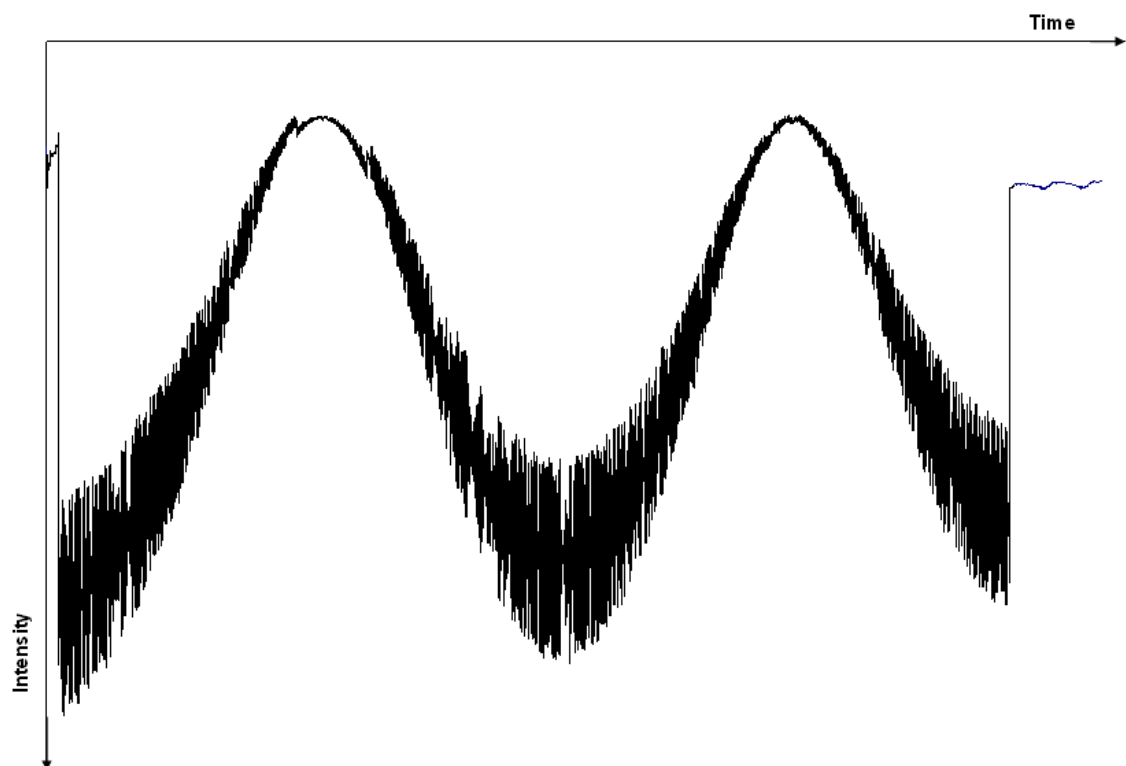

Figure 5.1: Example of an interference pattern from an interferometer and the inherent inaccuracies from reading a wave pattern.

The accuracy of growing a predetermined thickness of thin film depended upon the precision of information that the trace monitor can provide. The deposition duration is controlled by the use

of a shutter and provides an accurately controlled period of deposition. However, determining when the target thickness has been reached is not as accurate. The overall intensity of the reflected laser light reduces as the deposited material grows thicker and the rate of growth generally increases as the target ages, creating uncertainty in reading the measurement (Figure 5.1).

The calibration is created using Bragg diffraction ($m\lambda=2nd$), along with reflectance spectrometry (Section 3.4.1) measurements to confirm the accuracy. The response from the trace monitor means that 5.5 cycles is the equivalent to an 800nm film of ZnS; and 600nm ≡ $4^{1}/_{8}$ cycles, 400nm ≡ $2^{3}/_{4}$ cycles and 200nm ≡ $1^{3}/_{8}$ cycles. The number of cycles versus thicknesses is determined by the relationship between the difference in optical path length of the light reflected from the substrate and that reflected from the surface of the growing film – where interference maxima are produced at $m\lambda=2nd$.

5.2.1.4. Contaminants

To verify the effectiveness of the re-commissioned system, a ZnS based phosphor known to luminesce as a thin film when grown by RF Magnetron Sputtering, was tested. The phosphor was ZnS:Mn and exhibits a broad luminescent emission spectrum peaking at 583nm. This emission spectrum is significantly different to ZnS:Ag,Cl (450nm), making it easy to define when observed in successive PL measurements. The ZnS:Mn phosphor was grown to a thickness of 200nm and was then tested for its emission spectrum. This was done using the experimental setup described in Chapter 3 using the N_2 (337nm) laser as the source of excitation.

5.2.2 Growth

Twenty five thin films were grown from a ZnS:Ag,Cl pressed powder target by the technique of RF Magnetron sputtering (Table 5.1-Table 5.5). This technique was chosen for its ability to grow high purity and uniform thin films of semiconductor materials. It has numerous variables that can be fine-tuned to optimise the process. The main variables considered in this work were a range of thin film thicknesses, deposition temperatures, annealing temperatures, electrode power and partial pressure.

Table 5.1: Applied power to the heater, the corresponding deposition temperatures and number of times it was

carried out.

Power	6.5%	7.8%	8.4%	8.8%	9.2%	9.5%	9.7%
Temperature	100℃	140℃	160℃	180℃	190℃	195℃	200℃
Number	2	5	1	1	14	1	1

Table 5.2: Applied power to the heater, the corresponding annealing temperatures and number of times it was carried out.

Power	9.50%	27.20%	30%
Temperature	200℃	500℃	560℃
Number	1	19	5

Table 5.3: Applied power to the electrode and number of times it was carried out.

Wattage	70	80	100
Number	1	20	4

Table 5.4 The partial pressure of processing gas and the number of times it was carried out.

Pressure	3mTorr	4mTorr	5mTorr
Number	14	1	10

The distributions of the variables applied to the growth of thin films (Table 5.1-Table 5.4) were due to specific tests to determine optimum growth conditions, the difference in actual applied temperature for pre-calibration and post-calibration, or mistakes. An example of a mistakes was not changing the applied power to the heater when ‘annealing’ the thin film once it had been grown, i.e. in Table 5.2 there is an annealing temperature of 200℃.

Table 5.5: The range of values applied to thin film growth.

Range of deposition temperatures	100℃
Range of annealing temperatures	360℃
Range of electrode powers	30 W
Range of partial pressures	2 mTorr

5.2.3 Thin Film Characterisation

Uniformity and quality of the thin film following deposition were characterised for thickness, surface roughness, adhesion, X-ray diffraction and one sample was tested by Ion Beam Analysis. This work is directed at thin films for scintillators - hence, the luminescence testing is the most important element of film characterisation.

The thicknesses of the thin films were measured using metrology equipment discussed in Chapter 3 (reflectance spectroscopy, stylus profiler, optical profiling system) following their deposition to test the thickness uniformity over the area of the specimen and to determine accuracy of the trace monitor. Along with thickness measurements, the optical profiling system also characterises surface roughness over the measured region.

Adhesion was examined using the simple adhesive tape test. The applying and removal of the adhesive tape to the thin film surface gives an indication of how well the thin film is adhered to the substrate. Poor adhesion of the thin film to the substrate would be shown by the removal of the thin film by the tape.

The XRD technique was used to verify chemical composition and crystal structure of the thin films grown from a ZnS:Ag,Cl pressed powder target using RF Magnetron Sputtering. The technique used a beam of X-rays reflected from the target sample. At critical angles that conform to Bragg diffraction the reflected X-rays form constructive interference. The X-ray detector and sample move through a range of angles (2θ and θ respectively), with the source, being fixed (Section 3.5.1). XRD was used to compare the thin films to the target material and also to evaluate the effect of annealing. A crystalline Si chip was used as a control sample to ensure that each test could be compared for intensity and angular response. Angular per step and time per step define the angular resolution, where the step size ranged from 0.0021° to 0.0167° and the time per step ranged from 59.69 to 250.19 seconds. The start 2θ angle of either 20° or 25° and end angle of 65° or 90°. The start angle was increased from 20° to 25° to reduce the range of angles scanned so an increased resolution could be attained when maintaining scan duration. The increase of end angle from 65° to 90° was to increase the number of detected peaks of the samples in an attempt to increase the accuracy of results.

Ion Beam Analysis (IBA) uses beams of low mass particles accelerated towards a target material and their interaction with the target can determine the target's chemical composition.

This work was carried out at the Ion Beam Centre[4] (IBC) located at Surrey University under the Supervision of Dr. Chris Jeynes[5] and Dr. Melanie Bailey[6].

A sample of thin film grown onto a Si substrate from a pressed powder target of ZnS:Ag,Cl was taken to the IBC for analysis to determine the composition. This was to verify if the film had become contaminated or if the thin film had been altered in some way so that it would not function as a phosphor material and produce visible emission.

5.3 Results

Once calibrated and tested using the ZnS:Mn phosphor, thin films were grown from the ZnS:Ag,Cl powder target. To test their effectiveness to function as a thin film phosphor they were characterised by their luminescence, uniformity, thickness, adhesion, crystal structure and composition.

5.3.1 Calibration

5.3.1.1. Calibration of Trace Monitor

The thicknesses of the samples were measured using reflectance spectroscopy to confirm the thickness post deposition, and compared with the predicted thickness obtained during growth, which had been monitored via the interference thickness monitor.

Testing of this was done using three ZnS thin films grown to 400nm from a ZnS solid target[7] (These films were subsequently used for ion implantation studies). 400nm was the equivalent of 2.75 oscillations on the trace monitor, with the finish position half way along the descent of a cycle. The laser for the trace monitor was incident at the approximate centre of the substrate with thickness measurements taken at this location.

The stylus profiler was not suitable for this task as it would only be able to measure the step change at the edge of the wafer, not the centre where the trace monitor was measuring. The

---

[4] Surrey Ion Beam Centre, Nodus Laboratory, University of Surrey, Guildford, Surrey, GU2 7XH
[5] c.jeynes@surrey.ac.uk
[6] m.bailey@surrey.ac.uk
[7] Purchased from Testbourne.

results of this test are presented in Table 5.6 and show that reflectance spectroscopy has a low level of error and was chosen for this suitability to the task along with its ease of use.

Table 5.6: Thin film thickness measurements using reflectance spectroscopy and the error observed for each growth.

	Desired (nm)	Thickness (nm)	Error (nm)	%Error
Sample 1	400	415.67	15.67	3.9
Sample 2	400	406.33	6.33	1.6
Sample 3	400	421.24	21.24	5.3

5.3.1.2. Heater Calibration

Calibration of the substrate heater using a Si substrate was completed and the results demonstrated a small variation in temperature over the surface of the substrate. The temperature difference over the surface of the 100 mm Si substrate at the prebake/annealing temperature (500°C) was 14°C (Figure 5.2) and a temperature difference at the deposition temperature (190°C) was 5°C (Figure 5.3). Below 7.5% power, the ambient chamber temperature has the most significant factor affecting the substrate temperature, shown by a 0°C difference between centre and edge. A 45% power setting was the upper limit to this test and was the equivalent to 622°C at the central location of the Si substrate.

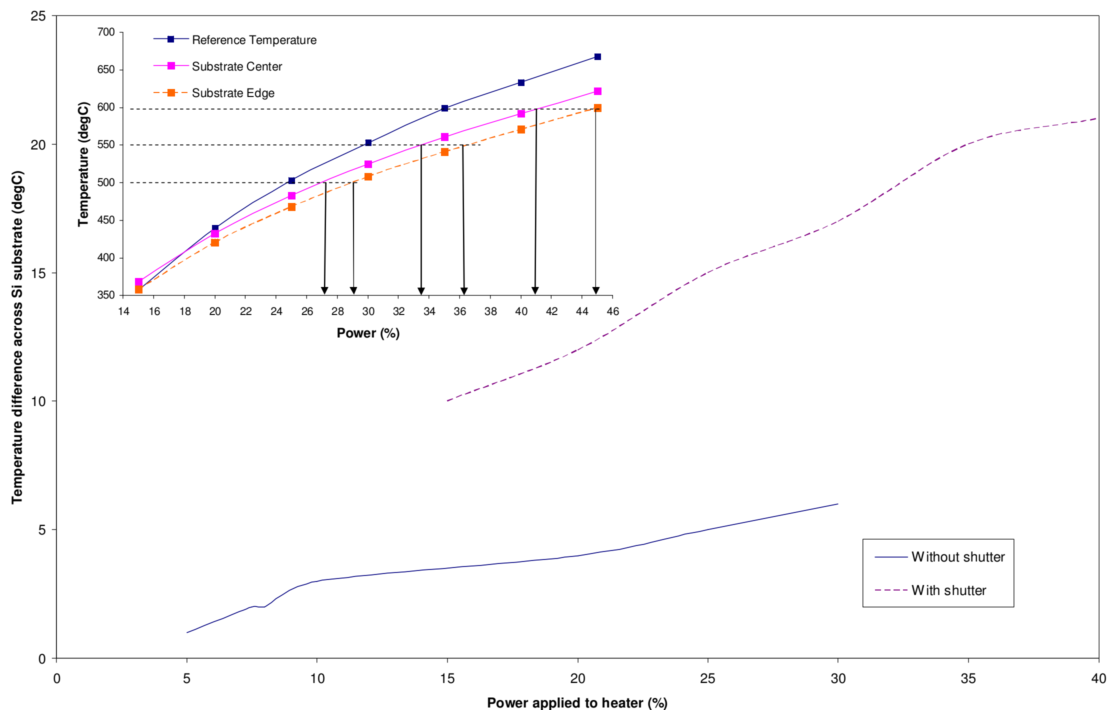

Figure 5.2: Power requirements to achieve annealing temperatures of 500, 550 and 600°C at the centre and edge of a Si wafer when using the shutter. Insert - Temperature difference across the Si substrate with and without the shutter.

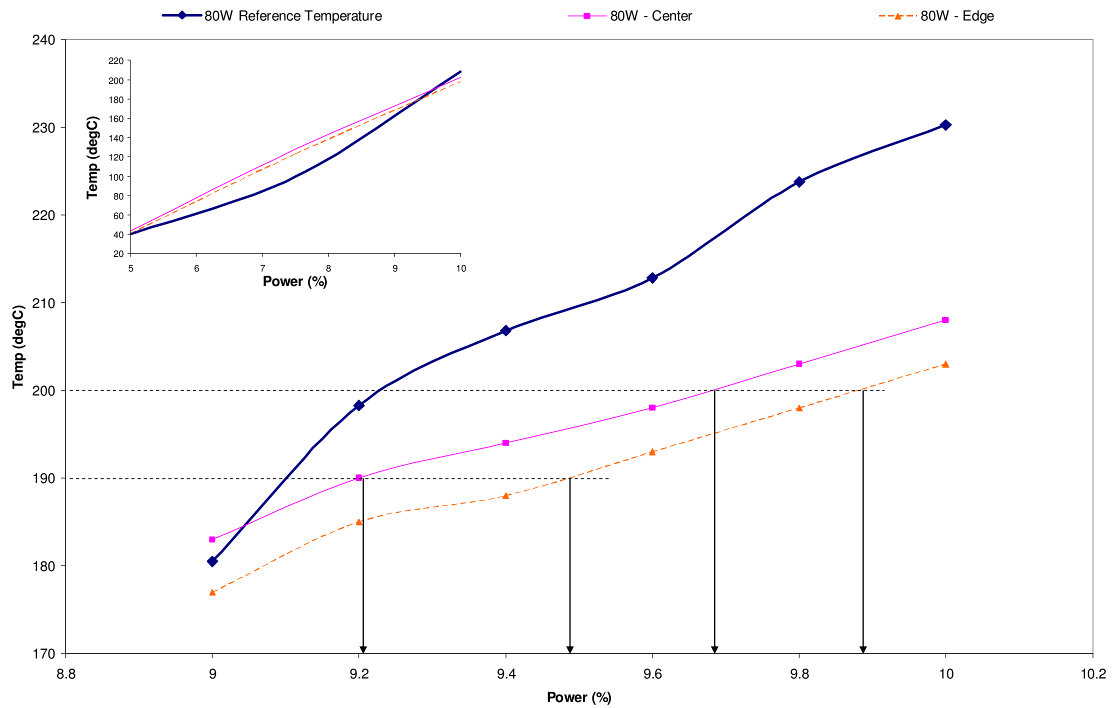

Figure 5.3: Power requirements to achieve a deposition temperature of 190℃ and 200℃ at the centre and edge of a Si wafer at 80W electrode potential. Insert - Original test done for a larger power range.

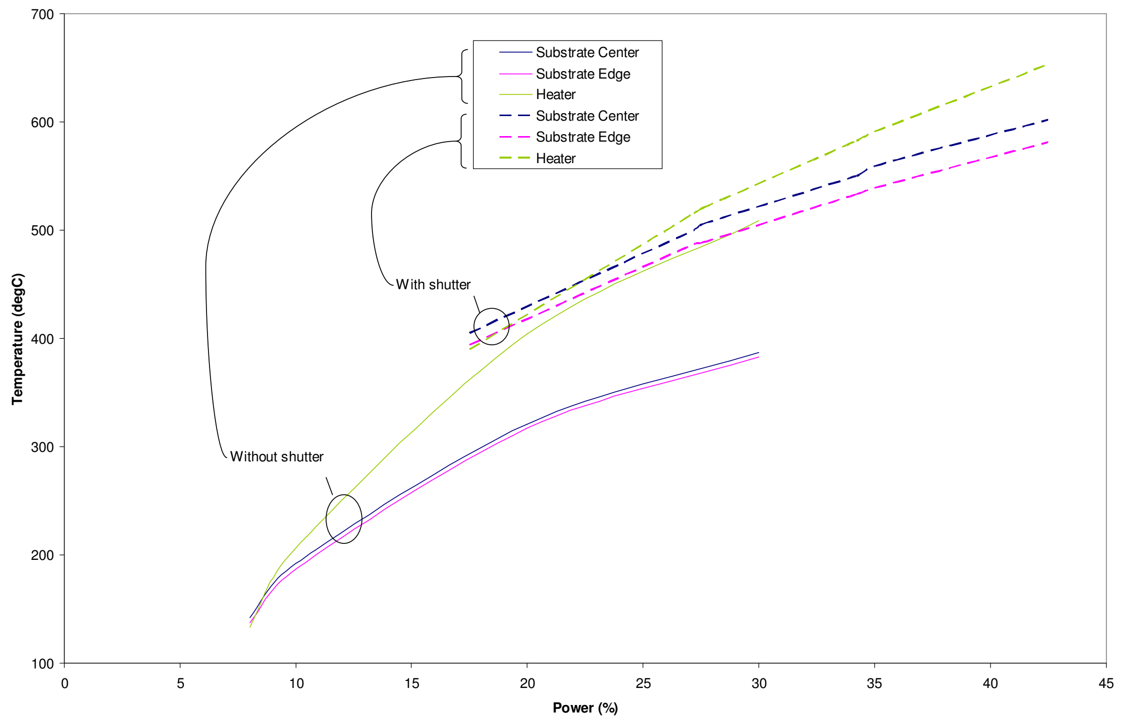

Figure 5.4: Calibration of the heater efficiency over a range of powers with and without a shutter and the temperature difference between across the Si substrate, along with the measurement of the thermocouple linked to the heater.

A comparison of substrate temperatures with and without the shutter and at the 500℃ (27.5%) annealing power gave an annealing temperature of 407℃ without the shutter, nearly 100℃ less than with the shutter in use (Figure 5.4). This makes it an effective tool in increasing the annealing temperatures without increasing the overall chamber temperature.

100W as well as 80W electrode power was used for some depositions, the main trend was that the substrate temperatures were lower for the 100W than the 80W electrode power (Figure 5.5). However, within a vacuum there would be limited heat transfer between electrode and substrate. When combined with the observed temperature differences between the reference thermocouple, it can be assumed that it was a difference in the applied power or measurement, rather than an effect of the increased power. This is indicative of the experimental error in the calibration (Figure 5.5 - Insert).

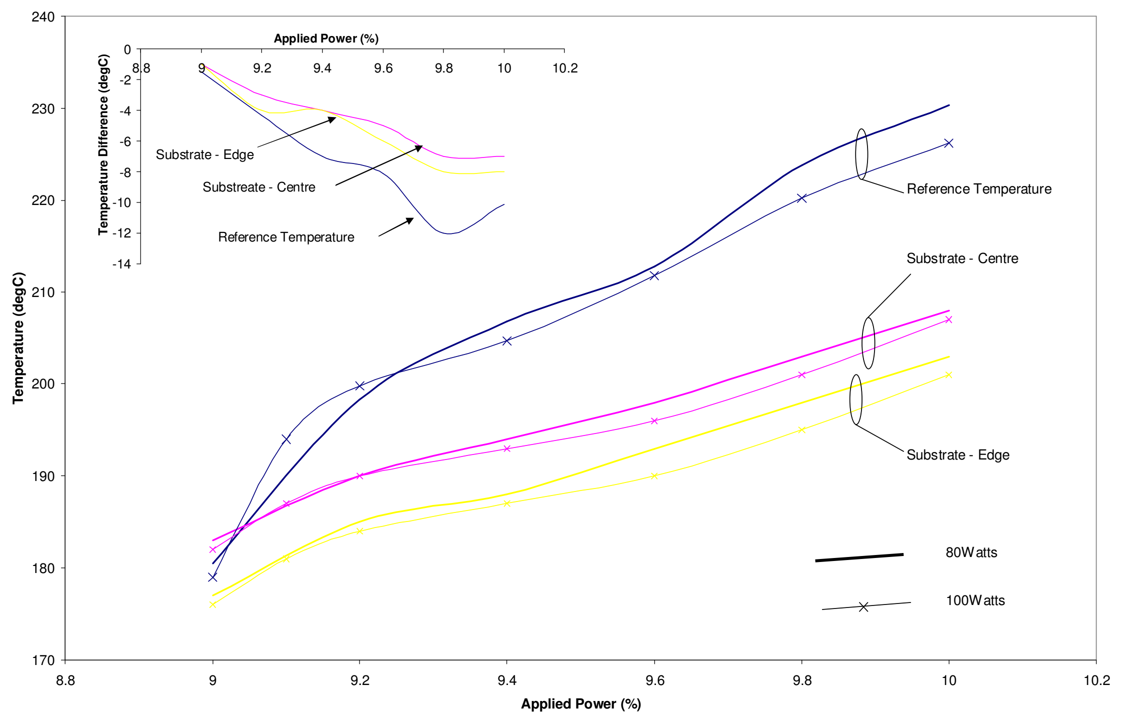

Figure 5.5: Temperature at the centre and edge of a Si substrate as well as reference temperature of heater thermocouple when sputtering at 80W and a 100W electrode potential for a Si wafer. Insert - Temperature difference between the 80W and 100W applied power.

The corresponding power setting for the prebake/annealing and deposition temperature were 27.2% and 9.2% to deliver 500℃ and 190℃ at the substrate respectively. Comparing these to the previously held results, 5.6% for 190℃ and 19.5% for 600℃, makes this a considerable change.

A factor that was incorporated into the deposition procedure was the rate at which the temperature changed during ramp up and cooling. To achieve an accurate period of annealing or deposition the calibration process was used to determine the period for the system to warm up or to cool down to a required temperature. This period was up to 19 minutes to reach the annealing temperature (500℃) and between 5 and 10 minutes to reach deposition temperatures (190℃). To allow for variations, the general procedure was to leave 10 minutes before deposition and to monitor the temperature readings from the reference thermocouple to ensure a more defined period.

5.3.1.3. ZnS:Mn Calibration

A 400nm thin film of ZnS:Mn was grown from a ZnS:Mn solid target within the reconditioned chamber. The thin film was then tested for PL emission using the system described in chapter 3 and using N_2 (337nm) laser excitation source. The emission spectrum created by the thin film compared to the bulk material gave positive results (Figure 5.6).

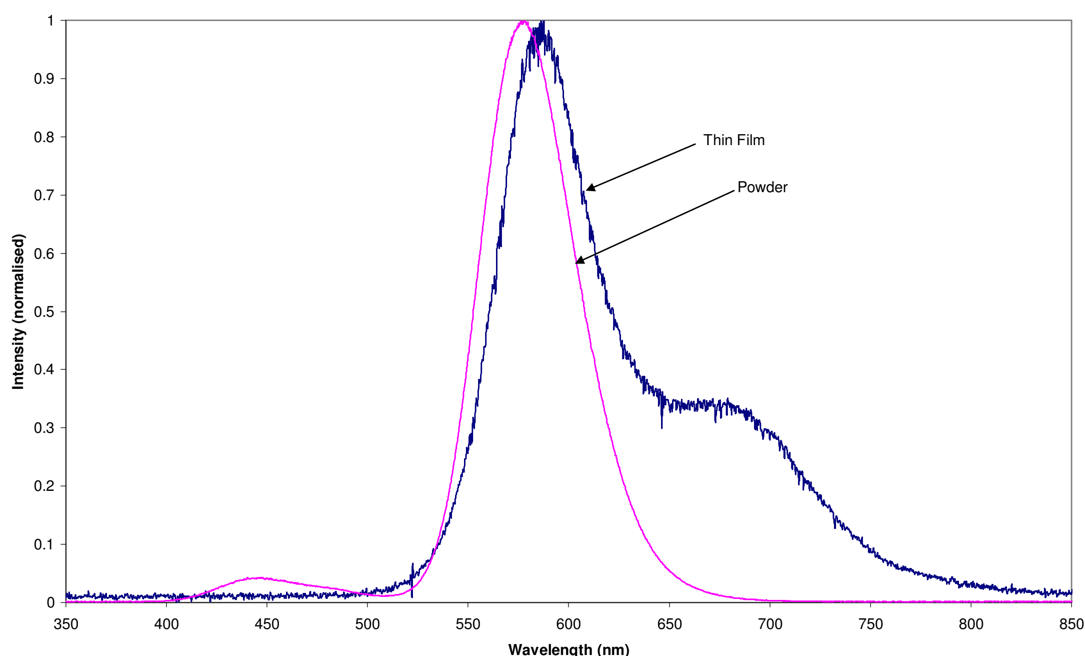

Figure 5.6: Calibration of the system by growth of a ZnS:Mn thin film.

There is an alteration to the shape and position of the emission peak between bulk and thin film form. The shape of the emission peak of the thin film form exhibits a shoulder peak between

the wavelengths of 640 nm and 800 nm. The change in wavelength of the main emission peak was from 579nm for the bulk material to 587nm for the thin film. Reports in the literature for the emission spectrum of the ZnS:Mn phosphor have identified a shift in peak intensity of 6nm, 584nm for the powder and 590nm for the thin film [78, 111, 112]. In thin film form, the development of the shoulder peak has also been commented on in the literature [113] and can be attributed to increased Mn concentrations, which creates additional emission routes.

Though there is this change in emission spectrum, it is evidence that the sputtering chamber is capable of growing thin films of a phosphor that produce a visible emission under laser excitation. Showing that there is minimal contamination and few prominent luminescent killers for the ZnS based phosphor.

5.3.2 Characterisation of ZnS:Ag,Cl Thin Film Phosphors

The most significant aspect of thin film phosphors are that they produce emission when excited. This indicates that the composition of the thin film is the same as the source material used as the target in this technique. The emission characteristics of the thin film, such as emission intensity, emission spectrum and decay time, can change in this process. When using a previously untested (within the research group) phosphor it is likely to produce a weak emission as each phosphor requires different parameters before it is optimised for the growth technique. However, this phosphors did not produce an emission for any of the variations in growth parameters tested in Table 5.1 to Table 5.4.

Without an emission, the emission spectrum, emission intensity and decay time cannot be compared to the source material or be improved upon to make a viable thin film detector using the process of RL.

5.3.2.1. Thickness

Three thin film samples were grown from a ZnS:Ag,Cl target with varying thicknesses and were tested by the three thickness measurement techniques. Each of the samples was tested three times and an average is presented in the result table below.

Table 5.7: A comparison of thickness measurements of thin films grown from a ZnS:Ag,Cl target.

		Sample 1 (nm)	Sample 2 (nm)	Sample 3 (nm)
Reflectance Spectroscopy	Centre	206.21	231.78	324.63
	Difference to edge	3.72	9.84	4.45
Stylus Profiler	Centre	195.5	221.3	338.6
	Difference to edge	1.9	4.05	10.2
Optical Profile System	Centre	198.9	226.4	328.85
	Difference to edge	0.75	8.65	13.75
Average	Centre	200.2	226.5	330.7
	Difference to edge	2.1	7.5	9.5

There is not a definite relationship in the results produced by the three techniques, none of them over or underestimates the thickness compared to the other techniques. There is conformity between centre and difference-to-edge values of Sample 1 and Sample 2, but Sample 3 counters these trends.

A sample was tested for the thickness distribution across the sample at five equidistant points from the centre to edge of the sample instead of just the centre and edge (Figure 5.7). This was an 800nm (using trace monitor) ZnS:Ag,Cl sample grown onto a Si substrate and tested by reflectance spectrometry.

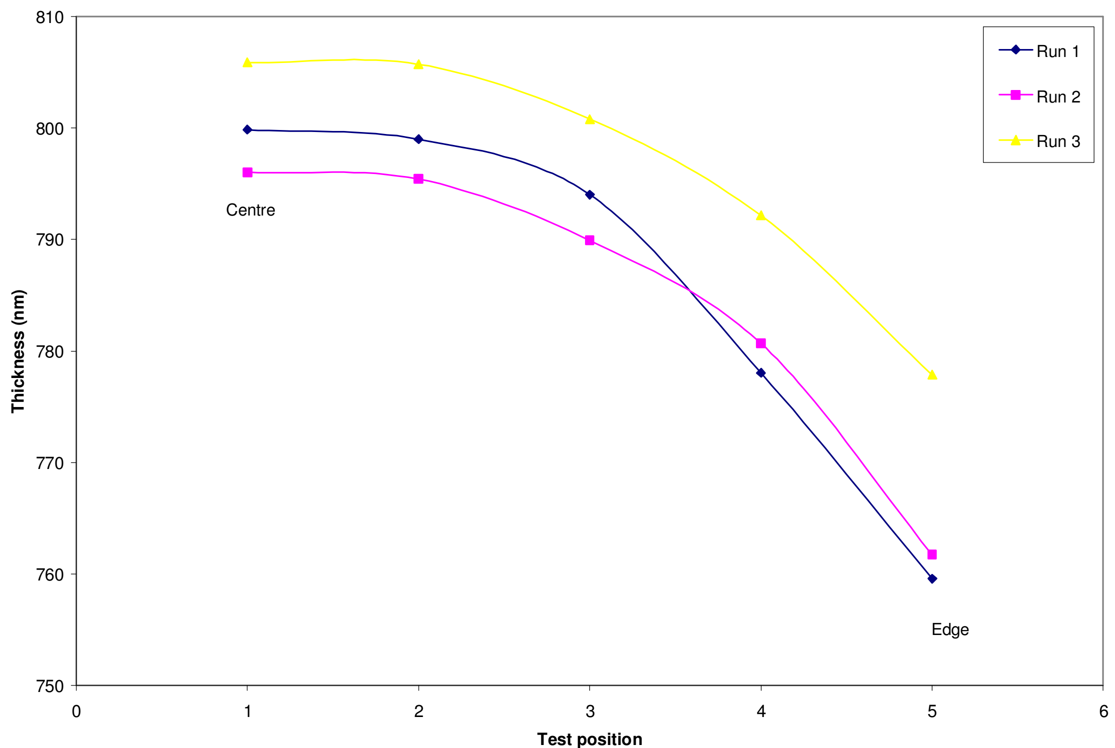

Figure 5.7: A ZnS:Ag,Cl thin film grown to 800nm on a Si substrate and it's thickness measured across three positions from centre to the edge.

The measurements show that the trend of this sample was to reduce in thickness towards the edge, with the centre being domed in appearance. This coincides with the visual appearance of the sample that created a range of colours, indicating a change in thickness. This can be attributed to the geometry of the system (Section 3.2.1 - Figure 3.2), as the electrode is located at an angle of 45° to the substrate.

5.3.2.2. Adhesion

The films of all thicknesses have shown good adhesion to the substrate by passing the adhesive tape test.

5.3.2.3. XRD Analysis

Using XRD, the chemical composition, crystal structure and dimensions of the thin film phosphor was evaluated.

Control - Prior to each characterisation by XRD, an amorphous Si disk was used as a control to determine the accuracy of the measurement with the results presented in (Figure 5.8) and Table 5.8).

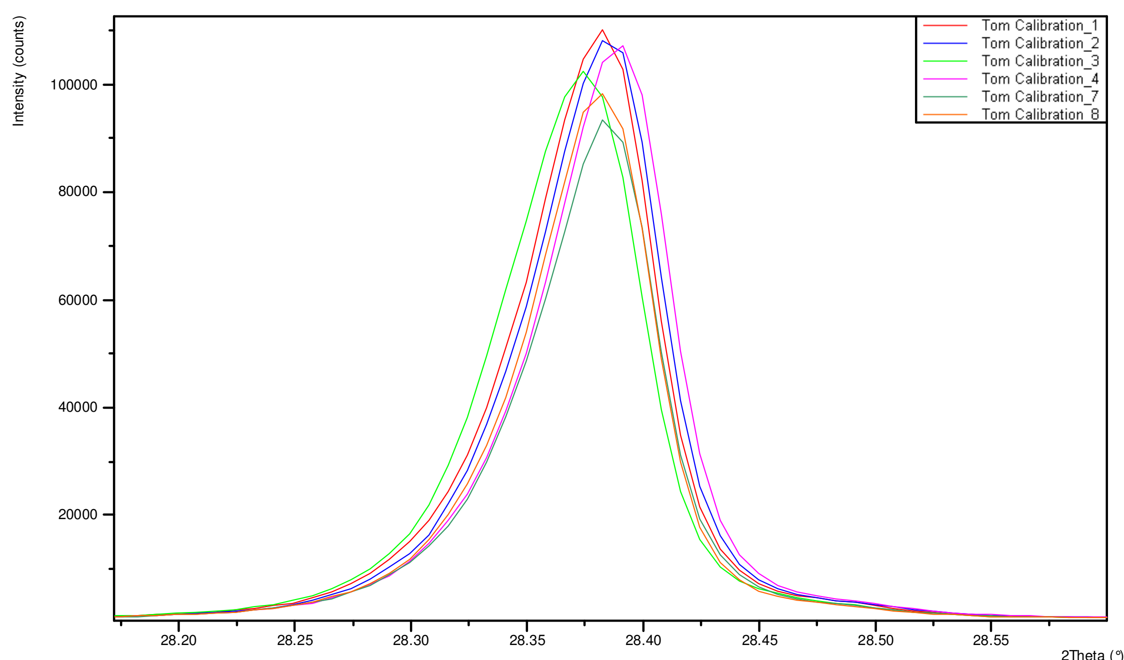

Figure 5.8: XRD peak created by amorphous Si disk and used at a control.

Table 5.8: Position of a XRD peak created by an amorphous Si disk to be used as a control.

`	Average	Range	Range (%)
Peak wavelength(2θ)	28.38°	0.015°	±0.026
FWHM (2θ)	0.0634°	0.0005°	±0.394
Intensity (au)	98534	18966	±9.6%

Over the XRD tests, the maximum spread of peak intensity was between 28.375 and 28.400°. This is a small value and put into context by the percentage ranges, this could be the difference of one data point. However, the intensity, fluctuated much more significantly, which could be attributed to a number of factors, such as the fluence of X-rays, or an alteration in the positioning of the sample.

ZnS:Ag,Cl Powder - The XRD pattern created by the ZnS:Ag,Cl powder over the 2θ range of 20-65° (Figure 5.9) was most closely matched in phase and interspatial value by the face-centred cubic phase of sphalerite, a naturally occurring form of ZnS, with the lattice parameter a = 5.4145Å. The powder diffraction file (PDF) for this XRD pattern was most closely represented by the file 01-077-2100 (PDF1).

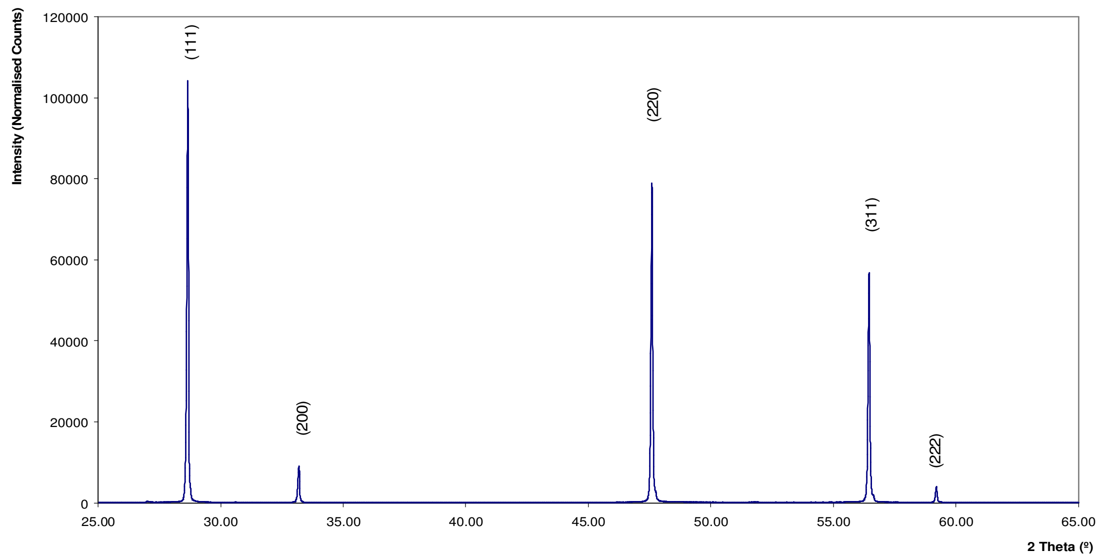

Figure 5.9: XRD pattern of the ZnS:Ag,Cl phosphor powder.

Table 5.9: Positional data and FWHM of XRD peaks exhibited by ZnS:Ag,Cl powder.

No.	Pos. (°2Th.)	FWHM (°2Th.)	h	k	l	Backgr.(cts)	Height (counts)
1	28.6542	0.0693	1	1	1	112.00	107923.90

2	33.1864	0.0744	2	0	0	92.00	9252.77
3	47.5930	0.0744	2	2	0	144.97	80696.55
4	56.4508	0.0764	3	1	1	133.00	57879.81
5	59.1985	0.0746	2	2	2	116.00	3975.29

When the base line was magnified, five additional peaks were observed at 27.02°, 30.62°, 39.79°, 51.98° and 55.68° with that largest of these being at 27° and was ~300 counts above the background and using alternative PDFs was found to be the (101) peak. These were minute on the scale of the ones observed in Figure 5.9, with the (111) peak creating 100,000 counts. These peaks can be linked to hexagonal phase of ZnS, however in the hexagonal phase there can be more than a hundred peaks that span the range of angles examined and won't match completely with the measured XRD pattern.

ZnS:Ag,Cl Powder and ZnS Solid Target - The ZnS:Ag,Cl phosphor is a ZnS lattice with Ag and Cl doped to approximately 0.01at%. This would suggest that the XRD pattern of ZnS:Ag,Cl should be dominated by the ZnS peaks. The results presented in (Figure 5.10) show the XRD spectra for the ZnS:Ag,Cl and ZnS source materials, indicating the expected correlation.

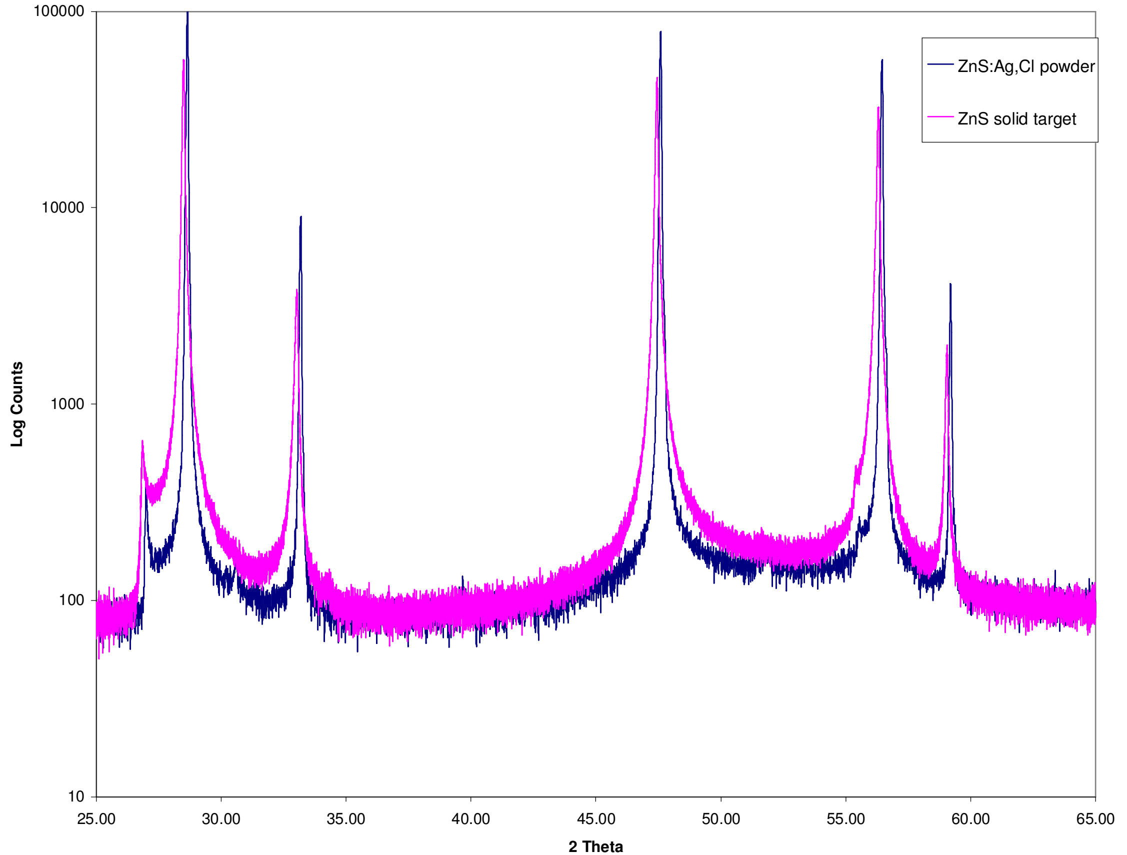

Figure 5.10: XRD pattern of ZnS:Ag,Cl powder and ZnS solid target.

Table 5.10: Positional data and FWHM of XRD peaks exhibited by ZnS and ZnS:Ag,Cl.

	ZnS:Ag,Cl		ZnS		Difference to ZnS:Ag,Cl (bulk)	
No.	Pos. (°2Th.)	FWHM (°2Th.)	Pos. (°2Th.)	FWHM (°2Th.)	Pos. (°2Th.)	FWHM (°2Th.)
1	28.6542	0.0693	28.5008	0.1097	-0.1534	+0.0404
2	33.1864	0.0744	33.0239	0.1637	-0.1625	+0.0893
3	47.5930	0.0744	47.4440	0.1220	-0.149	+0.0476
4	56.4508	0.0764	56.3030	0.1262	-0.1478	+0.0498
5	59.1985	0.0746	59.0485	0.1264	-0.15	+0.0518

Put into the logarithmic scale to highlight potential differences between the ZnS and ZnS:Ag,Cl, it can be seen that these two are very similar. The most significant feature about these is the slight difference in peak position of between 0.14° - 0.16° (2θ). This is less likely to be the effect of the silver dopant, but more the difference of the processing used to manufacture the samples. The degree of the shift suggests it is not experimental error as the error associated with this was much smaller. The ZnS:Ag,Cl phosphor has additional processing during its formation than the ZnS, which would only require purification rather than the chemical incorporation of the silver dopant.

The FWHM of the peaks though small, are different between the two samples. The ZnS has corresponding peak widths of between 58% and 120% larger than the ZnS:Ag,Cl. This means that the ZnS is less ordered than the ZnS:Ag,Cl, this can be attributed to the processing technique. The process to create ZnS:Ag,Cl uses temperatures of 940°C [74] during formation, where as ZnS would be unlikely to have had this during its formation.

Si Substrate - The Si substrate shows five peaks between the 2θ range of 25-90° with the (400) plane dominating the pattern (Figure 5.11). It is usually the first peak that is the largest in intensity, but the (400) peak dominates the others by more than three orders of magnitude (Figure 5.11 - insert).

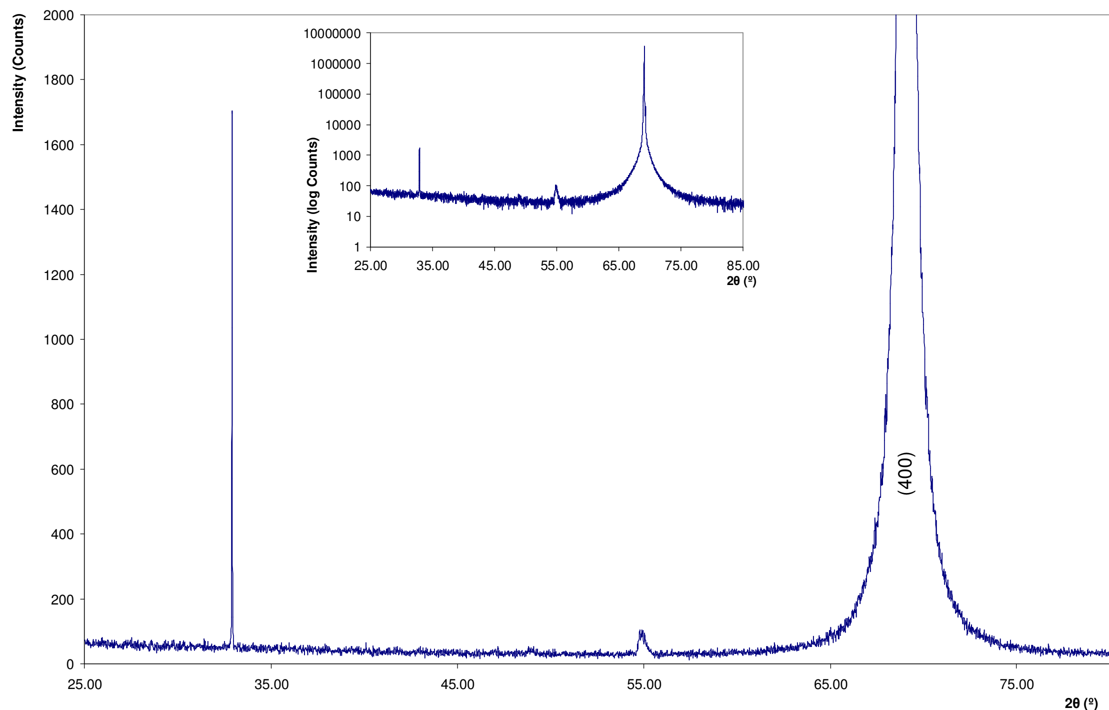

Figure 5.11: XRD pattern of a Si substrate

Examination of this pattern was not as straight forward as the ZnS:Ag,Cl powder. The first peak was observed in some of the patterns and there was no PDF that included both the very larger (400) peak as well as the first peak. The closest pattern to represent the XRD pattern was a Si PDF with a face-centred cubic with a = 5.4309Å. It is worth highlighting the close lattice size match between the Si substrate used and the ZnS thin films – which is expected to reduce stress in the deposited films and enhance the adhesion properties.

ZnS:Ag,Cl Thin Film on a Si Substrate - This XRD pattern (Figure 5.12) demonstrates a polycrystalline material and was best described by a PDF (03-065-1691) with cubic dimensions of a = 5.4109Å. The significant aspect of this XRD pattern in comparison to the bulk material (Figure 5.9) was the effect of the Si background dominating the maximum difference in intensity.

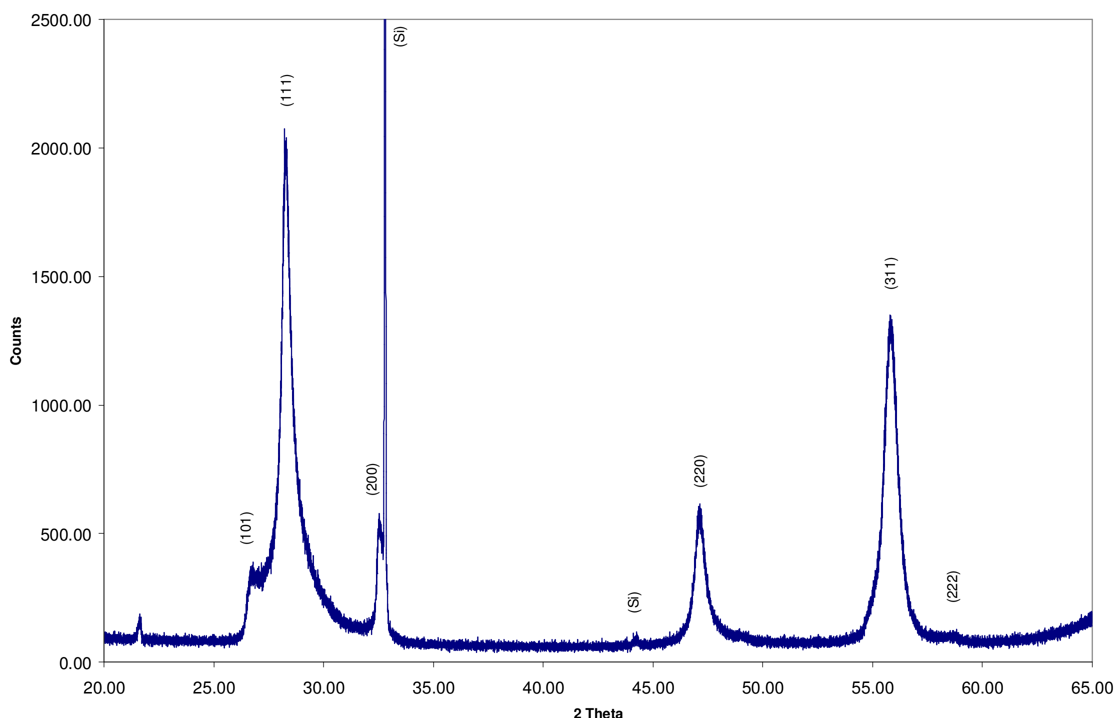

Figure 5.12: XRD pattern of a thin film grown from a ZnS:Ag,Cl pressed powder target onto a Si substrate by RF Magnetron Sputtering

Broadening of the peaks is significant and is indicative of the inherent disorder in the resultant thin films by RF Magnetron Sputtering. There is also a peak shift associated with a smaller lattice size – *a* = 5.4109Å for the thin film compared to *a* = 5.4145 Å for the bulk. This is greater than the difference observed between ZnS:Ag,Cl powder and ZnS.

Table 5.11: Positional data and FWHM of XRD peaks exhibited by ZnS:Ag,Cl powder and thin film grown on a Si substrate from ZnS:Ag,Cl.

	Thin film on Si		ZnS:Ag,Cl powder		Difference to ZnS:Ag,Cl (bulk)	
No.	Pos. (°2Th.)	FWHM (°2Th.)	Pos. (°2Th.)	FWHM (°2Th.)	Pos. (°2Th.)	FWHM (°2Th.)
1	28.3024	0.7371	28.6542	0.0693	-0.3518	0.6678
2	32.5705	0.3625	33.1864	0.0744	-0.6159	0.2881
3	47.1545	0.7705	47.593	0.0744	-0.4385	0.6961
4	55.8378	0.763	56.4508	0.0764	-0.613	0.6866

ZnS:Ag,Cl Powder, Si Substrate and ZnS:Ag,Cl Thin Film on Si Substrate - From the overlapping XRD patterns (Figure 5.13) it is clear to see how the combination of materials (ZnS:Ag,Cl and Si) form the resultant thin film of ZnS:Ag,Cl on a Si wafer. The most significant feature from this is the change in peak intensity of the ZnS:Ag,Cl when formed into a thin film

and the broadening of peaks. Identification of the ZnS peaks at the 2θ angles of approximately 33° and 56° was made difficult by the presence of Si peaks.

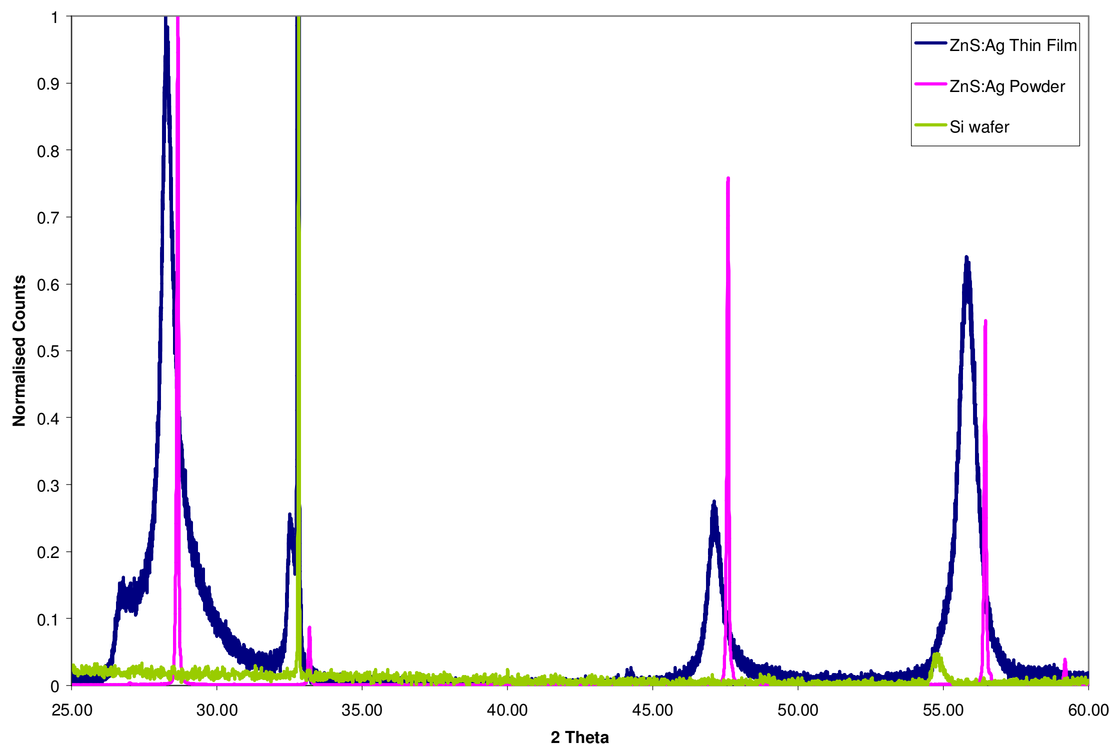

Figure 5.13: The XRD Pattern of ZnS:Ag.Cl in powder, the thin film form grown onto Si wafer and the Si wafer.

5.3.2.4. Ion Beam Analysis

The technique of Rutherford Backscattering (RBS) was used to measure the composition of a thin film sample grown onto a Si substrate from a pressed powder target of ZnS:Ag,Cl.

A beam of alpha particles with energy of 1.562 MeV was used to probe the sample. The resultant emission from this interaction was measured by two detectors generating the spectra shown in Figure 5.14 and Figure 5.15. Each is from a different detector positioned at 172.8° (detector A = z1f0101) and 148.2° (detector B = z1f0102) to the beam line.

The beam is in a near normal direction to the sample to maximise detection efficiency.

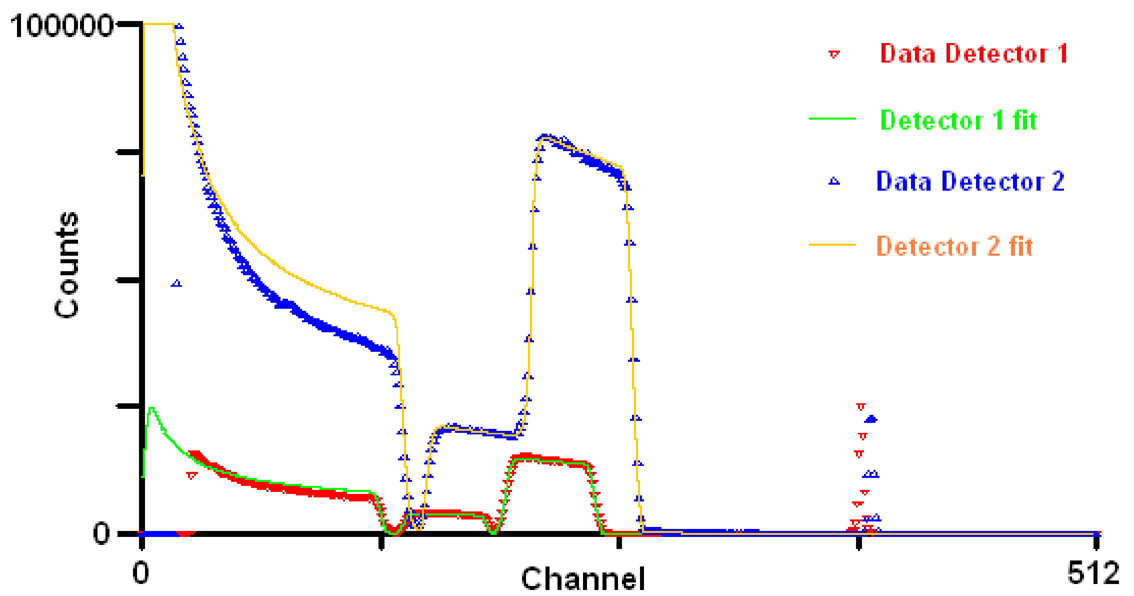

Figure 5.14: RBS spectra generated from two detectors from a ZnS:Ag,Cl thin film.

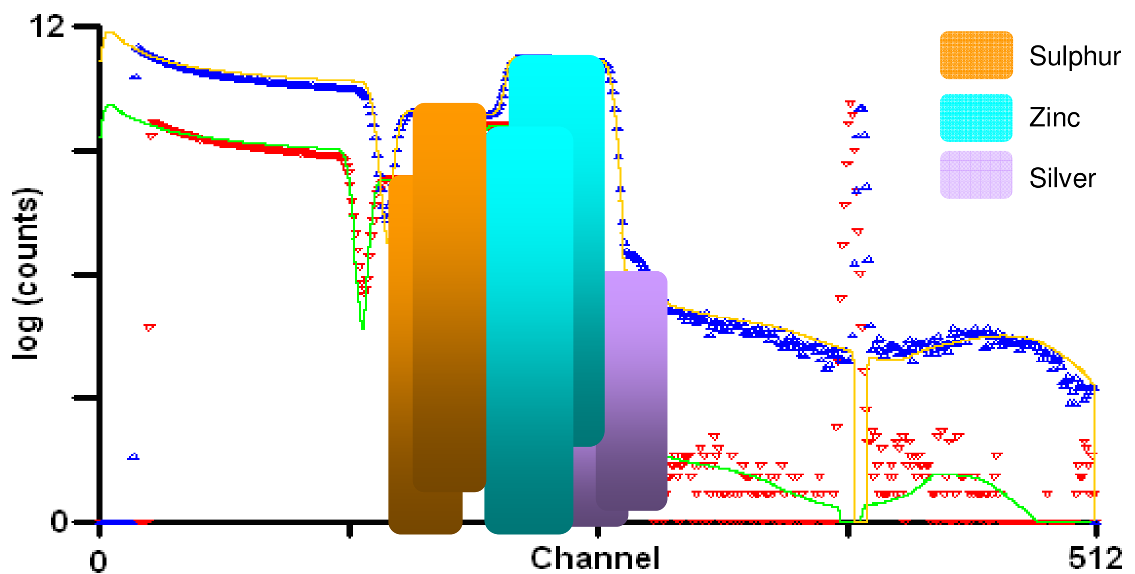

Figure 5.15: RBS spectra of the data in Figure 5.14 in log form.

The results from the Ion Beam Centre on this sample were that the concentration of silver was 0.07at%. The concentration ZnS was determined to be at 98.6at% with the Zn to S ratio at 526 parts Zn to 474 parts S. There was no detection of Cl within the samples. This deviation from stoichiometry may be due to sulphur loss during the deposition and could have an effect on luminescent efficiency.

5.3.2.5. Luminescence Characteristics

The luminescent emission spectrum from the thin film excited by the N_2 laser was expected to be the same or similar to the one measured from the source material, which was a pressed powder target of ZnS:Ag,Cl[8] (as reported Chapter 4). The expected result would therefore be a broad emission peak around the wavelength of 450nm with a FWHM of 71nm (or 66nm depending on the spectrometer used) and a decay time of 30 μs.

However, all attempts to excite the phosphor to produce luminescence using a N_2 (337nm), Nd:YAG (255nm) or the HeCd (325nm) laser in the setup described in Chapter 3 were unsuccessful, i.e. there was no observable luminescence from these thin films by the spectrometer or by dark adapted eyes, which are more sensitive than the spectrometer.

Visible emission was observed in the bulk material, however the thin films have not shown luminescence for variation in film thickness (50nm - 2.5μm), deposition temperature (100-200℃), annealing temperatures (200℃ - 560℃) or partial pressure of processing gas (3-5mTorr).

5.4 Conclusions

5.4.1 Calibration

The temperature at the substrate using these calibrations, though improved, would not be repeatable and were expected to fluctuate by up to 3%. This imprecision would be insignificant compared to other variables such as the sputter rate and partial pressure of processing gas.

The trace monitor provided a suitable method to determine film thickness in real time. However, interpreting the oscillation from the trace was unreliable, hence films tended to be thicker than intended, but generally not by more than 20nm.

The visible emission detected from the ZnS:Mn thin film (Figure 5.6) was evidence that the system was working effectively following the reconditioning and tests for potential contaminants. The emission spectrum of the thin film was of slight variation to the bulk material (Figure 5.6), but was within known variation.

---

[8] Purchased from Phosphor Technology Ltd.

5.4.2 Thin Film Properties

5.4.2.1. Growth Parameters

The thin films grown showed good uniformity with a thickness variation of just 1-14nm over the surface of the thin film. For the purposes of this work 14nm centre-to-edge variation is adequate, with optimisation, this could be reduced and would be desired for production.

The reduced substrate temperature, used to increase growth rate would be expected to have the effect of reducing crystallinity of the thin film. If these samples produced a visible emission when excited by UV laser, this property could have been examined in more detail. The alternative approach was to undertake XRD characterisation of these specific samples, and examine the peak widths. This was not tested, but could be an area of further study on how significant the growth rate was to emission intensity. In addition, would annealing counter this disorder significantly enough to address this issue.

5.4.2.2. Surface Characterisation

The primary measurement technique chosen as being the most suitable for measuring the thickness of thin films was reflectance spectroscopy. The stylus profiler allows only edge measurements as does the optical profiler.

On the measured samples, there was a reduction in film thickness from the centre to the edge. This contradicts the heater calibration, which has the edge of the wafer cooler than the centre, which causes sputtered material to condense at an increased rate. The predominant effect is therefore the orientation of the source and substrate. A cone of sputtered material is projected from the target, which has the effect that a greater amount of sputtered material is incident at the centre of the substrate than the edge.

5.4.2.3. XRD Analysis

The ZnS:Ag,Cl powder has a cubic structure that is maintained once grown into a thin film. Though there is a large amount of interference from the Si substrate, there was still sufficient data to determine the crystal structure and composition. The bulk material has a lattice parameter of 5.4145Å, the Si wafer has a lattice parameter of 5.4309 Å and the thin film has a lattice parameter of 5.4109Å.

Kazmerski [114] reported, initially the film will grow primarily to the lattice parameter of the substrate and further growth tends towards the natural crystalline size of the powder.

The similarity in lattice parameter and type of the bulk phosphor and the substrate means that the thin film has a greater adhesion to the substrate. This was demonstrated by the adhesive tape test.

By using the logarithmic scale for intensity, it becomes possible to view the combined components as one entity. However, this created a misleading representation of the pattern where the relative importance of a small peak was made to appear significant.

5.4.2.4. RBS Analysis

The most significant result from the ion beam analysis was that no chlorine was detected using this technique. The concentration of chlorine was of the same order or greater than the silver concentration. However, the relative measure of this is that the silver peak would have nearly an eight times greater peak intensity than the chlorine. Coupled with the silver peak being over 2000 times smaller than the zinc peak, chlorine might be present but not detected. The lack of Cl detection, along with an indicated sulphur deficiency would provide possible reasons for the lack of luminescence in the thin films, due to the nature of the films produced by sputtering.

Contaminants that would have been expected within the films, due to known materials previously employed in the growth system were yttrium, manganese, oxygen, carbon and silicon. However, no detection of these elements was observed in the RBS results. Yttrium and manganese were both components of materials grown in the sputtering chamber, ZnS:Mn and Y_2O_3 respectively. Oxygen and carbon are present in the air and have the potential to react with the thin film.

5.4.3 Chlorine Co-activator

Although commonly labelled as ZnS:Ag, this phosphor requires a charge compensator to balance the charge build-up that would develop as Ag was incorporated into the ZnS lattice.
Using this model of understanding, when the target was sputtered, it would breakdown into its component parts (zinc, sulphur, silver, chlorine and associated compounds), then during the process, any isolated chlorine becomes gaseous in nature and it would be removed by the pumping system along with the argon processing gas. The chlorine would be potentially less likely to adhere to the thin film than Zn, S and Ag due to its volatility. A proportion is also likely to be lost in the annealing of the thin film. Subsequently, a proportion of the co-activator is likely to be lost, limiting the amount of Ag that can be incorporated into the lattice, or leading to non-compensated/activated Ag.

The complication of growing ZnS:Ag,Cl phosphor as a thin film due to the requirement of a Cl charge compensator leads to a set of additional experiments to develop a method to enhanced the incorporation of Cl into the thin film. The work presented in chapter 6 was directed at investigating this issue, which was not anticipated.

6 Alternative Methods of ZnS:Ag,Cl Thin Film Phosphor Fabrication.

6.1 Introduction

Chlorine (Cl) has been identified as a key element in the composition of the zinc sulphide doped with silver (ZnS:Ag) phosphor and acts as a charge compensator to the silver (Ag). Rutherford Backscattering (RBS) was used to examine a thin film grown by the technique of RF magnetron sputtering from a ZnS:Ag,Cl pressed powder target. The chlorine was not detected in the sample, indicating potentially that it was lost during the sputtering process. In this chapter, the results of a series of experiments undertaken in an attempt to overcome this problem are presented.

6.2 Method

Two approaches were used to investigate enhanced incorporation of chlorine, for it to form the co-activator within the ZnS:Ag,Cl thin film. To ensure that each dopant was situated in the thin film, the process was broken up into stages with dopants incorporated individually until a complete phosphor was grown or formed. This permitted intermediate testing points where the importance of the charge compensator was examined using photoluminescent (PL) measurements.

Both techniques use RF Magnetron Sputtering to form a thin film of undoped ZnS onto a substrate to which Ag and Cl were added. The first technique uses a sputter coater and thermal annealing to transfer Ag and Cl dopants into the thin film and the second technique uses ion implantation and thermal annealing. Both methods have their advantages and disadvantages.

Sputter coating of dopants was quick and cost effective, but it has a low level of control over dopant concentration and relies heavily on diffusion. Ion implantation of dopants is a technique where accurate doping is feasible, but it is a time consuming and costly process. Using ion implantation, it is possible to dope the thin film precisely with the small level of dopant required for this work (0.01at% of Ag [22, 74]). The dopants are distributed throughout the sample using

multiple energy implantations and then annealed to promote local diffusion and incorporation into the lattice.

Annealing of the samples was undertaken by two methods, either within a furnace in air or within the sputtering chamber under vacuum. For the sputter-coated samples the furnace was used, as the incorporation of Cl uses powders and is not suitable for the sputtering chamber. For the ion implanted samples, both annealing methods were employed.

The samples were characterised by their PL emission spectrum and by ion beam analysis, with the latter used to probe five samples for their chemical composition and to find chemical composition in relation to the depth. The ion beam techniques used were Rutherford Back Scattering (RBS) and Particle-Induced X-ray Emission (PIXE).

6.2.1 Diffusion

An important consideration for the work presented in this chapter is the rate at which the dopants diffuse in the lattice. This affects the required duration and temperature needed for the dopants to diffuse throughout the phosphor to activate it. The semiconductor components will move relative to each other toward equilibrium as well as the dopants. Therefore, within the ZnS semiconductor Zn and S also have a diffusion coefficient as well as that of the Ag dopant (Table 6.1).

Table 6.1 Diffusion coefficients of the elements of ZnS:Ag within a ZnS lattice.

Diffusant	D_0 (cm^2/s)	Q (eV)	Temperature Range (ºC)
Zn	3×10^{-4}	1.5	925<T<940 [22]
	1.5×10^{4}	3.26	940<T<1030 [22]
	1×10^{16}	6.5	1030<T<1075 [22]
S	2.16×10^{4}	3.15	600-800 [22]
	8×10^{-5}	2.2	740-1100 [22]
Al	5.69×10^{-4}	1.28	800-1000 [22]
Ag	8×10^{-9}	0.1	80-400 [80]

There was no reported data on Cl diffusion in ZnS found, however it could be assumed it would be faster than Ag in ZnS due to its smaller atomic number.

6.2.2 Sputter Coating

RF Magnetron Sputtering using the technique presented in Chapter 3 and used within Chapter 5 to grow two 600nm thin films of ZnS onto a silicon wafer. An Emitech K-575 sputter coater was then used to deposit 20nm of Ag from a 0.25mm thick silver foil source (purity of 99.99%) through a mask, forming circular dots on the ZnS thin film. The thickness of the sputtered Ag layer was confirmed using the Stylus Profiler as described in Chapter 3. The silver was deposited through an aluminium mask with 78 perforations of 2.9mm in diameter, which further limits the quantity of silver applied. The area of the mask was divided into sectors with different spacing between perforations ranging from 3.1mm to 22.0mm. Following deposition the mask was removed leaving silver spots on the ZnS thin films.

The objective was to create a concentration of 0.01at% of silver in the ZnS thin film. A 20nm thickness of Ag combined with the reduced quantities sputtered onto the thin film through the mask created a ratio of Ag to ZnS with a range of 1:120 to 1:1200, an equivalent range of approximately 0.83% to 0.083% of Ag by volume.

The sample was thermally annealed at 800ºC for 1 hour in a Carbolite CF1200 furnace to initiate Ag diffusion through the thin film (Figure 6.1). This value was chosen to create a faster diffusion rate than the one quoted in Table 6.1 for Ag in ZnS and to match annealing temperatures of later samples.

Following annealing, the sample was characterised by its emission spectrum using a N_2 laser in the setup described in Chapter 3.

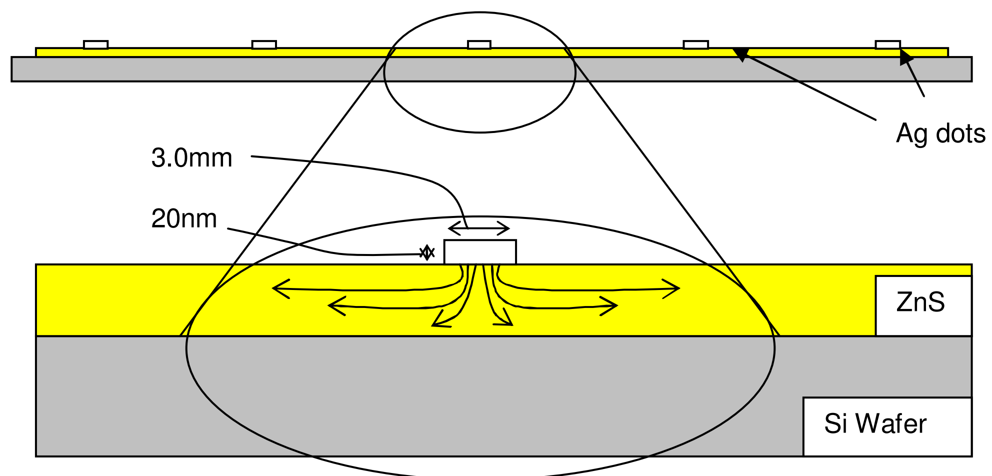

Figure 6.1: Thermal annealing of the sample following deposition for the diffusion of Ag through the ZnS thin film.

Diffusion of dopants from the Ag dot creates a concentration gradient, where the maximum concentration originates at the Ag dot and reducing approximately exponentially as it spreads radially. This has the advantage of creating a range of Ag concentrations that could highlight an optimum Ag concentration using PL, if luminescence were created.

Once silver has been sputtered onto the sample, the sample is then annealed or is brought together with a Cl material and annealed. The Cl in this work was in the form of powdered NaCl or ZnS:Cl, which was applied with spatula to form a layer on the thin film and heat treated to promote the Cl to transfer from its original form and become a charge compensator in the thin film.

6.2.2.1. Incorporation of Cl (NaCl)

Chlorine is most commonly found combined with sodium in the form of salt (NaCl). To create the ZnS:Ag,Cl powder characterised in Chapter 4, Phosphor Technology use NaCl in a chemical reaction to introduce the Cl component. Generally Cl from this compound is obtained by oxidising agents or more often by electrolysis [80].

The preparation method to create ZnS:Ag powder uses NaCl:

100g ZnS +2g NaCl +0.016g $AgN0_3$ and process at 940℃ [74]

On its own, the Cl would not undergo spontaneous diffusion into the thin film. The sample was heat treated to promote the transfer of Cl from salt form into the ZnS thin film to act as the charge compensator to the Ag ions. 20 grams of NaCl was layered onto the sample of ZnS with sputtered Ag (Figure 6.2). In these tests, a control sample of ZnS without sputtered Ag and without previous annealing was used and underwent the same annealing tests as the other sample. This control was used to characterise the importance of the annealing process in creating a PL material.

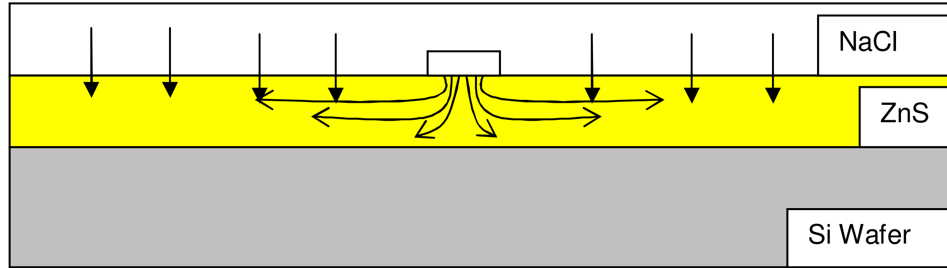

Figure 6.2: Process of Cl incorporation into a ZnS thin film by thermal annealing from NaCl.

Annealing was carried out at 800ºC in the Carbolite CG1200 furnace with an air atmosphere for periods ranging from 30 minutes up to a total of 120 minutes. Following each period (30 minutes) the samples were removed and tested for PL emission using a N_2 laser (337nm) excitation.

6.2.2.2. Incorporation of Cl (ZnS:Cl)

ZnS:Cl does not introduce new elements into the chemical reaction resulting in reduced contamination. It also creates a barrier to reduce sulphur loss within the thin film, which has been reported to affect the emission characteristics [79].

A quantity of 20 grams of ZnS:Cl was used to cover a ZnS thin film, which was then thermally annealed in the Carbolite furnace with an air atmosphere at 700°C to promote diffusion of Cl into the thin film (Figure 6.3). This temperature was chosen to match the upper limit of an experiment reported by Nakanishi [71], discussed below, and by Aven [87] as the optimum nucleation temperature. The annealing process matched that of the NaCl test by using a series of 30 minute periods of annealing with PL characterisation, using the N_2 laser (337nm) as the excitation source, at each stage.

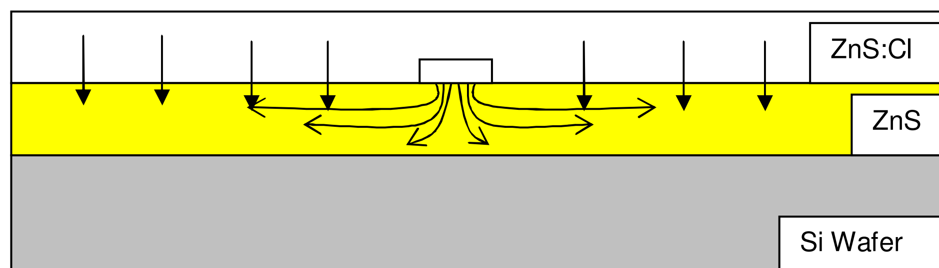

Figure 6.3: Process of Cl incorporation into a ZnS thin film by thermal annealing from ZnS:Cl powder.

Annealing of the sample means that some chlorine is lost to the surroundings; however, the contrast in volumes of the two forms (bulk and thin film) would mean that chlorine can potentially be incorporated into the thin film. Nakanishi [71] performed a similar diffusion experiment to the one undertaken here. Simultaneously evaporating Ag and ZnS to create the thin film, then placing the sample into ZnS:Cl powder and annealing at 600-700°C in air. Following characterisation of the sample, it was found that the characteristic 450nm, blue, emission peak was present and the optimum temperature for embedding the chlorine was anywhere between 600-700°C. Above this temperature range the surface degraded and emission intensity was reduced.

6.2.3 Ion Implantation

This technique accelerates Cl and Ag ions at a thin film of ZnS. The ions penetrate into the thin film to a range of depths and create a concentration curve relative to depth that is Gaussian in shape. The optimum concentration of Ag dopant is in the range of 0.01at%, which means that for one part silver (and chlorine) there are 5000 parts of zinc sulphide. Due to the volatility of Cl a range of target concentrations were applied, 0.01at%, 0.05at% and 0.2at%, in an attempt to compensate for any loss mechanisms.

Four ZnS thin films at 800nm thickness were used for the ion implantation study and four stages of implantation were used in total, three for Ag implantation and one for Cl implantation (Figure 6.4).

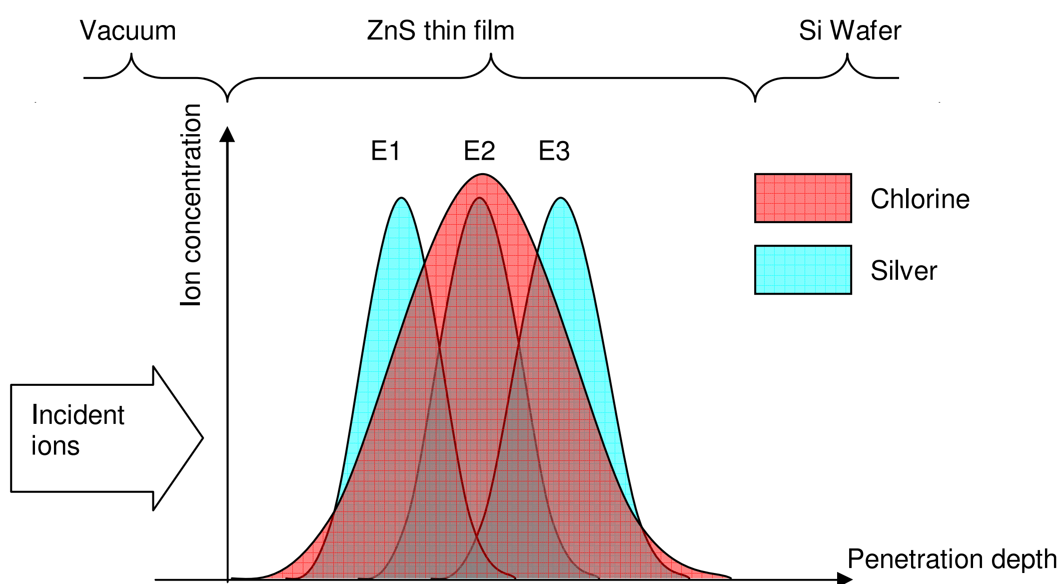

Figure 6.4: A representation of implanted Ag and Cl ions within a ZnS thin film.

The three Ag implantations were used to form a concentration spread through the depth of the thin film (Figure 6.5), with the objective of a more uniform doping, requiring less diffusion to distribute the silver uniformly. A single chlorine implantation was required due to the larger relative straggle associated with this lighter element, which spans the volume of the ZnS thin film. A key point to mention regarding the Ag implantation is that the implantation at the highest energy penetrates the greatest distance and has the greatest relative straggle (Figure 6.5). These differing energies mean that there was a distributed concentration of Ag within the volume of the ZnS thin film.

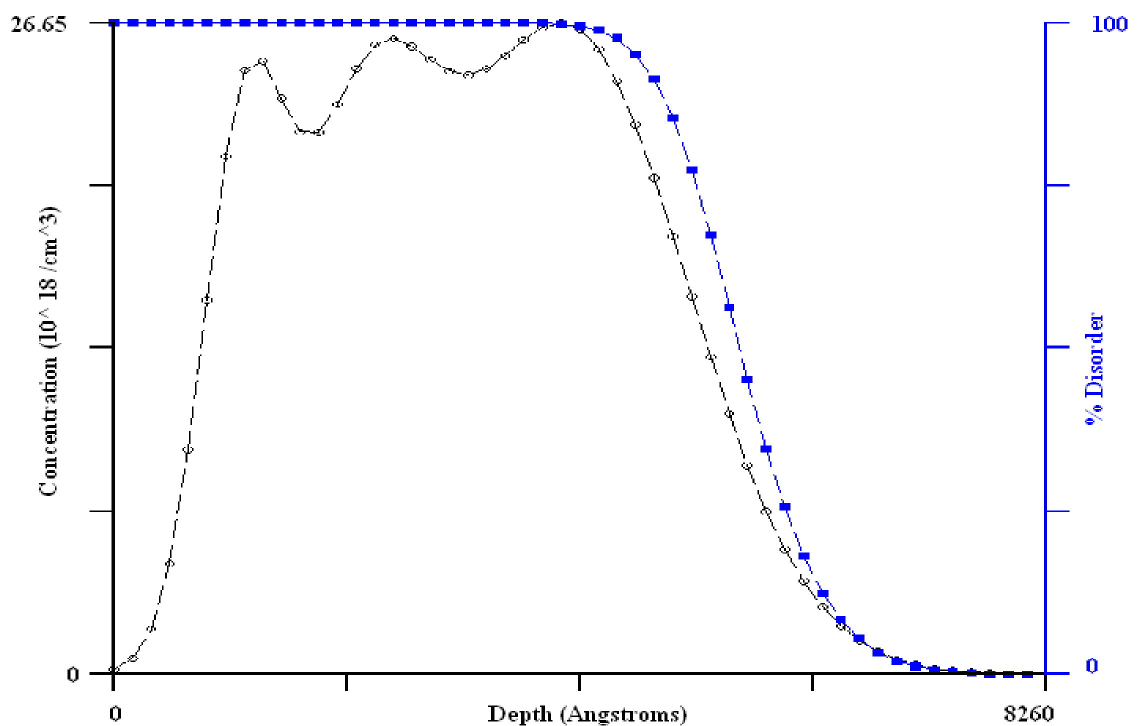

Figure 6.5: A computer generated depth profile based on the implantation of Ag ions into a 800nm ZnS thin film and the suggested disorder it would create (provided by Dr. Smith[9]).

The disorder suggested in Figure 6.5 is for a single crystalline material, which does not undergo annealing. Annealing post implantation would be expected to counteract this disorder so that ions are incorporated into the lattice structure, resulting in the electron band structure reforming as the lattice reforms.

[9] Andy Smith - A.J.Smith@surrey.ac.uk - Surrey Ion Beam Centre, Surrey University.

Table 6.2: Implantation concentrations of silver and chlorine ions into a ZnS thin film.

Sample	Chlorine	Silver
1	0.01 at%	0.01 at%
2	0.05 at%	
3	0.20 at%	

Table 6.3: Implantation Energies and concentrations for the silver and chorine ions.

Implantation	Cc	at%	Energy
Ag - 1	7×10^{14}	0.006	1200 KeV
Ag - 2	3×10^{14}	0.0025	675 KeV
Ag - 3	1.7×10^{14}	0.0015	350 KeV
Cl	2.4×10^{19} - 50×10^{19}	0.01 – 0.20	435 KeV

The samples were rotated and tilted to reduce channelling of the implanted ions. Channelling is the effect where incident ions penetrate a greater distance compared to the standard range and straggle, by travelling along crystal planes. This would not have been a significant problem as the samples were polycrystalline, but the option was available and was taken.

This work was preformed at the Ion Beam Centre (IBC) at the University of Surrey with Dr. Andy Smith[10] acting as chief liaison. Before undertaking the work, a workshop was attended to introduce users to the facilities at the IBC. Due to the complexity of the system, the process of implantation was performed using the expertise of Dr. Smith, and observed by the author. Prior to its commencement, details of the work were discussed at length with Dr. Smith to learn the limitations and strengths of the system being used and to fully utilise what was available.

Ion implanted samples were thermally processed in vacuum and in air to test the most appropriate method. Annealing in air was undertaken in a furnace at temperatures of 800ºC for periods of 15, 30 and 60 minutes. This was to determine if the same emission spectrum would be obtained for the sputter coated samples as well as the ion implanted samples.

The vacuum annealing was undertaken in the RF Magnetron Sputtering chamber using the heater powers of 25% and 27.5% , which correspond to 592ºC and 620ºC respectively, for periods of 15 minutes to a total of 8 hours. The vacuum was in the region of 10^{-6} mbar throughout the anneal.

---

[10] a.j.smith@surrey.ac.uk

6.2.4 Ion Beam Analysis

Five thin film samples of ZnS were sent to the Ion Beam Centre for ion beam analysis by RBS and PIXE.

- (Sample 1 and 2) ZnS implanted with Ag and 0.2at% Cl, one post-annealing and one pre-annealing respectively. This would determine the effectiveness of the implantation process to dope the ZnS thin film effectively, as well as determining the effect annealing has on the sample.
- (Sample 3) There was also a control sample consisting of an unimplanted thin film ZnS. This would be a test for the possible contaminants in the system during growth.
- (Sample 4 and 5) ZnS implanted with Ag and with either 0.01at% or 0.05at% of Cl. These were thermally annealed with the same parameters as the 0.2at% Cl sample. This would verify implantation effectiveness and compliment the annealed 0.2at% Cl.

Ion beam analysis was performed using PIXE and RBS. PIXE uses two beams of light ions to probe the samples; a 1560 keV beam of alpha particles ($^{4}He^{+}$) with a beam current of 30nA – 60nA, with a nominal beam size of 1mm and a 2587 keV beam of protons ($^{1}H^{+}$). Cornell geometry and IBM geometry X-ray detectors are positioned at 172.8° and 148.2° to the beam line respectively to detect the resultant emission from the samples [97].

6.2.5 X-ray Diffraction

The areas of interest for these tests were to find the effect, if any, on crystallinity, produced by ion implantation and subsequent annealing. Ion implantation is expected to generate some disorder of the thin film as the ions embed, but annealing of these samples should help to increase crystallinity of the lattice. A comparison of ZnS grown on the Si wafer to an implanted sample of ZnS on a Si wafer provides information on the level of disorder that the implantation has on the lattice.

A comparison of the pre-annealed implanted samples and post-annealed sample provided the information on how the crystallinity is affected by annealing.

6.2.6 Thermal Processing

For sputter coated samples the thermal energy provided by the Carbolite CF1200 furnace was used to allow the Ag and Cl to diffuse throughout the thin film. This was carried out in air within a lidded quartz crucible to contain the samples and powders as well as to reduce contamination. When accelerated ions, in the ion implantation process, come to rest within the thin film they transfer kinetic energy to atoms in the target material. This series of collisions can cause the target material to become disordered and loose its crystalline structure (as indicated by the prediction shown in Figure 6.5). Only when the ions are chemically bound into the lattice is the phosphor activated and the luminescent characteristics are present. The implantation of ions means the dopants are incorporated into target but does not necessarily mean that they are fully incorporated into the lattice. Thermal processing of the samples provides the energy for the Ag and Cl ions to be chemically incorporated into the lattice structure by substitution. It also provides the energy to 'repair' the structure, reduce defects and improve general crystallinity within the thin film (Figure 6.6).

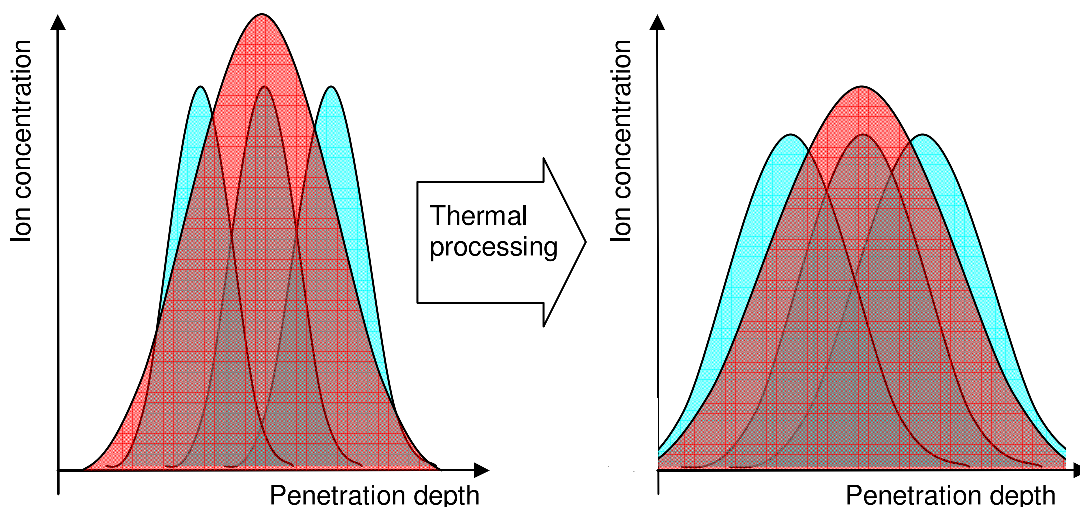

Figure 6.6: Schematic diagram to illustrate the effect of annealing on the distribution of ions within a material

6.3 Results

With the aim being to create a thin film phosphor of ZnS:Ag,Cl the expected emission would be the same as the one observed from the bulk form (Figure 6.7). Therefore, the desire was to detect a blue PL emission that has a broad peak around the 450nm wavelength using the PL setup described in Chapter 3. The emission spectra from these tests were collected using the

Ocean Optics S2000 spectrometer and therefore caution should be paid to peaks that appear around 485nm (see Section 4.3.2.1 for details), as the values in this wavelength region are likely to be preferentially enhancements and could cause incorrect characterisation of the emission spectra.

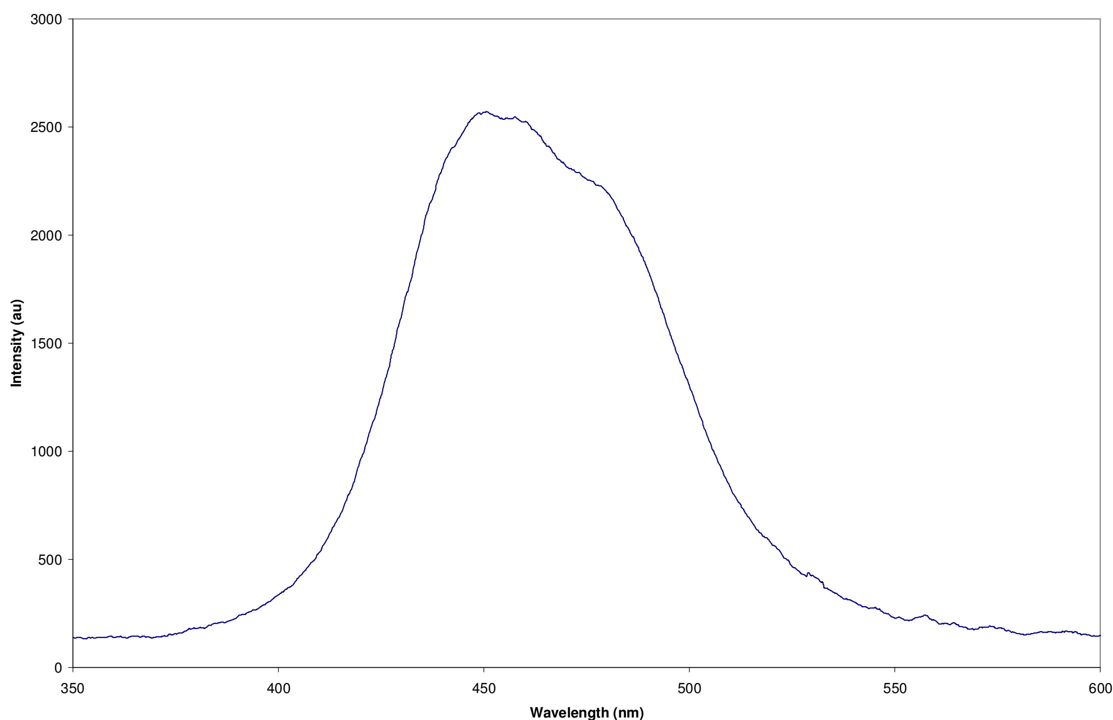

Figure 6.7: PL emission spectrum of ZnS:Ag,Cl powder excited by N_2 (337nm) laser.

6.3.1 Luminescence of Ag Sputter Coated Films

An emission was detected from a ZnS thin film with Ag dots annealed in the furnace, however, this luminescent emission cannot be attributed to the ZnS:Ag,Cl phosphor. Three emission peaks were detected, the predominant one at 511nm (Peak 2) and two minor ones at 383nm (Peak 1) and 772nm (Peak 3) with an intensity of 15% and 1% respectively compared to Peak 2 (Figure 6.8).

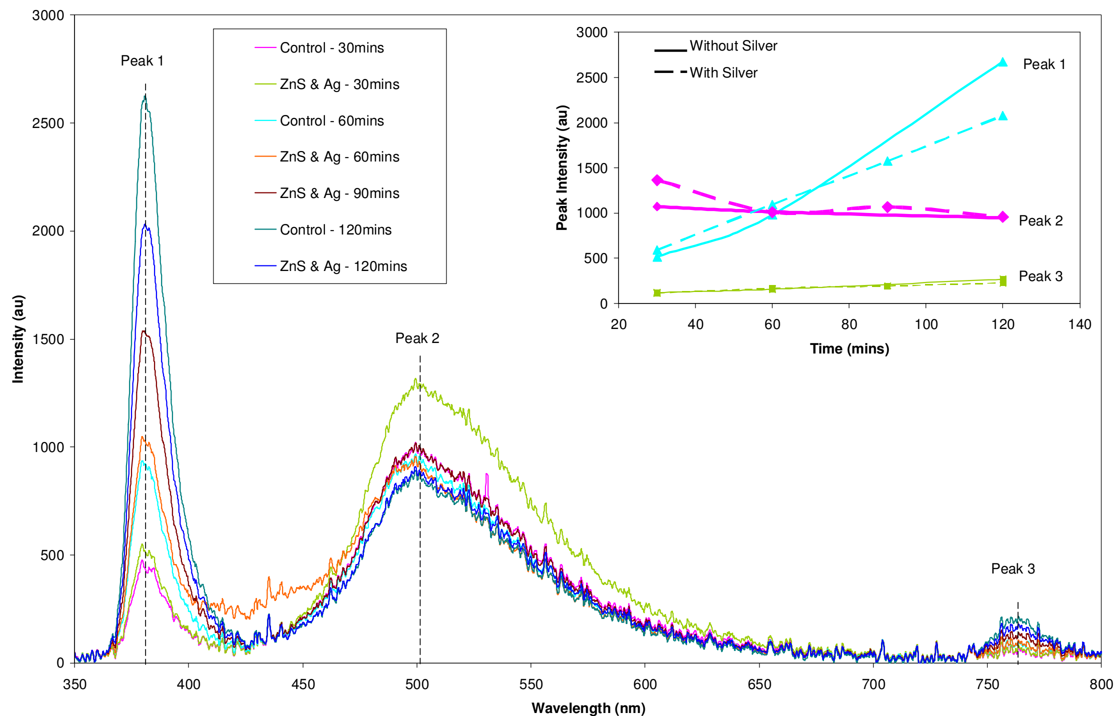

Figure 6.8: PL emission spectrum of ZnS thin film with and without sputter coating of Ag and annealed in a furnace. Insert - Values for peak intensity at the three emission peaks for increasing annealing periods.

Examination of the emission spectrum of ZnS thin films with annealing times of 30-120 minutes in the furnace indicated a change to the peak intensity measurements. The intensity of Peak 3 developed over the annealing period, but not at the rate of Peak 1. Peak 1 became the dominant peak after 60 minutes of annealing (Figure 6.8 - Insert).

Comparing the intensity measurements of the three peaks over the two hour period it can be seen how the magnitude of the intensities change. Peaks 1 and 3 increase linearly and Peak 2 creates a general downward trend in intensity over time.

The most significant finding from these results was that the addition of Ag appeared to make no change to the results, as both the sample with Ag and the control followed the same trends, indicating that whatever was happening was not related to the sputter coated Ag. Subsequent analysis by XRD (presented below) indicates that the ZnS had oxidised into ZnO, which is known to produce peaks around these values [22, 74]. This is discussed in Section 6.3.4.3.

6.3.1.1. Luminescence of Samples Doped Using NaCl

These did not develop the expected ZnS:Ag,Cl emission peak. When tested using the PL measurement system there was no visible luminescence that can be attributed to the ZnS:Ag,Cl phosphor.

6.3.1.2. Luminescence of ZnS:Cl

The most significant effect to the thin film was that it had deteriorated during the process of annealing. In an attempt to remove the excess ZnS:Cl powder from the sample using a dust-can to blow the powder away, the thin film was removed as well. Thin film in close proximity to the Ag dots (~1mm-2 mm) was left, leaving the rest of the area either bare Si wafer or Ag dots. The Ag dots remained prominent, showing that large amounts of the Ag had not diffused into the ZnS thin film within the annealing periods.

Testing the sample for PL with a N_2 laser around these dots created a visible emission. When compared to the annealed ZnS thin film with sputtered Ag, it is clear that the same dominant peaks have been generated, as shown in Figure 6.9. This is evidently an annealing effect leading to the change of material from ZnS to ZnO, since the peaks produced are significantly different to the expected ZnS:Ag,Cl peak at 450 nm, or that of ZnCl (Figure 6.10) as it does not show any evidence of the peak at 383nm and the dominant peak is at 490nm.

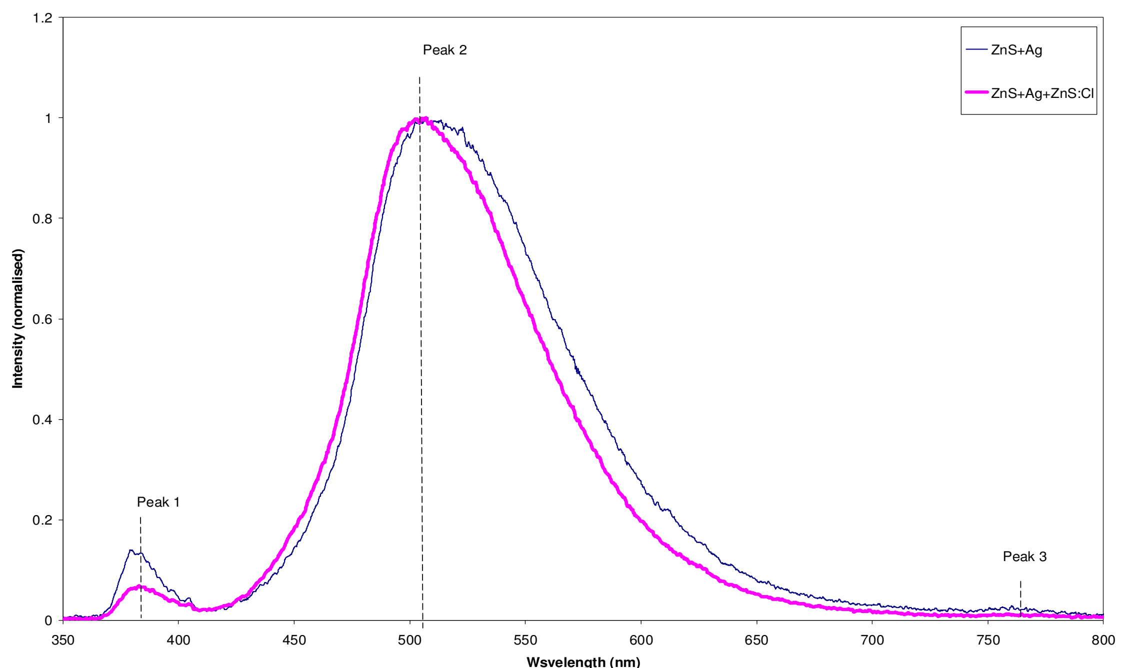

Figure 6.9: PL Emission spectrua of a ZnS + Ag thin film annealed with and without ZnS:Cl powder after 30 minutes.

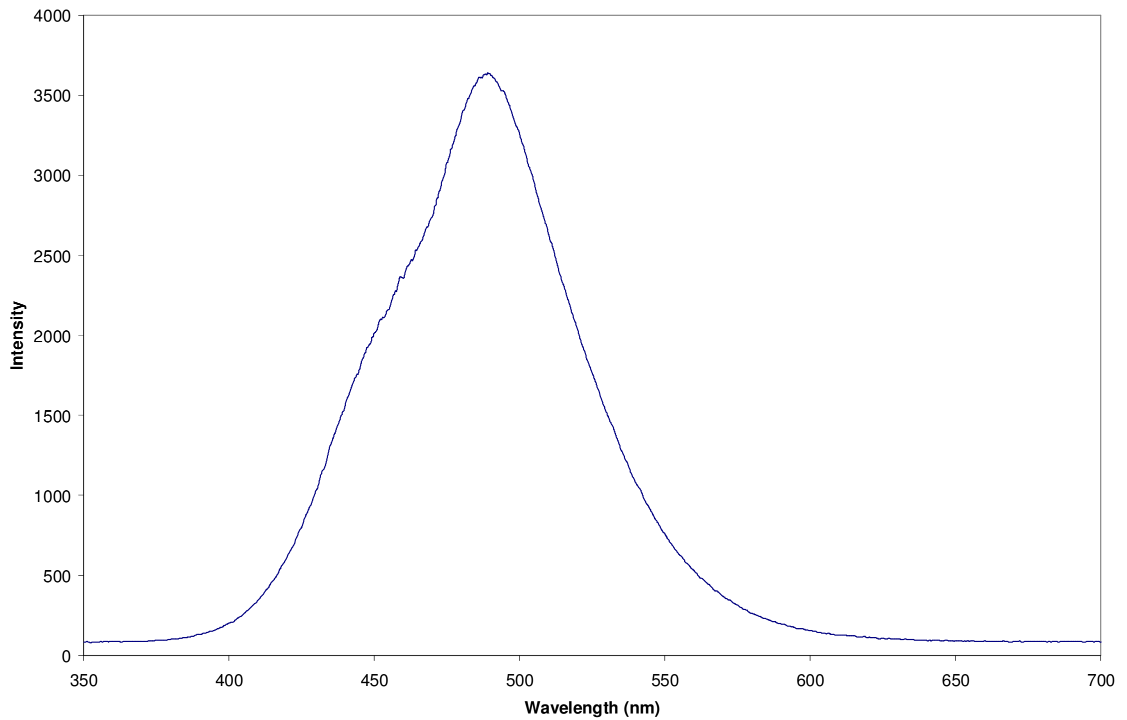

Figure 6.10: PL emission spectrum of ZnS:Cl powder excited by a N_2 (337nm) laser.

6.3.2 Ion Implantation

The ion implanted samples were annealed under vacuum as well as within the furnace. This was not possible for the previous tests without causing large scale contamination of the sputtering chamber by the ZnS:Cl or NaCl powder. As expected following the contamination effects produced by the furnace for the sputter doped samples, the PL emission spectra from vacuum annealing (Figure 6.12 - Figure 6.15) were different to the ones created in the furnace (Figure 6.11). Once again, the peaks that are characteristic of the annealing in air process are present.

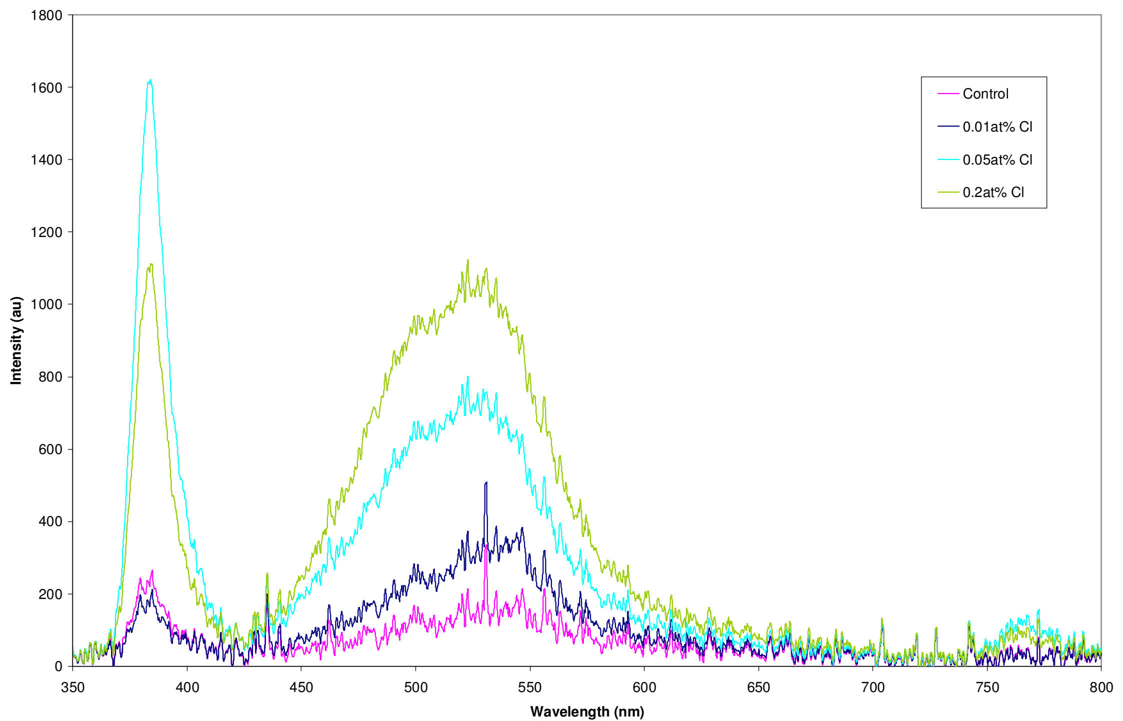

Figure 6.11: PL emission of ion implanted ZnS and annealed for 15 minutes in the furnace at 700°C and excited with the N_2 laser.

The PL from the vacuum annealed samples were difficult to interpret as there appear to be several overlapping spectra, although this may include ZnS:Ag,Cl emission, when excited by the N_2 laser (Figure 6.7). At 30% heater power and above, the thin films delaminate from the substrate within a short period (1-10 minutes) of annealing within the vacuum. Subsequently, for the 27.5% power measurements, controlled ramping was introduced to apply heat more gradually in an attempt to minimise chances of delamination. However, in following tests, this did not appear significant as with or without ramping at 27.5% and 30% power the outcome was not affected.

There is apparent ZnS:Ag,Cl emission (Figure 6.12 - Figure 6.15) when excited by the N_2 laser, there is also a consistent change in the intensity of the peaks around 450nm in terms of Cl doping, with the emission rising from 0.01at% to 0.05at% doping, and reducing again at 0.2at% doping. This would imply an optimum doping value less than 0.2at%, and indicates that the implantation technique is viable.

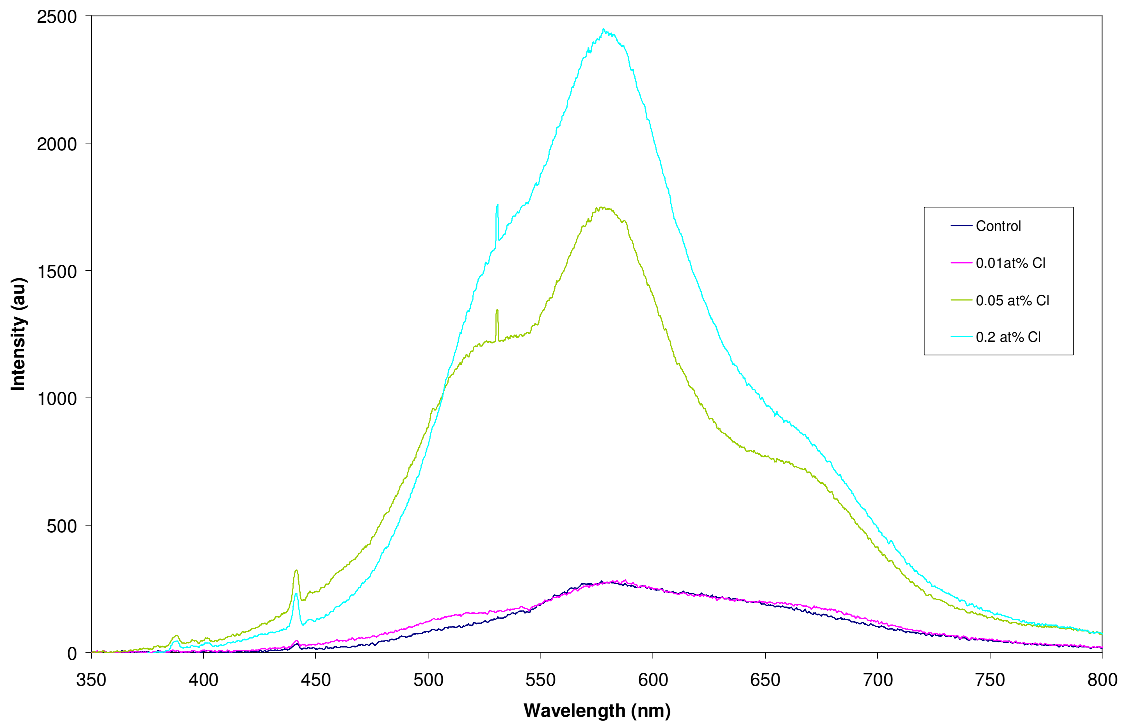

Figure 6.12: PL emission spectrum of ion implanted ZnS thin film annealed at 25% for 8 hours under vacuum and excited using the HeCd laser.

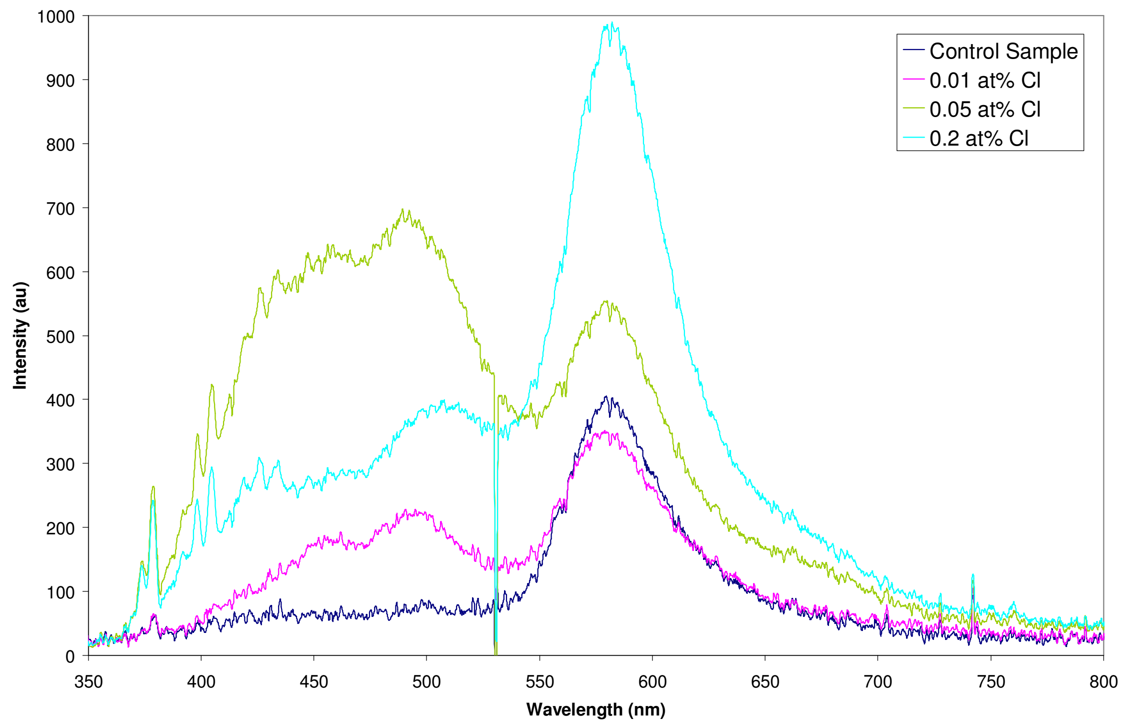

Figure 6.13: PL emission spectrum of ion implanted ZnS thin film annealed at 25% for 8 hours under vacuum and excited using the N_2 laser.

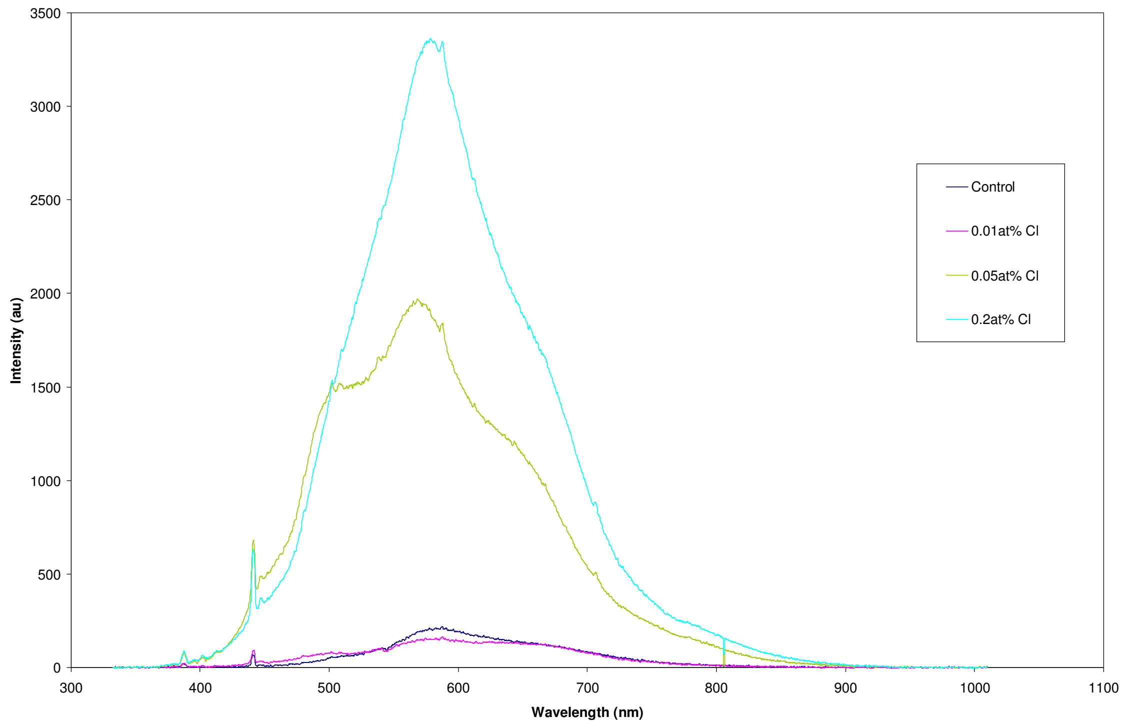

Figure 6.14: Normalised PL emission spectrum of ion implanted ZnS thin film annealed at 27.5% for 8 hours under vacuum and excited using HeCd laser.

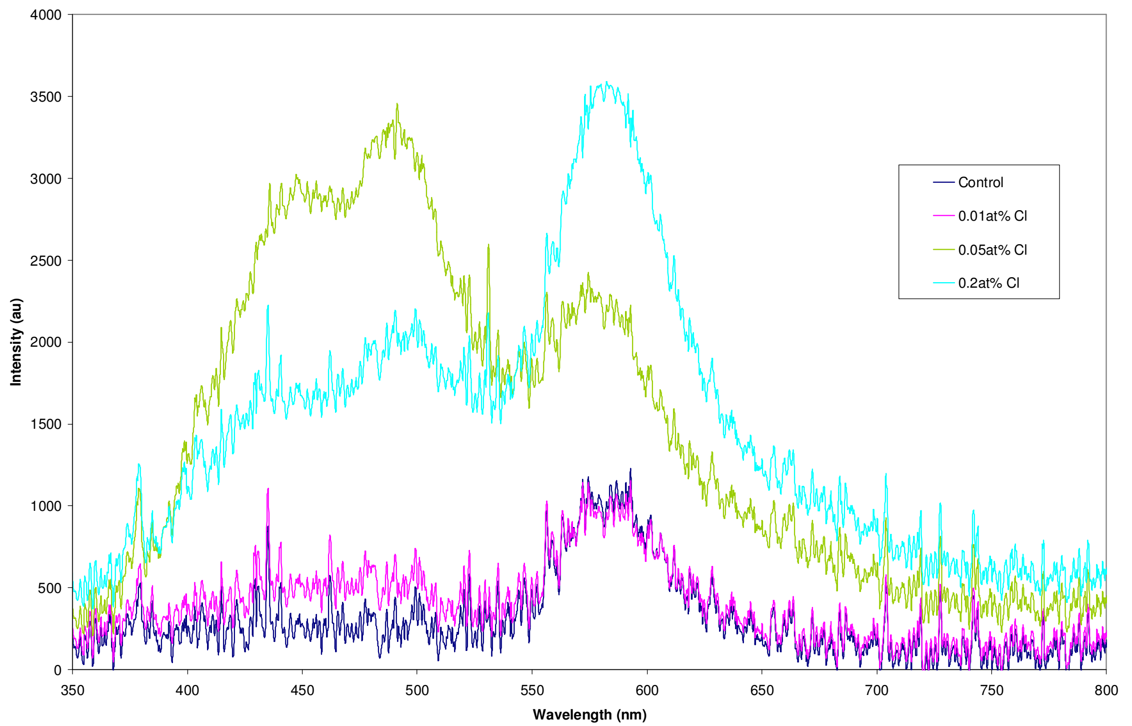

Figure 6.15: PL emission spectrum of ion implanted ZnS thin film annealed at 27.5% for8 hours under vacuum and excited using N_2 laser.

6.3.3 Ion Beam Analysis

The five samples analysed at the IBC were numbered for ease of identification and the results are labelled according to this numbering. The sample number, what the samples represent and the reason why the sample were examined are presented in Table 6.4.

Table 6.4: The sample analysed by ion beam analysis, their number and reason for analysis.

Sample	Implantation	Annealed	Reason
#1	0.01at% Cl	Yes	Complimentary measurement to sample #4
#2	None	No	A control for the thin film growth technique
#3	0.2 at% Cl	No	Test the effectiveness of the implantation process
#4	0.2 at% Cl	Yes	Test the effect the annealing of implanted ions
#5	0.05at% Cl	Yes	Complimentary measurement to sample #4

6.3.3.1. PIXE

It was found that PIXE is insensitive to Cl in the presence of S, as Cl was not observed in any of the five samples (Figure 6.16). S and Zn peaks where observed in the samples and where consistent in their response. The full set of results from PIXE using 2.5MeV protons at normal exit into X-ray detector (60° beam incidence), PIXE using 2.5MeV protons at 60° exit into X-ray detector (normal beam incidence) and three samples analysed with 1.5MeV He at normal exit into X-ray detector (60° beam incidence) can be found in the Appendix (Section 9.1: Figure 9.6 - Figure 9.8).

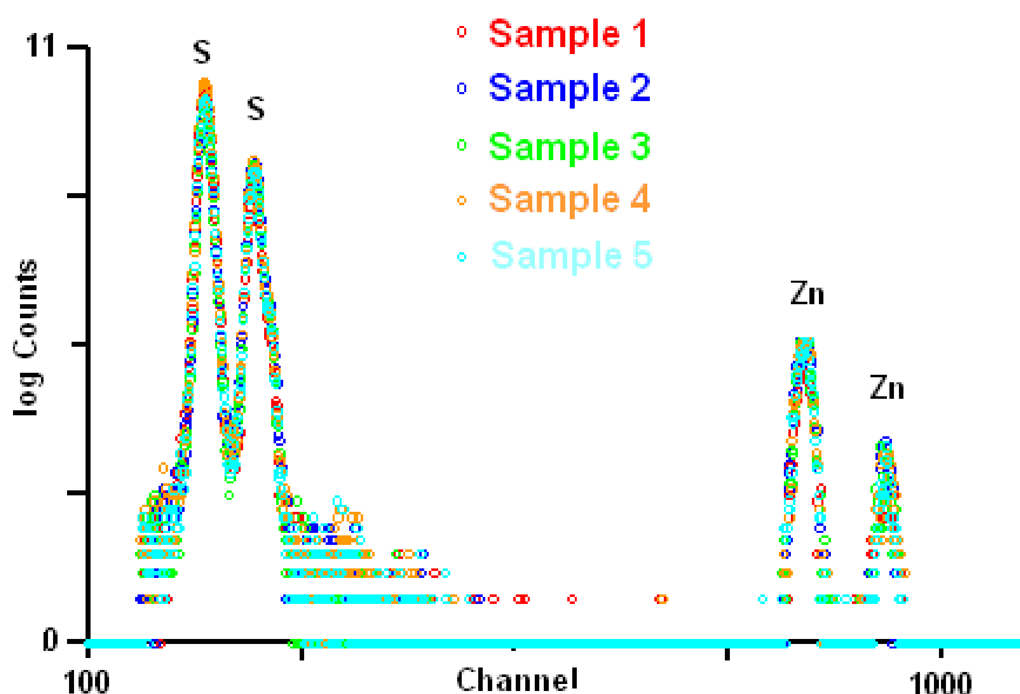

Figure 6.16: Example of the PIXE results.

For PIXE, the $^{4}He^{+}$ and $^{1}H^{+}$ beams are sufficiently powerful to penetrate the sample and interact with the Si substrate. This was predicted by previous use of the system with thin films of these thicknesses and was found confirmed during an initial experiment. To reduce the observed Si component and intensify the thin film component, the samples were rotated to 60° incidence to enhance absorption within the thin film. However, neither the Ag L nor Cl K lines are visible.

6.3.3.2. RBS Results

Though RBS was not conclusive, it was able to highlight the presence of Zn, S and Ag but was unable to detect the chlorine. There was no obvious reason why Cl was not detected, the two most prominent reasons are explored in the conclusions, section 6.4.3.

The results showed the long high-energy tail is the pileup signal.

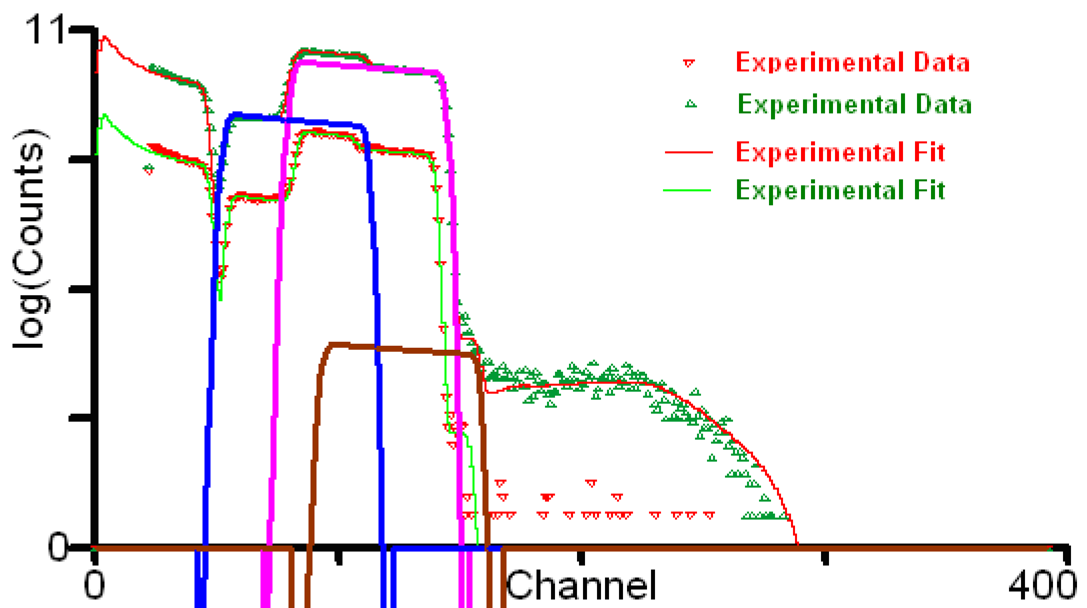

Figure 6.17: A labelled RBS spectrum of Sample 2 on a logarithmic scale. Ag (brown), Zn (mauve), S (blue).

The RBS spectra of samples 1 to 5 can be found in the Appendix for completeness (section 9.1: Figure 9.1- Figure 9.5) along with composition relating to thickness of the five samples.

6.3.4 X-ray Diffraction

6.3.4.1. ZnS Thin Film on a Si Substrate

The files in the PDF database held on the computer linked to the XRD machine are based on single-phase crystalline materials, therefore the limitation of using the database is that a nonstandard sample does not appear in the database with matching peak positions. However, the thin films examined all exhibit peaks consistent with ZnS.

Figure 6.18 shows how the XRD pattern of ZnS deposited on a Si wafer demonstrates how the peaks associated with Si protrude on the ZnS peaks.

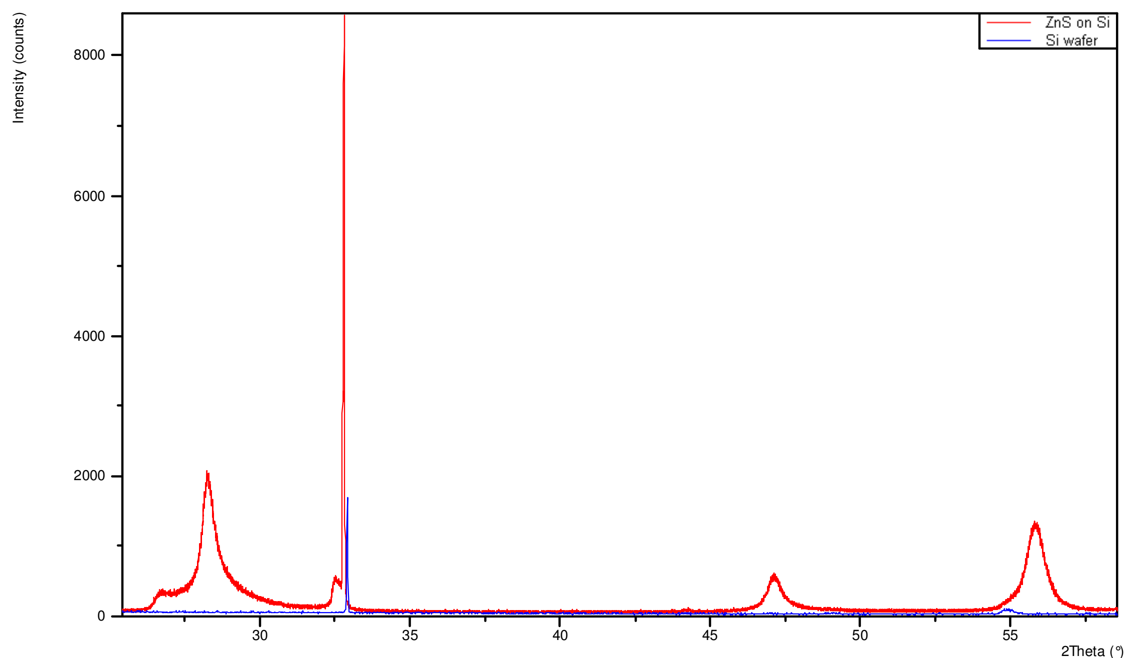

Figure 6.18: XRD pattern of ZnS on a Si wafer and the Si wafer.

Figure 6.19 shows how ZnS is effected by its growth onto a Si substrate to ZnS in its bulk form. The most prominent feature being the reduction in peak intensity.

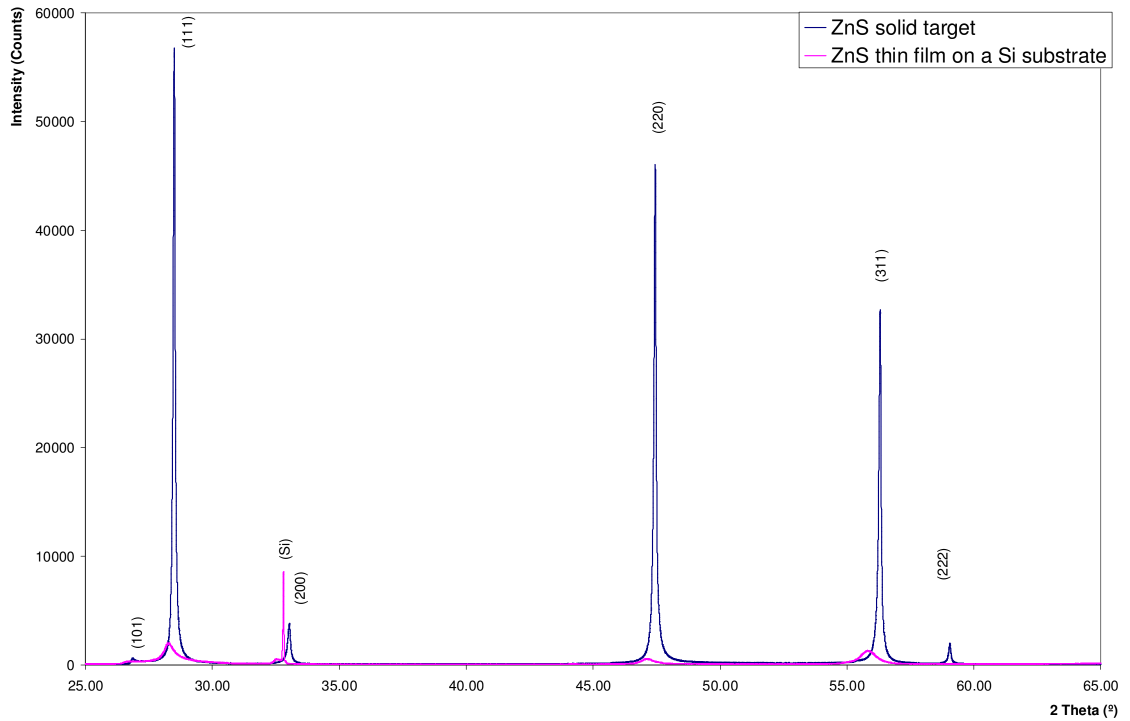

Figure 6.19: XRD pattern of ZnS solid target and the sputtered ZnS on a Si substrate.

6.3.4.2. ZnS Thin Film on a Si Substrate with Ion Implanted Dopants

The XRD patterns of implanted samples compared with the unimplanted samples of ZnS thin films on Si substrate were very close in appearance. Four samples were assigned with 15 peaks, which were used to represent the XRD pattern (Figure 6.20).

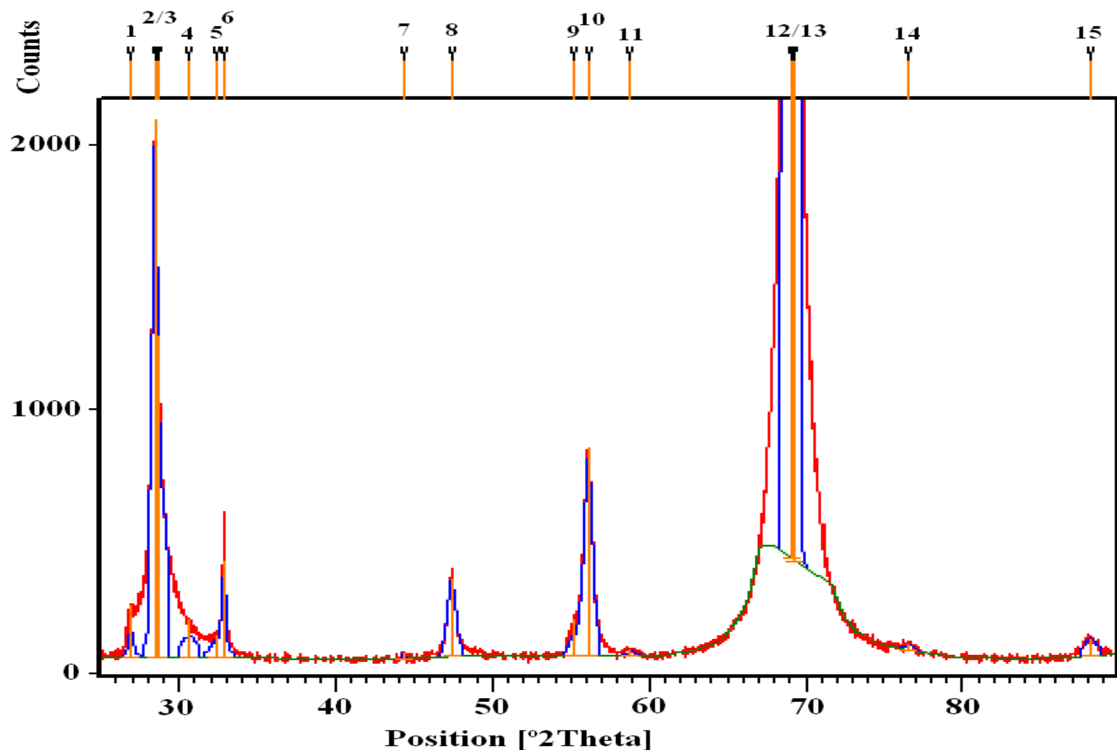

Figure 6.20: A labelled XRD pattern of ZnS thin film on a Si wafer after ion implantation, shown with profile fitting.

Not all the peaks labelled in Figure 6.20 relate to an XRD peak. To accurately define an XRD pattern mathematical peaks are applied to the pattern, these are then correlated to a database of XRD patterns to determine the most suitable material. Peaks can be close enough together that they overlap however, peaks labelled 1 to 4 can also represent just two peaks (Figure 6.19) when matched to the most likely pattern in the XRD database. Countering this generalisation are peaks labelled as 5 and 6, which represent over lapping peaks of the Si and ZnS (Figure 6.19).

The matching of an XRD pattern was the method of clarification or identification of material after a chemical process. The method to best represent changes to a material is comparing XRD patterns of the material before and after the process or of the component parts that can sum together to form the final XRD pattern, as shown in Figure 6.18.

When comparing a non-implanted sample with the sample containing 0.01 at% Ag and the highest concentration of Cl at 0.2 at%, there was no significant difference in the peaks produced (Figure 6.21). This indicates that prior to thermal annealing the position of atoms within the thin film had not been significantly affected by the ion implantation process.

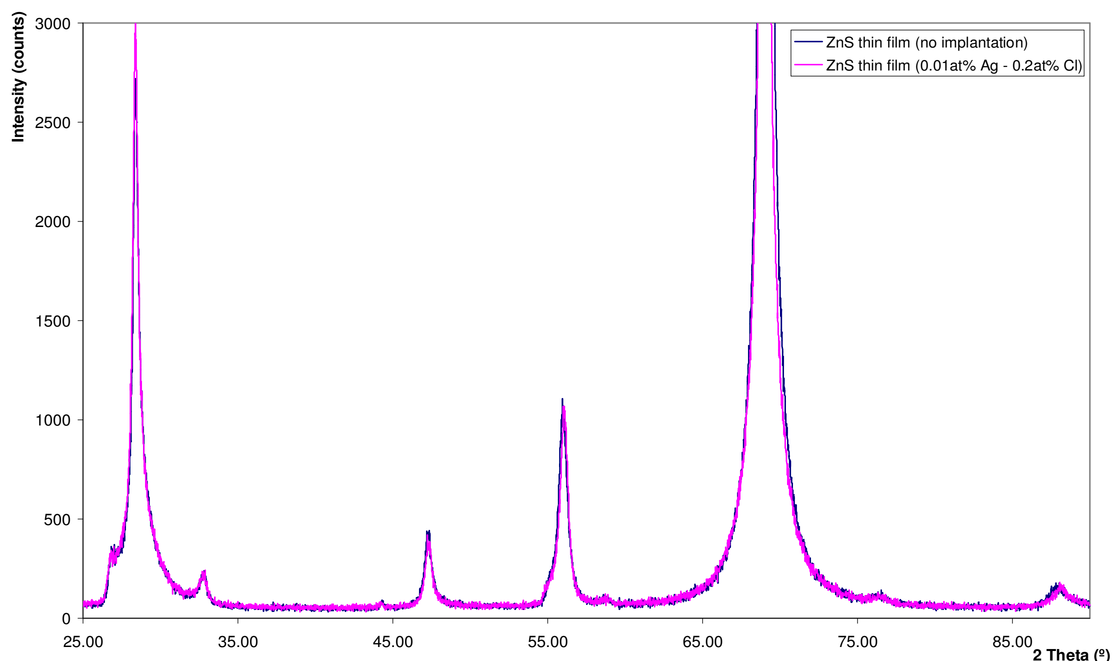

Figure 6.21: ZnS thin films XRD pattern with and without implantation.

6.3.4.3. ZnS Thin Film on a Si Wafer Implanted With Ag and Cl Ions then Annealed in Air

The thin film of ZnS grown on a Si wafer with ion implanted Ag and Cl was annealed at 700ºC in air for five periods with 1-minute increments increasing up to 5 minutes for the final period (hence total anneal time was 15 minutes). After each of the annealing periods, the samples were tested for PL emission. After the 15 minutes of annealing the sample were also tested for XRD (Figure 6.22). The sample maintained its visible appearance but the resultant XRD spectra were significantly different to previous XRD results obtained for these films.

Using the PDF database it was found that the XRD pattern most resembled a PDF of hexagonal zinc oxide (ZnO) thin film and the Si substrate. The hexagonal ZnO crystal system had the lattice parameters a = 3.2200Å, c = 5.2000 Å. It means that the ZnS thin film has oxidised with O_2 in the air to form ZnO, as well as the likely production of gaseous sulphur dioxide (SO_2).

The samples with different ion implantations do not create a significant difference in the XRD pattern when the ZnS thin films have oxidised into ZnO (Figure 6.23). This is not a surprise, as the quantities of dopant implanted into the thin film are very low (0-0.01at% Ag and 0-0.2at%Cl). If incorporated into the lattice the quantities would not significantly alter the lattice parameters that would then affect the XRD pattern.

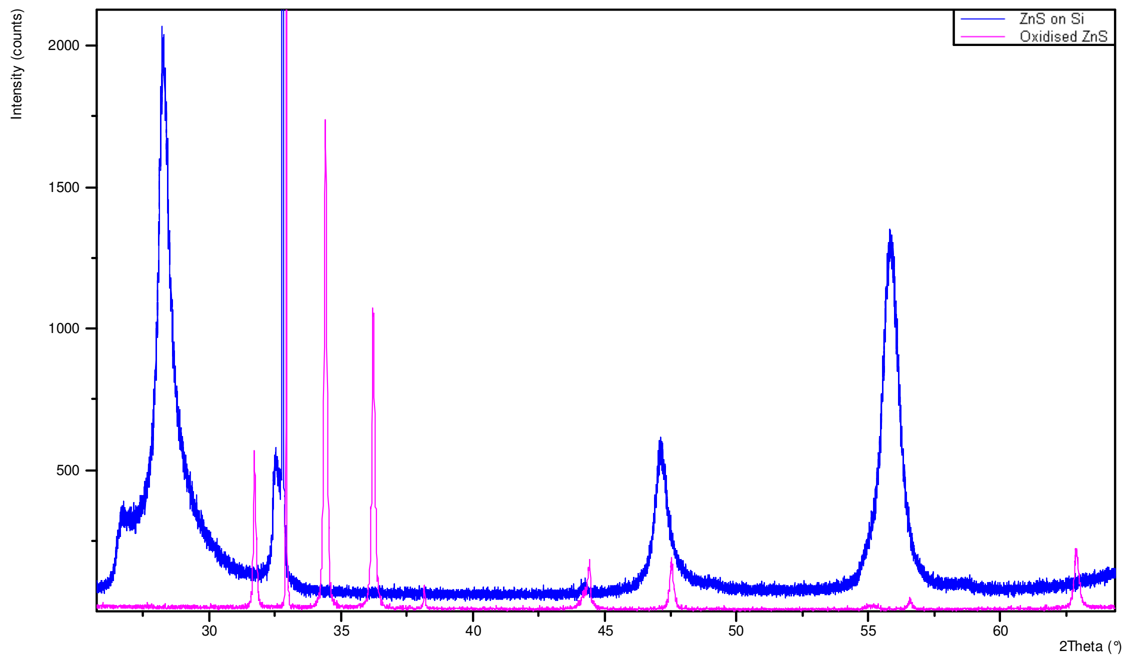

Figure 6.22: XRD pattern of ZnS on a Si wafer and the same sample after annealing in air at 700°C.

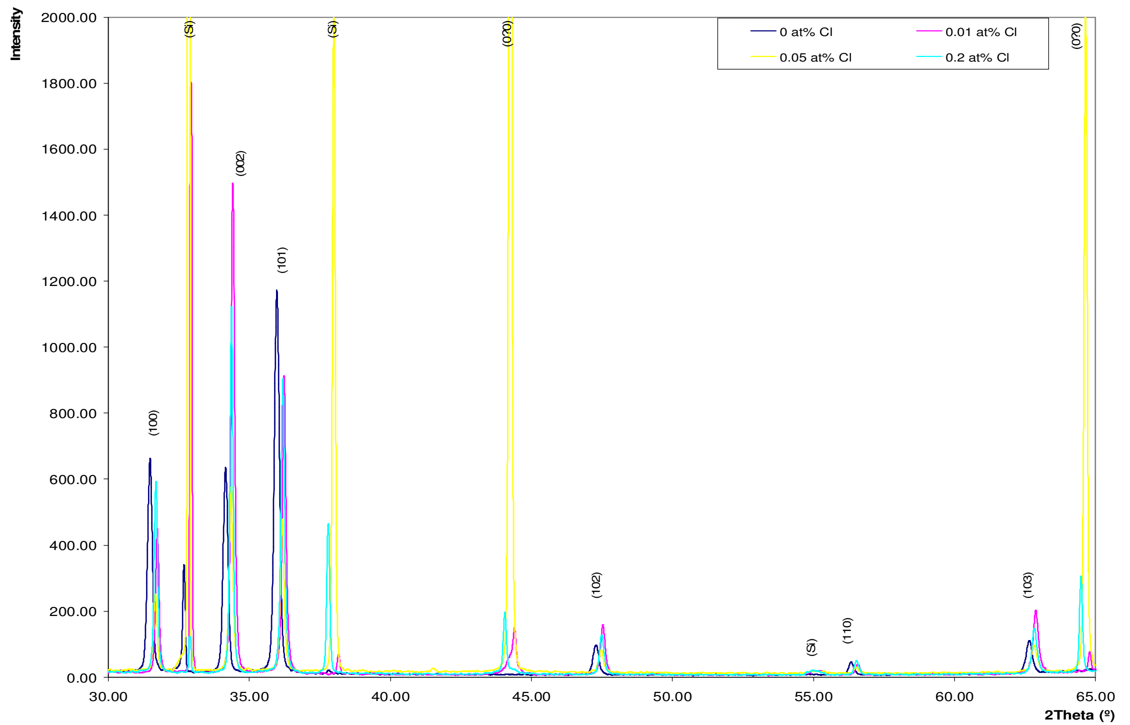

Figure 6.23: XRD pattern on the implanted ZnS thin films annealed in a furnace at 800ºC

6.3.4.4. ZnS Thin Film on a Si Wafer Implanted With Ag and Cl Ions and Annealed in Vacuum.

The annealed samples of doped (Figure 6.25) and undoped ZnS (Figure 6.24) both show a marked improvement in the FWHM of the peaks. The peak position has also moved to a larger cubic crystal lattice, this is evident in the separation of the Si peak and ZnS peak in Figure 6.25, which before annealing was indefinable. This means that the samples have an increased proportion of crystalline material, which leads to this change in peak position and more defined peak position (reduced FWHM).

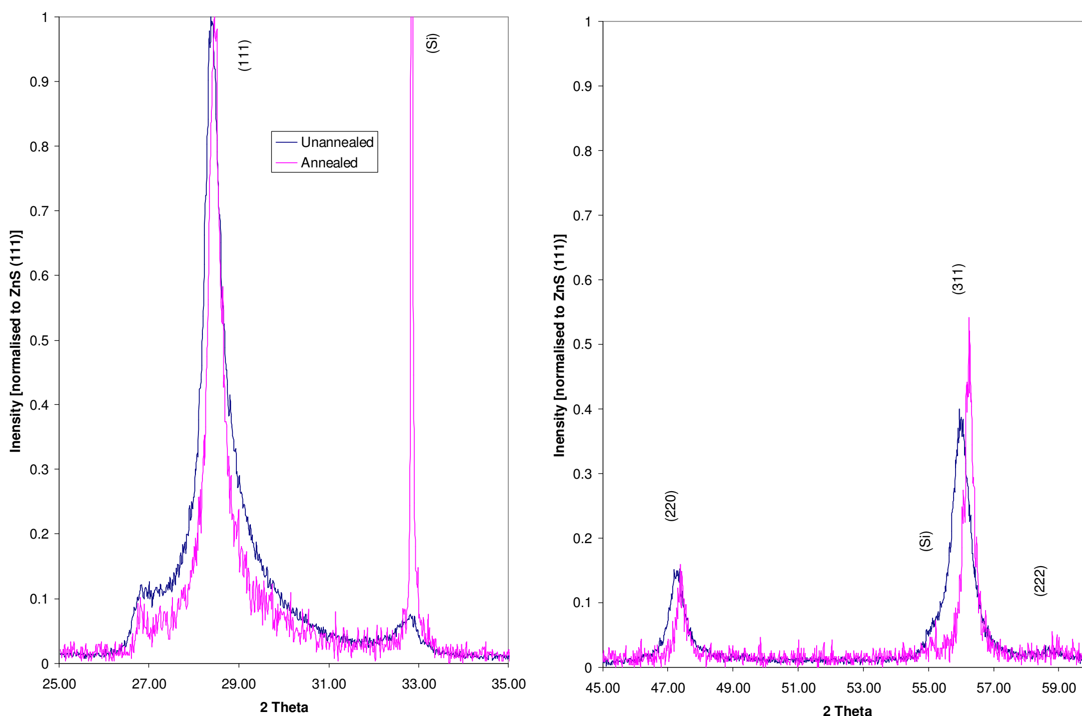

Figure 6.24: XRD Pattern of vacuum annealed and unannealed undoped ZnS.

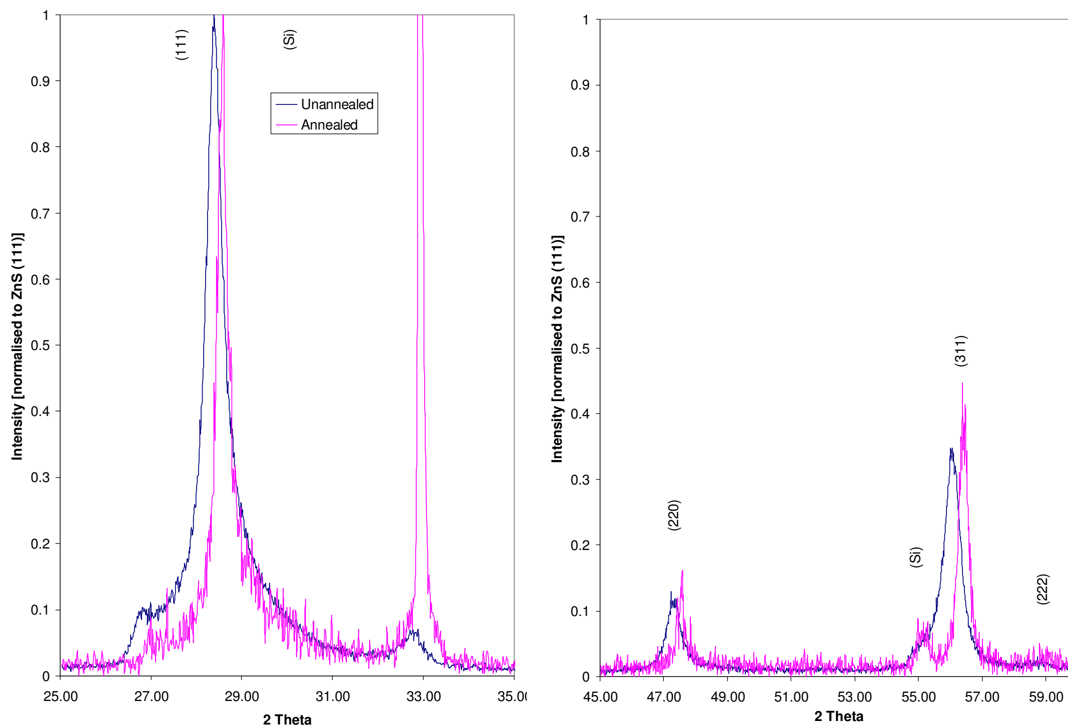

Figure 6.25: XRD Pattern of vacuum annealed and unannealed ZnS implanted with Ag and 0.2at% Cl.

6.3.5 Annealing

Examining the furnace for possible contaminants found the firebricks produced a PL emission when excited with the N_2 laser - 337nm (Figure 6.26).

There were two broad peaks consistent with all the samples - one at 742nm, the other with peak intensity between 527 and 535nm. For one firebrick there was also a broad peak in the 400nm range. Following this test the fire bricks were removed, the furnace given a vacuum clean and samples were placed in a lidded quartz crucible to reduce contaminants and to confine the ZnS:Cl or NaCl.

A calibration of the chamber heater was carried out so that the samples annealed in the vacuum of the chamber. The results of this are in section 3.2.4.1.

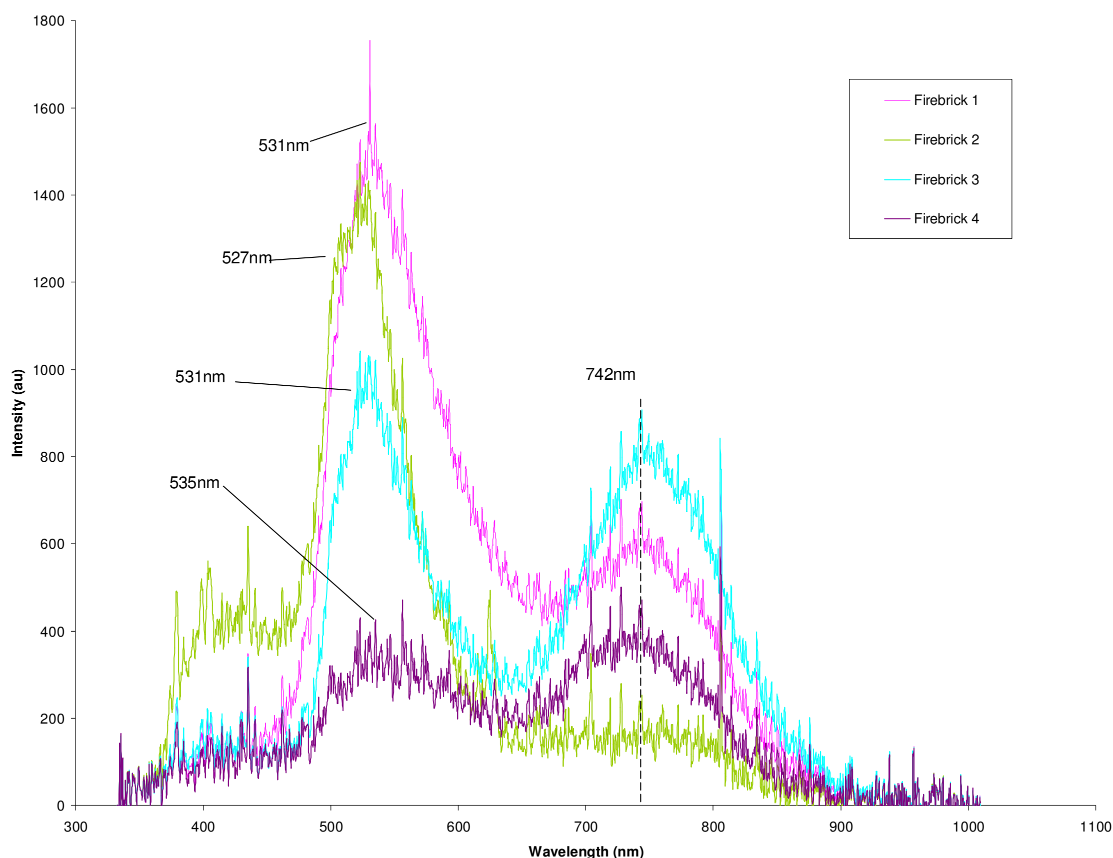

Figure 6.26: PL emission spectra of firebricks used within the furnace when excited by a N_2 laser.

The origin of the peaks in Figure 6.26 was not determined. There are test that could be preformed on the firebrick to determine the chemical composition. However, this was not important to the fabrication of thin film and was only important as a method to characterise an unknown thin film luminescent emission.

6.4 Conclusions

This chapter presents the results of an investigation into doping ZnS thin films to produce the ZnS:Ag,Cl thin film phosphor. Attempts to dope the film by thermal diffusion and by ion implantation have been studied. Of these techniques, ion implantation is the most successful, of the films tested, and has a luminescent emission that is correlated to the doping of the Cl charge compensation dopant. Unfortunately, while these results are interesting from the perspective of being the first report of the use of ion implantation for this material, the luminescent emission produced by the films is insufficient to be of use in thin film phosphor

fabrication. The samples produced emissions but were not the isolated emission associated with the ZnS:Ag,Cl phosphor. The emission spectrum from the thin films were not easily distinguishable from the background without some processing of the data.

6.4.1 Sputter Coating

This technique has been unsuccessful in creating the ZnS:Ag,Cl thin film phosphor, the process did however, oxidise the thin film with a demonstrated conversion from a ZnS lattice to a ZnO lattice. This was determined using XRD by a distinct change in the number, position and magnitude of the peaks and by the luminescent peaks generated via PL.
The emission spectrum for ZnO by Wang [115], who undertook a similar experiment to intentionally create a ZnO thin film from a ZnS thin film, had a singular peak at 377nm. This peak could be attributed to peak labelled as Peak 1 (Section 6.3.1 - Figure 6.8) in the emission spectrum at approximately 383nm. Both significant peaks were accounted for in Leverenz [74] work where they have an emission spectrum of a hexagonal ZnO that has a relative narrow FWHM for the 385nm peak with a broader FWHM for the 505nm peak correlating to Peaks 1 and Peak 2 respectively. The interesting result here is the very dramatic change from ZnS to ZnO, as indicated by both PL and the XRD results. However, this was unfortunately not what was desired of the ZnS thin film.

An additional problem to this technique was the loss of adhesion of the thin film to the substrate. The cause of this was unknown but was likely to be directly or indirectly related to the ZnS:Cl powder as the other components of the experiments were standard between the experiments.

6.4.2 Ion Implantation

The O_2 in the air oxidising the ZnS and the potential slow rate of diffusion are the primary factors affecting the success of the sputtered Ag experiments. These have been removed or reduced as significant factors by using ion implantation in conjunction with thermal annealing under a vacuum.

Comparison of the emission spectra and the characterisation by XRD, the sputter coated and ion implanted samples oxidised into ZnO when annealed in air. With the air removed as a factor in the annealing process of the ion implanted samples, the observed PL emissions can be attributed to a combination of the expected phosphor material based on the doping, and the effect of contaminants during growth and annealing. Large-scale diffusion is less significant now that the dopants are implanted with good distribution within the thin films, therefore requiring a smaller annealing period to incorporate the dopants into the lattice to form luminescent centres. This would indicate that the Ag dopant requires a long annealing duration for the samples to activate, eight hours in the case of the implanted samples.

The ion-implanted samples did not follow any known emission spectrum in their entirety, however when broken down into defined peaks some information was gained from them.

There appears to be a peak at 450nm in some but not all the samples, it is potentially an indication of this phosphor. Interestingly, and importantly, the intensity of this peak is closely related to the Cl doping level, with intensity rising as the doping increases from the expected values of 0.01at% to 0.05at% and then dropping as the concentration is increased to 0.2at%. This is indicative of Cl being incorporated into the lattice as a charge compensator for the Ag, with an optimum concentration potentially lying between 0.05 and 0.2at%

The 570nm-584nm peak, the most defined peak observed, appears to be related to Mn contamination, since it is known that the emission peak of ZnS:Mn can vary from 578nm to 590nm [78]. Manganese contamination has the potential of being introduced in the annealing stage or before implantation during the ZnS growth stage. The RF magnetron sputtering chamber used was one that was primed for co-sputtering of ZnS and ZnS:Mn to determine optimum manganese concentration. Hence, when using this chamber and the ZnS solid target, Mn appears to have had the opportunity to cause contamination of the thin film. An alternative RF Magnetron sputtering system was utilized to grow the ZnS thin films, which primarily grows ZnS:Mn thin films and had not undergone the intensive cleaning process to which the primary system had.

The delamination of the thin film from the substrate at the 27.5% annealing temperature had not been seen within the group for ZnS thin films. In this case, it could be due to either the long duration between growth and annealing during which time the samples had been implanted, due to the ion implantation process or the phosphor.

Ion implantation was utilised to overcome the problem of imprecise doping and dopes the ZnS thin film with a high level of accuracy. Compared to conventional doping methods such as diffusion, ion implantation offers better reproducibility, lower processing temperatures and a more precise control over the dopant profile.

The PL spectra created by Nakanishi [115] who simultaneously evaporated ZnS and Ag and embedded the samples in ZnS:Cl powder contained emissions originating from wavelengths above 550nm. Although the emission spectra do not match the ion-implanted samples that were annealed under vacuum it does indicate that this might not be an abnormality observed only in this set of experiments.

6.4.3 Ion Beam Analysis

In the results presented in Table 6.5 are those obtained for samples 2 and 3 by RBS and are in Thin Film Units (10^{15}atoms/cm^2). The S/Zn ratio is about 10:9 which obtained by integrating areas in the spectra - this procedure has a small absolute uncertainty.

Table 6.5: Concentration of Zn and S in the thin film samples tested by RBS.

Sample number	Zn		S		Ratio	
	Detector A	Detector B	Detector A	Detector B	Detector A	Detector B
2	1770	1770	1948	1951	0.908	0.907
3	1784	1786	1998	1981	0.893	0.902

Only samples 2 and 3 produced results, because they had a smooth surface and the rough samples cannot be analysed with great precision since the roughness severely distorts the spectra in ways that cannot currently be calculated.

Unfortunately, neither Ag nor Cl were detected by PIXE, and the Ag is only just visible in the RBS. A reliable measurement cannot be made near the Zn edge in the presence of significant pileup, where there is overlapping signals from different sources. However, Ag was detected, as with the RBS of the films deposited from the ZnS:Ag,Cl source.

6.4.4 XRD

6.4.4.1. Ion Implantation – Effects on Structure

From the XRD analysis undertaken, there is no detectable change to the crystal structure induced by the implantation process. The Cl and Ag ions have been added to the thin film but the bulk polycrystalline structure has not been significantly affected. The thin films were not annealed before implantation to promote crystallinity. Therefore, there would be a reduced effect on disordering by the implantation compared with the thin film if it had been annealed before implantation.

6.4.4.2. Thermal Annealing – in Air

Once these thin films had been annealed in a Carbolite CWF 1200 furnace at 700ºC they were emitting a visible emission when excited with a N_2 (337nm), but with an emission spectrum that was different to the one that was captured using the same PL setup for the ZnS:Ag,Cl powder sample.

To verify if the sample had changed to its hexagonal form due to the high temperatures, XRD was an obvious choice to determine structure. It actually showed that the ZnS thin film had not changed from the cubic to hexagonal form but had oxidised into hexagonal ZnO.

This is consistent with the PL results as ZnS can oxidise at 700ºC to produce ZnO and will emit PL emission (354 - 387nm) [116]. ZnO is most stable in the wurtzite phase (hexagonal) [30], which is the structure that has been the principle structure when ZnS oxidised.

Annealing of a ZnS thin film was an important property in the fabrication of ZnO phosphor thin films. Wang [115] uses thermal evaporation to create ZnO from ZnS thin films and reports that temperatures above 400ºC could cause this oxidisation to occur.

An example that confirmed what was shown in the XRD patterns was an XRD pattern that was partially oxidised ZnS and was therefore a mixture of ZnS and ZnO [117].

6.4.4.3. Annealing in Vacuum

The annealing of the thin film samples under vacuum has improved the crystal structure and meant that the sample has not oxidised into ZnO. Previously hidden peaks have been made visible by the narrowing of the peaks and their movement to increased angles.

In overall conclusion, it is clear that doping of ZnS thin films to produce ZnS:Ag,Cl is not trivial, particularly since the material is highly sensitive to contamination effects when processed at the high temperatures required to induce dopant diffusion. Ion implantation is a potential method for controlled doping, but further studies would be required to optimise.

7 Conclusions and Future Work

The aim of this work was to study the growth and characterisation of thin film phosphors for use in neutron scintillation detection. This has been addressed by the research presented in this thesis. However, attempts to improve the detection capabilities of the scintillator for increased emission intensity, increase rate of measurements, improved gamma discrimination or reduced pixel area, have not been successful. Hence, the main area of progress has come from developing an improved understanding of the limitations of thin film fabrication within the context of this work. In this chapter, a summary of conclusions from the work undertaken is presented, along with suggestions for future work.

Much of the work was concerned with depositing thin films of ZnS:Ag,Cl, using techniques which are constantly used for ZnS:Mn. However difficulties in controlling the dopancy of the ZnS:Ag,Cl film were encountered.

In general the ZnS:Ag,Cl phosphor was difficult to work with due to the combination of dopants and the extremely small dopant concentration. The problem was enhanced by limited information in the literature on the co-activator dopant in the ZnS:Ag phosphor, chlorine, which is essential for this phosphors luminescent characteristics.

The optimum concentration of chlorine is that of the optimum concentration of silver, as there is an equal amount of chlorine required to charge compensate for the silver. This makes a dopant level of 0.01at% for silver and chlorine in the ZnS:Ag,Cl phosphor putting it below the range of most measurement techniques. In practice, for manufacture, this was found to be incorrect as an excess of chlorine is required for the phosphor to be synthesised, with the surplus washed away to purify the phosphor. However, sputtering does not have this excess, and loss mechanisms within this technique has meant that the chlorine was not present in sufficient quantities to permit the effective incorporation of silver into the zinc sulphide lattice.

7.1 Characterisation of the Phosphors

The initial experiments required a characterisation of the scintillator currently in use at ISIS for its luminescent properties. Photoluminescence tests included - peak emission intensity, distribution of emission intensities, transient decay time and uniformity of emission intensity. The ISIS self-supporting scintillator and its powder counterpart from Phosphor Technology were compared by their emission intensity and distribution of emission intensities when excited by α-particles and UV light to create radioluminescence and photoluminescence.

The primary factor for why alternatives to ZnS:Ag,Cl were being considered was due to the slow luminescent decay time. Although it has a decay time of 200ns, which is on a similar scale to other phosphors with rapid decay times, there is also a dominating slower afterglow of 30µs. The range of measured decay times of the ZnS:Ag phosphor (1µs -37µs) indicated difficulty in defining a method of characterisation that would generate values consistent with those reported in the literature (30µs). Measures to increase the intensity of emission detected were implemented for the purpose of eliminating the effect of the interference caused to the decay time measurement by the laser pulse. A monochromator had been used to isolate the decay time signal at wavelengths close the peak emission and comparing these with the results from the full emission (by removing the monochromator). This resulted in values that more closely represented those in the literature and generated a repeatable 30µs result. This was not a significant change to those decay constants measured while using the monochromator, hence the emission appears to be dominated by a single decay process. This contradicts literature that has ZnS:Ag,Cl having two decay rates. However, the two decays would not be resolved by this method, as the two decay rates are not limited to a single range of wavelengths as they might for a phosphor with an indirect bandgap.

The phosphor was for use as a detector of alpha particles, but was primarily characterised by PL measurements. The more appropriate method would be for alpha or tritium excitation, however the weakness of emission from the bulk phosphors with the alpha sources available to this project made this technique unsuitable for luminescence characterisation. The random nature of radiation emission also limits decay time measurements that require a pulse source.

The closeness of fit of the decay time and emission spectra of the ISIS wafer and the Phosphor Technology powder indicated it was a suitable material for use as a potential sputtering target in RF magnetron sputtering.

7.2 Deposition and Characterisation of Thin Films

Once the characterisation of the bulk phosphors had been completed, RF magnetron sputtering was investigated as a method of growing thin films from a commercial source of the phosphor material. The thin films were grown to a range of thicknesses to optimise the phosphor for maximum photoluminescent excitation. The deposition temperature was varied to investigate the effect on growth rate, which effects thin film quality. The annealing temperature was varied to investigate its effect on crystallinity, which effects emission intensity.

The thin films were examined for their thickness uniformity, surface roughness, PL, decay time, alpha luminescence and the uniformity of these over the area of the sample. Crystal structure and composition were tested using XRD and ion beam analysis.

The thin films grown from a ZnS:Ag,Cl target by RF magnetron sputtering were good quality in terms of thickness uniformity, roughness and cohesion to the substrate. However, they did not produce a visible emission when excited by a 337nm nitrogen laser or alpha particles from a ^{241}Am source. Hence, the conclusion is that RF magnetron sputtering was not an appropriate technique for deposition of phosphor materials where there is sensitivity to the charge compensation, which appears to be the case here where Cl is the issue.

The significant aspect of the ion beam analysis undertaken on the thin films to determine composition was that while no chlorine was detected it was still possible that due to the small dopant quantities there was chlorine present but was below the detection limit.

7.3 Annealing of Thin Film

Once RF magnetron sputtering was indentified as an unsuitable techniques of doping thin films of ZnS:Ag,Cl, alternatives investigated were sputter coating and ion implantation. Both techniques required annealing for dopant diffusion and phosphor activation by incorporation.

Annealing in vacuum and annealing in a furnace were investigated as methods to improve thin film crystallinity as well as to cause the dopant ions to diffuse throughout the lattice. The samples annealed in air were found to have oxidised from ZnS into ZnO, hence methods of applying heat to the samples would require an oxygen free atmosphere.

XRD was used to determine the chemical composition and structure of the powders and thin film samples. It was also able to give an indication of the lattice spacing and grain size. In particular, the technique demonstrated a clear transition from ZnS to ZnO when attempting to increase the doping efficiency for Cl by thermally annealing the thin films in air.

7.4 Future work

7.4.1 Deposition

The method used to deposit thin films of ZnS:Ag,Cl was unsuccessful. However, not all variables were examined. Alternative processing gases could still potentially deliver a viable thin film phosphor using RF magnetron sputtering. With an optimised mixture of Ar and Cl, an increased concentration of Cl would be available and would intentionally introducing Cl contamination in the ZnS thin films. Cl would be present as the sputtered material condenses on the substrate to form a thin film and so be capable of countering a charge imbalance as Ag is incorporated into the ZnS lattice. During this study Cl was not considered as an alternative processing gas because of chlorine's reactivity, which could cause corrosion of the sputtering system.

Co-sputtering is an alternative method that could be investigated to increase the Cl concentration within the chamber. The simultaneous sputtering of a ZnS:Cl target with a higher than optimum concentration of Cl and a ZnS:Ag target, would increase the potential for Cl incorporation in to the thin film. The Cl concentration could be increased further by applying a

greater power to the ZnS:Cl target than the ZnS:Ag target, hence increasing the sputter rate from the ZnS:Cl target. However, only with a series of ZnS:Ag targets with differing dopant concentrations can this be achieved for the correct ratios to be derived.

For a deposition system where excess Cl was not required, silver chloride (AgCl - silver horn), a crystalline solid with a melting point of 455ºC [30], could be used as a second target to ZnS. This would make it possible to optimise Ag doping by varying the ratios of sputtered target delivered to the growth substrate.

7.4.2 Annealing

A different approach would be required to make the thermal annealing using the furnace more feasible so that the ZnS thin film would not oxidise at temperatures above 400℃ [115] in air. A non-reactive processing gas used in a confined area, such as Ar in an airtight crucible would significantly reduce oxygen content, so allow for higher annealing temperatures. Using an Ar-Cl atmosphere could enhance the phosphor emission by having Cl available to counteract loses of the charge compensator. This would act as a method to remove the oxygen content as well as introducing an excess of the charge-compensator to the thin film material.

An alternative to thermal annealing in air or under vacuum would be to use a focused laser beam from a KrF Excimer laser (248nm) [88-90]. This technique applies an intense pulse of energy for a defined period in a defined area. This gives the ions and atoms in the beam area the energy required for small-scale diffusion, improving localised crystallinity. Hence, ion implanted thin films are more suitable than sputtered samples for laser processing, as the sputtered samples require large-scale solid-state diffusion. Laser processing has been used successfully on ZnS:Mn phosphor thin films. A series of pulses, generally between one and five, are incident on a thin film. The samples are under increased pressure to reduce ablation effects, where the material is evaporated. The gas used is typically inert Ar, but the use of reactive gases have been employed and could be a mixture of Ar and Cl (with suitable enhancement of safety equipment). This would reduce Cl loss and potentially provide the excess of Cl required for effective incorporation of Ag into the ZnS lattice.

Oxygen contamination of ZnS:Ag,Cl (bulk) degrades the emission intensity as it forms either an oxide layer or ZnO[118]. $AlCl_2$ was been used to react with the oxygen to deoxygenate the sample. Not mentioned in the journal paper, was that the Al and Cl would also potentially increase the intensity of the luminescent emission. Both the Al and Cl would be capable of becoming the co-dopant to the Ag and acting as additional charge compensators.

An accurate experimental value for Cl and Ag diffusion in ZnS thin films would be required so that effective annealing could be accomplished. Diffusion experiments have been carried out on Ag in thin film ZnS formed by spray pyrolysis using XRF [80]. XRF is not as sensitive as RBS/PIXE for the concentration of dopants that were used in the ZnS:Ag,Cl phosphor, but using Ag with quantities that were detectable by XRF the diffusion coefficient was measured. The sample was heated, the concentration curve was measured and diffusion rate (Flicks Law) was calculated from this. The resultant diffusion rates were very small, at between 3×10^{-13} cm^2/s and 5×10^{-12} cm^2/s. Slow diffusion like this would mean that the ion-implanted work where the film is approx 800nm in thickness and the dopants are distributed throughout the thin film would have the most post potential for quick results.

For a truer understanding of the thin films, it is important to know what has been produced, as well as the components were that were used to create the thin film. To ensure that it was the lack of Cl and not the lack of detection of Cl due to the methods used, it would have been advisable to have found an alternative method of analysing the thin film composition. Cl and Ag have been detected in a ZnS:Ag,Cl phosphor using Secondary Ion Mass Spectroscopy [35] and this could be a potential technique to determine dopant concentrations where RBS and PIXE had not been successful.

7.4.3 Radioluminescence

A differently designed setup would be required to enhance RL measurements. It would likely need a more active alpha source than the one available (5μCi) and an improved technique to

collect a greater proportion of the emission. A more active ^{241}Am source (25μCi) was used [42], with the result that there was a detected decay time of 4μs and an emission spectrum with peak intensity at ~450nm. Hence, a number of alpha sources could be used over an increased area of the phosphor, to enhance the amount of emission. An increase in the detection intensity could be achieved by using larger diameter or multiple optical fibres in combination with a lens (Figure 7.1).

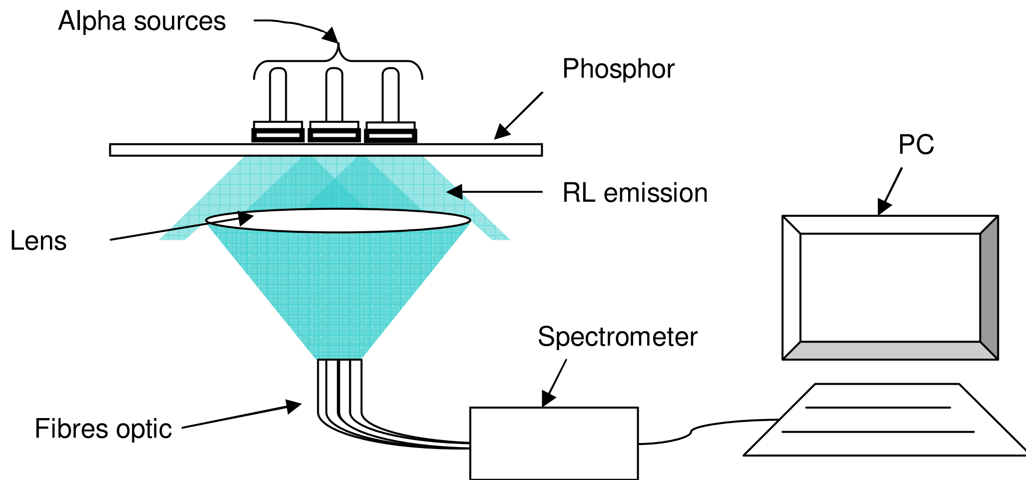

Figure 7.1: An example of how the intensity of RL emission increased.

The amount of alpha particles interacting with the phosphor can be increased by enclosing the phosphor and alpha source in a vacuum. The alpha particles can be stopped by air, so removing it will give the alpha particles a longer mean free path. A design using this concept for improving RL intensity measurements is shown in Figure 7.2.

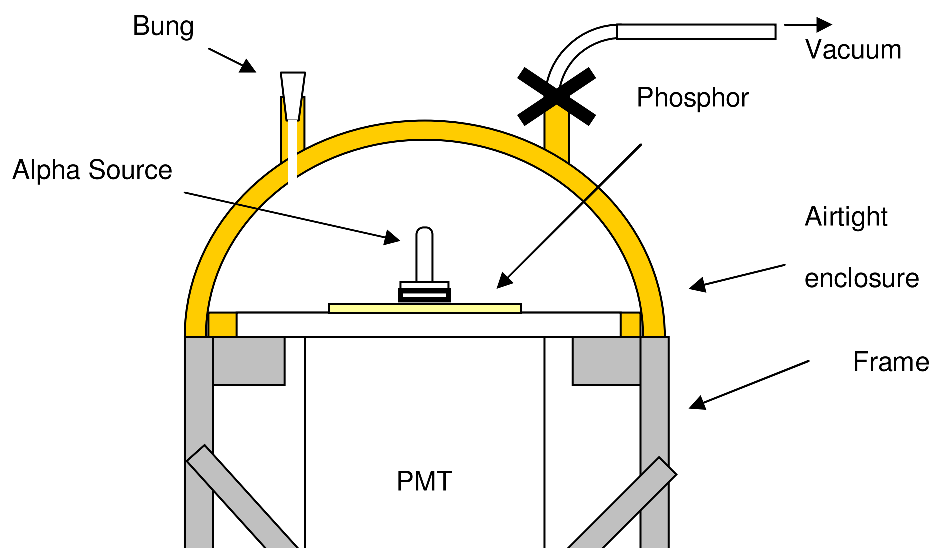

Figure 7.2: An example of alpha luminescent experiment using a vacuum to improve emission intensity.

A version of this was investigated as part of this research as a possible approach for use with a PMT for decay measurements. However, the method looked at was not determined to be safe for the equipment and was not followed through to take measurements.

7.4.4 Micro-engineering

The main advantage of thin film growth was to create a phosphor in a form that could be used as the active part of a microstructure designed to enhance scintillation detection in terms of spatial resolution and in terms of enhanced signal to noise ratio. The project has unfortunately suffered from a range of setbacks in terms of a luminescent thin film, so not allowing for the study of thin film microstructure techniques to combine phosphor and detector. The work presented relates primarily to an investigation into the growth and characterisation of thin film ZnS:Ag,Cl phosphor layers.

Only when a thin film of radioluminescent phosphor was formed and shown to produce a detectable emission, could the thickness be optimised for maximum emission with negligible gamma induced emission. A balance would be created between optimising against gamma interactions, whist maintaining a suitable level of alpha and tritium detection.

Once a radioluminescent film was formed it would then be compared to self supporting wafer such as that used by ISIS. This would determine if thin films could be a viable technique for improving neutrons detection capabilities.

Although in its infancy, a large amount of work has been done in the last five years on Si based detectors, such as Si, SiN and SiC [119-121]. This is where a neutron converter is directly coupled to the Si component, ions are created during the reaction of the neutron with the converter and detected by the Si detector. These charged particles are electrically propelled towards the detector and create electron-hole pairs in the detector. These electron-hole-pairs create the electronic charge that is measured to determine the presence of neutrons.

Neutron converters mentioned in this work are:

- Enriched Lithium (^{6}Li) in the form of ^{6}LiF and ^{6}Li [119, 122, 123]
- Boron (B) in the form of ^{10}B, MgB_2, pBN, B_4C and $Bi_4Ge_3O_{12}$ (BGO)[122-126]
- Synthetic diamond [127, 128]

Multi-layers, different configurations of detector, converter and electrical contact, as well as microstructures using etched Si with a neutron converter as the back fill material have been investigated. The etched Si has generally been circular wells filled with powdered ^{6}LiF or B converter with a thin film of the converter grown on top of this powder to form a cap as well as be an additional converter volume. Alternatives to the etched wells are an oscillating waves cut across the wafer (appears like a coherent wave pattern) and a rounded square blocks of CsI(Tl) covered with Gd_2O_3 - designs to increase the surface area around the neutron capture component.

The Si component replaces the phosphor component in the scintillator, hence removing the need for optical collection using fibre optics and photomultiplier tubes. Although this has the potential to replace RL phosphors, there would be a crossover for some designs relating to phosphor microstructures to be interchangeable with Si based microstructures.

Comparison of the efficiency of the scintillator to semiconductor-based detector is limited. Detection efficiencies of the semiconductor range greatly, without clear explanation. This makes the comparison of effectiveness of the Si compared to conventional detectors difficult, but still interesting area of development.

As the self-supporting scintillator wafers have been engineered to increase their detection capabilities by rotating them, thin films and micro engineering have the potential to increase detection capabilities. Changing the angle of interception that the neutrons have with the wafer increases the capture capabilities but maintains the light capture capabilities. Growing a thin film of a ZnS based phosphor was designed as being the stepping stone to creating a neutron detector, but would require a neutron converter as well as the phosphor.

The work did not progress from the phosphor stage and therefore optimisation of scintillator thin film thicknesses was not investigated. Although thin film deposition of ZnS:Ag,Cl for

radioluminescent detection was not successful, this does not rule out other phosphors being suitable, leading to thin film detectors for neutron diffraction analysis.

Assuming a thin film can be grown, a draw back to having two layers, one of a phosphor and one of a neutron converter, is that to create a visible emission it requires one process to follow on from the last. The neutron must interact with the neutron converter, and then the products of the reaction must travel in the direction of the phosphor component and interact with that. A technique to make this more efficient would be to have more than one layer. An investigation into having a sandwich of phosphor (Ph) and neutron converter (NC) in the arrangement of Ph-NC-Ph would mean that it would increase the quadrants in which the products of the neutron converter ration could interact with the phosphor. General theory suggests that:

- The front side phosphor should be thinner than the backside as neutrons would be required to penetrate through this to reach the neutron converter.
- The neutron converter would be required to be thicker than the phosphor layers as neutrons penetrate a greater distance than alpha and tritium particles.
- The scintillator must still be sufficiently thin for emission to escape and be detected without it being reabsorbed.

This theory should also be able to be extended to the use of many layers, where each addition of the two layers improving the detection capabilities.

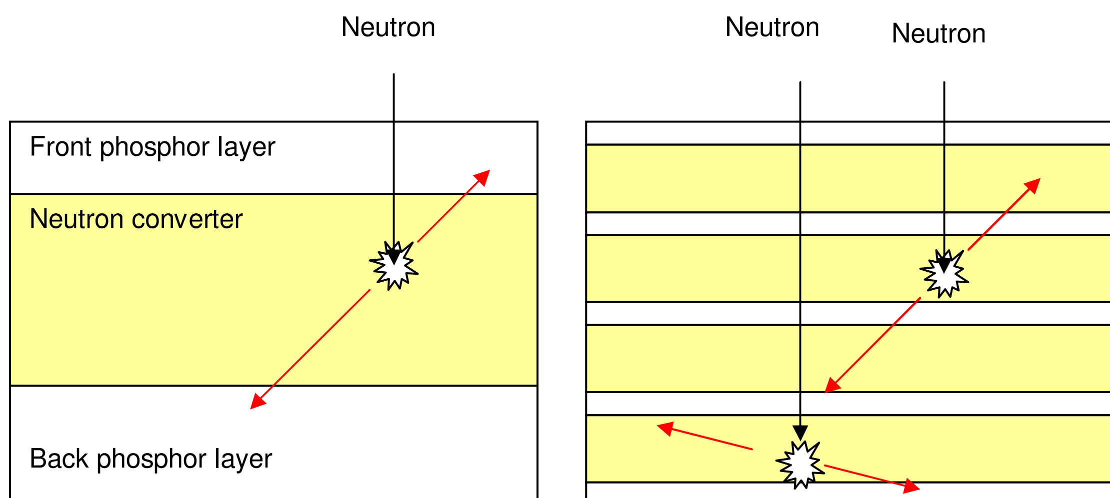

Figure 7.3: Proposed layered neutron converter and phosphor for potential improvement in detection using thin films.

This technique relies on the lattice of the two layers being similar to each other so that one layer will grow on the previous layer. The technique of RF magnetron sputtering works well for growing single composition thin films from one target or multiple targets (co-sputtering) if the two targets are made of the same primary composition (e.g. ZnS and a ZnS:Mn target).

As discussed in Chapter 2, a mixture of the two components is preferable and can be viewed as an extension of the layered approach. However, having a mixture of neutron converter and phosphor has a limitation on the thickness, as at thicknesses that are approaching the grain size of these components, hence the area in which they can form cohesion is limited. The way the self-supporting scintillator counters the lack of adhesion between the components is to use a binding agent, a similar technique could be used in RF magnetron sputtering, as an intermediate layer is sandwiched between two others to improve bond linkage between the components.

7.4.5 Co-dopant

The alternative charge compensator for the ZnS:Ag phosphor other than Cl is Al. However, it was not investigated here due to its high reactivity to oxygen and its subsequent high stability once in its oxidised form. Therefore, utilisation of Al as a charge compensator would require the deposition and annealing under constant vacuum or in a controlled oxygen free atmosphere until the thin film phosphor was fully formed, making it a potential option if a suitable process can be developed.

7.5 Summary

The challenge of charge compensation doping has been highlighted, and the potential for ion implantation has been studied as a doping technique. This represents the first study of the use of ion implantation for ZnS:Ag,Cl thin film phosphor work and the results indicate the merit of further study. Once a suitable thin film phosphor has been demonstrated, the fabrication of microstructures to channel the RL excited light emission to integrated detectors would be an interesting micro-engineering project.

8 References

References

[1] J. P. Duke, D. J. S. Findlay, A. P. Letchford, G. R. Murdoch and J. W. G. Thomason, "Design and operation of a gas scattering energy spectrometer for the ISIS RFQ accelerator test stand," *Nuclear Instruments and Methods in Physics Research Section A: Accelerators, Spectrometers, Detectors and Associated Equipment,* vol. 538, pp. 127, 2005.

[2] N. J. Rhodes, A. G. Wardle, A. J. Boram and M. W. Johnson, "Pixelated neutron scintillation detectors using fibre optic coded arrays," *Nuclear Instruments and Methods in Physics Research Section A: Accelerators, Spectrometers, Detectors and Associated Equipment,* vol. 392, pp. 315, 1997.

[3] I. M. Sosnowska and B. T. M. Willis, "Neutrons and synchrotron X-rays in materials science," *J. Alloys Compounds,* vol. 286, pp. 174-179, 5/5, 1999.

[4] B. Lebech, "Bragg diffraction from magnetic materials," *Physica B: Condensed Matter,* vol. 318, pp. 251-260, 6, 2002.

[5] M. Ishikawa, H. Kumada, K. Yamamoto, J. Kaneko, G. Bengua, H. Unesaki, Y. Sakurai, K. Tanaka and T. Kosako, "Development of a wide-range paired scintillator with optical fiber neutron monitor for BNCT irradiation field study," *Nuclear Instruments and Methods in Physics Research Section A: Accelerators, Spectrometers, Detectors and Associated Equipment,* vol. 551, pp. 448, 2005.

[6] M. Tardocchi, A. Pietropaolo, R. Senesi, C. Andreani and G. Gorini, "Development of resonant detectors for epithermal neutron spectroscopy at pulsed neutron sources," *Nuclear Instruments and Methods in Physics Research Section A: Accelerators, Spectrometers, Detectors and Associated Equipment,* vol. 518, pp. 259, 2004.

[7] V. Illingworth and W. Czarnacki, *Dictionary of Physics.* Penguin Books, 2000.

[8] P. King, B. Jones and D. Clements, "ISIS annual report 2008," ESP Colour Limited and STFC Photographic and Reprographic Services, Tech. Rep. RAL-TR-2003-050, 2008.

[9] P. N. Cooper, *Introduction to Nuclear Radiation Detectors.* Cambridge University Press, 1986.

[10] Y. Tabata, Y. Ito and S. Tagawa, *Handbook of Radiation Chemistry.* CRC Press, 1991.

[11] J. B. Czirr, G. M. MacGillivray, R. R. MacGillivray and P. J. Seddon, "Performance and characteristics of a new scintillator," *Nuclear Instruments and Methods in Physics Research Section A: Accelerators, Spectrometers, Detectors and Associated Equipment,* vol. 424, pp. 15, 1999.

[12] M. Katagiri, "Development status of position-sensitive neutron detectors for J-PARC in JAERI--a comprehensive overview," *Nuclear Instruments and Methods in Physics Research Section A: Accelerators, Spectrometers, Detectors and Associated Equipment,* vol. 529, pp. 254, 2004.

[13] M. Katagiri, M. Matsubayashi, K. Sakasai, T. Nakamura, M. Ebine, A. Birumachi and N. Rhodes, "A compact neutron detector using scintillators with wavelength shifting fibers by

backside readout method," *Nuclear Instruments and Methods in Physics Research Section A: Accelerators, Spectrometers, Detectors and Associated Equipment,* vol. 529, pp. 313, 2004.

[14] T. Nunomiya, N. Nakao, P. Wright, T. Nakamura, E. Kim, T. Kurosawa, S. Taniguchi, M. Sasaki, H. Iwase, Y. Uwamino, T. Shibata, S. Ito and D. R. Perry, "Measurement of deep penetration of neutrons produced by 800-MeV proton beam through concrete and iron at ISIS," *Nuclear Instruments and Methods in Physics Research Section B: Beam Interactions with Materials and Atoms,* vol. 179, pp. 89-102, 2001.

[15] R. K. Crawford, J. R. Haumann, J. E. Epperson, P. Thiyagarajan, A. J. Schultz, G. P. Felcher, D. G. Montague and R. J. Dejus, "Experience with position-sensitive neutron detectors at the Intense Pulsed Neutron Source," *Nuclear Instruments and Methods in Physics Research Section A: Accelerators, Spectrometers, Detectors and Associated Equipment,* vol. 299, pp. 17-24, 1990.

[16] R. Bedogni, A. Esposito, C. Andreani, R. Senesi, M. P. De Pascale, P. Picozza, A. Pietropaolo, G. Gorini, C. D. Frost and S. Ansell, "Characterization of the neutron field at the ISIS-VESUVIO facility by means of a bonner sphere spectrometer," *Nuclear Instruments and Methods in Physics Research Section A: Accelerators, Spectrometers, Detectors and Associated Equipment,* vol. 612, pp. 143-148, 12/21, 2009.

[17] R. G. Cooper, "SNS detector plans," *Nuclear Instruments and Methods in Physics Research Section A: Accelerators, Spectrometers, Detectors and Associated Equipment,* vol. 529, pp. 394-398, 8/21, 2004.

[18] T. A. Gabriel, J. R. Haines and T. J. McManamy, "Overview of the Spallation Neutron Source (SNS) with emphasis on target systems," *J. Nucl. Mater.,* vol. 318, pp. 1-13, 5/15, 2003.

[19] C. L. Melcher, "Perspectives on the future development of new scintillators," *Nuclear Instruments and Methods in Physics Research Section A: Accelerators, Spectrometers, Detectors and Associated Equipment,* vol. 537, pp. 6, 2005.

[20] K. Sakai, K. Hirota, T. Adachi, K. Ikeda, T. Morishima, H. M. Shimizu, M. Furusaka, S. Sato, Y. Kiyanagi and N. Sakamoto, "Development of position-sensitive neutron detector based on scintillator," *Nuclear Instruments and Methods in Physics Research Section A: Accelerators, Spectrometers, Detectors and Associated Equipment,* vol. 529, pp. 301, 2004.

[21] L. A. Wraight, D. H. C. Harris and P. A. Egelstaff, "Improvements in thermal neutron scintillation detectors for time-of-flight studies," *Nuclear Instruments and Methods,* vol. 33, pp. 181-193, 3/2, 1965.

[22] S. Shionoya and W. M. Yen, *Phosphor Handbook.* CRC Press, 2000.

[23] K. Hirota, S. Satoh, K. Sakai, T. Shinohara, K. Ikeda, K. Mishima, S. Yamada, T. Oku, J. Suzuki, M. Furusaka and H. M. Shimizu, "Development of neutron Anger-camera detector based on flatpanel PMT," *Physica B: Condensed Matter,* vol. 385-386, pp. 1297-1299, 11/15, 2006.

[24] M. Matsubayashi and K. Soyama, "Preliminary examination of a CCD camera with a scintillator coated fiber optic plate for neutron imaging," *Nuclear Instruments and Methods in Physics Research Section A: Accelerators, Spectrometers, Detectors and Associated Equipment,* vol. 529, pp. 384-388, 8/21, 2004.

[25] G. C. Tyrrell, "Phosphors and scintillators in radiation imaging detectors," *Nuclear Instruments and Methods in Physics Research Section A: Accelerators, Spectrometers, Detectors and Associated Equipment,* vol. 546, pp. 180-187, 7/1, 2005.

[26] C. F. G. Delaney and E. C. Finch, *Radiation Detectors - Physical Principles and Applications.* Oxford Science Publications, 1992.

[27] J. Schelten, M. Balzhauser, F. Hongesberg, R. Engels and R. Reinartz, "A new neutron detector development based on silicon semiconductor and ^{6}LiF converter," *Physica B: Condensed Matter,* vol. 234-236, pp. 1084, 1997.

[28] J. Schelten, R. Reinartz, R. Engels, M. Balzhauser, J. Lauter, W. Schafer and K. D. Muller, "Position-sensitive neutron detection with ^{6}LiF layers on silicon semiconductors," *Nuclear Instruments and Methods in Physics Research Section A: Accelerators, Spectrometers, Detectors and Associated Equipment,* vol. 389, pp. 447, 1997.

[29] C. W. E. van Eijk, "Inorganic scintillators for thermal neutron detection," *Radiation Measurements,* vol. 38, pp. 337, 2004.

[30] D. R. Lide, *Handbook of Chemistry and Physics.* CRC Press, 1990-1991.

[31] G. W. C. Kaye, T. H. Laby, J. G. Noyes and G. F. Phillips, Eds., *Kaye & Laby Tables of Physical and Chemical Constants.* 1995.

[32] A. R. Spowart, "Measurement of the gamma sensitivity of granular and glass neutron scintillators and films," *Nuclear Instruments and Methods,* vol. 82, pp. 1, 1970.

[33] C. W. E. van Eijk, A. Bessiere and P. Dorenbos, "Inorganic thermal-neutron scintillators," *Nuclear Instruments and Methods in Physics Research Section A: Accelerators, Spectrometers, Detectors and Associated Equipment,* vol. 529, pp. 260, 2004.

[34] Y. Saito, K. Mishima, M. Matsubayashi, I. C. Lim, J. E. Cha and C. H. Sim, "Development of high-resolution high frame-rate neutron radiography," *Nuclear Instruments and Methods in Physics Research Section A: Accelerators, Spectrometers, Detectors and Associated Equipment,* vol. 542, pp. 309, 2005.

[35] M. Shiiki and O. Kanehisa, "Electroluminescence of zinc sulfide thin films activated with donors and acceptors," *Journal of Crystal Growth,* vol. 117, pp. 1035, 1992.

[36] K. Yasuda, S. Usuda and H. Gunji, "Properties of a YAP powder scintillator as alpha-ray detector," *Applied Radiation and Isotopes,* vol. 52, pp. 365, 2000.

[37] S. A. McElhaney, J. A. Ramsey, M. L. Bauer and M. M. Chiles, "A ruggedized ZnS(Ag)/epoxy alpha scintillation detector," *Nuclear Instruments and Methods in Physics Research Section A: Accelerators, Spectrometers, Detectors and Associated Equipment,* vol. 299, pp. 111-114, 1990.

[38] D. E. Husk and S. E. Schnatterly, "Photoluminescent efficiency of Y_2O_2S:Eu and ZnS:Ag phosphors as a function of irradiation intensity over 9 orders of magnitude," *Journal of the Optical Society of America B (Optical Physics),* vol. 7, pp. 2226, 1990.

[39] N. Kubota, M. Katagiri, K. Kamijo and H. Nanto, "Evaluation of ZnS-family phosphors for neutron detectors using photon counting method," *Nuclear Instruments and Methods in Physics Research Section A: Accelerators, Spectrometers, Detectors and Associated Equipment,* vol. 529, pp. 321, 2004.

[40] S. Usuda, "Simultaneous counting of [alpha]-, [beta]([gamma])-rays and thermal neutrons with phoswich detectors consisting of ZnS(Ag), 6Li-glass and/or NE102A scintillators," *Nuclear Instruments and Methods in Physics Research Section A: Accelerators, Spectrometers, Detectors and Associated Equipment,* vol. 356, pp. 334, 1995.

[41] T. L. White and W. H. Miller, "A triple-crystal phoswich detector with digital pulse shape discrimination for alpha/beta/gamma spectroscopy," *Nuclear Instruments and Methods in Physics Research Section A: Accelerators, Spectrometers, Detectors and Associated Equipment,* vol. 422, pp. 144-147, 2/11, 1999.

[42] M. Matsubayashi and M. Katagiri, "Development of scintillator for a high-frame-rate neutron radiography," *Nuclear Instruments and Methods in Physics Research Section A: Accelerators, Spectrometers, Detectors and Associated Equipment,* vol. 529, pp. 389, 2004.

[43] M. Katagiri, K. Sakasai, M. Matsubayashi, T. Nakamura, Y. Kondo, Y. Chujo, H. Nanto and T. Kojima, "Scintillation materials for neutron imaging detectors," *Nuclear Instruments and Methods in Physics Research Section A: Accelerators, Spectrometers, Detectors and Associated Equipment,* vol. 529, pp. 274, 2004.

[44] A. Bessiere, P. Dorenbos, C. W. E. van Eijk, K. W. Kramer and H. U. Gudel, "Luminescence and scintillation properties of $CS_2LiYCl_6:Ce^{3+}$ for [gamma] and neutron detection," *Nuclear Instruments and Methods in Physics Research Section A: Accelerators, Spectrometers, Detectors and Associated Equipment,* vol. 537, pp. 242, 2005.

[45] N. J. Rhodes, "Status and Future Development of Neutron Scintillation Detectors," *Neutron News,* Autumn. 2005.

[46] N. J. Rhodes, E. M. Schooneveld and R. S. Eccleston, "Current status and future directions of position sensitive neutron detectors at ISIS," *Nuclear Instruments and Methods in Physics Research Section A: Accelerators, Spectrometers, Detectors and Associated Equipment,* vol. 529, pp. 243, 2004.

[47] H. Rahmanian and J. I. W. Watterson, "Optimisation of light output from zinc sulphide scintillators for fast neutron radiography," *Nuclear Instruments and Methods in Physics Research Section B: Beam Interactions with Materials and Atoms,* vol. 139, pp. 466, 1998.

[48] F. Mantler-Niederstatter, F. Bensch and F. Grass, "An extremely thin scintillation detector for thermal neutrons," *Nuclear Instruments and Methods,* vol. 142, pp. 463, 1977.

[49] M. L. Crow, J. P. Hodges and R. G. Cooper, "Shifting scintillator prototype large pixel wavelength-shifting fiber detector for the POWGEN3 powder diffractometer," *Nuclear Instruments and Methods in Physics Research Section A: Accelerators, Spectrometers, Detectors and Associated Equipment,* vol. 529, pp. 287-292, 8/21, 2004.

[50] J. S. Brenizer, H. Berger, K. M. Gibbs, P. Mengers, C. T. Stebbings, D. Polansky and D. J. Rogerson, "Development of a new electronic neutron imaging system," *Nuclear Instruments and Methods in Physics Research Section A: Accelerators, Spectrometers, Detectors and Associated Equipment,* vol. 424, pp. 9-14, 1999.

[51] N. J. Rhodes, "Telephone Meeting," Dec 2006, 2006.

[52] N. J. Rhodes, "Private tour of ISIS facility by Nigel Rhodes," vol. Private tour of the ISIS facility by Nigel Rhodes for Thomas Miller, June 2005, 2005.

[53] A. R. Spowart, "Measurement of the absolute scintillation efficiency of granular and glass neutron scintillators," *Nuclear Instruments and Methods,* vol. 75, pp. 35, 1969.

[54] G. F. Knoll, *Radiation Detection and Measurement.* John Wiley & Sons, 2000.

[55] T. A. DeVol, S. B. Chotoo and R. A. Fjeld, "Evaluation of granulated BGO, GSO:Ce, YAG:Ce, CaF_2:Eu and ZnS:Ag for alpha/beta pulse shape discrimination in a flow-cell radiation

detector," *Nuclear Instruments and Methods in Physics Research Section A: Accelerators, Spectrometers, Detectors and Associated Equipment,* vol. 425, pp. 228, 1999.

[56] L. E. Dinca, P. Dorenbos, J. T. M. de Haas, V. R. Bom and C. W. E. Van Eijk, "Alpha-gamma pulse shape discrimination in CsI:Tl, CsI:Na and BaF_2 scintillators," *Nuclear Instruments and Methods in Physics Research Section A: Accelerators, Spectrometers, Detectors and Associated Equipment,* vol. 486, pp. 141, 2002.

[57] E. V. Sysoeva, V. A. Tarasov, O. V. Zelenskaya and V. A. Sulyga, "The study of [alpha]/[gamma] ratio for inorganic scintillation detectors," *Nuclear Instruments and Methods in Physics Research Section A: Accelerators, Spectrometers, Detectors and Associated Equipment,* vol. 414, pp. 274, 1998.

[58] C. W. E. van Eijk, "Inorganic-scintillator development," *Nuclear Instruments and Methods in Physics Research Section A: Accelerators, Spectrometers, Detectors and Associated Equipment,* vol. 460, pp. 1, 2001.

[59] K. N. Pandey and S. Balakrishna, "Photoluminescent characteristics of ZnS:Ag, Cl phosphors," *Indian Journal of Pure and Applied Physics,* vol. 11, pp. 889, 1973.

[60] T. Yokogawa, T. Taguchi, S. Fujita and M. Satoh, "Intense blue-emission band and the fabrication of blue light emitting diodes in I-doped and Ag-ion-implanted cubic ZnS," *IEEE Transactions on Electron Devices,* vol. ED-30, pp. 271, 1983.

[61] W. Jian, J. Zhuang, D. Zhang, J. Dai, W. Yang and Y. Bai, "Synthesis of highly luminescent and photostable ZnS:Ag nanocrystals under microwave irradiation," *Materials Chemistry and Physics,* vol. 99, pp. 494, 2006.

[62] T. Igarashi, T. Kusunoki, K. Ohno, T. Isobe and M. Senna, "A thermoluminescence study on the state of Cl in ZnS:Ag by electron beam," *Materials Research Bulletin,* vol. 37, pp. 533, 2002.

[63] M. Katagiri, T. Nakamura, M. Ebine, A. Birumachi, S. Sato, E. M. Shooneveld and N. J. Rhodes, "High-position-resolution neutron imaging detector with crossed wavelength shifting fiber read-out using two ZnS/6LiF scintillator sheets," *Nuclear Instruments and Methods in Physics Research Section A: Accelerators, Spectrometers, Detectors and Associated Equipment,* vol. 573, pp. 149-152, 4/1, 2007.

[64] J. Olmsted and G. M. Williams, *Chemistry - the Molecular Science.* Wm. C. Brown Publishers, 2003.

[65] L. E. Tannas, *Flat-Panel Displays and CRTs.* Van Nostrand Reinhold, 1985.

[66] G. Blasse and B. C. Grabmaier, *Luminescent Materials.* Springer-Verlag, 1994.

[67] Y. A. Ono, *Electroluminescent Displays.* World Scientific Publishing Co., 1995.

[68] X. Yan, "Detection by ozone-induced chemiluminescence in chromatography," *Journal of Chromatography A,* vol. 842, pp. 267–308, 21 May, 1999.

[69] L. Eckertova, *Physics of Thin Films.* Plenum Press, 1986.

[70] B. G. Streetman and S. Banerjee, *Solid State Electronic Devices.* Prentice Hall, 2000.

[71] Y. Nakanishi, G. Shimaoka, H. Tatsuoka and H. Kuwabara, "Preparation of ZnS:Ag,Cl thin films emitting blue luminescence," *Thin Solid Films,* vol. 187, pp. 323, 1990.

[72] P. K. Ghosh, S. Jana, S. Nandy and K. K. Chattopadhyay, "Size-dependent optical and dielectric properties of nanocrystalline ZnS thin films synthesized via rf-magnetron sputtering technique," *Materials Research Bulletin,* vol. 42, pp. 505, 2007.

[73] C. T. Hsu, "Epitaxial growth of II–VI compound semiconductors by atomic layer epitaxy," *Thin Solid Films,* vol. 335, pp. 284-291, 11/19, 1998.

[74] H. W. Leverenz, *An Introduction to Luminescence of Solids.* Dover Publications, inc. New York, 1968.

[75] R. M. Ranson, "Investigation into thermographic phosphors," 1999.

[76] L. Shan Chuan, "Study of Blue Emitting Electroluminescent Devices," vol. PhD, 2003.

[77] K. Seshan, *Handbook of Thin-Film Deposition Processes and Techniques.* Willaim Andrew Publishing, 2002.

[78] W. M. Cranton, "Growth and Characterisation of ZnS:Mn Based Laterally Emitting Thin Film Electroluminescent Device Structures," vol. Ph.D, 1995.

[79] C. Tsakonas, "Growth and analysis of ZnS thin films on silicon," vol. PhD, 1993.

[80] E. Bacaksiz, O. Gorur, M. Tomakin, E. Yanmaz and M. Altunbas, "Ag diffusion in ZnS thin films prepared by spray pyrolysis," *Materials Letters,* vol. 61, pp. 5239, 2007.

[81] S. L. Wilson, "Laser Processing of Inkjet Printed and RF Magnetron Sputtered SnO2:Sb," vol. PhD, 2008.

[82] T. Suda, K. Matsuzaki and S. Kurita, "Infrared quenching of photocapacitance in evaporated ZnS:Ag thin films," *Journal of Applied Physics,* vol. 50, pp. 3638, 1979.

[83] S. A. McElhaney, J. A. Ramsey, M. L. Bauer and M. M. Chiles, "A more rugged ZnS(ag) alpha scintillation detector," in San Francisco, CA, USA, 1990, pp. 868.

[84] G. Stuyven, P. De Visschere, A. Hikavyy and K. Neyts, "Atomic layer deposition of ZnS thin films based on diethyl zinc and hydrogen sulfide," *Journal of Crystal Growth,* vol. 234, pp. 690, 2002.

[85] S. J. Noh, S. K. Lee, E. H. Kim and Y. J. Kong, "Construction of an atomic layer deposition system for nano-device applications," *Current Applied Physics,* vol. 6, pp. 171-173, 2, 2006.

[86] Y. S. Kim and S. J. Yun, "Studies on polycrystalline ZnS thin films grown by atomic layer deposition for electroluminescent applications," *Applied Surface Science,* vol. 229, pp. 105, 2004.

[87] M. Aven and J. A. Parodi, "Study of the crystalline transformations in ZnS:Cu, ZnS:Ag and ZnS:Cu, Al," *Journal of Physics and Chemistry of Solids,* vol. 13, pp. 56-64, 5, 1960.

[88] D. C. Koutsogeorgis, E. A. Mastio, W. M. Cranton and C. B. Thomas, "Pulsed KrF laser annealing of ZnS:Mn laterally emitting thin film electroluminescent displays," *Thin Solid Films,* vol. 383, pp. 31-33, 2/15, 2001.

[89] E. A. Mastio, E. Fogarassy, W. M. Cranton and C. B. Thomas, "Ablation study on pulsed KrF laser annealed electroluminescent ZnS:Mn/Y_2O_3 multilayers deposited on Si," *Appl. Surf. Sci.,* vol. 154-155, pp. 35-39, 2/1, 2000.

[90] E. A. Mastio, C. B. Thomas, W. M. Cranton and E. Fogarassy, "The effects of multiple KrF laser irradiations on the electroluminescence and photoluminescence of rf-sputtered ZnS:Mn-based electroluminescent thin film devices," *Appl. Surf. Sci.,* vol. 157, pp. 74-80, 3, 2000.

[91] E. A. Mastio, W. M. Cranton, C. B. Thomas, E. Fogarassy and S. de Unamuno, "Pulsed KrF laser annealing of RF sputtered ZnS:Mn thin films," *Appl. Surf. Sci.,* vol. 138-139, pp. 35-39, 1, 1999.

[92] W. M. Cranton, P. H. Key, D. Sands, C. B. Thomas and F. X. Wagner, "XeCl laser ablation of thin film ZnS," *Applied Surface Science,* vol. 96-98, pp. 501, 1996.

[93] Filmetrics, *Operation Manual for the Filmetrics F20 Thin-Film Analyzer.* 2003.

[94] Veeco, *Dektak 6M Manual - Software Version 8.30.005.* 2002.

[95] D. Page, *WYKO Surface Profiles Techniqual Reference Manual by the Veeco Metrology Group.* 1999.

[96] L. C. Feldman and J. W. Mayer, *Fundamentals of Surface and Thin Film Analysis.* North-Holland, 1986.

[97] A. Simon, C. Jeynes, R. P. Webb, R. Finnis, Z. Tabatabaian, P. J. Sellin, M. B. H. Breese, D. F. Fellows, R. van den Broek and R. M. Gwilliam, "The new Surrey ion beam analysis facility," *Nuclear Instruments and Methods in Physics Research Section B: Beam Interactions with Materials and Atoms,* vol. 219-220, pp. 405-409, 6, 2004.

[98] C. Jeynes, N. P. Barradas, M. J. Blewett and R. P. Webb, "Improved ion beam analysis facilities at the University of Surrey," *Nuclear Instruments and Methods in Physics Research Section B: Beam Interactions with Materials and Atoms,* vol. 136-138, pp. 1229-1234, 3/2, 1998.

[99] C. Jeynes, "MeV ion beam analysis I: Introduction," in *Sixteenth Anual User Workshop - University of Surrey Ion Beam Centre,* 2007, .

[100] C. Jeynes, "MeV ion beam analysis II: Particle scattering spectrometry," in *Sixteenth Annual User Workshop - University of Surrey Ion Beam Centre,* 2007, .

[101] W. A. Hollerman, L. R. Holland, D. B. Nisen, J. H. Fisher and G. A. Shelby, "Development of the fluorescent materials test chamber," *Nuclear Instruments and Methods in Physics Research Section B: Beam Interactions with Materials and Atoms,* vol. 68, pp. 28-31, 5/2, 1992.

[102] S. V. Yap, "Phosphors for biomedical and environmental sensing technology," vol. PhD, 2009.

[103] Phosphor Technology Ltd., "Data sheet for ZnS:Ag phosphor powder (GL47/N-C2)," .

[104] Phosphor Technology Ltd., "Data sheet for ZnS:Cl phosphor powder (GL17/N-X)," .

[105] Phosphor Technology Ltd., "Data sheet for ZnS:Tm phosphor powder (GL:29/Tm)," .

[106] Phosphor Technology Ltd., "Data sheet for ZnS:Mn phosphor powder (GL:29 M/B-A1)," .

[107] Testbourne Ltd., "Data sheet for ZnS solid target (Z1-9006-D1)," .

[108] Motlan, G. Zhu, K. Drozdowicz-Tomsia, K. McBean, M. R. Phillips and E. M. Goldys, "Annealing of ZnS nanocrystals grown by colloidal synthesis," *Optical Materials,* vol. 29, pp. 1579-1583, 8, 2007.

[109] M. Katagiri, K. Sakasai, M. Matsubayashi and T. Kojima, "Neutron/[gamma]-ray discrimination characteristics of novel neutron scintillators," *Nuclear Instruments and Methods in Physics Research Section A: Accelerators, Spectrometers, Detectors and Associated Equipment,* vol. 529, pp. 317, 2004.

[110] L. Romero and J. Campos, "Luminescence decay of ZnS:Ag in the 10^{-7} to 1s range by means of laser excitation." *Physica Status Solidi (A) Applied Research,* vol. 67, pp. 259-262, 1981.

[111] H. Eilers, "Synthesis and characterization of CO_2-laser-evaporated ZnS:Mn thin films," *Mater Lett,* vol. 62, pp. 967-969, 3/15, 2008.

[112] W. A. Hollerman, N. P. Bergeron, S. M. Goedeke, S. W. Allison, C. I. Muntele, D. Ila and R. J. Moore, "Annealing effects of triboluminescence production on irradiated ZnS:Mn," *Surface and Coatings Technology,* vol. 201, pp. 8382-8387, 8/5, 2007.

[113] M. D. Bhise, M. Katiyar and A. H. Kitai, "Effect of Mn concentration on the cathodo- and photoluminescence of ZnS:Mn," *J. Appl. Phys.,* vol. 67, pp. 1492-6, 02/01, 1990.

[114] L. L. Kazmerski, *Polycrystalline and Amorphous Thin Film Devices.* Academic Press, 1980.

[115] S. Wang, G. Xia, J. Shao and Z. Fan, "Structure and UV emission of nanocrystal ZnO films by thermal oxidation of ZnS films," *J. Alloys Compounds,* vol. 424, pp. 304-306, 11/9, 2006.

[116] A. H. Jayatissa, "Preparation of gallium-doped ZnO films by oxidized ZnS films," *Semiconductor Science and Technology,* vol. 18, pp. L27-L30, 2003.

[117] H. Z. Zeng, K. Q. Qiu, Y. Y. Du and W. Z. Li, "A new way to synthesize ZnS nanoparticles," *Chinese Chemical Letters,* vol. 18, pp. 483, 2007.

[118] L. Ozawa, M. Makimura and M. Itoh, "Eradication of oxygen contamination in production of ZnS:Ag:Cl blue phosphor powder," *Materials Chemistry and Physics,* vol. 96, pp. 511, 2006.

[119] D. S. McGregor, S. L. Bellinger, D. Bruno, W. L. Dunn, W. J. McNeil, E. Patterson, B. B. Rice, J. K. Shultis and T. Unruh, "Perforated diode neutron detector modules fabricated from high-purity silicon," *Radiat. Phys. Chem.,* vol. 78, pp. 874-881, 10, 2009.

[120] D. S. McGregor, W. J. McNeil, S. L. Bellinger, T. C. Unruh and J. K. Shultis, "Microstructured semiconductor neutron detectors," *Nuclear Instruments and Methods in Physics Research Section A: Accelerators, Spectrometers, Detectors and Associated Equipment,* vol. 608, pp. 125-131, 9/1, 2009.

[121] S. Hallbeck, A. N. Caruso, S. Adenwalla, J. Brand, D. Byun, H. X. Jiang, J. Y. Lin, Y. B. Losovyj, C. Lundstedt, D. N. McIlroy, W. K. Pitts, B. W. Robertson and P. A. Dowben, "Comment on “Spectral identification of thin film coated and solid form semiconductor neutron detectors” by McGregor and Shultis," *Nuclear Instruments and Methods in Physics Research Section A: Accelerators, Spectrometers, Detectors and Associated Equipment,* vol. 536, pp. 228-231, 1/1, 2005.

[122] J. K. Shultis and D. S. McGregor, "Design and performance considerations for perforated semiconductor thermal-neutron detectors," *Nuclear Instruments and Methods in Physics Research Section A: Accelerators, Spectrometers, Detectors and Associated Equipment,* vol. 606, pp. 608-636, 7/21, 2009.

[123] M. Schieber, A. Zuck, G. Marom, O. Khakhan, M. Roth and Z. B. Alfassi, "Composite polycrystalline semiconductor neutron detectors," *Nuclear Instruments and Methods in Physics Research Section A: Accelerators, Spectrometers, Detectors and Associated Equipment,* vol. 579, pp. 180-183, 8/21, 2007.

[124] H. K. Gersch, D. S. McGregor and P. A. Simpson, "The effect of incremental gamma-ray doses and incremental neutron fluences upon the performance of self-biased 10B-coated high-purity epitaxial GaAs thermal neutron detectors," *Nuclear Instruments and Methods in Physics Research Section A: Accelerators, Spectrometers, Detectors and Associated Equipment,* vol. 489, pp. 85, 2002.

[125] M. Schieber, E. Mojaev, M. Roth, A. Zuck, O. Khakhan and A. Fleider, "Thermal neutron detection at outer electrode surfaces of composite polycrystalline B, BN, B4C and LiF through air ionization," *Nuclear Instruments and Methods in Physics Research Section A: Accelerators, Spectrometers, Detectors and Associated Equipment,* vol. 607, pp. 634-639, 8/21, 2009.

[126] D. S. McGregor, T. C. Unruh and W. J. McNeil, "Thermal neutron detection with pyrolytic boron nitride," *Nuclear Instruments and Methods in Physics Research Section A: Accelerators, Spectrometers, Detectors and Associated Equipment,* vol. 591, pp. 530-533, 7/1, 2008.

[127] A. Pietropaolo, G. Verona Rinati, C. Verona, E. M. Schooneveld, M. Angelone and M. Pillon, "A single-crystal diamond-based thermal neutron beam monitor for instruments at pulsed neutron sources," *Nuclear Instruments and Methods in Physics Research Section A: Accelerators, Spectrometers, Detectors and Associated Equipment,* vol. 610, pp. 677-681, 11/11, 2009.

[128] S. Almaviva, M. Marinelli, E. Milani, G. Prestopino, A. Tucciarone, C. Verona, G. Verona-Rinati, M. Angelone and M. Pillon, "Improved performance in synthetic diamond neutron detectors: Application to boron neutron capture therapy," *Nuclear Instruments and Methods in Physics Research Section A: Accelerators, Spectrometers, Detectors and Associated Equipment,* vol. In Press, Corrected Proof, .

-

9 Appendix

9.1 Ion Beam Analysis

Sample	Implantation	Annealed	Reason
#1	0.01at% Cl	Yes	Complimentary measurement to sample #4
#2	None	No	A control for the thin film growth technique
#3	0.2 at% Cl	No	Test the effectiveness of the implantation process
#4	0.2 at% Cl	Yes	Test the effect the annealing of implanted ions
#5	0.05at% Cl	Yes	Complimentary measurement to sample #4

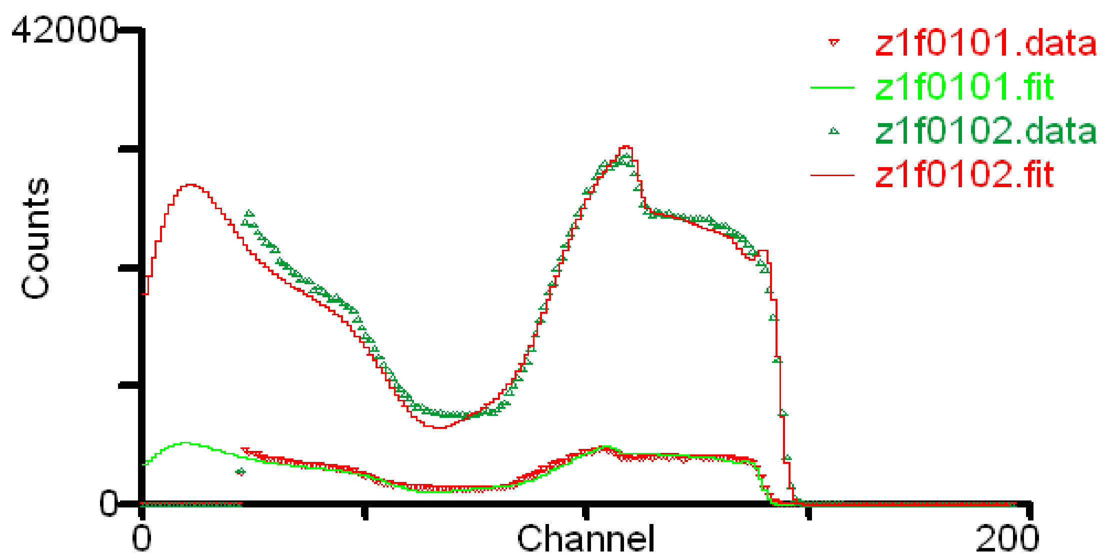

Figure 9.1: RBS spectrum of Sample 1

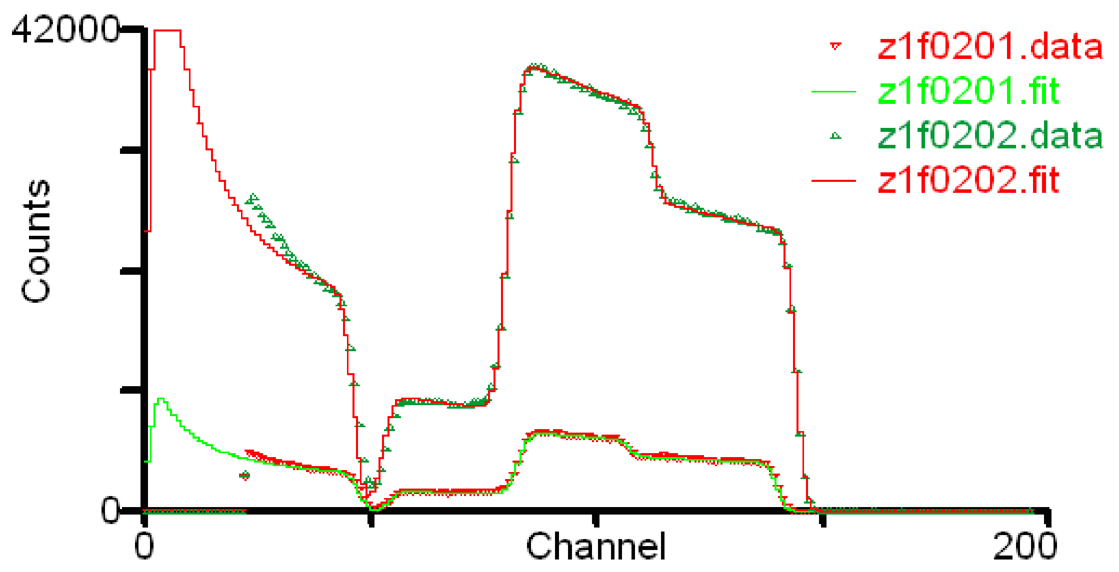

Figure 9.2: RBS spectrum of Sample 2

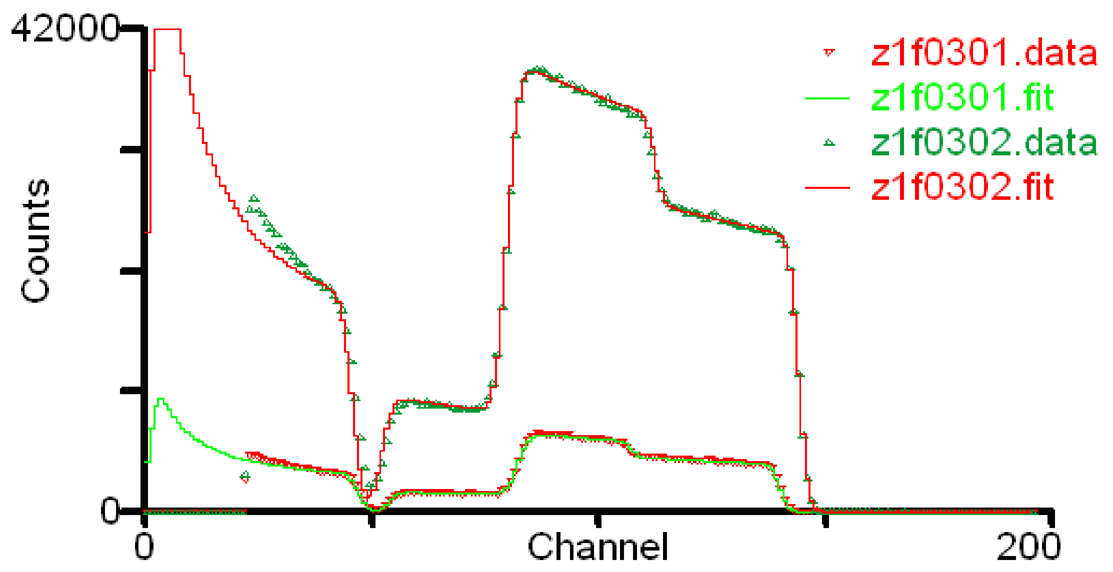

Figure 9.3: RBS spectrum of Sample 3

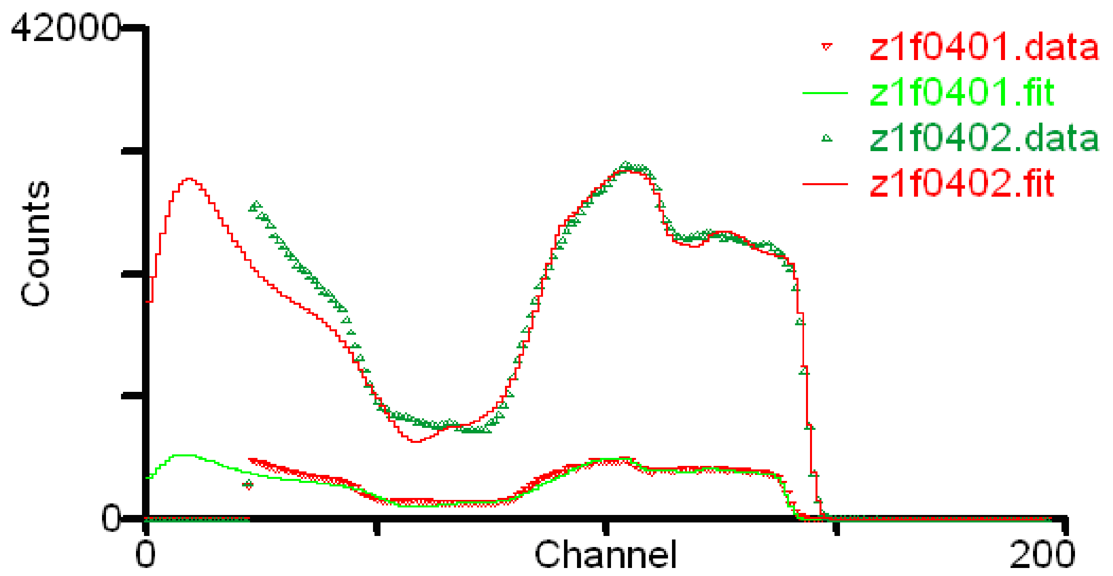

Figure 9.4: RBS spectrum of Sample 4

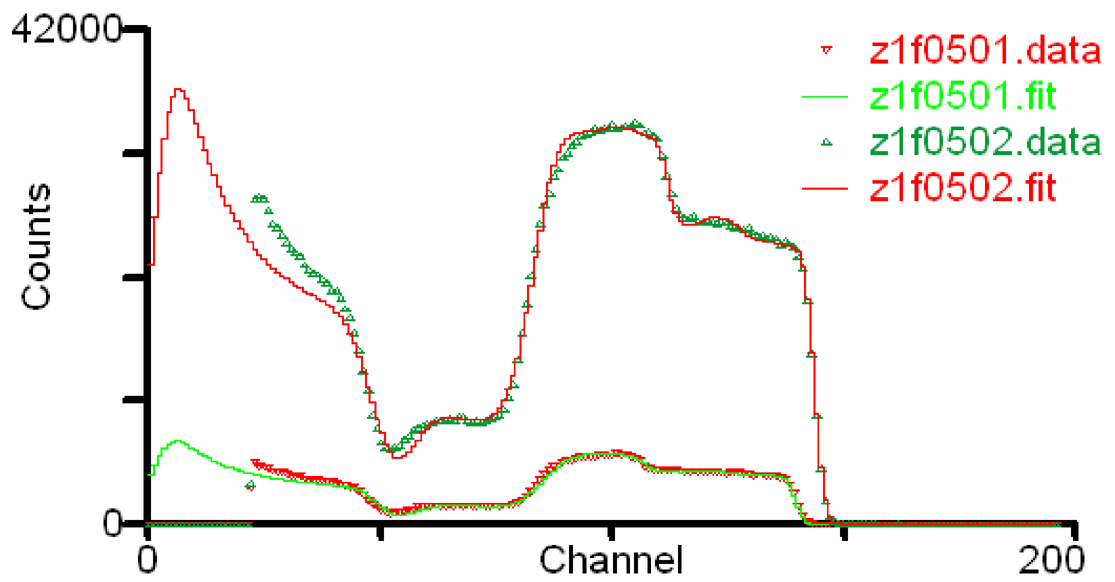

Figure 9.5: RBS spectrum of Sample 5

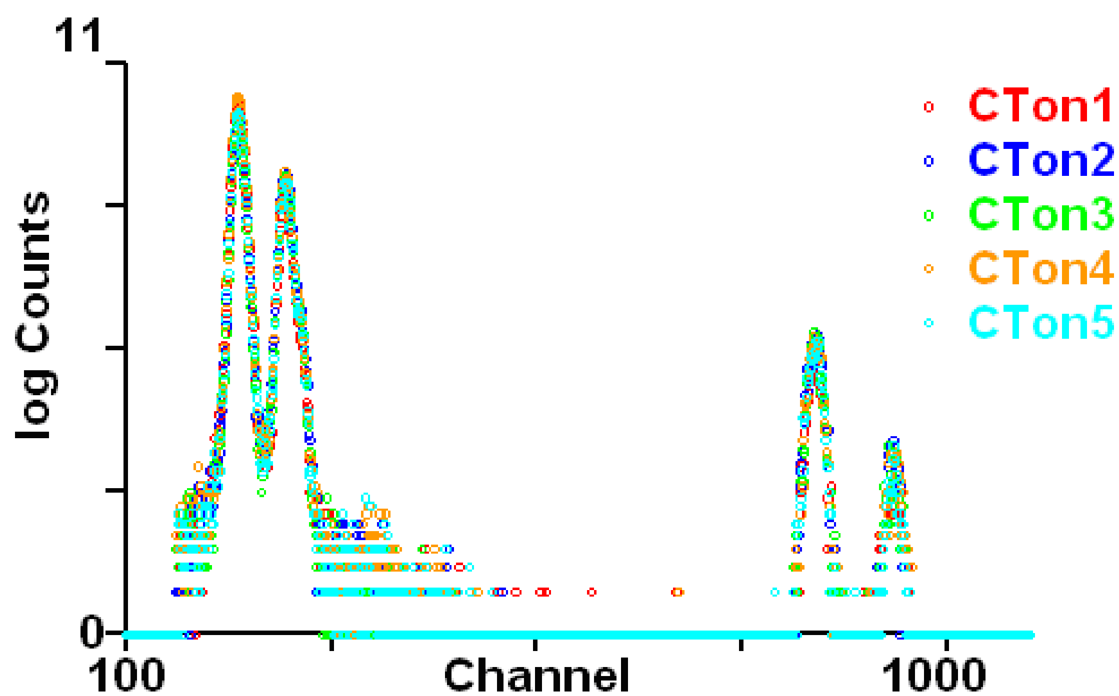

Figure 9.6: PIXE using 2.5MeV protons, normal exit into X-ray detector (60° beam incidence).

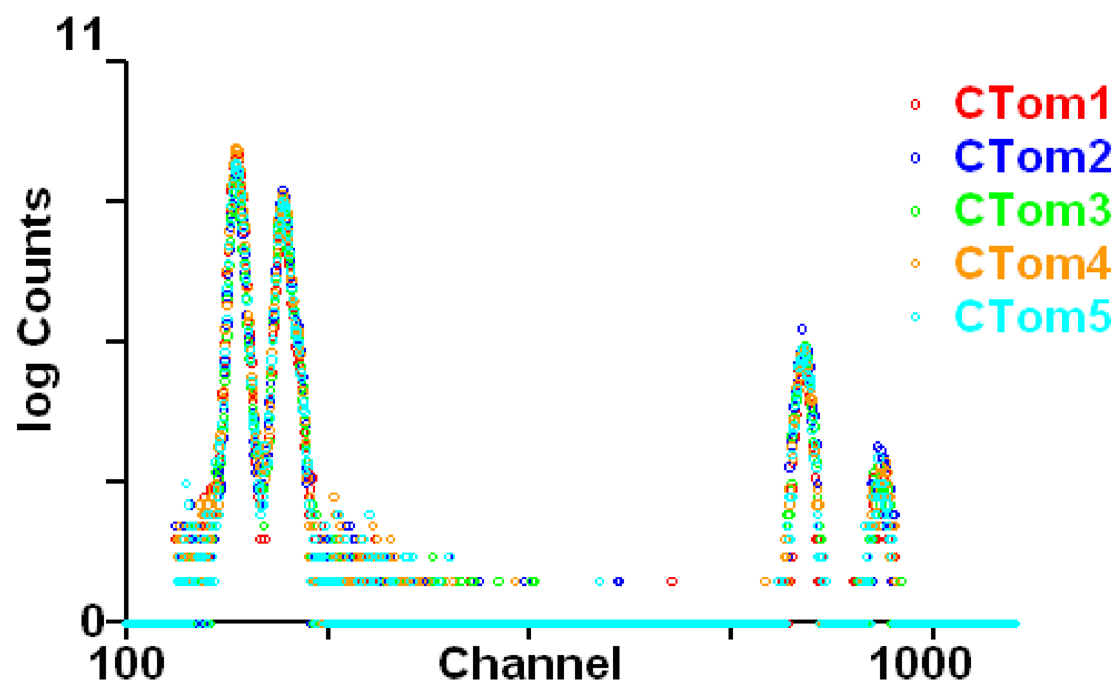

Figure 9.7: PIXE using 2.5MeV protons, 60° exit into X-ray detector (normal beam incidence).

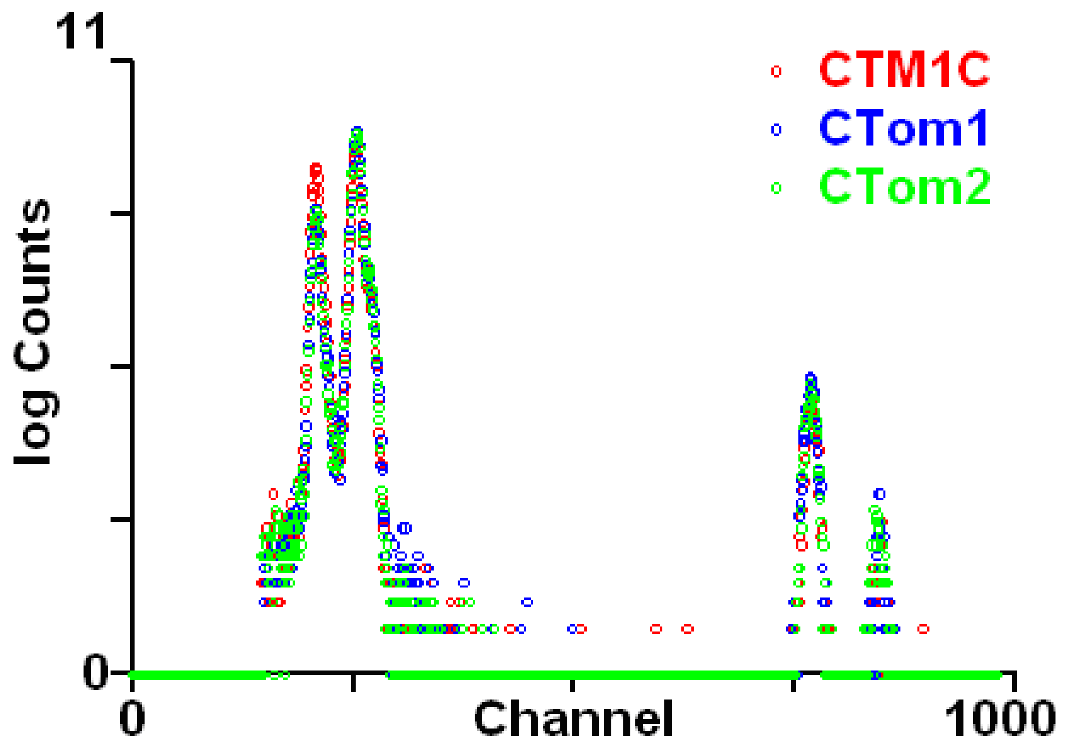

Figure 9.8: Three samples, 1.5MeV He, normal exit into X-ray detector (60° beam incidence).

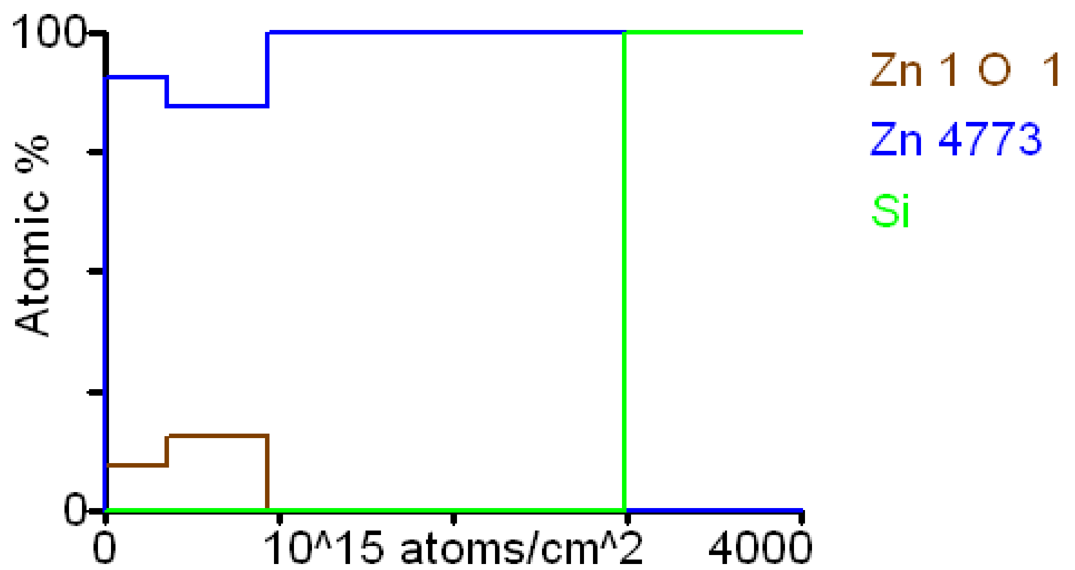

Figure 9.9: Chemical composition of Sample 1 in respect to thickness.

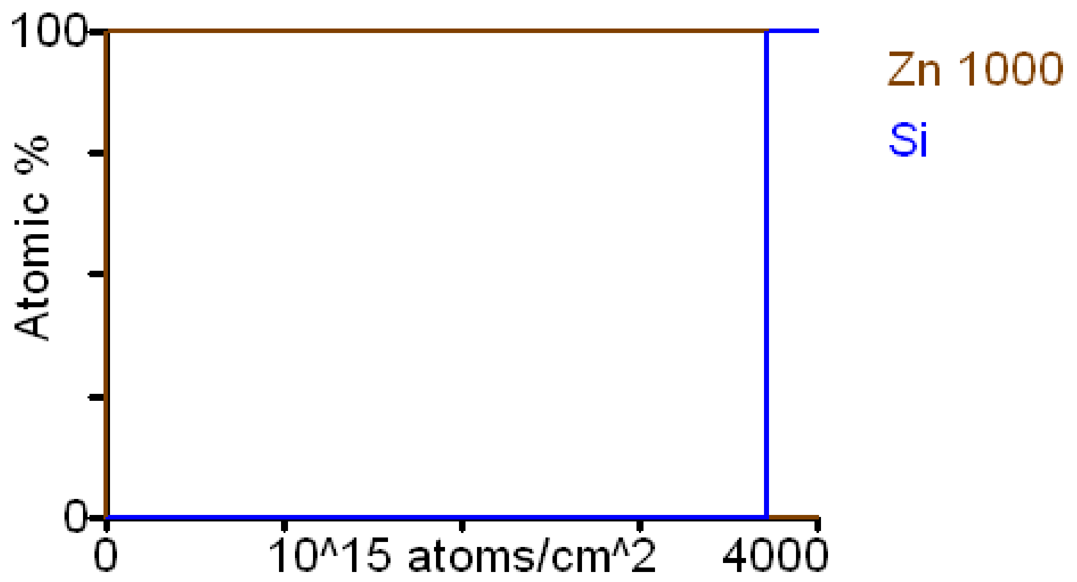

Figure 9.10: Chemical composition of Sample 2 in respect to thickness.

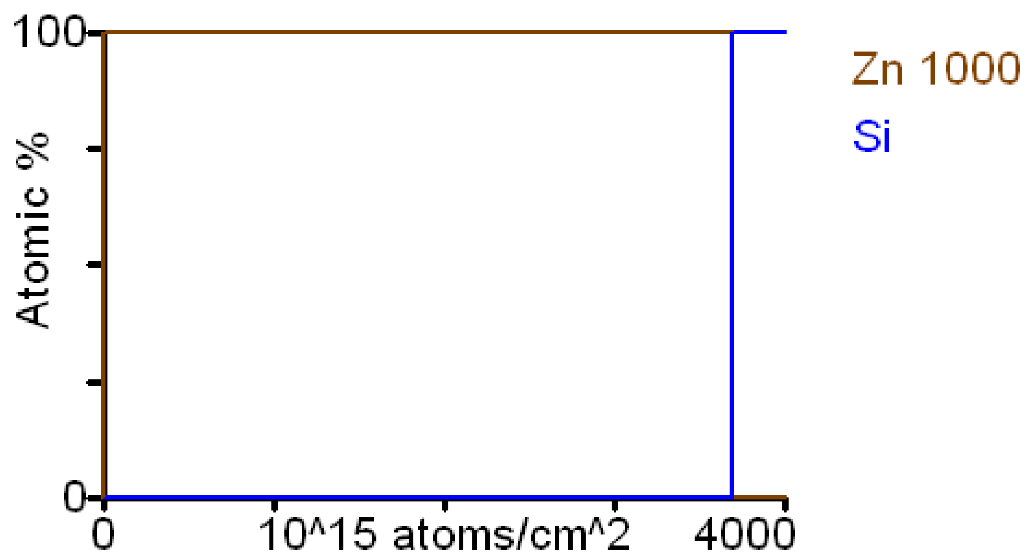

Figure 9.11: Chemical composition of Sample 3 in respect to thickness.

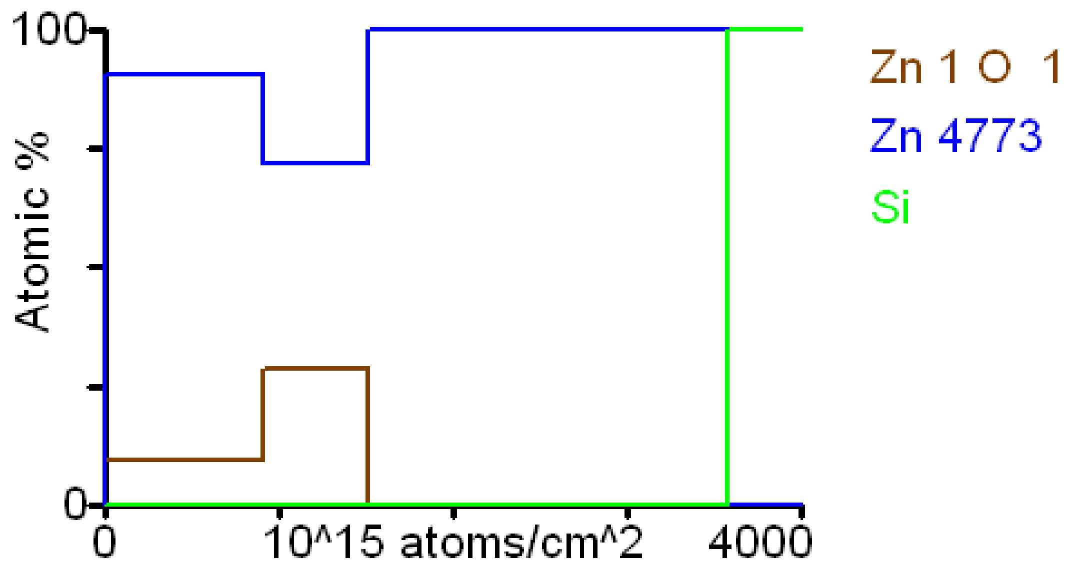

Figure 9.12: Chemical composition of Sample 4 in respect to thickness.

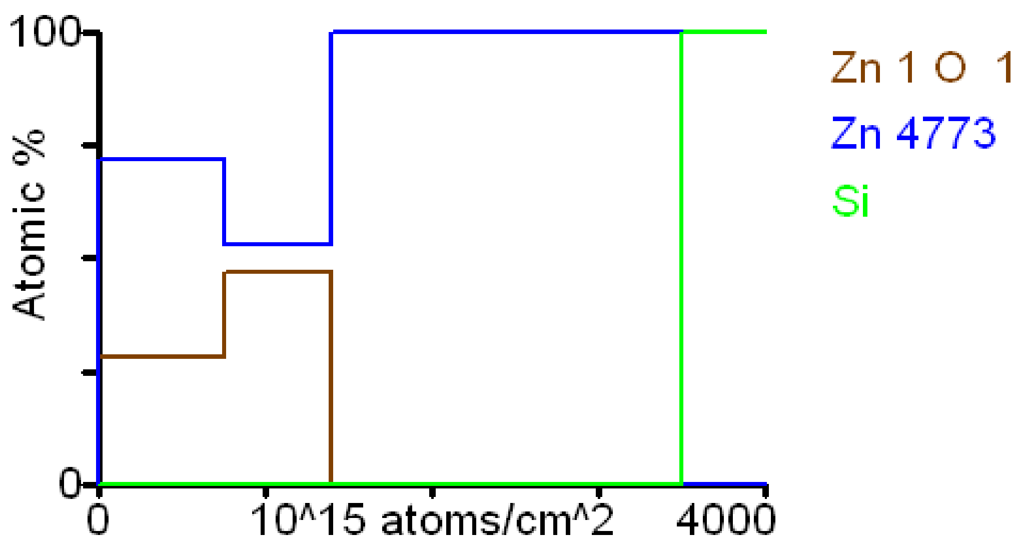

Figure 9.13: Chemical composition of Sample 5 in respect to thickness

9.2 Figures

Figure 2.1: Basic design of a neutron diffraction analysis technique. 6

Figure 2.2: A representation of a 2D captured pattern for neutron diffraction analysis....... 6

Figure 2.3: A representation of a neutron detector, after [12, 13]... 7

Figure 2.4: 2D representation of a neutron diffraction technique... 8

Figure 2.5 A typical luminescent spectrum of ZnS:Ag,Cl, with permission from Phosphor Technology [34]. 14

Figure 2.6: Neutrons incident on layered neutron converter and phosphor. 17

Figure 2.7: Neutrons incident on a mixture of neutron converter and phosphor. 18

Figure 2.8: Representation of scintillator in respect to the incident neutrons to achieve greater detection efficiency. 19

Figure 2.9: Zero crossing method of pulse shape discrimination: bipolar pulse shapes, signal timings, timing spread of zero crossing signal, after [54]. 20

Figure 2.10: Charge comparison method of pulse shape discrimination. Integrator outputs as a factor of time for gamma-ray and neutron signals, after [9]. 21

Figure 2.11: An example of a pulse shape spectrum from an alpha and beta source. 21

Figure 2.12: A representation of how silver and chlorine ions are incorporated a ZnS cubic lattice..25

Figure 2.13: Effect of a charged particle on electron orbits of atoms in its vicinity. 26

Figure 2.14: Types of atomic structure..29

Figure 2.15: Configuration of the atoms in three kinds of crystal structure. (a) rock-salt type, (b) zinc-blende type, and (c) wurtzeite type respectively, after [22]. 30

Figure 2.16: Example of excitation of an electron across the bandgap (for this case a direct bandgap) from the valence band to the conduction band. 31

Figure 2.17: Band diagram of emission from a doped phosphor 33

Figure 2.18 The Schematic diagram of energy levels of the ZnS:Ag nanocrystals, after [61]. 33

Figure 2.19: Summation of two Gaussian peaks with separations of 0.5, 1.0, 1.5, 2.0 FWHM (after [22])..34

Figure 2.20: A drawing of the intensity of emission from a phosphor over time, as an example of the decay curve. 36
Figure 2.21: An illustration of the ALD process, after [85]....43
Figure 3.1: Diagram of the sputtering system used for thin film deposition of phosphor material. 47
Figure 3.2: Orientation of electrodes in respect to the substrate for simultaneous / multiple sputtering....49
Figure 3.3: Setup for creating a pressed phosphor target in a hydraulic press. 50
Figure 3.4: Pressed powder phosphor target used in a hydraulic press. 50
Figure 3.5: Typical interferometer pattern from the growth of a thin film on a Si substrate. 52
Figure 3.6: A representation of the setup required for the temperature calibration of a silicon wafer using thermocouples. 56
Figure 3.7: System setup for the annealing of implanted samples using the RF magnetron sputtering system. 56
Figure 3.8: Temperature Difference between the reference temperature and the top and bottom surface of the Si wafer when using the shutter....57
Figure 3.9: Calibration curve of the temperatures for the top and bottom surface of a Si wafer using a shutter. Insert - Temperature difference between the top and bottom surface....58
Figure 3.10: Arrangement of sputter coater for the deposition of Ag onto ZnS thin film through a mask. 61
Figure 3.11: Representation of ion implantation with a single implantation energy into a target and its resultant depth profile....63
Figure 3.12: Schematic of the ion implantation method. 64
Figure 3.13: General setup of the Filmetrics thin film analyser for reflectance spectroscopy, after [93]....65
Figure 3.14: Typical measured and calculated reference spectra for ZnS on Si. 66
Figure 3.15: General description of Dektak 6M for stylus profiling. 67
Figure 3.16: General setup of the Wyko NT1100 system for optical profiling. 68

Figure 3.17: General setup of the XRD machine......70
Figure 3.18: Emission spectrum of X-rays emitted by a Cu target at 35 KeV excitation 71
Figure 3.19: Depiction of RBS and PIXE interaction with a target material, after [99]......73
Figure 3.20: Schematic of the ion beam analysis technique, after [100] 74
Figure 3.21: Pellet Press setup to create 5mm phosphor pellets. 77
Figure 3.22: The hydraulic press in which the body of the pellet press (Figure 3.21) is used....77
Figure 3.23: Experimental setup of equipment for the capture of the emission spectrum from the phosphor when excited by a UV laser......78
Figure 3.24: The emission wavelengths achieved by the Nd:YAG laser. 79
Figure 3.25: Experimental setup of equipment for the capture of the decay spectrum from the phosphor when excited by a N_2 laser. 81
Figure 3.26: Experimental setup of equipment for the capture of the emission spectrum from the phosphor when excited by an alpha source. 83
Figure 3.27 Experimental setup for the detection of relative emission intensities from phosphors under alpha excitation using a PMT. 84
Figure 4.1: Excitation and Emission spectrum of ZnS:Ag,Cl purchased from Phosphor Technology Ltd, with permission [103]......88
Figure 4.2: Excitation and Emission spectrum of ZnS:Cl (GL17/N-X) , with permission from Phosphor Technology Ltd. [104]. 89
Figure 4.3: Emission spectrum of ZnS:Tm (GL:29/Tm) excited by 360nm light, with permission from Phosphor Technology Ltd. [105]......90
Figure 4.4: Emission spectrum of ZnS:Mn (GL:29 M/B-A) excited by 360nm light, with permission from Phosphor Technology Ltd. [106]. 91
Figure 4.5: The arrangement of test location over an area of the ISIS wafer......93
Figure 4.6: Power of laser emitted by the N_2 laser against time with two periods of 'cool down'. 95
Figure 4.7: Power of laser emitted by the HeCd laser over time. 96
Figure 4.8: The ISIS wafer excited primarily by 266nm but also exhibiting its second harmonic (532nm). Spectra are captured using two spectrometers (S2000, S4000), ...97
Figure 4.9: Power of laser emitted by the Nd:YAG laser against time, with a repeat test. 98

Figure 4.10: Normalised PL emission spectrum from the ISIS scintillator excited by 307, 320 and 337nm laser wavelengths. Insert - arbitrary units of the same three emission spectra. 99

Figure 4.11: Measured PL emission spectrum from the ISIS phosphor excited by N_2 laser (337nm) resolved into two peaks. 100

Figure 4.12: Normalised emission spectrum created by two spectrometers by the excitation of a ZnS:Ag,Cl phosphor powder using the N_2 laser. 102

Figure 4.13: A normalised emission spectrum of ZnS:Ag,Cl phosphor using an S2000 spectrometers excited using the N_2 laser. 103

Figure 4.14: A normalised emission spectrum of ZnS:Ag,Cl phosphor using an S4000 spectrometers excited using the N_2 laser. 104

Figure 4.15: A normalised emission spectrum of ZnS:Cl phosphor using an S2000 and S4000 spectrometers excited using the N_2 laser. 105

Figure 4.16: A normalised emission spectrum of ZnS:Tm phosphor using an S2000 and S4000 spectrometers excited using the N_2 laser. 106

Figure 4.17: A normalised emission spectrum of ZnS:Mn phosphor using an S2000 and S4000 spectrometers excited using the N_2 laser. 106

Figure 4.18: A normalised emission spectrum of ZnS solid target using an S2000 and S4000 spectrometers excited using the N_2 laser. 107

Figure 4.19: A combination of the emission spectra created by the six samples using the S2000 spectrometer. 108

Figure 4.20: A combination of the emission spectra created by the six samples using the S4000 spectrometer. 108

Figure 4.21: Normalised peak emission intensity of six phosphors using a N_2 laser excitation source. 109

Figure 4.22: A typical image generated by the PMT and oscilloscope, with the highlighted area being the general region where decay time measurements were taken. 110

Figure 4.23: Emission spectrum filtered using the monochromator when tuned to 450nm and 500nm. 111

Figure 4.24: Decay measurements of the ISIS scintillator at the wavelengths 440, 485 and 510nm and the exponential equations expressing the experimental fit to the decay curves 112
Figure 4.25: Decay measurements of the ZnS:Ag,Cl phosphor measured at the wavelengths (440, 485 and 510nm) and the exponential equations expressing the decay curves. 112
Figure 4.26: Decay measurements of the ZnS:Ag,Cl phosphor measured at the wavelengths (430 and 450nm) and the exponential equations expressing the decay curves. 113
Figure 4.27: A decay curve detected without the excitation of a phosphor. 114
Figure 4.28: Activity detected at distances from the ^{241}Am source in air. 115
Figure 4.29: Peak intensity measurements against time for the ISIS phosphor using a Nd:YAG laser at 266nm excitation. 117
Figure 4.30: Peak intensity measurements against time with 15 and 20 minute break in excitation for the ISIS phosphor using a Nd:YAG laser at 266nm excitation, a continuation of Figure 4.29. 118
Figure 4.31: Repeat peak intensity measurements of ZnS:Ag,Cl (ISIS) excited by Nd:YAG (255nm). 119
Figure 5.1: Example of an interference pattern from an interferometer and the inherent inaccuracies from reading a wave pattern. 126
Figure 5.2: Power requirements to achieve annealing temperatures of 500, 550 and 600°C at the centre and edge of a Si wafer when using the shutter. Insert - Temperature difference across the Si substrate with and without the shutter. 131
Figure 5.3: Power requirements to achieve a deposition temperature of 190°C and 200°C at the centre and edge of a Si wafer at 80W electrode potential. Insert - Original test done for a larger power range. 132
Figure 5.4: Calibration of the heater efficiency over a range of powers with and without a shutter and the temperature difference between across the Si substrate, along with the measurement of the thermocouple linked to the heater. 132
Figure 5.5: Temperature at the centre and edge of a Si substrate as well as reference temperature of heater thermocouple when sputtering at 80W and a 100W electrode

POTENTIAL FOR A SI WAFER. INSERT - TEMPERATURE DIFFERENCE BETWEEN THE 80W AND 100W APPLIED POWER. 133

FIGURE 5.6: CALIBRATION OF THE SYSTEM BY GROWTH OF A ZNS:MN THIN FILM. 134

FIGURE 5.7: A ZNS:AG,CL THIN FILM GROWN TO 800NM ON A SI SUBSTRATE AND IT'S THICKNESS MEASURED ACROSS THREE POSITIONS FROM CENTRE TO THE EDGE. 137

FIGURE 5.8: XRD PEAK CREATED BY AMORPHOUS SI DISK AND USED AT A CONTROL. 138

FIGURE 5.9: XRD PATTERN OF THE ZNS:AG,CL PHOSPHOR POWDER..139

FIGURE 5.10: XRD PATTERN OF ZNS:AG,CL POWDER AND ZNS SOLID TARGET. 140

FIGURE 5.11: XRD PATTERN OF A SI SUBSTRATE 141

FIGURE 5.12: XRD PATTERN OF A THIN FILM GROWN FROM A ZNS:AG,CL PRESSED POWDER TARGET ONTO A SI SUBSTRATE BY RF MAGNETRON SPUTTERING 142

FIGURE 5.13: THE XRD PATTERN OF ZNS:AG.CL IN POWDER, THE THIN FILM FORM GROWN ONTO SI WAFER AND THE SI WAFER. 143

FIGURE 5.14: RBS SPECTRA GENERATED FROM TWO DETECTORS FROM A ZNS:AG,CL THIN FILM. 144

FIGURE 5.15: RBS SPECTRA OF THE DATA IN FIGURE 5.14 IN LOG FORM. 144

FIGURE 6.1: THERMAL ANNEALING OF THE SAMPLE FOLLOWING DEPOSITION FOR THE DIFFUSION OF AG THROUGH THE ZNS THIN FILM. 151

FIGURE 6.2: PROCESS OF CL INCORPORATION INTO A ZNS THIN FILM BY THERMAL ANNEALING FROM NACL. 153

FIGURE 6.3: PROCESS OF CL INCORPORATION INTO A ZNS THIN FILM BY THERMAL ANNEALING FROM ZNS:CL POWDER. 153

FIGURE 6.4: A REPRESENTATION OF IMPLANTED AG AND CL IONS WITHIN A ZNS THIN FILM. 154

FIGURE 6.5: A COMPUTER GENERATED DEPTH PROFILE BASED ON THE IMPLANTATION OF AG IONS INTO A 800NM ZNS THIN FILM AND THE SUGGESTED DISORDER IT WOULD CREATE (PROVIDED BY DR. SMITH). 155

FIGURE 6.6: SCHEMATIC DIAGRAM TO ILLUSTRATE THE EFFECT OF ANNEALING ON THE DISTRIBUTION OF IONS WITHIN A MATERIAL 158

FIGURE 6.7: PL EMISSION SPECTRUM OF ZNS:AG,CL POWDER EXCITED BY N_2 (337NM) LASER. 159

FIGURE 6.8: PL EMISSION SPECTRUM OF ZNS THIN FILM WITH AND WITHOUT SPUTTER COATING OF AG AND ANNEALED IN A FURNACE. INSERT - VALUES FOR PEAK INTENSITY AT THE THREE EMISSION PEAKS FOR INCREASING ANNEALING PERIODS. 160

FIGURE 6.9: PL EMISSION SPECTRUA OF A ZNS + AG THIN FILM ANNEALED WITH AND WITHOUT ZNS:CL POWDER AFTER 30 MINUTES. 161

FIGURE 6.10: PL EMISSION SPECTRUM OF ZNS:CL POWDER EXCITED BY A N_2 (337NM) LASER. 162

FIGURE 6.11: PL EMISSION OF ION IMPLANTED ZNS AND ANNEALED FOR 15 MINUTES IN THE FURNACE AT 700°C AND EXCITED WITH THE N_2 LASER. 163

FIGURE 6.12: PL EMISSION SPECTRUM OF ION IMPLANTED ZNS THIN FILM ANNEALED AT 25% FOR 8 HOURS UNDER VACUUM AND EXCITED USING THE HECD LASER. 164

FIGURE 6.13: PL EMISSION SPECTRUM OF ION IMPLANTED ZNS THIN FILM ANNEALED AT 25% FOR 8 HOURS UNDER VACUUM AND EXCITED USING THE N_2 LASER. 164

FIGURE 6.14: NORMALISED PL EMISSION SPECTRUM OF ION IMPLANTED ZNS THIN FILM ANNEALED AT 27.5% FOR 8 HOURS UNDER VACUUM AND EXCITED USING HECD LASER. 165

FIGURE 6.15: PL EMISSION SPECTRUM OF ION IMPLANTED ZNS THIN FILM ANNEALED AT 27.5% FOR8 HOURS UNDER VACUUM AND EXCITED USING N_2 LASER. 165

FIGURE 6.16: EXAMPLE OF THE PIXE RESULTS. 166

FIGURE 6.17: A LABELLED RBS SPECTRUM OF SAMPLE 2 ON A LOGARITHMIC SCALE. AG (BROWN), ZN (MAUVE), S (BLUE) 167

FIGURE 6.18: XRD PATTERN OF ZNS ON A SI WAFER AND THE SI WAFER. 168

FIGURE 6.19: XRD PATTERN OF ZNS SOLID TARGET AND THE SPUTTERED ZNS ON A SI SUBSTRATE. 169

FIGURE 6.20: A LABELLED XRD PATTERN OF ZNS THIN FILM ON A SI WAFER AFTER ION IMPLANTATION, SHOWN WITH PROFILE FITTING. 170

FIGURE 6.21: ZNS THIN FILMS XRD PATTERN WITH AND WITHOUT IMPLANTATION. 171

FIGURE 6.22: XRD PATTERN OF ZNS ON A SI WAFER AND THE SAME SAMPLE AFTER ANNEALING IN AIR AT 700°C. 172

FIGURE 6.23: XRD PATTERN ON THE IMPLANTED ZNS THIN FILMS ANNEALED IN A FURNACE AT 800°C ... 172

FIGURE 6.24: XRD PATTERN OF VACUUM ANNEALED AND UNANNEALED UNDOPED ZNS. 173

FIGURE 6.25: XRD PATTERN OF VACUUM ANNEALED AND UNANNEALED ZNS IMPLANTED WITH AG AND 0.2AT% CL. 174

FIGURE 6.26: PL EMISSION SPECTRA OF FIREBRICKS USED WITHIN THE FURNACE WHEN EXCITED BY A N_2 LASER........175
FIGURE 7.1: AN EXAMPLE OF HOW THE INTENSITY OF RL EMISSION INCREASED. 187
FIGURE 7.2: AN EXAMPLE OF ALPHA LUMINESCENT EXPERIMENT USING A VACUUM TO IMPROVE EMISSION INTENSITY. 187
FIGURE 7.3: PROPOSED LAYERED NEUTRON CONVERTER AND PHOSPHOR FOR POTENTIAL IMPROVEMENT IN DETECTION USING THIN FILMS. 190
FIGURE 9.1: RBS SPECTRUM OF SAMPLE 1........201
FIGURE 9.2: RBS SPECTRUM OF SAMPLE 2........202
FIGURE 9.3: RBS SPECTRUM OF SAMPLE 3........202
FIGURE 9.4: RBS SPECTRUM OF SAMPLE 4........203
FIGURE 9.5: RBS SPECTRUM OF SAMPLE 5........203
FIGURE 9.6: PIXE USING 2.5MEV PROTONS, NORMAL EXIT INTO X-RAY DETECTOR (60° BEAM INCIDENCE). 204
FIGURE 9.7: PIXE USING 2.5MEV PROTONS, 60° EXIT INTO X-RAY DETECTOR (NORMAL BEAM INCIDENCE). 204
FIGURE 9.8: THREE SAMPLES, 1.5MEV HE, NORMAL EXIT INTO X-RAY DETECTOR (60° BEAM INCIDENCE). 205
FIGURE 9.9: CHEMICAL COMPOSITION OF SAMPLE 1 IN RESPECT TO THICKNESS. 205
FIGURE 9.10: CHEMICAL COMPOSITION OF SAMPLE 2 IN RESPECT TO THICKNESS. 206
FIGURE 9.11: CHEMICAL COMPOSITION OF SAMPLE 3 IN RESPECT TO THICKNESS. 206
FIGURE 9.12: CHEMICAL COMPOSITION OF SAMPLE 4 IN RESPECT TO THICKNESS. 207
FIGURE 9.13: CHEMICAL COMPOSITION OF SAMPLE 5 IN RESPECT TO THICKNESS 207

9.3 Tables

TABLE 2.1: NEUTRON TYPES GROUPED BY THEIR ENERGIES [5, 6]. 5

TABLE 2.2: COMMON NEUTRON REACTIONS AND THE ENERGY DISTRIBUTION TO THE PRODUCTS [9, 10]. ...12

TABLE 2.3: CAPTURE CROSS-SECTION OF A GROUP OF ELEMENTS ALONG WITH THEIR DISTRIBUTION ENERGY [21]. 12

TABLE 2.4: PROPERTIES OF YAP, YAG AND ZNS:AG ALPHA DETECTORS. 15

TABLE 2.5: POTENTIAL SCINTILLATORS WITH CORRESPONDING PHOTON EMISSION AND DECAY CONSTANT [11, 33, 43-45]. 15

TABLE 2.6: RISE-TIME PROPERTIES OF Α AND Β(Γ) RAYS OBSERVED FROM THE YAP AND ZNS:AG POWDERS. 16

TABLE 2.7 .Α- AND Γ-LIGHT YIELD (Λ_α, Λ_γ; PHOTOELECTRONS/MEV) OF CSI:TL, CSI:NA AND BaF_2 CRYSTALS 22

TABLE 2.8: THE BINDING ENERGIES OF COMBINATIONS OF ELEMENTS WITHIN THE TARGET MATERIAL [30]. 37

TABLE 2.9: DEPOSITION PARAMETERS USED FOR RF MAGNETRON SPUTTER DEPOSITION OF ZNS [72]. 39

TABLE 2.10: EMISSION INTENSITY OF THREE PHOSPHORS AND THEIR DECAY TIME. 45

TABLE 3.1: RELATIVE INTENSITIES OF ELEMENTS DETECTED USING RBS. 75

TABLE 3.2: PROPERTIES OF LASERS USED TO EXCITE THE PHOSPHOR. 78

TABLE 4.1: EFFICIENCY OF ZNS:AG,CL (PHOSPHOR TECHNOLOGY) TO DIFFERENT LASER EXCITATIONS. ..92

TABLE 4.2: STABILITY OF LASER POWER 94

TABLE 4.3: PEAK INTENSITY MEASUREMENT FROM THE EMISSION SPECTRA OF THREE EXCITATION WAVELENGTHS AND THEIR COMPARISON TO THE EXPECTED RELATIVE INTENSITIES 99

TABLE 4.4: PEAK INTENSITY AND FWHM OF THE ZNS:AG,CL PHOSPHOR FROM LITERATURE AND MEASUREMENT. 99

TABLE 4.5: EXTRAPOLATED DATA COMPARING THE FWHM OF THE ZNS:AG,CL PHOSPHOR BY TWO SPECTROMETERS. 104

TABLE 4.6: WAVELENGTH OF PEAK INTENSITY AND FWHM DATA FOR THE PHOSPHOR SAMPLES EXCITED BY A N_2 LASER. 107

TABLE 4.7: INTENSITY MEASUREMENTS FOR THE PHOSPHORS USING TWO SPECTROMETERS. 109

Table 4.8: The data extracted from decay curves of three phosphors at three wavelengths. 114
Table 4.9: Extrapolated data of peak intensity measurements for the ZnS:Ag,Cl (ISIS) phosphor. 119
Table 5.1: Applied power to the heater, the corresponding deposition temperatures and number of times it was carried out....128
Table 5.2: Applied power to the heater, the corresponding annealing temperatures and number of times it was carried out....128
Table 5.3: Applied power to the electrode and number of times it was carried out. 128
Table 5.4 The partial pressure of processing gas and the number of times it was carried out. 128
Table 5.5: The range of values applied to thin film growth. 128
Table 5.6: Thin film thickness measurements using reflectance spectroscopy and the error observed for each growth. 131
Table 5.7: A comparison of thickness measurements of thin films grown from a ZnS:Ag,Cl target. 136
Table 5.8: Position of a XRD peak created by an amorphous Si disk to be used as a control. 138
Table 5.9: Positional data and FWHM of XRD peaks exhibited by ZnS:Ag,Cl powder. 139
Table 5.10: Positional data and FWHM of XRD peaks exhibited by ZnS and ZnS:Ag,Cl. 140
Table 5.11: Positional data and FWHM of XRD peaks exhibited by ZnS:Ag,Cl powder and thin film grown on a Si substrate from ZnS:Ag,Cl....142
Table 6.1 Diffusion coefficients of the elements of ZnS:Ag within a ZnS lattice....150
Table 6.2: Implantation concentrations of silver and chlorine ions into a ZnS thin film. ...156
Table 6.3: Implantation Energies and concentrations for the silver and chorine ions....156
Table 6.4: The sample analysed by ion beam analysis, their number and reason for analysis. 166
Table 6.5: Concentration of Zn and S in the thin film samples tested by RBS. 178

9.4 Equations

EQUATION 1 12

EQUATION 2 31

EQUATION 3 35

EQUATION 4 36

EQUATION 5 40

EQUATION 6 64

EQUATION 7 66

EQUATION 8 76

EQUATION 9 82